Electron Spectroscopy of Novel Charge Transfer Systems Based on Polycyclic Aromatic Hydrocarbons

Dissertation

zur Erlangung des Grades
„Doktor der Naturwissenschaften“
am Fachbereich Physik , Mathematik und Informatik
der Johannes Gutenberg-Universität
in Mainz

vorgelegt von

Katerina Medjanik (Kateryna Medyanyk)
geboren in Sumy/ Ukraine

Mainz, Januar 2011

1. Berichterstatter:

2. Berichterstatter:

3. Berichterstatter:

Tag der mündlichen Prüfung: 9. Mai 2011

D77 Mainzer Dissertation

Zusammenfassung

Organische Ladungstransfersysteme weisen eine Vielfalt von konkurrierenden Wechselwirkungen zwischen Ladungs-, Spin- und Gitterfreiheitsgraden auf. Dies führt zu interessanten physikalischen Eigenschaften, wie metallische Leitfähigkeit, Supraleitung und Magnetismus. Diese Dissertation beschäftigt sich mit der elektronischen Struktur von organischen Ladungstransfersalzen aus drei Material-Familien. Dabei kamen unterschiedliche Photoemissions- und Röntgenspektroskopietechniken zum Einsatz. Die untersuchten Moleküle wurden z.T. im MPI für Polymerforschung synthetisiert. Sie stammen aus der Familie der Coronene (Donor *Hexamethoxycoronen* HMC und Akzeptor *Coronen-hexaon* COHON) und Pyrene (Donor *Tetra-* und *Hexamethoxypyren* TMP und HMP) im Komplex mit dem klassischen starken Akzeptor *Tetracyanoquinodimethan* (TCNQ). Als dritte Familie wurden Ladungstransfersalze der *κ-(BEDT-TTF)$_2$X* Familie (X ist ein monovalentes Anion) untersucht. Diese Materialien liegen nahe bei einem Bandbreite-kontrollierten Mottübergang im Phasendiagramm. Sie wurden in der Gruppe von Prof. Lang (Univ.Frankfurt) synthetisiert.

Für Untersuchungen mittels *Ultraviolett-Photoelektronenspektroskopie* (UPS) wurden UHV-deponierte dünne Filme erzeugt. Dabei kam ein neuer Doppelverdampfer zum Einsatz, welcher speziell für Milligramm-Materialmengen entwickelt wurde. Diese Methode wies im Ladungstransferkomplex im Vergleich mit der reinen Donor- und Akzeptorspezies energetische Verschiebungen von Valenzzuständen im Bereich weniger 100meV nach. Ein wichtiger Aspekt der UPS-Messungen lag im direkten Vergleich mit ab-initio Rechnungen.

Das Problem der unvermeidbaren Oberflächenverunreinigungen von lösungsgezüchteten 3D-Kristallen wurde durch die Methode *Hard-X-ray Photoelectron Spectroscopy* (HAXPES) bei Photonenenergien um 6 keV (am Elektronenspeicherring PETRA III in Hamburg) überwunden. Die große mittlere freie Weglänge der Photoelektronen im Bereich von 15 nm resultiert in echter Volumensensitivität. Die ersten HAXPES Experimente an Ladungstransferkomplexen weltweit zeigten große chemische Verschiebungen (mehrere eV). In der Verbindung HMP_x-$TCNQ_y$ ist die N1s-Linie ein Fingerabdruck der Cyanogruppe im TCNQ und zeigt eine Aufspaltung und einen Shift zu höheren Bindungsenergien von bis zu 6 eV mit zunehmendem HMP-Gehalt. Umgekehrt ist die O1s-Linie ein Fingerabdruck der Methoxygruppe in HMP und zeigt eine markante Aufspaltung und eine Verschiebung zu geringeren Bindungsenergien (bis zu etwa 2,5eV chemischer Verschiebung), d.h. eine Größenordnung größer als die im Valenzbereich.

Als weitere synchrotronstrahlungsbasierte Technik wurde *Near-Edge-X-ray-Absorption Fine Structure* (NEXAFS) Spektroskopie am Speicherring ANKA Karlsruhe intensiv genutzt. Die mittlere freie Weglänge der niederenergetischen Sekundärelektronen (um 5 nm). Starke Intensitätsvariationen von bestimmten Vorkanten-Resonanzen (als Signatur der unbesetzte Zustandsdichte) zeigen unmittelbar die Änderung der Besetzungszahlen der beteiligten Orbitale in der unmittelbaren Umgebung des angeregten Atoms. Damit war es möglich, präzise die Beteiligung spezifischer Orbitale im Ladungstransfermechanismus nachzuweisen. Im genannten Komplex wird Ladung von den Methoxy-Orbitalen $2e(\pi^*)$ und $6a_1(\sigma^*)$ zu den Cyano-Orbitalen b_{3g} und $a_u(\pi^*)$ und – in geringerem Maße – zum b_{1g} und $b_{2u}(\sigma^*)$ der Cyanogruppe transferiert. Zusätzlich treten kleine energetische Shifts mit unterschiedlichem Vorzeichen für die Donor- und Akzeptor-Resonanzen auf, vergleichbar mit den in UPS beobachteten Shifts.

Abstract

Organic charge-transfer (CT) compounds are a class of materials that exhibit a variety of competing interactions between the charge, spin and lattice degrees of freedom, leading to a wide range of interesting physical properties. Metallic conductivity, superconductivity and magnetism result from the high degree of electronic correlation. This thesis focuses on the electronic structure of CT-compounds from three families of materials by applying various photoemission and X-ray techniques. The studied molecules were synthesized in the MPI für Polymerforschung. They derive from the parent molecules coronene (donor *hexamethoxy-coronene* HMC; acceptor *coronene-hexaone* COHON) and pyrene (donors *tetra-* and *hexamethoxypyrene* TMP and HMP) in complex with the classical strong acceptor *tetracyano-quinodimethane* TCNQ. As third family of compounds we studied CT-salts of κ-*(BEDT-TTF)$_2$X* type (X being various kinds of monovalent anions), which are located close to a bandwidth-controlled Mott transition in the phase diagram. These samples were synthesized in the group of Prof. Lang (University of Frankfurt).

For *ultraviolet photoelectron spectroscopy* (UPS) studies as UHV co-deposited thin films were prepared *in-situ*, employing a special double evaporator developed for milligram amounts of materials. This method revealed energetic shifts of valence levels (in the range of a few 100 meV) in CT complexes in comparison with the pure donor and acceptor moieties. An important aspect of the UPS measurements is the direct quantitative comparison with *ab-initio* calculations.

The problem of unavoidable surface contamination for solution-grown crystals was overcome by applying *hard X-ray photoelectron spectroscopy* (HAXPES) at photon energies of 6 keV at the new storage ring PETRA III in Hamburg. The large mean-free-path of about 15 nm range results in true bulk sensitivity. The first HAXPES experiment on CT complexes worldwide revealed large chemical core-level shifts of the order of several eV in the CT-complexes. HAXPES measurements were performed for thin-film samples and fractions of microcrystallites in different stoichiometries. In the compound HMP_x - $TCNQ_y$ the nitrogen 1s line (being a fingerprint of the cyano-group in TCNQ) shows a splitting and a shift to *higher* binding energies (up to about 6 eV) with increasing HMP content. Vice versa, the oxygen 1s line (being a fingerprint of the methoxy-group in HMP) shows a marked splitting and a shift to *lower* binding energies by up to about 2.5 eV, i.e. by more than one order of magnitude more than the shifts of the valence levels measured by UPS.

As second Synchrotron-radiation based technique, *near-edge X-ray absorption fine structure* (NEXAFS) spectroscopy was intensively used. The slow secondary electrons detected have a mean-free-path in region of 5 nm. Also for this technique the probing depth was large enough to enable the investigation of solution-grown crystals. The experiments from several beamtimes at the storage ring ANKA, Karlsruhe, revealed that NEXAFS provides a most direct access to details of the CT mechanism. It probes the unoccupied densities of states in the vicinity of a given atom. Strong intensity variations of certain pre-edge resonances directly show the change of occupation of the corresponding orbitals. This orbital selectivity allows to precisely elucidate the participation of specific orbitals in the charge-transfer process. Strong changes in certain pre-edge peaks reveal that charge is transferred from methoxy-orbitals 2e(π^*) and 6a_1(σ^*) to the cyano-orbitals b_{3g} and a_u(π^*) and - to a weaker extent - to b_{1g} and b_{2u}(σ^*). In addition, small energetic shifts with different signs for donor and acceptor resonances appear, similar as observed in UPS. The intensity of the 2e resonance directly reflects the anionic character of the methoxy group.

Outline

1. Introduction

Motivation

Organic charge-transfer (CT) compounds are a class of materials that exhibit a variety of competing interactions between the charge, spin and lattice degrees of freedom, leading to a wide range of interesting physical properties. Metallic conductivity, superconductivity and magnetism are properties resulting from the high degree of electronic correlation. Many of the organic conductors and superconductors are based on the bis (ethylenedithio) tetrathiafulvalene (BEDT-TTF) donor and various acceptors [Ish98, Kin90, Rit78]. Furthermore, poly cyano derivatives have mainly been used as acceptors like tetracyanoquinodimethane (TCNQ) [Nal97]. New organic CT-materials became more and more interesting, because they can behave as both semiconductors and insulators due to their covalent bonds. Flat aromatic molecules like polycyclic aromatic hydrocarbons (PAHs) are attracting much attention because of their extended π-electron systems [Cra03, Xia06]. The extension of the π-system would lead to a lowering of intramolecular Coulomb repulsion in the anions of the acceptors, resulting in more stable radical anions and might yield highly conducting CT complexes [Gar74].

Unusual behaviour was observed in magnetic, ferroelectric and optical properties, along with anomalies in conductivity, in the thermal expansion coefficient and in the low-frequency electronic noise [Toy07]. As a result, these materials are characterized by complex phase diagrams, substantial parts of which are only barely understood. Small variations of parameters such as temperature, pressure, or chemical composition can alter the materials' properties significantly. Therefore the understanding of the underlying mechanisms in this complex scenario poses a major challenge in basic research. Being prototypes for highly interacting systems, CT salts are one major issue studied in the Transregional Collaborative Research Centre SFB/TR 49 *Condensed Matter Systems with Variable Many-Body Interactions.* On the application side, CT compounds bear a high potential for future organic electronics and sensor applications [Roh98, Rie08, Suz06, Cas09, Cor96, Ish98].

This thesis focuses on the determination of the electronic structure of organic charge-transfer salts by applying a number of different photoemission and X-ray techniques. Strong emphasis is placed on the search for new CT complexes. New molecules with tuneable donor and acceptor strength such as *hexamethoxycoronene, coronene-hexaone, tetramethoxypyrene* and others have been synthesized in the Max Planck Institut für Polymerforschung in the group of Prof. Müllen and Prof. Baumgarten. These molecules with tailored properties serve as building blocks in new charge-transfer complexes. The electron and X-ray spectroscopic techniques of the present work are complemented by scanning tunnelling spectroscopy, performed in the group of Prof. Elmers in our institute and by diffraction and conductivity measurements by the group of Prof. Huth (Physikalisches Institut, Goethe-Universität Frankfurt/Main).

In addition to these extensive studies of novel CT compounds, we also performed a first electron spectroscopic investigation of CT-salts from the *κ-(BEDT-TTF)$_2$X family*, which are located close to a bandwidth-controlled Mott transition in the phase diagram [Mue02, Bar10]. These samples were synthesized in the group of Prof. Lang (Physikalisches Institut, Goethe-Universität Frankfurt).

As the initially-used technique of ultraviolet photoelectron spectroscopy (UPS) is highly surface sensitive, the mixed phases of donors and acceptors were fabricated by *in-situ* co-deposition in ultrahigh vacuum. In the third year of the present work, the bulk sensitive methods of near-edge X-ray absorption fine structure (NEXAFS) spectroscopy and hard X-ray photoelectron spectroscopy (HAXPES) were employed, using Synchrotron radiation at the storage rings ANKA, Karlsruhe and PETRA III, Hamburg. Due to their large information depth, these new techniques allowed studing the electronic structure of *ex-situ* prepared bulk crystals.

The purpose of this thesis was to gain comprehensive knowledge about the electronic structure of novel π-conjugated donor and acceptor moieties deposited in thin films, their behaviour at the interface to the surface of the supporting metal (clean Au films and SiO_x) and, as central question, the change of electronic structure upon complex formation.

Novel charge transfer compounds based on functionalized polycyclic aromatic hydrocarbons

Organic molecules with π-conjugated ring structures offer a huge potential for the design of novel charge-transfer compounds. Research in this field is not only fuelled by potential applications in organic electronics but also by fundamental questions regarding the nature of the new electronic states formed in the CT complex. It has long been known that *graphite* becomes superconducting when crystallized with a CT counterion in an intercalation compound [Han65]. Likewise, C_{60} shows superconductivity when doped with alkali atoms [Ram94]. The wavefunctions of the electronic π-system can be sensitively tuned via a change of the charge density through doping or through the formation of charge-transfer complexes. Similarly, the influence of doping on the special electronic structure of *graphene* is subject to intensive research [Sar07]. These properties of graphite-like conjugated systems thus draw attention to *polycyclic aromatic hydrocarbons* (PAHs).

Such PAHs have recently been made larger and larger and the molecules are then called *nanographenes* [Mue08, Wat01, Rn03, Wup07]. This versatile class of materials can be synthesized as shown for a large variety of species. Large planar PAHs with 90 carbon atoms and more can be synthesized in a bottom-up approach with the desired size, structure, and symmetry. Moreover, synthesis routes have been developed for functionalization, i.e., the defined attachment of ligand atoms or groups at the periphery. This has, for instance, been shown for the medium-size molecule *coronene* ($C_{24}H_{12}$) [Rie08]. The synthetic approach facilitated the realization of a new set of donor and acceptor molecules with a systematic variation of the electronic properties *via* the type and number of substituents at the periphery. Retaining the coronene ring system, the electron affinity and ionization energy can be controlled in a wide range from typical donor behavior for different degrees of *methoxy* substitution to strong acceptor behavior for *coronene-ketones*.

In the condensed phase of such molecules novel interesting phenomena can be expected, e.g. superconductivity, found for doped graphite, is also expected for appropriately modified large PAHs and nanographenes. Kato *et al.* predicted superconductivity of coronene in a charge-transfer configuration with transition temperatures of several Kelvin [Kat02]. Up to now, only few coronene-based charge-transfer compounds have been found. As early as 1977, Truong and Bandrauk crystallized a compound consisting of coronene and the prototypical acceptor *tetracyanoquinodimethane* ($C_8N_4H_4$, abbreviated as *TCNQ*) from solution and studied the optical properties of powder samples [Tru77, Lo05, Mya05]. Later, Chi *et al*. succeeded in crystallizing large single crystals of coronene-TCNQ that exhibit

alternate stacking of the donor and acceptor moieties [Chi04]. The amount of charge-transfer was estimated to be of the order of 0.2-0.3 *e* per molecule.

The present work presents the first electron and X-ray spectroscopic study of CT-compounds based on PAH-derived donors and acceptors. For various complexes of the coronene and pyrene-derivatives, the latter in combination with TCNQ, we observed shifts in the electronic levels in UPS, NEXAFS and HAXPES. Level positions and characteristic shifts of several 100 meV in UPS can be understood in terms of DFT calculations for these molecules (Thesis Shahab Naghavi, group Prof. Felser, Inst. für Anorganische und Analytische Chemie, Univ. Mainz). In a recent HAXPES experiment we have observed core-level shifts up to several eV upon formation of the complex. The shifts are fingerprints of a charge transfer and give evidence of the formation of novel all organic charge-transfer salts. The most direct spectroscopic evidence, however, are strong intensity changes of pre-edge resonances in NEXAFS. This discovery gives us a handle on the relative occupation of specific orbitals, being involved in the charge-transfer mechanism. The complexes of the novel donors hexa- and tetramethoxypyrene in different stoichiometries with the classical acceptor TCNQ indicate a systematic pathway to the synthesis of a new class of materials showing a valence instability, i.e. a neutral-ionic phase transition.

Charge transfer salts from the κ-(BEDT-TTF)$_2$X family

The organic (super-) conductors of the κ-(BEDT-TTF)$_2$X (X = $Cu_2(CN)_3$, $Cu(SCN)_2$, $Cu[N(CN)_2]Cl$, $Cu[N(CN)_2]Br$) family are characterized by a strongly-correlated π-electron system with close proximity of superconductivity and an antiferromagnetic insulating state (Mott metal-insulator transition). The BEDT-TTF molecules show strong dimerization. A charge transfer from BEDT-TTF to the polymeric X layer of 1 electron per dimer leads to a half-filled quasi-2D metallic conduction band.

This family of materials is synthesized and intensively studied in the TR 49 with special emphasis on questions related to the Mott transition - a key phenomenon in strongly correlated systems - and the nature of the nearby anomalous states. In experiments performed within the TR 49 anomalous lattice and specific heat effects have been observed upon crossing the Mott transition line. However, the complex phase diagram poses a major challenge to both experiment and theory and many basic questions are presently unsolved. Among these, the role of the *electronic degrees of freedom* in the so-called T^*-transition to the anomalous metallic state (for κ-Br, $T^* \sim 45$ K) and in the thermal glass-like transition ($T_g \sim 77$ K) is largely unknown. In a measuring campaign at the HAXPES-beamline of PETRA III we have performed the first pilot experiment using 6 keV-photons, looking at the sulphur 2s and carbon 1s core level spectra in 2 samples of this family of CT-salts. As sulphur is only contained in the metallic BEDT-TTF layer, its core-level spectrum provides a local probe in the donor material. The bulk sensitivity of HAXPES (probing depth 15 nm) overcomes the problem to obtain surfaces of good quality for such highly reactive delicate materials.

This experiment revealed that the electronic system reacts strongly on both transitions: With increasing temperature, close to the T^*-transition, additional core-level signals appear at higher binding energies. When approaching the thermal glass-transition temperature T_g, the intensity of the S 2s main line drops to 40 % of its initial value and several new peaks appear, being strongly shifted by up to more than 10 eV. Above the thermal glass-like transition, all satellites disappear instantaneously and the main line intensity is restored to its

initial value. This gives strong evidence for changes in the electronic degrees of freedom at the T^* crossover and indicates that the latter may be involved in the glass-like transition as well, as was already speculated in literature [Mue02, Wol07].

Our first experiment on this highly interesting class of *κ-phase* CT-compounds gives by far not a complete picture of what happens with the electronic structure in the regime of the special anomalous states that occur in the vicinity of the Mott transition. However, the first data show very clearly that the electronic system is largely involved or at least strongly responds to the various low-temperature phase transitions.

The measurements on the fully protonated and fully deuterated *κ*-(BEDT-TTF)$_2$Cu[N(CN)$_2$]Br constitute a *proof-of-principle* of the feasibility of HAXPES studies for this fascinating class of highly-correlated 2D systems. The results show how core-level spectroscopy with bulk sensitivity provides direct access to subtle electronic details in the vicinity of the Mott transition and shine a light on the importance of the electronic degrees of freedom. The chapter on the measurements on this *κ-phase* CT-salt can be considered as basis for future systematic work on this and related classes of materials.

The thesis is organized as follows: chapter 2 presents the basics and the theoretical background of the underlying physics of CT systems and of the electron and X-ray spectroscopies. Chapters 3 and 4 describe the experimental part, i.e. the measurement and the sample preparation techniques, respectively. Chapters 5 and 6 are the main part of the thesis and present and discuss the results for the coronene and pyrene derivatives, respectively. The short chapter 7 presents the HAXPES results obtained in the first beamtime in November 2010. Chapter 8 gives a summary and a conclusion.

2. Basics and Theoretical Background

The novel types of functionalized polycyclic aromatic hydrocarbons (PAHs) studied in this work contains several aromatic rings with hydrogen plus functional groups (keto- or methoxy-groups) at their periphery. Therefore we discuss the corresponding bonds (C=O, C-OCH_3) in some detail. Simple single-electron theory (*Hückel* approximation) can describe the carbonyl bond in reasonable approximation as will be discussed in section 2.1. For the methoxy group, a many-electron approach like *Hartree-Fock* (HF) is indispensible. The UPS spectra shown and discussed in sections 5.2 and 6.3 are compared with *density functional theory* (DFT) calculations as discussed in 2.2. Finally, the metallic behaviour of the materials of the *κ-(BEDT-TTF)$_2$X*-family discussed in section 7.2 exhibit hopping conductivity. Thus they are properly described within the *Hubbard model*, see section 2.3. No calculations have been performed in the framework of this thesis. However, in order to understand the theoretical data and their discussion in the results sections, we discuss the basics of the three theoretical scenarios in sections 2.1 – 2.3.

The theoretical background of the techniques of *photoemission*, *X-ray absorption* and *near-edge X-ray absorption fine structure* is discussed in sections 2.4 - 2.6, respectively. The experimental aspects of these spectroscopies will be discussed in chapter 3. Finally, the basics of charge transfer (CT) systems are presented in section 2.7, in order to show the present state of knowledge.

2.1 Single-Electron Theory (Hückel)

The Atomic Orbitals of a Carbon Atom, C—H and C—C Bonds

Carbon has the electron structure $1s^2 2s^2 2p^2$. The 1s orbital does not contribute to bonding, because the two electrons in it are tightly bound to the nucleus and there is no significant overlap with valence orbitals. The electrons simply screen the nucleus, effectively giving it less positive charge. These 1s electrons are well suited for the core-level spectroscopies discussed in sections 3.3 and 3.4. The 2s orbital is spherically symmetric, but it has a node, with a wave function like that shown in Fig. 2.1a, and a contour plot like that in Fig. 2.1b.

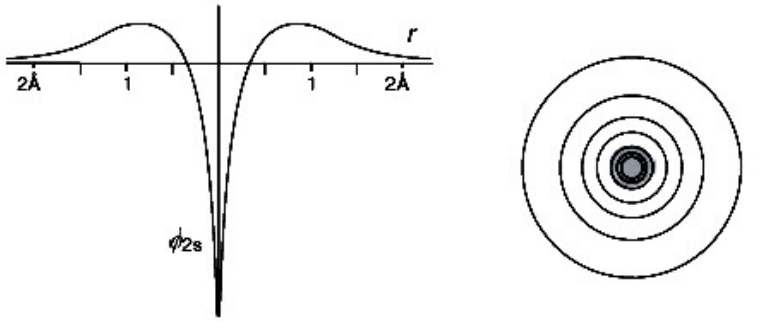

(a) Wave function of a 2s orbital on carbon

(b) Contours for the wave function

Figure 2.1 The 2s orbital of carbon (from [Fle10]).

The attractive force on the 2s electrons is high because the nucleus has six protons, even though this is offset by the larger average distance of the electrons from the nucleus and by

the shielding from the other electrons. Slater's rules suggest that the two 1s electrons reduce the nuclear charge by 0.85 atomic charges each, and the other 2s and the two 2p electrons reduce it by 3 x 0.35 atomic charges, giving the nucleus an effective charge of 3.25.

The 2p orbitals of carbon also have one node each, but they have odd parity. When described in Cartesian coordinates they point mutually at right angles, each one along the three axes, x, y and z. A plot of the wave function for the $2p_x$ orbital is shown in Fig. 2.2a, and a contour plot of a slice through the orbital is shown in Fig. 2.2b. Scale drawings of p orbitals based on the shapes defined by their functions would clutter up any attempt to analyze their contribution to bonding, and so it is conventional to draw much narrower lobes, as in Fig. 2.2c, and we keep in mind that this is not their true size and shape. In the free C-atom, the 2p orbitals (at –10.7 eV) are higher in energy than 2s (at –19.5 eV), because they are held on average further from the nucleus. When wave functions for all three p orbitals, p_x, p_y and p_z, are squared and summed, the overall electron probability has spherical symmetry, just like that in the corresponding s orbital, but the charge is concentrated further away from the nucleus.

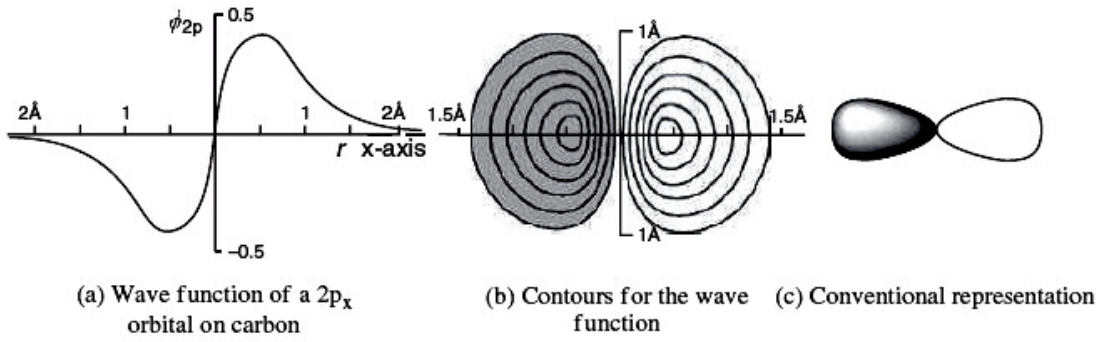

Figure 2.2 The $2p_x$ orbital of carbon (from [Fle10]).

Chemical bonds between carbon atoms are made up by overlap of s and p- orbitals, leading to sp^3 or sp^2 hypbride wavefunctions. The overlap integrals *S* are dependent upon the angles at which the two atoms approach each other. The overlap integral for a head-on approach of an s orbital of hydrogen along the axis of a p orbital of carbon with a lobe of the same sign in the wave function (Fig. 2.3a), leading to a σ–bond, grows as the orbitals begin to overlap (D), goes through a maximum when the nuclei are a little over 0.9 Å apart (C), drops rapidly as some of the s orbital overlaps with the back lobe of the p orbital (B), and goes to zero when the s orbital is centred on the carbon atom (A). In the last configuration, whatever bonding there would be from the overlap with the lobe of the same sign (unshaded lobes are conventionally used to represent a positive sign in the wave function) is exactly cancelled by overlap with the lobe (shaded) of opposite sign in the wave function. Of course this configuration is never reached, since the nuclei cannot coincide.

The overlap integral for two p orbitals approaching head-on in the bonding mode with matching signs (Fig. 2.3b) begins to grow when the nuclei approach (G), rises to a maximum when they are about 1.5 Å apart (F), falls to zero as overlap of the front lobes with each other is cancelled by overlap of the front lobes with the back lobes (E), and would fall eventually to –1 at superposition. The signs of the wave functions for the individual s

and p atomic orbitals can get confusing, that is why we adopt the convention of shaded and unshaded areas. In both cases, s overlapping with p and p overlapping with p, the overlap need not be perfectly head-on for some contribution to bonding to be still possible. For imperfectly aligned orbitals, the integral is inevitably less, because the build up of electron population between the nuclei, which is responsible for holding the nuclei together, is correspondingly less; furthermore, since the overlapping region will also be off centre, the nuclei are less shielded from each other. The overlap integral for a 1s orbital on hydrogen and a 2p orbital on carbon is actually proportional to the cosine of the angle of approach θ, where θ is 0° for head-on approach and 90° if the hydrogen atom is in the nodal plane of the p orbital [Fle10].

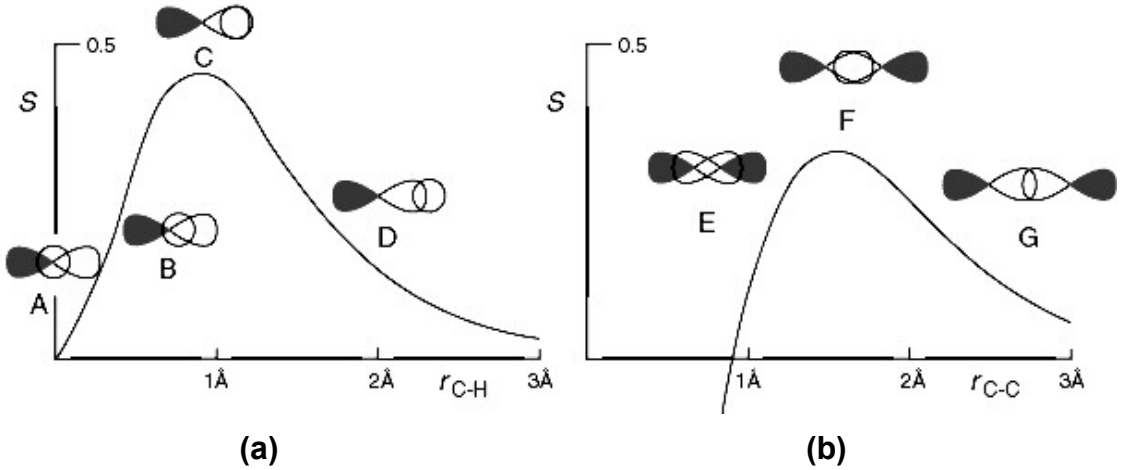

Figure 2.3 Overlap integrals *S* for σ overlap of a p orbital of carbon with a hydrogen s orbital (a) and between two p orbitals of carbon (b) (from [Fle10]).

π Bonds of Carbonyl (C=O)

This type of bond is present in the *keto-groups* of coronene-hexaone, discussed in chapter 5. Setting up the molecular orbitals of a C=O π bond is relatively straightforward, because the p orbitals in the π system in Hückel theory are free from the complicating effect of having to mix with contributions from s orbitals. In Fig. 2.4 the p_x orbital of oxygen is placed at a level somewhat more than 1β (β used as a reference with which to compare the degree of bonding in other π-bonding systems) below that of the p_x orbital on carbon, although not to scale. As with π bonds in general, the raising of the unoccupied π* and lowering of the occupied π orbitals above and below the atomic p orbitals is less than it is for a C—O σ bond, and less than the corresponding π bond between two carbon atoms. Both the $\pi_{c=o}$ and the $\pi^*_{c=o}$ orbitals are now lower in energy than the $\pi_{c=c}$ and $\pi^*_{c=c}$ orbitals of ethylene, respectively, which by definition are 1β above and 1β below the α level (in simple Hückel theory, the energy of the π orbital on carbon is given by the value α, which is used as a reference point from which to measure rises and drops in energy). The *polarisation of the carbonyl group* is away from carbon towards oxygen in the bonding orbital, and in the opposite direction in the antibonding orbital, as usual.

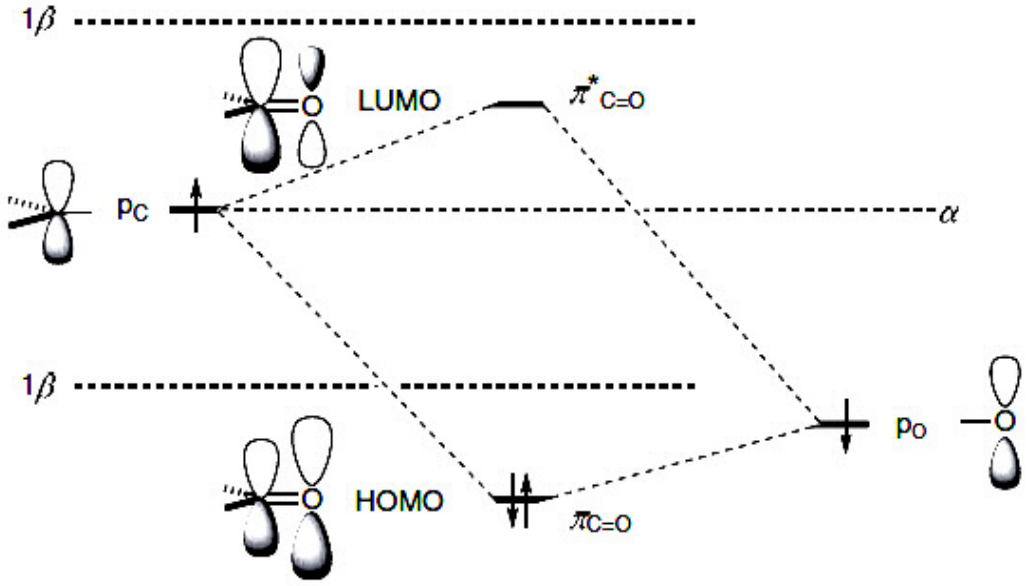

Figure 2.4 The carbonyl (C=O) π bond (from [Fle10]).

There is no set of fundamentally sound values for α and β to use in Hückel calculations with heteroatoms. Everything is relative and approximate. The values for energies and coefficients that come from simple calculations on molecules with heteroatoms must be taken only as a guide and not as rule. In simple Hückel theory, the value of α to use in a calculation is adjusted for the element in question X from the reference value for carbon α_0 by eq. 2.1.

Likewise, the β value for the C=C bond in ethylene β_0 is adjusted for C=X by eq. 2.2.

$$\alpha_x = \alpha_0 + h_x \beta_0 \tag{2.1}$$

$$\beta_{cx} = k_{cx} / \beta_0 \tag{2.2}$$

Single- particle theory can only describe simple systems. For the functional groups studied in the present work, it works until carbonyl (C=O). For the more complex systems like the methoxy group (C-OCH_3), many- electron theory is needed. In the following, we outline the basics of the Hartree-Fock (HF) self consistent field method and the density functional theory that was used for the calculation of orbital energies of the molecules investigated.

2.2 Many-Electron Theory (Hartree Fock, DFT)

Molecular orbital theory at the *Hartree-Fock* (HF) level and beyond is an important concept in chemistry and is employed extensively to describe chemical behavior. The highest occupied molecular orbital (HOMO) and lowest unoccupied molecular orbital (LUMO), in particular their energy positions, are most important for charge transfer complexes and also in general chemistry. Experimentally accessible quantities are the *ionization potential* (IP) and the *electron affinity* (EA). Koopmans' theorem suggests that the energy of the HOMO is in good approximation identical to the negative IP. Similarly, it suggests that the EA for an N-electron system is equal to the negative of the LUMO energy, assuming that the orbitals do not relax. However, the prediction of the EA using Koopmans' theorem is unreliable due to the large effect of orbital relaxation on the LUMO eigenvalue. In fact, the HF LUMO energy goes to zero in the complete basis set limit.

Hartree Fock (HF) Self Consistent Field

A common starting point for obtaining reasonably accurate wavefunctions for electrons in ground states of more complex systems is *the Hartree-Fock self-consistent-field* (SCF) method [Sza82]. The HF equations are derived from the quantum mechanical variation principle. ψ_e is approximated by a single Slater determinant ψ of N orthonormal one-electron spin-orbitals ϕ_i

$$\psi_e \cong \psi = \frac{1}{\sqrt{N!}} \left| \phi_1(x_1) \cdots \phi_N(x_1) \right|, \quad \left| \phi_1(x_N) \cdots \phi_N(x_N) \right|. \tag{2.3}$$

If the expectation value of the total energy,

$$\overline{E_0} = \langle \psi | H | \psi \rangle \tag{2.4}$$

is calculated from an approximate solution ψ of the Schrödinger equation then $\bar{E}_0$ is always larger than the exact ground state energy E_0 for the Hamiltonian. The difference

$$E_{cor} = \bar{E}_0 - E_0 \geq 0 \tag{2.5}$$

is called the *correlation energy* and reflects the fact that correlation, i.e., the dependence of the motion of one electron on the position of a second electron, cannot be represented by a simple product of functions of individual electron coordinates as given by eq. 2.3. If by variation of the $\phi_i's$ the total energy $\bar{E}_0$ is minimized we obtain N Hartree-Fock equations. The equation for the i-th electron at site x_1, with spin orbital $\phi_i(x_1)$ is given by

$$F\phi_i(x_1) = \sum_{k=1}^{N} \lambda_{ik} \phi_k(x_1) \tag{2.6}$$

For a molecule consisting of P different nuclei, the Fock operator *F* is given by

$$F = -\frac{\hbar^2}{2m}\nabla_1^2 - \sum_{n=1}^{P}\frac{Z_n e^2}{r_{1n}} + \sum_{k=1}^{N}\left(J_k - K_k\right) \tag{2.7}$$

where the *Coulomb operator* J_k, defined by the operation

$$J_k\left|\phi_i(x_1)\right\rangle = \left(\int \phi_k^*(x_2)\frac{e^2}{r_{12}}\phi_k(x_2)dx_2\right)\left|\phi_k(x_l)\right\rangle \tag{2.8}$$

gives the average repulsive Coulombic potential energy between all the electrons in the system and the electron at position x_1, and the *exchange operator*, defined as

$$K_k\left|\phi_i(x_1)\right\rangle = \left(\int \phi_k^*(x_2)\frac{e^2}{r_{l2}}\phi_i(x_2)dx_2\right)\left|\phi_k(x_1)\right\rangle \tag{2.9}$$

takes account of the spin correlation according to the Pauli principle.

This latter term is a consequence of the tendency of electrons with same spins to avoid one another, thereby lowering, on the average, the Coulomb repulsion between them. The wavefunctions depend on spin such that the terms in eq. 2.9 vanish unless ϕ_i and ϕ_k correspond to spins in the same direction.

For spectroscopists, it is a special form of the HF equations, namely the diagonal or canonic form, which is of fundamental importance. Fortunately it is always possible to find a unitary transformation of the orbitals ϕ_i under which the Fock operator, the total wavefunction ψ, and the total energy E_0 are invariant. This yields the canonical HF equations

$$F\phi_i(x_1) = E_i\phi_i(x_1) \tag{2.10}$$

The orbitals ϕ_i are called canonical orbitals and they have an orbital energy E_i. In practice, the HF equations are solved in the canonical form and for this reason the term "molecular orbitals" or "MOs" is used in the sense of canonical molecular orbitals.

Since J_k and K_k depend on all $\phi_i's$, the integro-differential equations 2.10 have to be solved self-consistently. This involves the evaluation of matrix elements of the Fock operator,

$$E_i = \left\langle\phi_i(x_1)\middle|F\middle|\phi_i(x_1)\right\rangle = H_{ii} + \sum_{k=1}^{N}\left(J_{ik} - K_{ik}\right) \tag{2.11}$$

where we have introduced the following integrals:

$$H_{ii} = \int \phi_i^*(x_1)\left(-\frac{\hbar^2}{2m}\nabla_1^2 - \sum_{n=1}^{P}\frac{Z_n e^2}{r_{1n}}\right)\phi_i(x_1)dx_1, \tag{2.12}$$

$$J_{ik} = \int\int \phi_i^*(x_1)\phi_k^*(x_2)\frac{e^2}{r_{l2}}\phi_k(x_2)\phi_i(x_1)dx_2dx_1, \tag{2.13}$$

and

$$K_{ik} = \int\int \phi_i^*(x_1)\phi_k^*(x_2)\frac{e^2}{r_{12}}\phi_i(x_2)\phi_k(x_1)dx_2dx_1. \quad (2.14)$$

J_{ik} is called the *two-electron Coulomb integral* and K_{ik} the *two-electron exchange integral*. The iteration process is terminated when the difference in total energy between two consecutive iterations is less than some threshold value.

Density Functional Theory (DFT)

In 1964 Hohenberg and Kohn published a groundbreaking paper that was the birth of *density functional theory* DFT [Hoh64]. Shortly thereafter, Kohn and Sham [Koh65] introduced the concept of a non-interacting reference system built from a set of one-electron functions such that the major part of the kinetic energy can be computed to good accuracy. This leads to independent particle equations for the non-interacting system that can be considered soluble. They suggested using an expression similar to the non interacting Hartree-Fock approach in order to obtain the exact kinetic energy of a non-interacting reference system with the same density as the real interacting one. All unknown contributions are summarized in the *exchange-correlation energy E_{xc} functional*. It should be noted that no approximation is used in the Kohn-Sham approach and if E_{xc} was known, the total energy would be calculated exactly.

Over the decades, DFT has developed into a widely used class of quantum chemical methods because of its ability to predict relatively accurate molecular properties at reasonable computational effort. It has been widely used to calculate the electronic structure of molecules, solids and surfaces.

The experimental results presented in chapters 5 and 6 have been accompanied by DFT calculations. This theoretical basis is the main content of the thesis of Shahab Naghavi [Nag10b], so we only briefly recall the basic issues in this section.

Commonly used DFT exchange-correlation functionals that are continuum approximations, such as conventional GGA functionals, do not exhibit an integer discontinuity. Thus, their HOMO eigenvalues are shifted up from -IP by half of the magnitude of the discontinuity and similarly their LUMO eigenvalues are shifted down from -EA by the same amount. The calculated HOMO-LUMO gap gives a reasonable approximation to the lowest excitation energy. The calculations in [Nag10b] use the most popular hybrid functional, B3LYP.

DFT calculations for the donor-acceptor pair derived from the parent molecule coronene

The electronic structure of coronene is well known [Sch02, Yam09,Yam98]. However, for the hexaketo- (COHON) and hexamethoxy (HMC) -derivatives (see Fig. 2.5) substantial changes of molecular level binding energies and possibly their sequence are to be expected. DFT calculations turned out to be a valuable guideline for the orbital structure of the functionalized coronenes. The binding energies given below were calculated as total energy difference between the N-electron molecule and the (N-1)-electron molecule in the sudden approximation, i.e. without structural relaxation of the final ionic state. The calculation has proven to be very useful for the interpretation of the measured spectra. In particular, it predicts the trends of binding energy shifts induced by the different ligands in very good agreement with experiment. Moreover, it also predicts the trends induced by the formation of the complex in qualitative agreement with experiment (details concerning this

comparison are discussed in chapters 5 and 6). In this section we illustrate the powerful DFT approach as applied to the donor hexamethoxycoronene and to acceptor hexaketocoronene. These molecules can be chemically transformed in a single reaction step [Rie08].

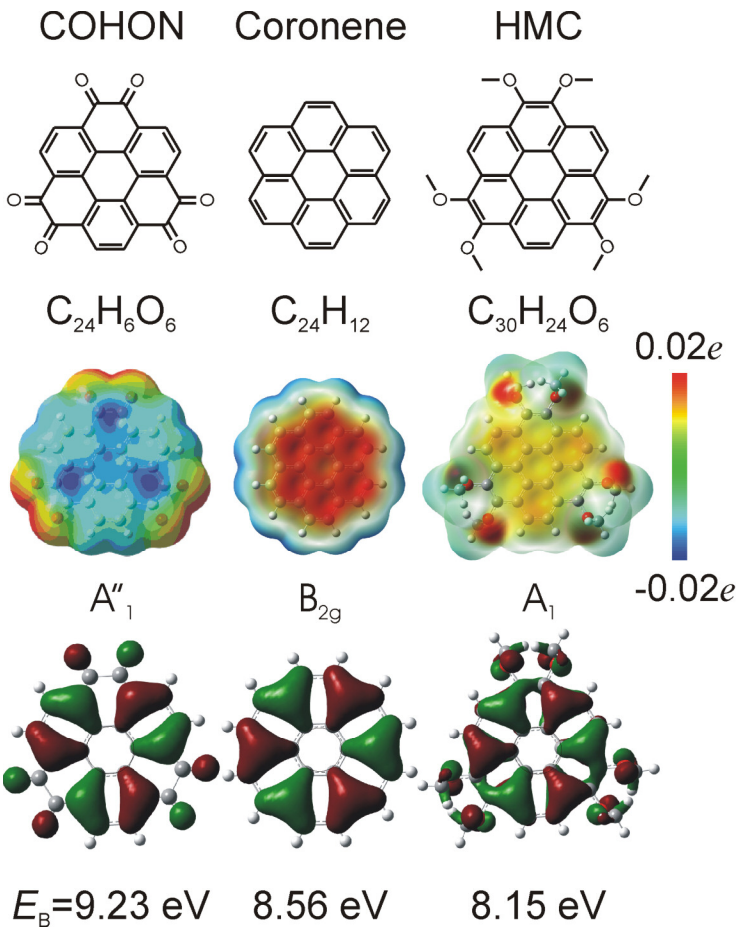

Figure 2.5 Molecular structure (top), charge density distribution (centre) and three equivalent orbitals (bottom) for the acceptor coronene-hexaone (COHON, point group D_{3h}), unsubstituted coronene (D_{6h}), and the donor hexamethoxycoronene (HMC, D_3).

All calculations were performed using the program code *Gaussian 03* [Fri03]. The energies and geometries of different molecules were calculated using B3LYP, equivalent to hybrid 3-parameter functional with Becke88 exchange part, Lee-Yang-Parr correlation part and approximately 20% exact HF exchange [Ste94]. The 6-31G basis set was employed for geometry optimization and energy calculation. The spin-unrestricted version of B3LYP (UB3LYP) was used when species were ionized as having an open-shell (one unpaired electron) electronic configuration. Vibrational frequency calculations on all species studied confirmed the stationary geometries. Atomic charge and molecular orbitals studies were based on Mulliken populational analysis.

Electron binding energies or ionization potentials of molecules are calculated by the delta self-consistent (ΔSCF) method applied together with the B3LYP hybrid functional [Gav08, Sie03, Gos75]. Vertical ionization potential are calculated using ΔSCF method in order to

compare with UPS data in which vertical ionization potentials (IP_v) final and ground state have the same geometry. First vertical ionization potentials ($IP_{v,1}$) are calculated as the difference in total energy between a molecule and its radical cation at the former geometry. For the higher ionization energies ($IP_{v,1+n}$), the energy of next higher orbitals $\varepsilon_{HOMO\text{-}n}$ as a uniform shift is

$$\begin{aligned} IP_{v,1} - \left|\varepsilon_{HOMO}\right| &= \Delta E \\ \left|\varepsilon_{HOMO-n}\right| + \Delta E &= IP_{v,1+n} \end{aligned} \tag{2.15}$$

According to the second equation the eigenvalues of the HOMO-n orbital should be used in order to calculate the electron binding energy (BE) of HOMO-n. A standard view about Kohn-Sham (KS) orbital energies of the occupied molecular orbitals lower than HOMO, is that they are merely auxiliary quantities. However, several authors have pointed to the interpretative power of KS orbitals in traditional qualitative molecular orbital scheme, and KS orbitals also show a uniform shift with respect to ionization energies. In this scheme, B3LYP with its exact Hartree-Fock exchange contribution leads to a better description of ionization energies by reduction the related shift. [Nag10a]. The electrons in the HOMO have the first ionization potential of E_B= 8.78 eV for COHON and 6.41 eV for HMC. HF/6-31G(d) calculation yields considerably higher binding energies, e.g. 8.86 eV for HMC. Fig. 2.5 also shows the charge density distribution, i.e., the charge deficit (blue) in the π-system of the acceptor molecule (left) and the charge excess (yellow-red) in the donor (right).

As a guideline for comparison with the measured UPS spectra orbital energies and symmetries of the lower-lying orbitals have also been calculated. The level schemes are shown in Fig. 2.6. Full and dashed lines denote π- and σ-orbitals, respectively. Equivalent orbitals are connected by lines. All E-type orbitals are double degenerate. The HOMO and LUMO have π-symmetry and consist of two degenerate states of E_{2u} (HOMO) and E_{1g} symmetry (LUMO) for coronene. The reduced symmetry in the substituted species deforms these orbitals substantially (in particular in the case of COHON). The change of the charge density leads to an increase in the HOMO binding energy by 2 eV for COHON and a decrease by 0.45 eV for HMC compared to the parent molecule coronene. The LUMO of HMC (E-symmetry, E= 1.3 eV) is the analogue of the LUMO of coronene, whereas the LUMO of COHON has a different symmetry (A_2'') and contains a substantial contribution from the oxygen ligands. The calculated LUMO-level for COHON lies close to the electron affinity level (EAL, chain line in Fig. 2.6) determined by cyclovoltammetry [Rie08]. The calculated HOMO binding energy for HMC is 0.9 eV larger than the cyclovoltammetry value for the ionization energy (IE).

For COHON, two orbitals with σ-symmetry are located close to the HOMO (E′ and A_1' labeled α and β) and another two close to E_B= 10 eV (E′ and A_2'). The orbital plots reveal that these are to a large extent oxygen $2p_{x,y}$-like, with only small amplitudes of the wavefunctions at the neighboring C-atoms of the ring system. The former shows even, the latter odd symmetry with respect to the mirror plane between the two adjacent O-atoms. The fact that these states are oxygen-derived is important for the interpretation of the measured spectra (see below). These orbitals have no analogues in the parent molecule coronene. However, there are equivalent orbitals in HMC, also labeled α, β. The π-orbital A_1'' of COHON (E_B= 9.23 eV), showing three-fold rotational symmetry, is equivalent to B_{2g} of coronene (E_B= 8.56 eV) and to A_1 of HMC (E_B= 8.15 eV). As an example, these three equivalent orbitals are shown in Fig. 2.5 (bottom). Orbitals E" and A_2" (E_B= 10.33 eV and

10.70 eV, labeled δ and γ, respectively) have π-symmetry and contain only small contributions from oxygen $2p_z$.

For HMC there is no mirror plane, so the distinction of π- and σ-orbitals is no longer valid. However, many of the orbitals involving the aromatic ring are to a large extent π- or σ-like with only small deviations from the pure symmetry. Full and dashed lines for HMC denote such "π- or σ-like" symmetry, in analogy to COHON and coronene. The topmost four occupied orbitals have π-like symmetry (E=HOMO, E, A_2 and A_1 at E_B= 6.41 eV, 7.7 eV, 7.8 eV and 8.15 eV, respectively). They are the analogues of the topmost four coronene orbitals as denoted by the connecting lines in Fig. 2.6. The σ-like orbitals E and A_1 (close to E_B= 8.4 eV, labeled α and β) show an interesting behaviour. They are the analogues of E′ and A_1′ in COHON (α and β, close to the HOMO) except that in HMC the H-atoms of the methoxy group are involved. The binding energies of levels α and β in HMC and COHON differ only slightly. In contrast, π-like levels like δ and γ appear substantially shifted. We thus can conclude that σ-like orbitals are much less affected by the charge depletion or charge excess of the acceptor and donor moieties. Some HMC orbitals deviate strongly from π- or σ-symmetry; they are denoted by dotted lines.

It is eye-catching in Fig. 2.6 that the whole level scheme is shifted substantially downwards (to higher orbital energies) for COHON and slightly upwards for HMC with respect to coronene, serving as "neutral" reference. The six double-bonded oxygen atoms effectively pull charge *out of* the π-system (thereby increasing E_B), whereas the six methoxy groups donate electron charge *into* the π-system (decreasing E_B). This is further quantified by the Mullikan population analysis. The large dipole moment of the keto-bond is evident (-0.420 e at the O-atom *vs.* +0.348 e at the C-atom). The bond of the methoxy group to the aromatic edge is also polar (-0.536 e at the O-atom *vs.* +0.237 e at the C-atom of the aromatic ring), but it is partially shielded by the CH_3 group (-0.218 e at the C-atom and +0.149 e, +0.158 e and +0.170 e at the three H-atoms).

As a consequence of this intramolecular charge-transfer also the bond lengths change (calculated for free molecules). The methoxy groups increase the C-C distance slightly, the keto groups increase it strongly and thereby lead to a decrease in the intramolecular forces. For unsubstituted coronene the C-C bond length at the periphery is 0.1372 nm, at the inner ring 0.1427 nm. The distance at the substituted site is expanded, for HMC by about 1%, for COHON by about 12% (and still by 2 % in the inner ring). The interaction of the keto-bonds with the aromatic core also shows up in the optical spectra and is the reason for the red color of this compound. In addition, the absorption bands become markedly broadened when an increasing number of keto groups are added to the coronene core as observed experimentally [Rie08].

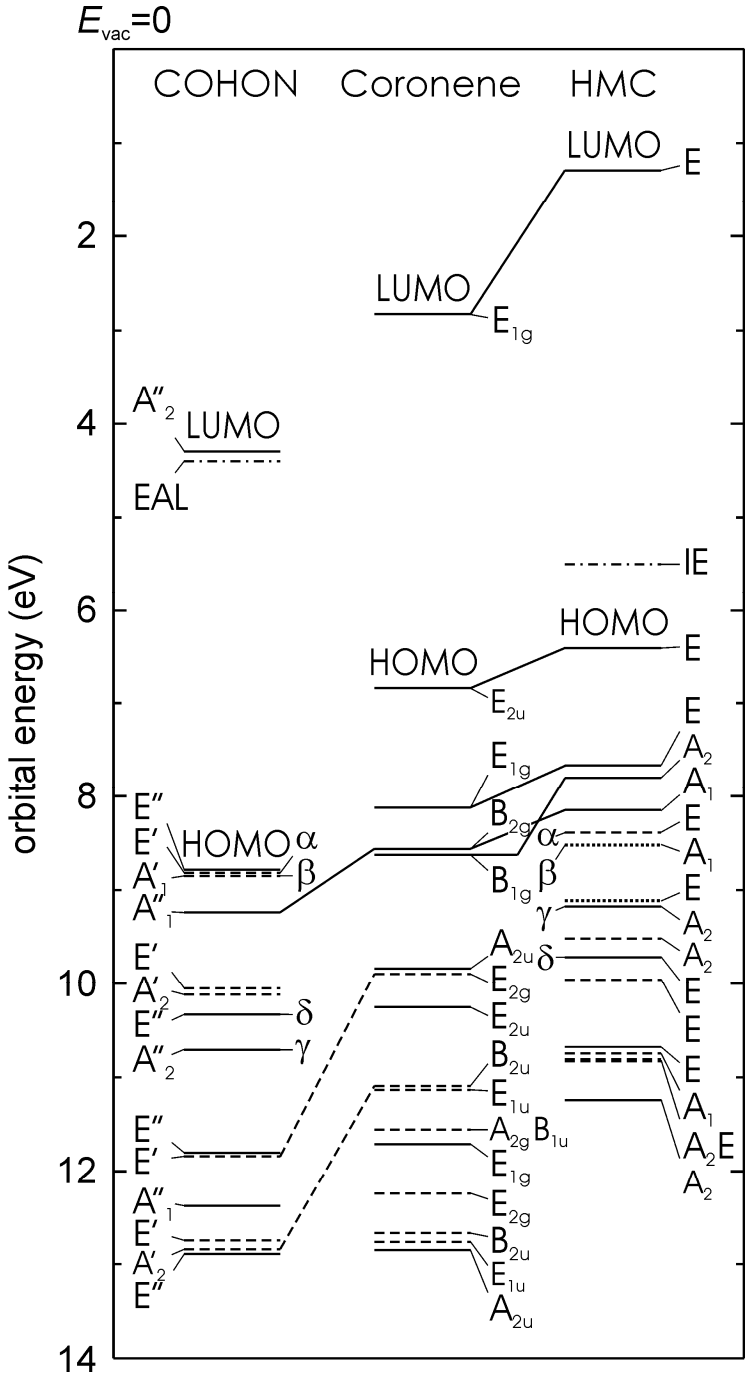

Figure 2.6 Calculated orbital energy scheme for COHON (left) and HMC (right) with respect to the parent molecule coronene (centre). Orbital energies (referred to the vacuum level) have been calculated by means of ΔSCF. Full and dashed lines denote orbitals with π- and σ-symmetry (for HMC π-like and σ-like symmetry), respectively. Dotted lines for HMC denote orbitals that strongly deviate from π- and σ- symmetry. All E-orbitals are double degenerate. Equivalent orbitals are connected by lines or labeled by α-δ. EAL and IE denote the electron affinity level and the ionization energy as determined by cyclovoltammetry (from [Med10a] courtesy Shahab Naghavi).

Methoxy group

In chemistry (particularly organic chemistry), methoxy refers to the functional group consisting of a methyl group bound to oxygen. This alkoxy group has the formula O–CH_3. According to molecular orbital (MO) calculations for the methoxy species the highest occupied molecular orbital (HOMO) 2*e* of the methoxy anion is largely of oxygen p-type (lone pair) mixed with some C-O antibonding π*. This orbital will play a central role in our interpretation of the NEXAFS results, discussed in section 6.5. Its orbital structure is schematically presented in Fig. 2.7. All calculations of the electronic structure of methoxy group were done using DFT method (Ame99).

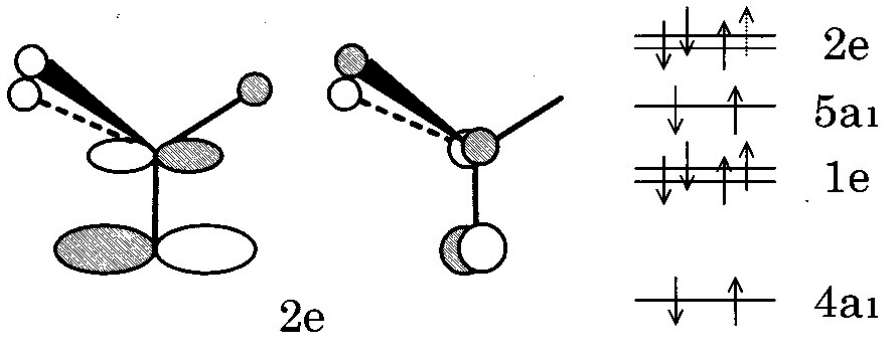

Figure 2.7 Schematic views of the degenerate orbitals 2e (left) and corresponding energy diagram (right) for the methoxy species. Note that 2e is the HOMO (from [Ame99]).

2.3 Hubbard model

The metallic behaviour of the strongly correlated cationic radical salts of the ***κ-(BEDT-TTF)$_2$X*** family discussed in section 7.2 cannot be described by HF or DFT in a reasonable way. An appropriate description is given by the Hubbard model, which is one of the fundamental models in the theory of strongly correlated systems [Izy08].

Typical condensed matter system consists of a macroscopic number (of the order of 10^{23}) atomic nuclei and electrons. For this case, a complete description of the system is impossible, particularly Schrödinger equation cannot be solved completely due to the huge number of elements, suitable approximations are needed. We can neglect intra-nuclear effects, "weak" and "strong" interaction and gravitation. We assume that nuclei and electrons interact by the Coulomb 1/r potential and have no internal degrees of freedom other than the spin.

In this case the Hamiltonian is transformed into:

$$H = \sum_{i=1}^{N_e} \frac{p_i^2}{2m} + \sum_{k=1}^{L} \frac{P_k^2}{2M_k} + \sum_{i<j} \frac{e^2}{|r_i - r_j|} + \sum_{k<l} \frac{z_k z_l e^2}{|R_k - R_l|} - \sum_{i,k} \frac{z_k e^2}{|r_i - R_k|} \tag{2.16}$$

Where $\boldsymbol{r}_i$ ($\boldsymbol{R}_k$), $\boldsymbol{p}_i$ (P_i) and m (M_k) label the positions, momenta, and masses of the electrons (ions), e is electron charge, N_e the number of electrons, L the number of ions and Z_k the atomic number of the ion with index k. The exact solution of this equation is not possible; to simplify it we will use the Born-Oppenheimer approximation, i.e., use immobile ions consider forming a periodic lattice and view them as an external potential for the electrons. The resulting Hamiltonian after these approximations is:

$$H = \sum_{i=1}^{N_e} \frac{p_i^2}{2m} + \sum_i V(r_i) + \sum_{i<j} \frac{e^2}{|r_i - r_j|} \tag{2.17}$$

where the external potential V ($\mathbf{r}$) = V ($\mathbf{r}$ + $\boldsymbol{R}_\alpha$) is periodic on the lattice (with primitive lattice vectors $\boldsymbol{R}_\alpha$ for α = 1,…., d, where d is the dimension), defines the electronic lattice problem.

The Hamiltonian takes the form:

$$H = \sum_{i=1}^{N_v} \frac{p_i^2}{2m} + \sum_{i=1}^{N_v} V^{\text{ion}}(r_i) + \sum_{i=1}^{N_v - 1} \sum_{j=i+1}^{N_v} V^{ee}(r_i, r_j) \tag{2.18}$$

where N_v is the number of valence electrons and V^{ion} the shielded lattice potential.

The Hamiltonian for electrons with spin σ takes the form

$$\hat{H} = \hat{H}_0 + \hat{H}_{\text{int}}$$

where

$$\hat{H}_0 = \sum_\sigma \int \mathrm{d}r \hat{\psi}_\sigma^\dagger(r) \left[-\frac{\hbar^2}{2m} \Delta + V^{ion}(r) \right] \hat{\psi}_\sigma(r),$$

$$\hat{H}_{\text{int}} = \frac{1}{2} \sum_{\sigma\sigma} \int \mathrm{d}r \int dr' \, V^{\text{ee}}(r, r') \hat{n}_\sigma(r) \hat{n}_{\sigma'}(r'). \tag{2.19}$$

Here, $\hat{\psi}_\sigma(r), \hat{\psi}_\sigma^\dagger(r)$ are creation (annihilation) operators for electron with spin σ at site $\boldsymbol{r}$, respectively; Δ is the Laplace operator, $\hat{n}_\sigma(r) = \hat{\psi}_\sigma^\dagger(r)\hat{\psi}_\sigma(r)$ the operator measuring the local density of electrons with spin σ at position $\boldsymbol{r}$ [Blü02].

Wannier Representation

In terms of the lattice momentum $\boldsymbol{k}$ and Bloch eigenfunctions $\phi_{\nu\boldsymbol{k}}(\boldsymbol{r})$ of the noninteracting Hamiltonian (2.19), we may introduce Wannier functions predominantly localized at site $\boldsymbol{R}_i$ by

$$\chi_{i\nu}(r) = \frac{1}{\sqrt{L}} \sum_k e^{-ik\cdot R_i} \phi_{k\nu}(r) \tag{2.20}$$

where the sum is over all $\boldsymbol{k}$ in the band. The Wannier functions are in fact associated with primitive unit cells but in simple structures with one atom per cell they may be associated with that one atom [Har70].

The creation (annihilation) operators $\hat{c}_{i\nu\sigma}^\dagger, \hat{c}_{i\nu\sigma}$ for electrons with spin $\sigma \in \{\uparrow, \downarrow\}$ in the band at site $\boldsymbol{R}_i$ are described as

$$\hat{c}_{i\nu\sigma}^\dagger = \int dr \chi_{i\nu}(r) \hat{\psi}_\sigma^\dagger(r) \leftrightarrow \hat{\psi}_\sigma^\dagger(r) = \sum_{i\nu} \chi_{i\nu}^*(r) \hat{c}_{i\nu\sigma}^\dagger \tag{2.21}$$

Using this relation, the Hamiltonian may be written in the lattice representation as:

$$\hat{H} = \sum_{ij\nu\sigma} t_{ij}^\nu \hat{c}_{i\nu\sigma}^\dagger \hat{c}_{j\nu\sigma} + \frac{1}{2} \sum_{\nu\nu'\mu\mu'} \sum_{ijmn} \sum_{\sigma\sigma'} v_{ijmn}^{\nu\nu'\mu\mu'} \hat{c}_{i\nu\sigma}^\dagger \hat{c}_{i\nu'\sigma'}^\dagger \hat{c}_{n\mu'\sigma'} \hat{c}_{m\mu\sigma} \tag{2.22}$$

where the *matrix elements* are given by

$$t_{ij}^\nu = \int dr \chi_{i\nu}^*(r) \left[-\frac{\hbar^2}{2m} \Delta + V^{ion}(r) \right] \chi_{j\nu}(r),$$

$$v_{ijmn}^{\nu\nu'\mu\mu'} = \int dr \int dr' V^{ee}(r, r') \chi_{i\nu}^*(r) \chi_{j\nu'}^*(r') \chi_{n\mu'}(r') \chi_{m\mu}(r). \tag{2.23}$$

The matrix elements of the kinetic energy t^ν_{ij}, are called hopping amplitudes.

One-Band Hubbard Model

If we restrict the Hamiltonian eq.2.22 to one valence band ($\nu = \nu' = \mu = \mu' = 1$) with isotropic hopping to nearest neighbors (NN) only and assume "perfect"screening, i.e., we choose

$$t_{ij}^\nu \equiv t_{ij} = \begin{cases} -t \text{ if } i \text{ NN of } j \\ 0 \text{ otherwise,} \end{cases}$$

$$v_{ijmn}^{\nu\nu'\mu\mu'} \equiv v_{ijmn} = U \delta_{ij} \delta_{im} \delta_{in} \tag{2.24}$$

In the representation of second quantization, the *Hubbard Hamiltonian* is written as:

$$\hat{H}_{\text{Hub}} = -t \sum_{\langle i,j\rangle,\sigma} \left(\hat{c}^{\dagger}_{i\sigma}\hat{c}_{j\sigma} + \text{h.c.}\right) + U \sum_{i} \hat{n}_{i\uparrow}\hat{n}_{i\downarrow} \qquad (2.25)$$

where $\langle i, j\rangle$ represents the nearest-neighbour interaction on the lattice. H.c. is called hermitian conjugate.

Here, t parameterizes the kinetic energy, U the Coulomb interaction, and the bracket $\langle i, j\rangle$ restricts the sum to nearest-neighbor pairs *i,j*. The operator $\hat{n}_{i\sigma} = \hat{c}^{\dagger}_{i\sigma}\hat{c}_{i\sigma}$ measures the occupancy of the site *i* with electrons of spin σ. Consequently, $\hat{n}_{i\uparrow}\hat{n}_{i\downarrow}$ is the double occupancy, i.e., its expectation value corresponds to the density of doubly occupied sites.

These two terms of the Hamiltonian are responsible for opposite tendencies, namely, toward *delocalization* and toward *localization* of electronic states. Thus, either a metal or an insulator state (Mott-Hubbard insulator) can form, depending on the relation between U and t. Of course, the model contains one more parameter, namely the electron concentration n, which strongly affects the realization of the phase transition in the metal–insulator system. It is well-known that the most favourable conditions for this phase transition occur at half filling (n = 1). An electron–hole symmetry is realized in this case, and the chemical potential is equal to $\mu = 0$ [Iyz08].

In this case Hamiltonian takes form:

$$H = \sum_{\langle ij\rangle,\sigma} t\left(c^{\dagger}_{i\sigma}c_{j\sigma} + \text{h.c.}\right) + \sum_{[ij],\sigma} t'\left(c^{\dagger}_{i\sigma}c_{j\sigma} + \text{h.c.}\right) + U \sum_{i} \hat{n}_{i\uparrow}\hat{n}_{i\downarrow} \qquad (2.26)$$

where $\langle i, j\rangle$ and $[ij]$ indicate sums over nearest and next nearest neighbours, respectively [Kan09].

Although extremely simplified the Hubbard model allows to describe strong correlation physics in real system. One of the systems, where this description is needed for understanding of the physical properties of materials are organic charge transfer salts of the *κ-(BEDT-TTF)2X* family, where depending on substitution X (*X* = $Cu_2(CN)_3$, $Cu(SCN)_2$, $Cu[N(CN)_2]Cl$, $Cu[N(CN)_2]Br$) different ground state properties could be realized (cf. section 2.7).

2.4 Photoelectron Spectroscopy (PES)

Photoelectron spectroscopy (PES) is based on Einstein's law describing the photoelectric effect.

$$h\nu = E^{'f}(k) - E^{i} + E^{'}_{kin} \tag{2.27}$$

where $h\nu$ - photon energy, E^{i} - total initial energy of the atom, molecule or solid state, $E^{'f}(k)$ – total energy of the system in a final state after the release of an electron from a state with quantum number k, $E^{'}_{kin}$ - kinetic energy of the ejected electron. A photon can remove an electron from a molecule if its energy is larger than the binding energy of the electron in the molecule. Any photon energy in excess of that needed for ionization is carried by the outgoing electron in the form of kinetic energy [Nem76].

As a consequence of the existence of an electric contact between the sample and the spectrometer, the Fermi levels of a metallic sample and the spectrometer adjust to each other. That is why for metal samples the measured binding energy E_B relative to the Fermi level of the spectrometer, can be described as:

$$E_B = h\nu - E_{kin} - \phi_{sp} \tag{2.28}$$

where $h\nu$ – photon energy, ϕ_{sp} – work function of the spectrometer.

A thorough consideration of the energetics of photoemission, in particular of adsorbate systems is given by Cahen and Kahn [Cah03]. Photoemission in general is discussed in the book of Hüfner [Hue03]. Here we resume the basic facts. The Fermi levels of sample and spectrometer are aligned in thermodynamic equilibrium. In most cases the work function of the spectrometer ϕ_{sp} will be different from ϕ_{sample}, and accordingly E_{vac} will show a variation along the electron trajectory. However, the measured kinetic energy of the electron E_{kin} is not influenced by the variation of E_{vac}, as only the potential difference between the sample surface and the spectrometer is relevant (as electrostatic interaction is conservative). Consequently, the following relation applies for E_{kin}:

$$E_{kin} = h\nu - E_B - \phi_{sp} - \phi_{sample} = E^{'}_{kin} - (\phi_{sp} - \phi_{sample}) \tag{2.29}$$

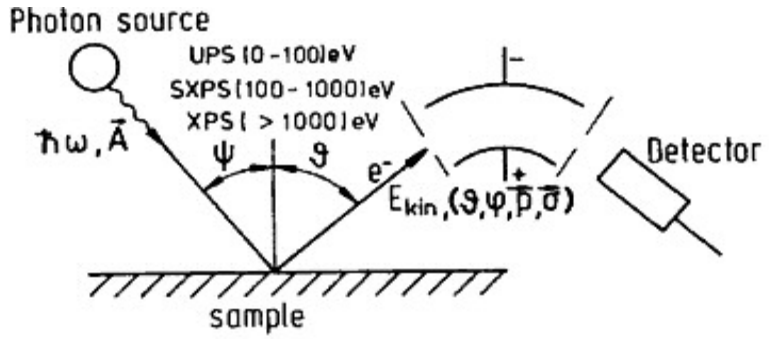

Figure 2.8 Schematic sketch of a photoemission experiment. The light source can be a UV discharge lamp, a laser, an X-ray tube or a storage ring. The electrons are detected by a dispersive (electrostatic or magnetic) or time-of-flight energy analyzer (from [Hue03]).

In a photoelectron spectroscopy (PES) experiment, the sample is irradiated with monochromatic electromagnetic radiation of energy hν and photoelectrons are emitted. The light source is either a gas-discharge lamp, a laser, an X-ray tube, or a synchrotron-radiation source. The sketch of a modern PES experiment is shown in Fig 2.8.

The light (vector potential $\boldsymbol{A}$) irradiates the sample, which is a gas or the surface of a solid, and the electrons excited by the photoelectric effect are then analyzed with respect to their kinetic energy E_{kin}, their momentum $\boldsymbol{p}$ (wave vector $\boldsymbol{p}/\hbar$) in the energy analyzer and their spin polarization vector $\boldsymbol{\sigma}$. The polarization of the light is playing an important role in an angle- resolved PE experiment. The important parameters to be measured are the kinetic energy E_{kin} of the photoemitted electron, and its angle with respect to the impinging light ($\psi + v$) and the surface (v, ϕ). The kinetic energy can be described by re-ordering of eq. 2.30 yielding:

$$E_{kin} = h\nu - \phi - |E_B| \tag{2.30}$$

The momentum $\boldsymbol{p}$ of the outgoing electron is determined from its kinetic energy by

$$E_{kin} = \frac{p^2}{2m} \tag{2.31}$$

The direction of $\boldsymbol{p}/\hbar$ is obtained from v and ϕ which are the polar and azimuthal angles under which the electrons leaves the surface.

Fig. 2.9 shows the energy - level diagram and the energy distribution of photoemitted electrons relate to each other. The electronic structure of a solid sample consists of core levels and the valence band. The Fermi level is the energy equivalent to the chemical potential of the system in the ground state at zero absolute temperature. The physical meaning of the Fermi level is the probability to find a particle at the Fermi level (i.e. at value 0.5 of the Fermi function) at any temperature. In this picture, the Fermi energy E_F is at the top of the valence band and is separated from the vacuum level E_{vac} by the work function. If photoabsorption takes place in a core level with binding energy E_B (again $E_B = 0$ at E_F) the photoelectrons can be detected with kinetic energy according to eq. 2.30 in vacuum. If the energy distribution of the emitted electrons is plotted as in Fig. 2.9 their number per energy interval gives approximately a "replica" (neglecting cross section and polarization effects) of the electron-energy distribution in the solid. This is an attractive feature of PES; it is able to provide us with information on the electron energy distribution in the material.

The PES experiment should be performed in ultra-high vacuum (UHV) conditions. The reason for needing UHV conditions for the study of solid surfaces can be obtained from Fig. 2.10, which shows the „universal" electron mean free path curve. The mean free path λ is given as function of the kinetic energy for a few selected metals from threshold to 10,000 eV. λ depends only weakly on the material, the figure gives a mean value. Between 8 and about 1000 eV, the mean free path is less than 1 nm.

It means that photoelectron spectroscopy in this region can only give information about a very thin surface layer of the sample. Of course, the investigations of surface states or adsorbed molecules require UHV conditions to prevent interference from adsorbed contaminations. Only at very low energies (range of two Photon Photoelectron Spectroscopy (2PPE)) and very high energies (Hard X-ray Photoemission (HAXPES) range) an enhanced bulk sensitivity is possible.

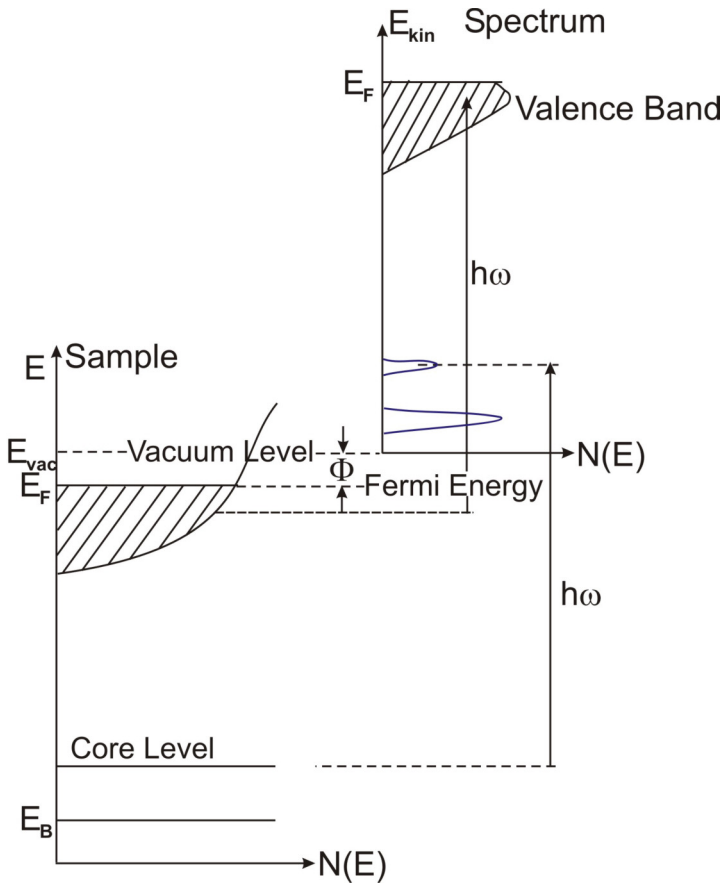

Figure 2.9 Relation between the energy levels in a solid and the electron energy distribution resulting from excitation at a photon energy $\hbar\omega$. The natural abscissa for the photoelectrons is the kinetic energy with its zero at the vacuum level of the sample $E_{kin} = hv - \phi - |E_B|$. Experiments generally prefer to use E_B as the abscissa. E_B is the binding energy of the electrons, which in solids is generally referred to the Fermi level and in free atoms or molecules to the vacuum level (from [Hue03]).

The *inelastic mean free path* (IMFP) of the electrons is defined by electron-electron and electron-phonon interactions. Electron-phonon scattering plays a role only at very low energies and in special cases. That is why it is often neglected in simple cases. The cross-section σ for electron-electron scattering is given by

$$\frac{d^2\sigma}{d\Omega d\omega} = \frac{h^2}{(\pi e a_0)^2}\frac{1}{q^2}\mathrm{Im}\left\{-\frac{1}{\varepsilon(q,\omega)}\right\} \tag{2.32}$$

Where $\hbar\boldsymbol{q}$ is the momentum transfer and ω the energy transfer in the scattering process, a_0= 0. 529 Å (Bohr radius), and Ω is the solid angle into which the electrons are scattered. From this equation the inverse of the average mean free path λ^{-1} is obtained by integration over all energy transfers (ω) and momentum transfers ($\hbar\boldsymbol{q}$). We conclude that λ^{-1} is essentially defined by the dielectric function $\varepsilon(\boldsymbol{q},\omega)$. The dielectric function is different from material to material which means that the mean free path is a characteristic property of the material and cannot be strictly "universal".

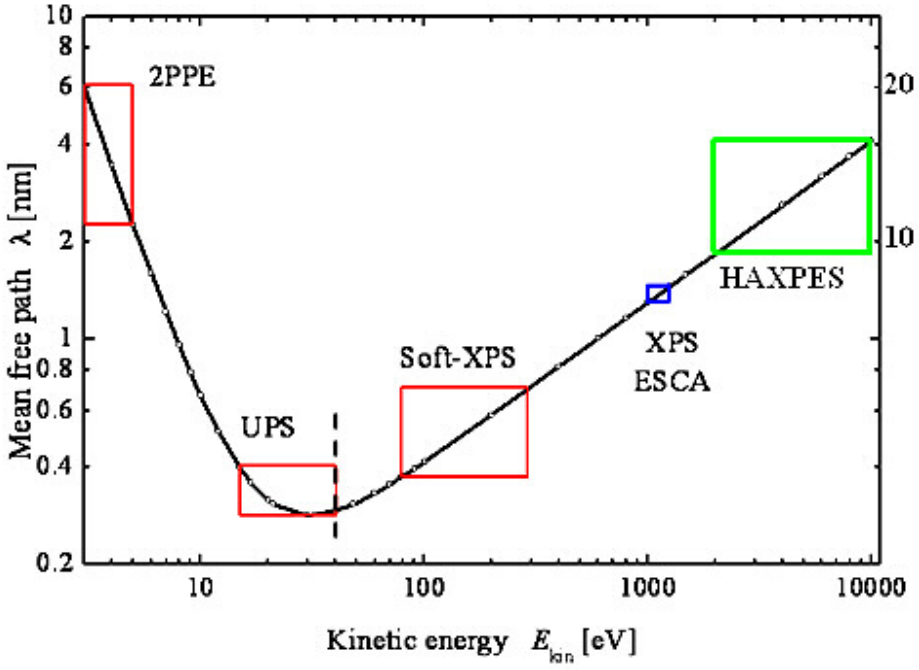

Figure 2.10 Electron mean free path as a function of their kinetic energy (referenced to the Fermi level) for various metals. The data indicate a universal curve with a minimum of 2-5 Å for kinetic energies between threshold and 10000 eV. The different ranges are denoted by the rectangles. The high-energy range is described by the right-hand scale (after [Sea79]).

In the PES experiment the photons impinging on the sample release the photocurrent, the origin of which has a depth distribution (relative to the surface). This is generally called the *escape depth distribution function*. Neglecting elastic scattering events, the electron inelastic mean free path λ can be defined as the distance over which the probability of an electron escaping without significant energy loss due to inelastic processes drops to e^{-1} of its original value. The electron current *dI,* originating from a layer of thickness d*z* at depth *z* detected at an angle ϑ with respect to the surface normal is given by:

$$dI \propto \exp(-z/\lambda\cos\vartheta)dz \qquad (2.33)$$

where ϑ is the angle at which the electrons are detected with respect to the surface normal. In order to evaluate the *escape depth* Δ one has for Δ = z

$$\Delta = \lambda\cos\vartheta \qquad (2.34)$$

and therefore for normal detection (ϑ=0) one has Δ = λ = IMFP.

The actual determination of λ is very often performed by using the overlayer method, in which the intensity of the photoelectron (or Auger electron) signal from a substrate is monitored as a function of the thickness of the overlayer *l*. The *effective attenuation length* (EAL) is obtained from the electron current from the overlayer (I_l):

$$I_l = I_l^{\infty}[1-\exp(-t/\lambda_l\cos\vartheta)] \qquad (2.35)$$

or that from the substrate (I_s):

$$I_s = I_s^0 \exp\left(-t/\lambda_s \cos\vartheta\right) \tag{2.36}$$

where α is again the electron detection angle measured with respect to the surface normal and I_l^∞ is the photocurrent from the thick overlayer, I_s^0 is the signal from the substrate without the overlayer and t is the overlayer thickness.

Definitely, in these experiments the instrumental parameters often influence the electron current and since the overlayers are hardly ever homogeneous, one often calls $\lambda_l \cos\vartheta$ and $\lambda_s \cos\vartheta$ determined by this type of experiment the EAL. Under "ideal" conditions they are identical to the mean escape depth Δ, meaning that λ determined in this way corresponds to the inelastic mean free path.

The mathematical description of the full inelastic mean free path curve is not trivial. A convenient form for the inelastic electron mean free path λ has been given by Tanuma et al. [Tan91], which has approximately the form of the curve in Fig. 2.10:

$$\lambda = E / \left\{ E_p^2 \left[\beta \ln(\gamma E) - (C/E) + (D/E^2) \right] \right\} \tag{2.37}$$

where

λ = IMFP in Å

E = electron kinetic energy in eV

E_p = $28.8(N_v q/M)^{1/2}$ free electron plasmon energy density

ρ = density in g • cm^{-3}

N_v = number of valence electrons per atom (for elements) or molecule (for compounds)

M = atomic or molecular weight

Analyzing data for a number of elements the authors found the following empirical relations for the following parameters:

ß = $-0.0216 + 0.944/\left(E_p^2 + E_g^2\right)^{1/2} + 7.39 \cdot 10^{-4} q$

γ = $0.191 \rho^{-0.50}$

C = 1.97-0.91 U

D = 53.4-20.8 U

U = $N_v q/M = E_p^2 / 829.4$

where E_g is the band gap energy in eV for insulator.

Free electron final-state model

In this model the dispersion relation of the final state is assumed to have the form:

$$E_f = (\hbar^2 / 2m)(k + G)^2 + E_0 \qquad (2.38)$$

where the energies are measured with respect to the Fermi level. This leaves as the parameter to be determined the *inner potential* $V_0 = E_{vac} - E_0 = |E_0| + \Phi$. For the determination of V_0 two methods have been established: either it is adjusted in such a way that the agreement between experimental and theoretical band structure for the occupied states is optimal or one uses the theoretical muffin-tin zero for this value. Having chosen V_0, the procedure is simple and is demonstrated for simplicity for the normal emission case as described in [Hue03].

2.5 X-ray Absorption Spectroscopy (XAS)

Time Scales in Inner-Shell Excitations; Electron and Hole Lifetimes

The basics of X-ray absorption spectroscopy (XAS) is described in detail in the book of Stoehr [Sto92]. Here we recall the most important facts and give an outline of the theoretical concept of modeling XAS spectra. The description of the X-ray absorption process in atoms and molecules requires knowledge of electronic energies and wavefunctions. In the following we will first discuss techniques for obtaining the electronic ground state energy and the 1s initial state wavefunction from which the electron is excited in the X-ray absorption processes considered. After that, we will consider the excitation step itself.

For an explanation of the most detailed features nuclear vibrations must be considered. Before entering into a theoretical treatment let us first consider the *time scales* involved in electronic excitations and nuclear motions. Sudden vertical electronic excitation caused by the electric field of a photon occurs in the time that it takes the photon to travel the diameter d of the inner shell. With $c = 3 \cdot 10^{18}$ Å /s and $d \approx 0.1$ Å for the K-shell of oxygen we can estimate that the excitation takes place in about 10^{-17} to 10^{-18} s.

The excitation leads to a molecule in a non-equilibrium state subject to electronic rearrangements and nuclear motions. Resonances in inner shell excitation spectra correspond to an excitation from an initial to a resonant final state. The full width of the resonance Γ is determined by the lifetime τ of the final state, according to Heisenberg uncertainty principle $\Gamma \cong \hbar / \tau$. In discussing X-ray absorption spectra it is convenient to separate τ into two contributions, the *resonance lifetime* τ_e of the excited electron within the molecular potential and the *hole lifetime* τ_h of the inner-shell hole state according to

$$\frac{1}{\tau} = \frac{1}{\tau_e} + \frac{1}{\tau_h} \tag{2.39}$$

Note that the separation of the core hole and electron lifetimes used in (2.39) relies on a somewhat simplified model. For example, there is evidence that the core hole lifetime in a given molecule depends on the excitation energy. It can be estimated in two ways. Using high resolution X-ray absorption spectra, we can estimate τ_h from the measured lifetime width Γ of a bound-state resonance since such a transition is characterized by $\tau_e = \infty$. The measured width Γ is related to the hole lifetime by the uncertainty relation $\tau_h \Gamma \cong \hbar = 6.6 \cdot 10^{-16}$ eVs. Alternatively, we can use photoemission spectroscopy. In the limit of negligible instrumental broadening the width of the inner-shell photoemission peak, i.e., the measured kinetic energy distribution of the inner-shell photoelectron, is also determined by τ_h according to the above uncertainty relation.

Hole lifetime widths of low-Z atoms for the K and L_3 shells have been estimated by Parr and Brown [Par59, Bro74] and Krause and Oliver [Kra79a, Kra79b] and are shown in Fig. 2.11. Note that the bound-state lifetime widths correspond to the total hole lifetime according to $1/\tau_h = 1/\tau_a + 1/\tau_f$ where for low-Z atoms the *Auger lifetime* τ_a, is much shorter than the *fluorescence lifetime* τ_f. If we use a hole lifetime width of $\Gamma \cong 0.1$ eV for the K-shell of a nitrogen atom we obtain a characteristic lifetime in the 10^{-15}-10^{-14}s range. In contrast to bound state resonances, the width of continuum resonances is determined by τ_e, the lifetime of the resonantly trapped electron. Using a value of 10 eV for a characteristic continuum

resonance width we obtain a lifetime in the 10^{-17}-10^{-18} s range. Hence the longer lived core hole will influence the trapped photoelectron.

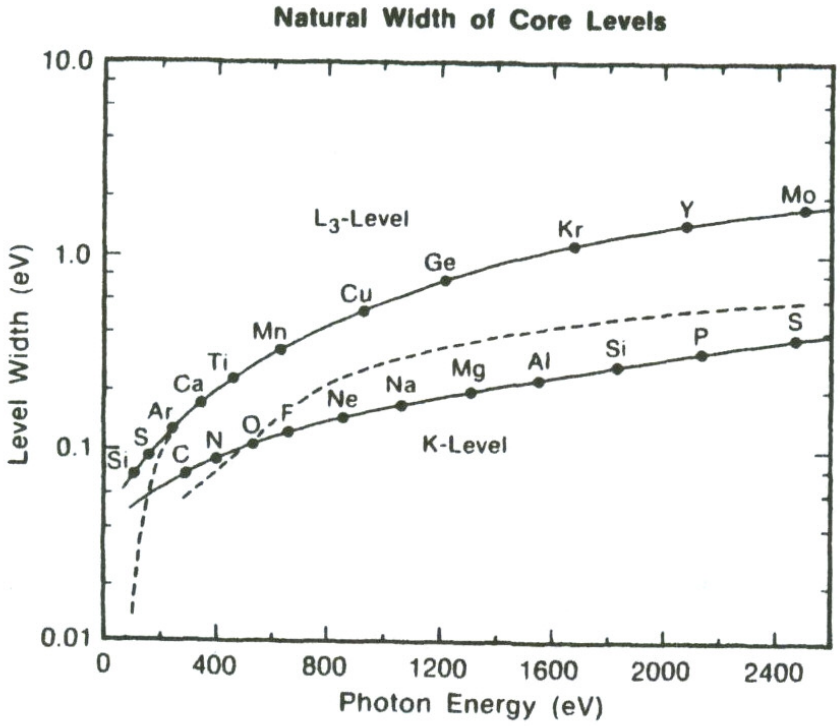

Figure 2.11 Full width at half maximum for the K and L_3 levels of the lighter elements as a function of photon energy (from [Bro74]). The dashed lines are semiempirical values taken from the tables of Krause and Oliver [Kra79a, Kra79b].

Separation of Electronic and Nuclear Degrees of Freedom; Franck-Condon Principle

Compared to the total lifetime of the electronic final state, the vibrational motions of the nuclei are slow because of their large mass (the ratio of proton and electron masses is 1836) and typically occur on a timescale of 10^{-13}s. This allows separation of the electronic and nuclear degrees of freedom in the *Born-Oppenheimer approximation* [Tin64] and facilitates solution of the Schrödinger equation for a fixed geometry (usually the ground-state equilibrium geometry) of the molecule. Furthermore, the *Franck-Condon principle* [Her50] can be employed, which states that the internuclear distance can be assumed to be constant during the fast electronic excitation process.

According to the Born-Oppenheimer approximation, the total wavefunction for a molecule consisting of N electrons and P nuclei can be separated into a product of an electronic and a nuclear part

$$\psi_{tot} = \psi_e \psi_n , \tag{2.40}$$

and the Schrödinger equation for the electrons is

$$H\psi_e = E_0\psi_e \tag{2.41}$$

Here the Hamiltonian, in which we ignore relativistic and spin-orbit effects, is written in an internal coordinate system such that the nuclear kinetic energy term does not enter and is given by

$$H = -\frac{\hbar^2}{2m}\sum_{i=1}^{N}\nabla_i^2 - \sum_{i=1}^{N}\sum_{n=1}^{P}\frac{Z_n e^2}{r_{in}} + \sum_{i=1}^{N}\sum_{k>i}^{N}\frac{e^2}{r_{ik}} + \sum_{i=1}^{P}\sum_{n>l}^{P}\frac{Z_l Z_n e^2}{R_{in}} \tag{2.42}$$

The different sums are the electron kinetic energy, the electron-nuclear attraction, the electron-electron repulsion, and the nuclear-nuclear repulsion terms, and m is the electronic mass, e the electronic charge, and $Z_l e$ the charge of the lth nucleus. The denominators $r_{in} = |r_i - R_n|$, $r_{ik} = |r_i - r_k|$, and $R_{in} = |R_l - R_n|$ specify distances between electronic (r_i) and/or nuclear (R_i) coordinates. The solutions ψ_e and E_0 of eq. 2.41 are parametric functions of the nuclear positions. If the Schrödinger equation is solved as a function of the internuclear separations, $E_0 = E_0(R_{in})$ can provide the potential in which the nuclei move. The solution to a second Schrödinger equation for the nuclear motion then yields vibrational energies E_{vib} and wavefunctions $\psi_{vib}(R)$ for the molecule as shown in Fig. 2.12. For example, for a diatomic molecule the total energy as a function of internuclear distance, $E_0(R)$, often approximates the form for a harmonic oscillator. Then

$$E_{vib}(v) = \hbar\omega_{vib}(v + 1/2) \tag{2.43}$$

where ω_{vib} is the classical vibration frequency and $v = 0, 1, 2, \ldots$ is the vibrational quantum number. Rotational splittings are typically too small to be resolvable in K-shell spectra. For excitations of core electrons the equilibrium internuclear distance in the electronic ground and excited states may be slightly different as shown in Fig. 2.12. According to the Franck-Condon principle, in a vertical transition only those vibrational levels $E_{vib}(v_f)$ of the excited electronic state can be reached whose eigenfunctions $\psi_{vib}(v_f, R)$ have nonvanishing overlap with the wavefunction of the lowest vibrational state of the electronic ground state $\psi_{vib}(v_f = 0, R)$.

The overlap integral is the Franck-Condon factor. The range of internuclear distances spanned by the ground state vibrational wavefunction is shown shaded. For case A (see below inset), maximum wavefunction overlap occurs for the $v_f = 0$ excited state, while for the higher vibrational states the overlap is nearly zero, owing to similar positive and negative contributions. For case B (upper inset), the overlap is largest for the first excited vibrational state $v_f = 1$ with finite, but smaller, contributions from $v_f = 0$ and $v_f = 2$. Note that vibrational splittings in X-ray absorption are only observed in cases where the electronic lifetime τ, given by eq. 2.39, is sufficiently long. So the lifetime width is smaller than the separation between the vibrational levels of the excited state.

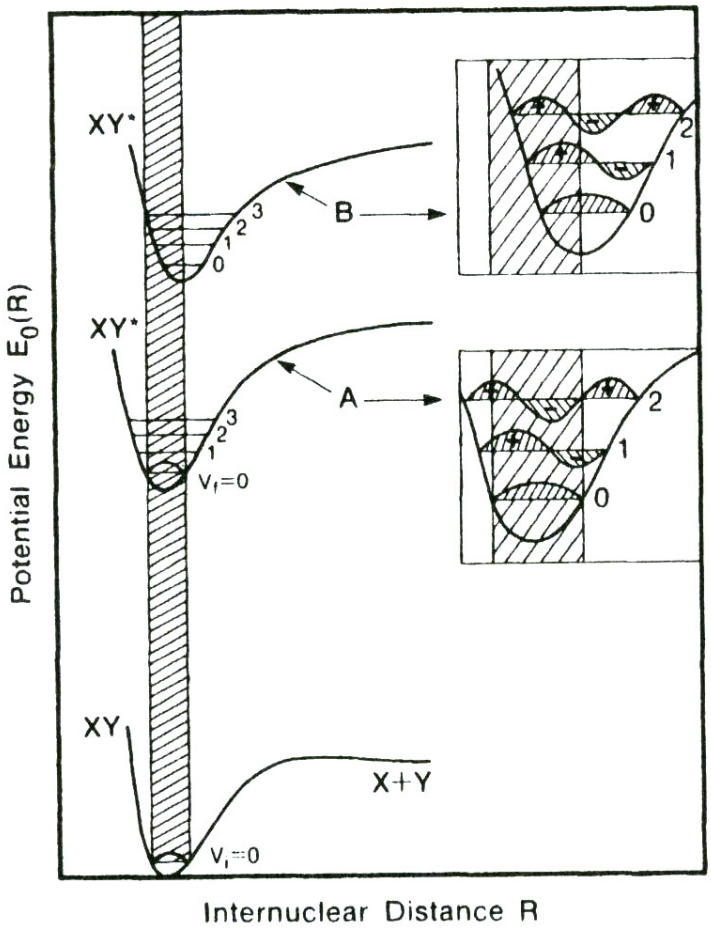

Figure 2.12. Illustration of the Franck-Condon principle. Through X-ray absorption a molecule X Y undergoes an electronic transition from an initial state (the K-shell) to a bound final state (a Rydberg or unfilled valence orbital). For the initial and final electronic states the potential in which the nuclei move is given by the energies E_0(R) obtained from the Schrödinger equation eq. 2.41 for the molecular ground (XY) and the core excited (XY*) states, respectively, as a function of the internuclear separation R. In case A the potential for the ground and excited states have a minimum at the same internuclear distance R, while for the excited state in case B the minimum falls at a larger R value. The Franck-Condon principle states that during an electronic transition the internuclear distance can be assumed to be constant (from [Hue03]).

Transition Energies and Koopmans' Theorem

In the previous section we discussed techniques for obtaining the electronic ground state energy and the 1s initial state wavefunction from which the electron is excited. We shall now take the next step and consider the energetics of electronic excitations. At this point we shall restrict ourselves to *bound state* transitions in which the atom or molecule is not ionized. This restriction is appropriate, because experimentally we will focus on the so-called “pre-edge structures” that are exactly such kind of transitions. The case of ionization corresponds to transitions to *continuum states*. Before we continue, another point needs to be made. In the following we shall often use the terms "states" and "orbitals". In principle, a

"state" is an observable, while an "orbital" is a theoretical construction. We shall use the terms in this sense, noting that in quantum mechanics orbital configurations are a convenient way of describing electronic states (in the sense of spatial probability distributions).

An important quantity in the discussion of K-shell excitation spectra is the $1s$ ionization potential, defined as the minimum energy necessary to excite a $1s$ electron to the continuum of states above the vacuum level. The ionization potential $IP(i)$, or binding energy $E_b(i)$, associated with a particular electron i in an atom or a molecule is conveniently measured by photoelectron spectroscopy (PES) as we have discussed in the previous section. We may write

$$IP(i) = E_b(i) = h\nu - E_{kin} \tag{2.44}$$

The *1s* IP is the threshold energy (usually characterized by an absorption step) for transitions to continuum states. In contrast to PES, which directly measures the "free" photoelectron at photon energies larger than the IP, the lowest-energy transitions observed in X-ray absorption spectroscopy *occur at photon energies less than the IP*! These bound state transitions involve final states below the vacuum level. Such states arise naturally as solutions of the Schrödinger equation for atoms and molecules and they correspond to the well-known *Rydberg orbitals*. Similarly, in core excited molecules unfilled or empty (virtual) molecular orbitals can have orbital energies below the vacuum level and transitions to such orbitals also require excitation energies less than the 1s IP.

The question arises how one may calculate the IPs or transition energies associated with bound state transitions. In principle, this is straightforward if we ignore electron correlation. All we need to calculate is the difference in total energy between the initial (ground) and final (excited) electronic states. For a bound state transition to a Rydberg state, an electron is removed from the $1s$ shell and inserted in a Rydberg orbital in the final state calculation; for the calculation of the IP the final state is assumed to be that of an ion with an electron missing from the K-shell. This scheme, usually referred to as ΔSCF, is cumbersome and, in practice, approximations are employed which yield sufficiently accurate results in a single calculation. These are discussed below.

The most famous approximation, *Koopmans' theorem,* links the IPs or binding energies measured for valence and core electrons by PES to the orbital energies E_i, calculated by means of the HF equation for specific atomic or molecular orbitals. It states that the binding energy or IP of an electron i is equal to the negative of its orbital energy E_i. Koopmans' theorem is derived by considering the difference in total energy between the ionized species ($\bar{E}_0$) with an electron missing from orbital i and the neutral species (J_0), which by definition is the ionization potential IP(i). In contrast to the rigorous ΔSCF approach, however, Koopmans' approximation assumes that upon excitation, i.e., removal of an electron from some orbital ϕ_i, none of the other $\phi_k s$ change, i.e., they remain frozen. Then by use of the difference in total energy, i.e., the ionization potential, can be shown to satisfy the relation

$$IP(i) = E_0 - E = -E_i \tag{2.45}$$

This result also follows logically from the definition of E_i as the sum of the kinetic energy, the potential energy in the nuclear field and the average interaction energy with all other

electrons. For bound states, E_i is negative such that the IP and the binding energy are positive.

For inner shell X-ray excitations of atoms from the second row the frozen-orbital assumption made in the derivation of Koopmans' theorem is inadequate and the predicted binding energies have an error by 10-20 eV [Gel74, Shi73, Mar78]. To account for this error it is common to introduce a *relaxation energy correction* ΔE_R in the comparison of E_i with experimental binding energies. Other shortcomings of this approach are the neglection of relativistic effects, accounted for by a correction E_r and of correlation effects, except those introduced by the Pauli exclusion principle. The correlation energy correction ΔE_{cor} accounts for the difference in energy stabilization of the final and initial states through configuration interaction, which would require description of the states by a linear combination of Slater determinants. Finally, for open shell systems the *multiplet structure* cannot be ignored and it is accounted for by a term ΔE_m, which can be calculated from tabulated Slater integrals. We can then write the following expression linking experimental binding energies and theoretical quantities:

$$E_b(i) = -E_i - \Delta E_R + \Delta E_{cor} + \Delta E_r + \Delta E_m \qquad (2.46)$$

For the K-shells of carbon, nitrogen and oxygen (i.e. those studied experimentally in the following chapters) the various corrections have been calculated and their approximate values are $\Delta E_R \approx 15$ eV, $\Delta E_{cor} \approx 1$ eV, and $\Delta E_r \approx 0.2$ eV. For the open shell molecules NO and O_2 the multiplet splitting of the 1s photoemission peak is 2 $\Delta E_m \approx 1$ eV. We see that the relaxation correction is especially large and must be accounted for in the calculation of inner-shell X-ray absorption spectra.

One method for including relaxation uses the so-called equivalent cores approximation [Jol78]. Here, it is assumed that outer electrons are affected by ionization of a core electron in essentially the same way as they would be if the nuclear charge were increased by one unit, i.e., by the "equivalent core" of the next element in the periodic table.

The Sudden Approximation

A great simplification in the calculation of the matrix element is achieved by a fundamental assumption, known as the sudden approximation. Its essence lies in assuming a strongly "one-electron" character of the electronic transition and that the primary excitation event is rapid or "sudden" with respect to the relaxation times of the other "passive" electrons. This allows separation of the initial and final state wavefunctions into an *"active" one-electron* and a *"passive" multi-electron part*, and the transition matrix element becomes

$$D_{if} = \left\langle \psi_f(N) \middle| \sum_{k=i}^{N} P_k \middle| \psi_i(N) \right\rangle = \left\langle \kappa_f | P_i | \phi_l \right\rangle \left\langle \psi_f(N-l) | \psi_i(N-l) \right\rangle + \ldots\ldots \qquad (2.47)$$

Here ϕ_l is the orbital from which an electron is excited, χ_f the wavefunction of the excited electron, and the functions ψ_i(N-1) and ψ_f(N-1) are the passive N-1 electron remainders in the initial and final states. They are (N-l)-dimensional Slater determinants in which one row and column corresponding to ϕ_l or χ_f have been deleted [Mar 78]. In eq. 2.47 higher-order terms which are associated with excitations of one or more of the "passive" electrons have been omitted. In the sudden approximation we thus obtain as the leading term a one-electron matrix element and an overlap integral between the passive (N-1)-electron wavefunctions in

the initial and final states. For the overlap integral to be nonzero, the two functions ψ_i(N-1) and ψ_f(N-1) must correspond to the same atomic symmetry or irreducible representation of the symmetry point group of the molecule, the so-called monopole selection rule. The overlap term is always less than but close to 1 (≈ 0.7-0.9) [Car75] and reflects the intensity lost from the "main" one-electron transition by multi-electron effects.

Details of the various multi-electron excitation mechanisms and intensities are contained in the higher-order terms omitted from eq. 2.47. The form of this equation suggests that there is a sum rule for the balance of the "one-electron" and "multi-electron" intensities in the sudden approximation. The *sum rule* states that the sum of the one- and multi-electron peak intensities for a given initial state is equal to the peak intensity calculated by use of an unrelaxed final state wavefunction. In the latter the matrix element stems from omission of the passive-electron terms in eq. 2.36, i.e.

$$D_{if} = \langle \kappa_f | P | \phi_i \rangle \tag{2.48}$$

where the momentum operator is associated with the "active" electron. The cross sections calculated using eq. 2.48, called the *active electron approximation*, are larger than those obtained in photoemission spectroscopy from the "main peak" intensity alone, neglecting the satellite intensities [Fad74a, Fad74b].

In X-ray absorption spectroscopy two cases need to be distinguished. If only the *average cross section* is of interest, e.g., all resonance effects are eliminated by a smoothing procedure, then the measured cross section is well predicted by the one-electron unrelaxed cross section since the measurement inherently sums over all one- and multi-electron excitations. On the other hand, *near edge resonances (as studied in the present work)* or the EXAFS structure [Reh78, Ste83] are reduced in size by multi-electron effects, similar to photoemission. The reason is that only those photoelectrons which correspond to the "main peak" in photoemission are coherent and therefore give rise to scattering resonances, while the electrons created in multi-electron events are incoherent because of their smeared energy distribution.

A second sum rule, derived by Manne and Aberg [Man70], should also be mentioned, and is best thought of in conjunction with core-level photoemission spectra. In Koopmans' approximation all multi-electron effects are ignored and the dipole matrix element describing the excitation of an electron in orbital ϕ_i has the simplest possible form given by (2.48). In this case a single photoemission peak is observed corresponding to a binding energy $E_b(i) = -E_i$. If we allow passive electrons to relax and additional multi-electron excitations to occur, the photoemission spectrum will exhibit a main "one-electron" line at a lower binding energy $E_b(l) = -E_i - \Delta E_R$ and higher binding energy multi-electron satellites, i.e., shake-up and shake-off features. The sum rule states that there exists a "lever arm" relationship between the one- and multi-electron peaks such that the center of gravity of all photoemission features is at the Koopmans' binding energy.

2.6 Near Edge X-ray Absorption Fine Structure (NEXAFS)

In this section NEXAFS will be presented as a powerful tool for understanding details of the charge transfer mechanism. NEXAFS is a special type of X-ray absorption spectroscopy as discussed in the previous section. The fundamental phenomenon underlying NEXAFS is the absorption of an X-ray photon leading to excitation from a core level of an atom in a solid to the unoccupied density of states above the Fermi level. In particular, the resonant excitation from the core level to an unoccupied discrete state leads to energetically "sharp" (of course, lifetime-broadened) resonance features in the absorption spectra. The resulting core hole is filled either via an Auger process or by capture of an electron from another shell followed by emission of a fluorescent photon.

The difference between NEXAFS and traditional photoemission experiments is that in photoemission, the initial photoelectron itself is detected, while in NEXAFS the fluorescent photon or Auger electron yield (so called partial yield) or the total electron yield, including the high signal of inelastically scattered electrons is measured.

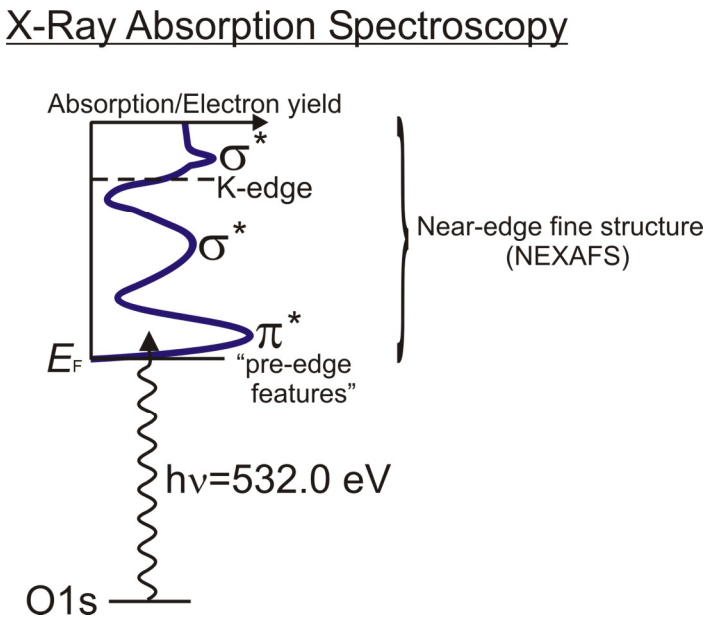

Figure 2.13 Transition scheme for an oxygen K-edge NEXAFS experiment. Below the K-edge (dashed line), resonance-like "pre-edge structures" occur that are a fingerprint of the unoccupied density of states.

There is a long practice of correlating the formal charge state with absorption edge shifts. In the following consideration we follow the paper by G. Bunker [Bun10]. It is clear from simple physical arguments that shifts of a few eV can indeed occur by transferring charge, but the amount of charge transfer that actually occurs in chemical binding is much less than the formal charge would suggest. Atoms remain nearly neutral even when chemical bonds are formed. The K-edge position (dashed in Fig. 2.13) is the onset of emission from the 1s level into the open continuum. In contrast, the final states in the pre-edge regime are fairly localized. As a simple model of chemical charge transfer between atoms, imagine the

central atom is surrounded by a spherical shell of charge Q and radius R. When charge is chemically transferred because of chemical bonding, the effective radius of this shell of charge changes slightly. From electrostatics we know that the energy levels of everything inside the sphere then is shifted by Δ(q/R). The initial 1s state and any final state orbital that is entirely contained within the spherical shell would be shifted the same amount by the change Δ(q/R), so the transition energy in the spectrum would not be affected. The more diffuse orbitals (such as the 4p orbital in 3d transition elements) would be more strongly affected, however, because some part of the final state orbital would be contained within the sphere, and some other part would not.

It has been observed earlier (since the 1930s) that there is an inverse relationship between the extent in energy of the edge and the average bond length. Hartree et al. suggested that the principal maximum occurs when the electron wavelength equals the interatomic distance. In eV-Å units, this gives $E - E_0 \approx 150/r^2$. From a scattering point of view the charge transfer would enter into the calculation only through alterations to the partial wave scattering phase shifts and μ_0. It has been argued [Bun84] that although small shifts of a few eV may be directly due to such effects, larger shifts (10–20 eV) are more often due to chemically induced changes in bond length. An aphoristic way to state this is that (i) the chemistry (charge transfer) tells the atoms where to go, and (ii) physics (scattering) tells us where they are. Since there is, at least in some materials such as Mn oxides, a strong correlation between the formal charge state and the average bond length, it is difficult to experimentally distinguish between the direct correlation (formal-charge → edge-shift) and the indirect one (formal-charge → bond distance → edge-shift).

After the initial resonant excitation step, Auger recombination of the core hole leads to Auger electrons and finally to a secondary electron cascade with very small kinetic energies right above the vacuum level. According to the mean free path curve Fig. 2.10 this is connected with an escape depth of about 5 nm [Sto03].

Fig. 2.14 shows the analogous scheme for hard X-ray photoemission. Here the transition ends up very high in the continuum states (the Figure is approximately to scale). It leaves an ionic state behind (N → N-1 transition). In contrast, in X-ray absorption spectroscopy a neutral complex, or, more precisely, an additional valence electron in a formerly unoccupied level in the presence of a core hole is studied (N → N* transition). This was discussed in detail in section 2.5. For the oxygen 1s-case shown in Fig. 2.14 the binding energy is more than a factor of 10 smaller than the photon energy of about 6 keV. The excess energy of 5.425 eV (kinetic energy) lies in the HAXPES regime of Fig. 2.10. Therefore, we have a probing depth of the order of 10-15 nm in a HAXPES experiment.

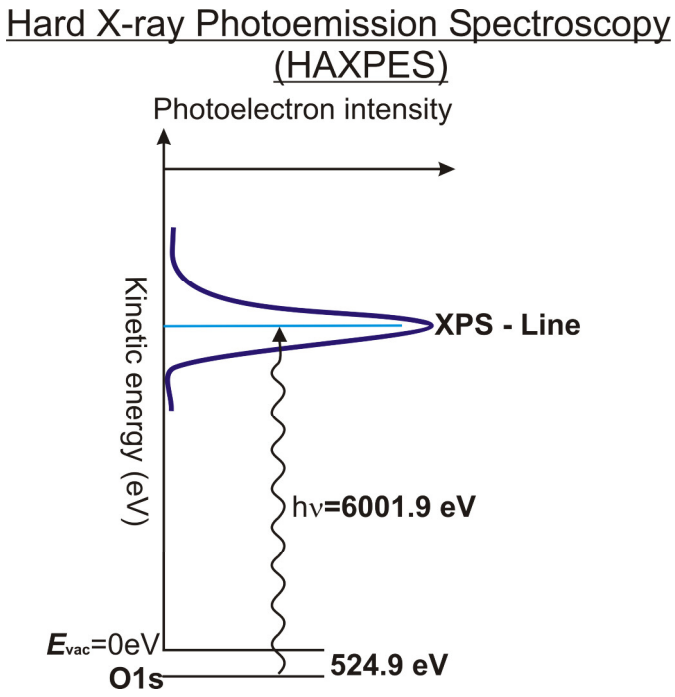

Figure 2.14 Transition scheme for an oxygen 1s HAXPES experiment. Note that the high photon energy leads to a large excess energy (kinetic energy).

2.7 Classical and Novel Charge Transfer Complexes

The past decade has witnessed tremendous advances in the development of organic conductive molecular and polymeric materials and this field continues to be of great scientific and commercial interest. This field of science flourished on discovering new π-conjugated materials and by tailoring their electrical conductivity from semiconducting to metallic to a superconducting regime, when doped. Characteristic for such compounds is a highly correlated electronic ground state that can exhibit superconductivity, spin density waves, or charge density waves [Wil92]. The first category of organic conductive and superconductive molecules are based on charge-transfer salts, where BEDT-TTF [bis(ethylenedithio)tetrathiafulvalene], $M(dmit)_2$ (dmit = 1,3-dithio-2-thione-4,5-dithiolate), DCNQI (N,N'-dicyano-p-quinonediimine) perylene, tetrachalcogenafulvalenes and their structurally related analogs are just a few of the most commonly studied in the past decade. Fullerenes constitute another class which also exhibit superconductivity when doped with alkali metals. Research activities are being carried out around the world to produce pure fullerenes (C60, C70, C76, C78, C82, C84, C90, and higher fullerenes) and to prepare their derivatives as well as polymers [Nal97]. Another class of materials of high current interest are the nanographenes [Mue08, Wat01, Ran03, Wup07] which can be functionalized at their periphery to design large disc-type donors and acceptors.

A charge-transfer (CT) complex or electron-donor-acceptor complex is an association of two or more molecules in which a fraction of electronic charge is transferred between the molecular parts. The resulting electrostatic attraction provides a stabilizing force for the molecular complex. The source molecule from which the charge is transferred is called the electron donor and the receiving species is called the electron acceptor.

When two species of molecules with donor and acceptor character are combined in a compound, they may form a charge transfer salt. It resembles a classical ionic crystal like NaCl, but the degree of charge transfer is often incomplete, i.e. on average, only a fraction of an elementary charge is transferred from the donor to the acceptor. Such compounds form, when the total energy of the donor-acceptor pairs is lowered via charge transfer. The main energy contributions are the ionisation energy of the donor E_{ion}^{D} (this energy must be spent by the system), the electron affinity of the acceptor E_{aff}^{A} (this energy is gained) and the Coulomb energy that can be written as $\alpha\langle e^2/a\rangle$ (this energy is also gained), where e is the elementary charge, a is the effective distance between donor and acceptor and α is a constant. The brackets denote integration over the average net charge, because we are not dealing with point charges. We further introduce the fraction of charge transfer ρ varying between ρ = 0 (neutral) and ρ = 1 (fully ionic). With this, we can write the total energy per donor-acceptor pair as:

$$E(\rho) = (E_{ion}^{D} - E_{aff}^{A})\rho - \alpha\langle e^2/a\rangle\rho^2 \qquad (2.49)$$

Fig. 2.15 illustrates the behaviour: In the CT complex (centre), the energy term (being a hybrid state of the donor HOMO and acceptor LUMO) lies lower than the HOMO of the neutral donor D^0.

In a simplistic view, we can give energy criteria for the formation of either a neutral ($\rho = 0$) ionic complex ($\rho = 1$):

$$\rho = 0 \quad \text{if} \quad (E_{ion}^{D} - E_{aff}^{A}) \quad > \quad \alpha < e^2 / a > \qquad (2.50)$$

$$\rho = 1 \quad \text{if} \quad (E_{ion}^{D} - E_{aff}^{A}) \quad < \quad \alpha < e^2 / a >$$

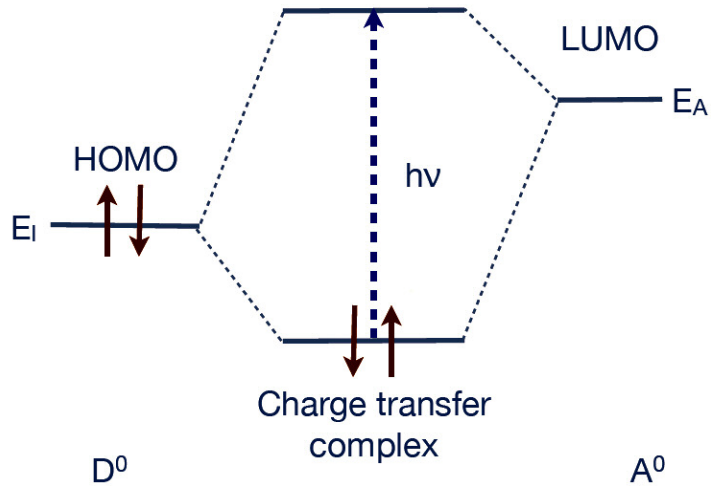

Figure 2.15 Schematic level scheme of the formation of a CT-complex from the neutral donor D^0 and acceptor A^0.

For many systems, in particular all systems studied in the present work, we find only a partial (i.e. non-integer) charge transfer. Complexes with $\rho < 0.5$ are often referred to as "neutral", those with $\rho > 0.5$ as "ionic". This definition is somewhat misleading, because the region around $\rho = 0.5$ is often characterized by a high conductivity as is the case for the quasi 2D-metallic κ-phases discussed below.

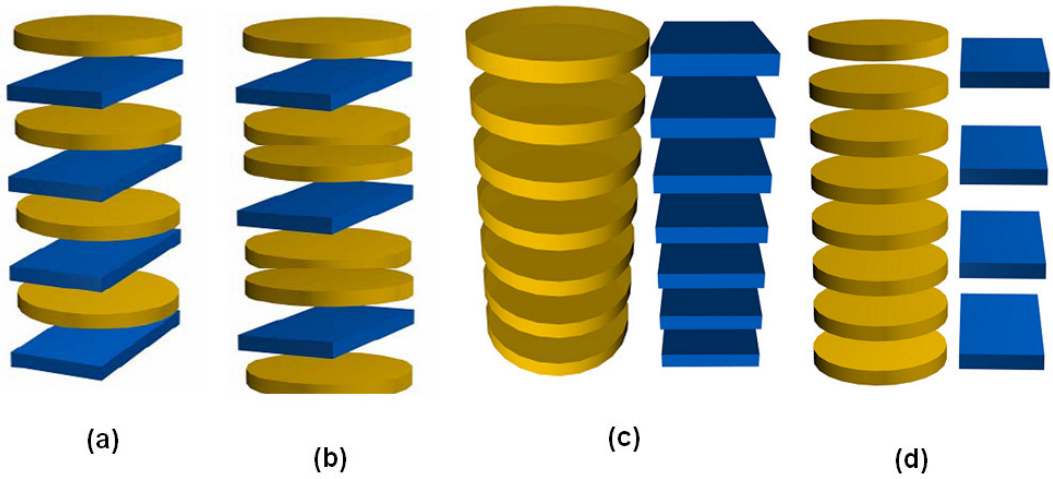

Figure 2.16 Different columnar structures of charge transfer complexes: Alternating stack in 1:1 (a) and 1:2 stoichiometry (b), segregated stack in 1:1 (c) and 1:2 stoichiometry (d) (after [Bau10]).

Depending on the types of molecules there are two possibilities for stacking in a CT complex, see Fig. 2.16. The donor and acceptor moieties can either arrange in a mixed stack, i.e. in an alternating sequence or in a segregated stack where both donors and acceptors form rows being closely spaced so that the charge transfer occurs between the donor row and acceptor row.

Alternating stack packing motif: Novel CT complexes based on polycyclic aromatic hydrocarbons

Chi *et al*. succeeded in crystallizing large single crystals of coronene-TCNQ. In the 1:1 stoichiometric crystal the complexes exhibit alternate stacking [Chi04]. The amount of charge-transfer was estimated to be of the order of 0.2-0.3 *e* and thus larger than observed for other hydrocarbon-based CT complexes in earlier work [Tic73, Lon65, Tic73, Wil68, Col70]. The charge-transfer compound showed semiconducting behavior with a moderate transport gap of 0.49 eV, along with a rather high charge carrier mobility of 0.3 cm^2/Vs [Tic73].

In the present work, we find the mixed stack packing motif according to Fig. 2.16a for the coronene and pyrene derivatives. The substituted pyrene complexes with TCNQ are simultaneously being studied in Frankfurt (in the framework of SFB/TR 49) by M. Huth and coworkers using other experimental techniques, complementary to the present work. Conductivity measurements have been performed at individual TMP-TCNQ crystals. A typical result is shown in Fig. 2.17a. In the range of 10^4 V/cm a current - electrical field dependence of $I \propto E^{5.2}$ has been found Rudloff [Rud11]. This is in very good agreement with the $I \propto E^5$ behaviour found by Iwasa [Iwa89] for $TTeC_1TTF$-TCNQ, see Fig. 2.16b. This behaviour is characteristic for a "neutral" CT complex. Here neutral refers to $\rho < 0.5$.

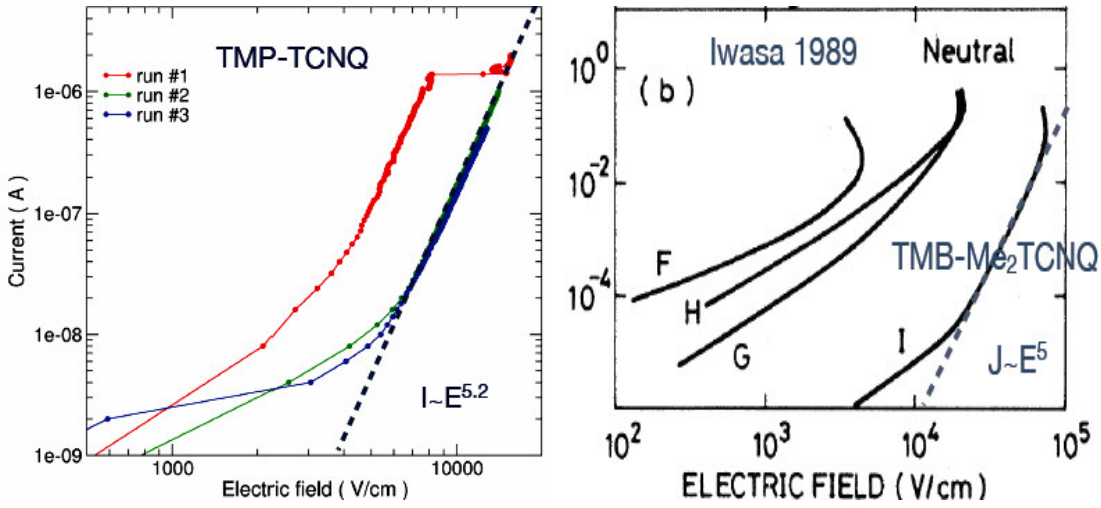

Figure 2.17 Conductivity measurements on TMP-TCNQ (left panel, from [Rud11]) in comparison with TMB-Me_2TCNQ (right panel, from [Iwa89]).

Segregated stack packing motif: TTF-TCNQ and κ-(ET)$_2$X

Segregated stack packing motifs are found, e.g., for the *κ*-(BEDT-TTF)$_2$Cu[N(CN)$_2$]Br phase discussed in section 7.2. This material represents a special case, because two donor molecules form a dimer and this dimer transfers a full charge to the acceptor. This leads to half filling of the donor bands and thus to quasi 2D metallic behaviour. This situation is illustrated in Fig. 2.16d.

The simplest segregated-stack system is the CT transfer salt tetrathiafulvalen (TTF)-TCNQ. Historically, this was the first metallic quasi-1D organic CT system found. It is characterized by a Peierls instability with charge density wave formation at 54 K. Fig. 2.18 shows its structure: It consists of alternating stacks of donors TTF and acceptors TCNQ, like illustrated in the scheme in Fig. 2.16c.

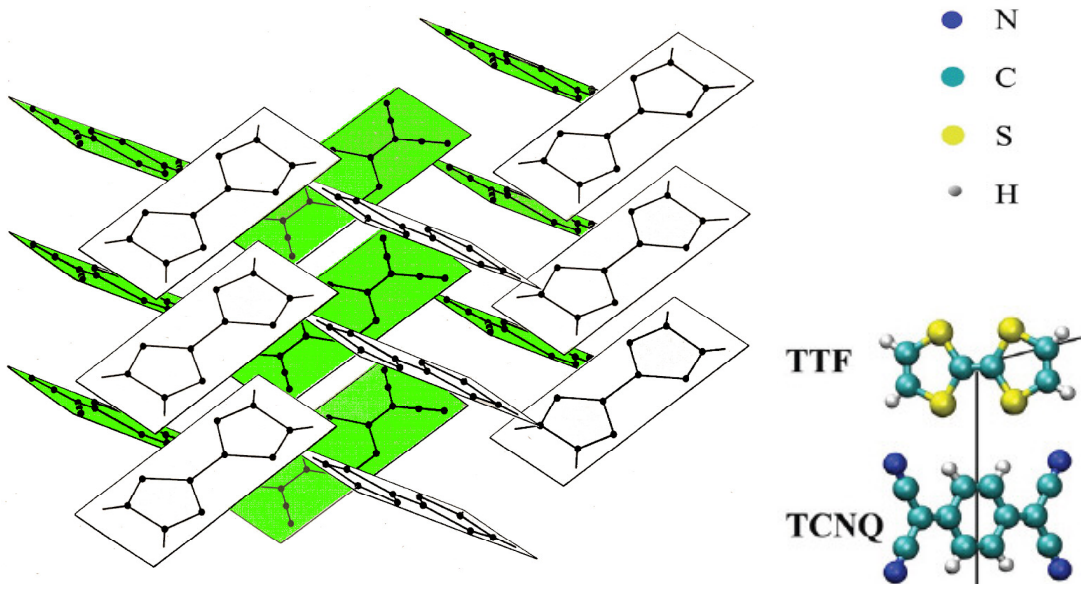

Figure 2.18 The classical organic CT system tetrathiafulvalene-tetracyanoquinodimethane (TTF-TCNQ). The segregated stacks lead to quasi-1D metallic behaviour. The structure of the molecules is shown on the right (from [Lan10]).

Of high current interest is the family of *cation radical salts* κ-(BEDT-TTF)$_2$X, illustrated in Fig. 2.19. These materials exhibit a large variety of different phases, being characterised by the close proximity of a superconducting and an antiferromagnetic insulating phase. In the κ-phase (Fig. 2.19b) strong dimerisation of the BEDF-TTF (briefly ET) molecules (a) leads to a half-filled conduction band. This system is close to the boundary to a Mott insulator, depending on the ratio of bandwidth W and Coulomb energy U. The dimers constitute a triangular lattice with large anisotropy. In the θ-phase (Fig. 2.19c) weak dimerization of the ET molecules leads to a quarter-filled conduction band. The interplay of U and W together with $\lambda_{el\text{-}ph}$ leads to a charge-order insulator phase.

In chapter 7 we will discuss the first hard X-ray photoemission results for the κ-phase system with X = Cu[N(CN)$_2$]Br (briefly called κ-Br). The schematic phase diagram of the κ-(ET)$_2$X family is shown in Fig. 2.20. The s-shaped-line denotes a first order phase

transition between the metallic and the Mott insulator phase. Instead of physical pressure it is possible to induce *chemical pressure* by substituting Cl by Br, being equivalent to a physical pressure of 350 bar (arrow "H8-Br" in Fig. 2.20). If, in addition, hydrogen is substituted by deuterium the chemical pressure is reduced, driving the fully deuterated material "D8-Br" to the immediate vicinity of the first order transition line separating the Mott insulator from the metallic phase.

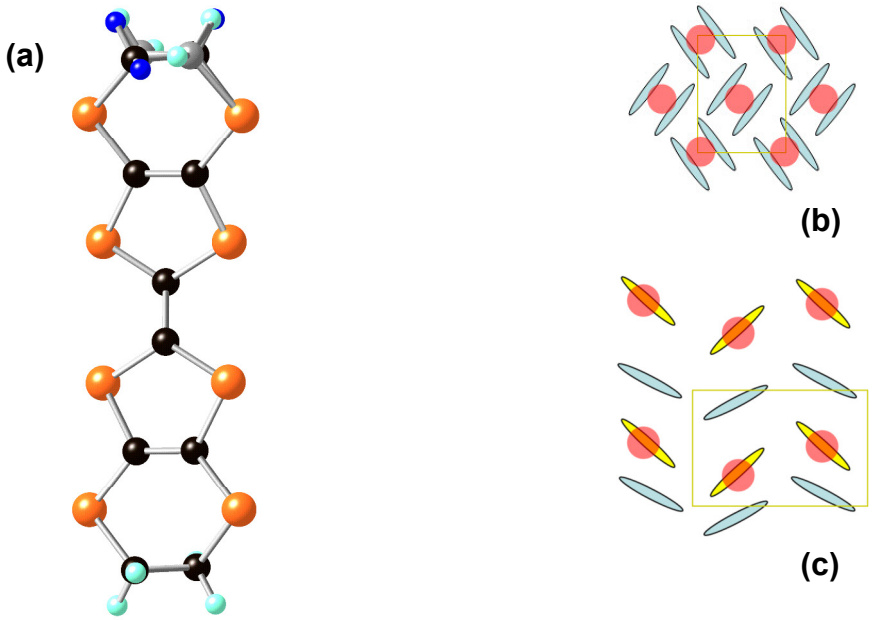

Figure 2.19 The BEDT-TTF (briefly ET) molecule (a) and its arrangement in κ-$(ET)_2X$ (b) and θ-$(ET)_2X$ (c) (from [Val10]).

As this material has been investigated using HAXPES, we discuss the structure of the κ-$(ET)_2X$ salts in more detail. The segregated stack packing motif is illustrated in Fig. 2.21 from different perspectives. The ET-layers form a quasi-2D metallic system, whereas the acceptor layers form a polymeric network as illustrated in the inset (in top view). Note that the ET-molecules are not planar, see view in Fig. 2.19a. The ethylene (CH_2) end groups play an important role for the thermal glass-like transition at 77 K in the phase diagram. This transition will be discussed in chapter 7.2.

The electronic band structure of κ-$(ET)_2Cu_2(CN)_3$ (briefly κ–CN) and κ-$(ET)_2Cu[N(CN)_2]Cl$ (briefly κ–Cl) has been calculated by Kandpal et al. [Kan09] using DFT. The results are shown in Fig. 2.22 in terms of energy bands in the vicinity of E_F (a, b) and energy bands in a wider range along with the corresponding density of states (c). The calculation reveals that the Fermi energy lies very close to a large global bandgap. The widths of the ET bands is smaller than in earlier theoretical work. However, the calculation did not reflect the electronic structure expected for a Mott insulator, because the Coulomb interaction is only accounted for in a mean-field approximation and is not treated quantitatively correct in this calculation [Val10].

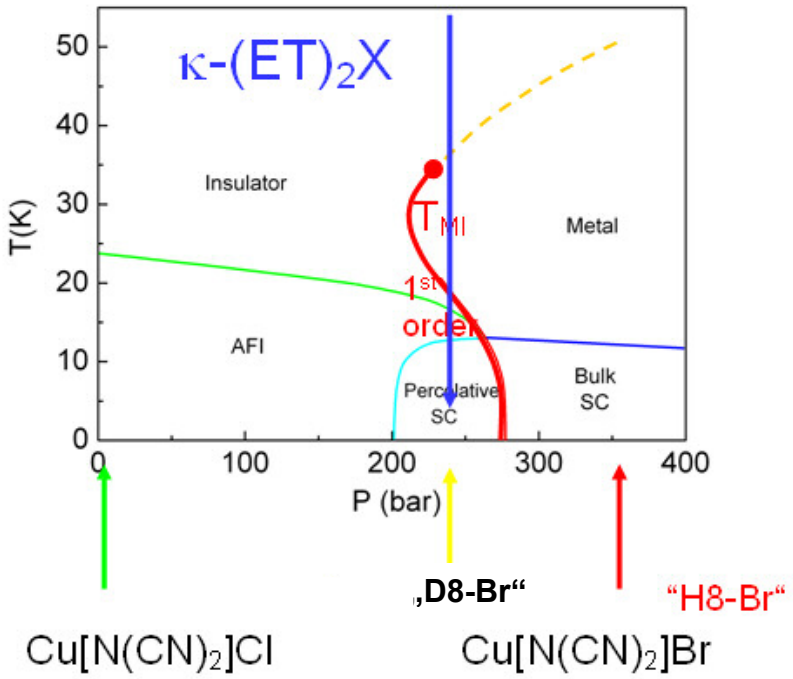

Figure 2.20 Phase diagram of the κ-$(ET)_2X$ family of CT-salts. The physical pressure P can be replaced by “chemical pressure”: Substituting Cl by Br brings the material from the antiferromagnetic insulator (AFI) - Mott insulator region to the superconducting (SC) - metallic region for the protonated material “H8-Br”. Further substitution of hydrogen by deuterium brings the material “D8-Br” into the region of the s-shaped first order transition between insulating and metallic/superconducting states (from [Sou07]).

A small change of the bandwidth of the topmost conduction bands or a change of the electron population in the quasi-2D metallic ET layer can drive the system into the insulating state. In other words, the system is very close to the metal-insulator transition. The Fermi energy will then shift into the gap thus ending up in the paramagnetic insulator state, see phase diagram Fig. 2.20.

Kandpal et al. [Kan09] have performed tight-binding fits to the bands in Fig. 2.22 in order to obtain the relevant parameters of the underlying Hubbard model. These parameters are summarized in Table 2.1.

		U/t	***t'/t***	**Ground state**
κ-$(BEDT\text{-}TTF)_2Cu_2(CN)_3$	κ-CN	7.3	0.83	nonmagnetic insulator
κ-$(BEDT\text{-}TTF)_2Cu(SCN)_2$	κ-SCN	6.0	0.58	nonmagnetic insulator
κ-$(BEDT\text{-}TTF)_2Cu[N(CN)_2]Cl$	κ-Cl	5.5	0.44	antiferromagnetic insulator
κ-$(BEDT\text{-}TTF)_2Cu[N(CN)_2]Br$	κ-Br	5.1	0.48	superconductor

Table 2.1 Characteristic parameters (Hubbard U and hopping parameter t' to the next but one lattice site, both normalized to the hopping parameter t to the next site) of the κ-$(BEDT\text{-}TTF)_2X$ family. The interplay between U and t' drives the system from the Mott insulator (for $Cu_2(CN)_3$ and κ-Cl) to the superconducting regime for κ-Br (from [Kan09]).

The results of [Kan09] had important consequences for the exact location of the four members of the κ-$(ET)_2X$ family in the phase diagram. In comparison with previous work, κ-Br is moved from the antiferromagnetic phase to the d-wave superconducting phase (in agreement with experiment) and κ-Cl is moved from the spin liquid phase to the border between the antiferromagnetic and superconducting phase.

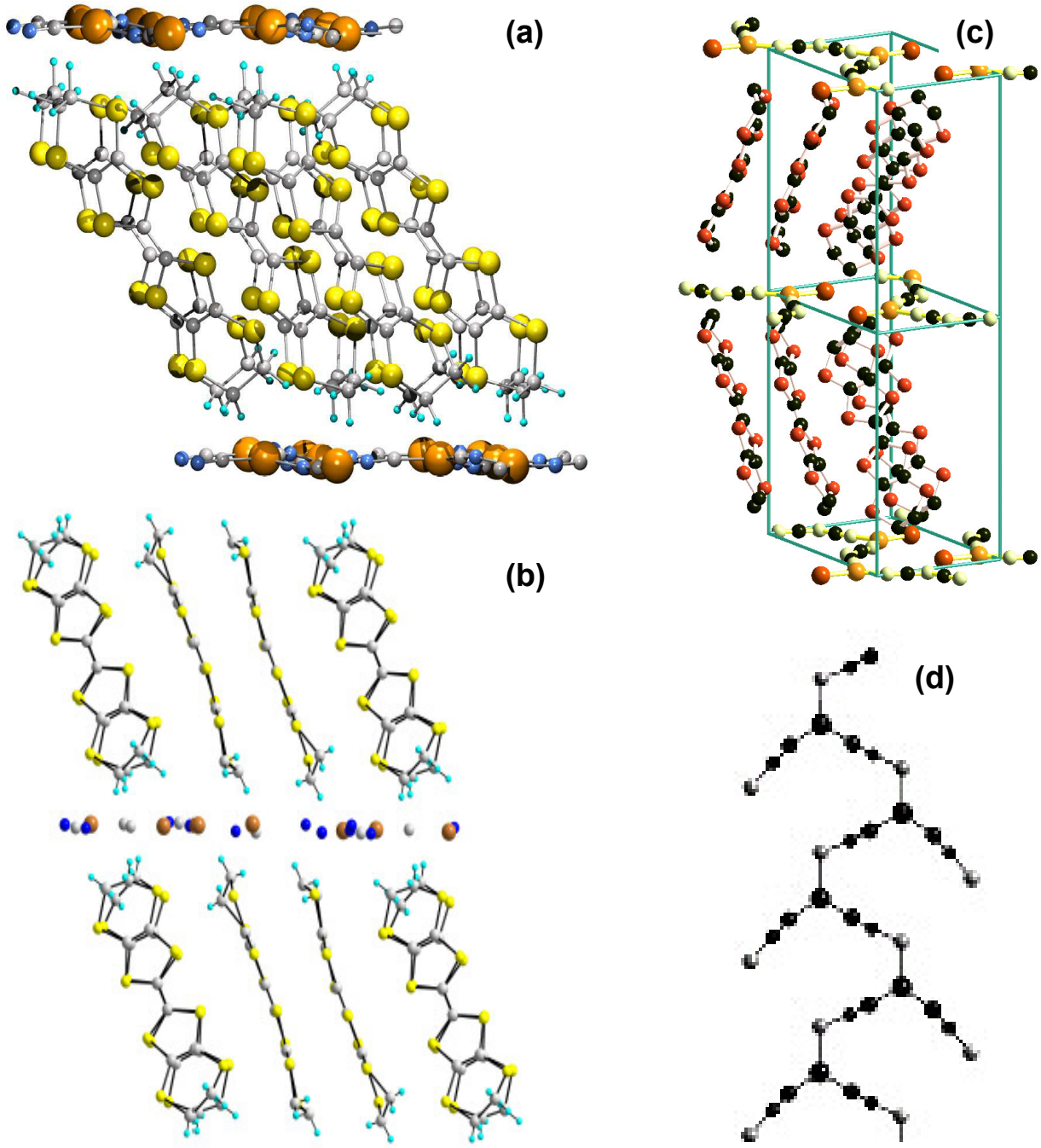

Figure 2.21 Molecular arrangement in the κ-$(ET)_2X$ family in different views (a and b), including the unit cell (c) and top view of the polymeric layer (d). The dimers form a strongly anisotropic triangular lattice (from [Val10]).

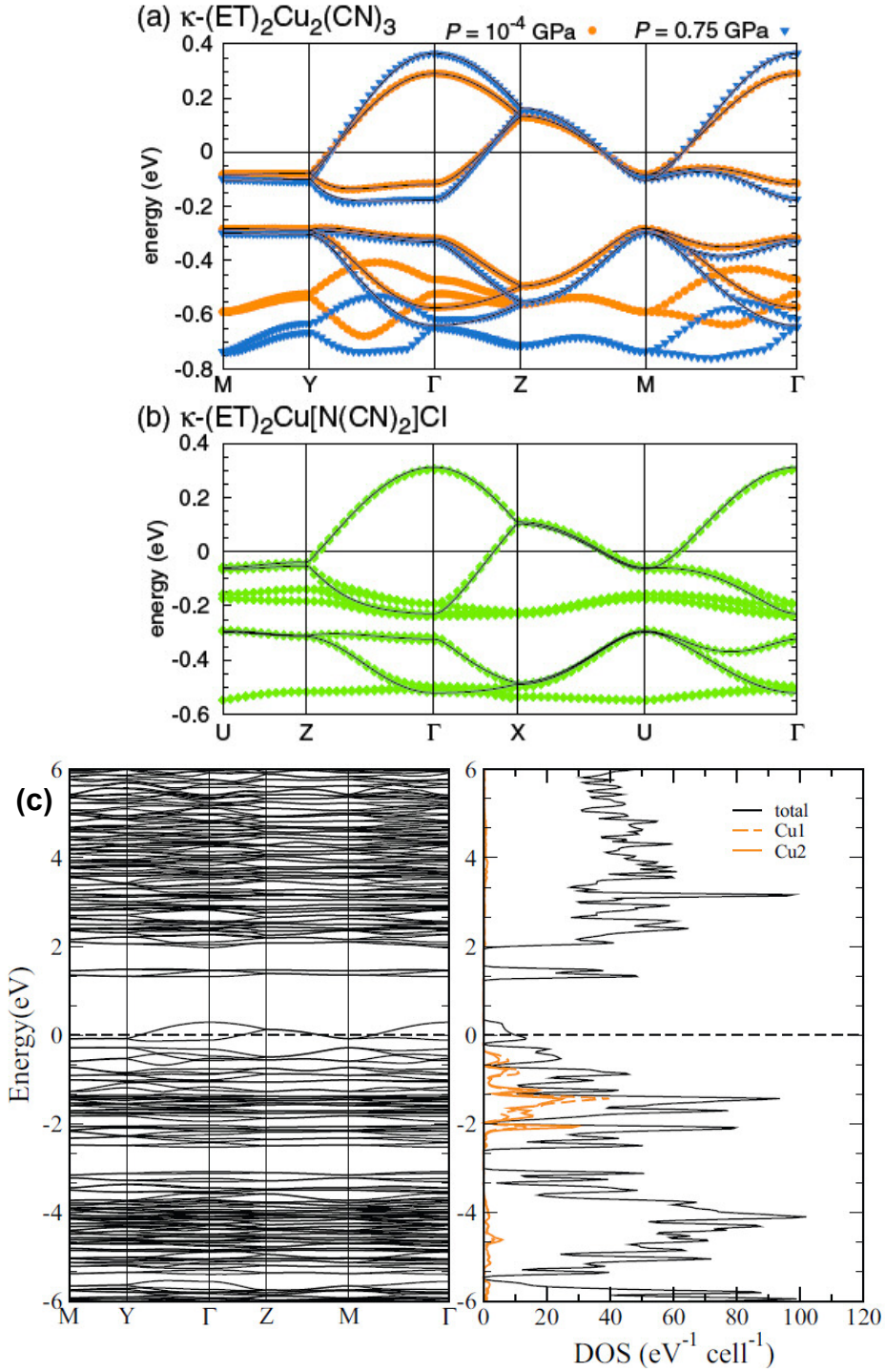

Figure 2.22 Ab-initio DFT calculation of the electronic band structure of κ-(BEDT-TTF)$_2$Cu$_2$(CN)$_3$ for ambient pressure and for 0.75 GPa (a) and of κ-(BEDT-TTF)$_2$Cu$_2$(CN)$_3$ (b) along several low-index directions of the Brillouin zone. A wider energy range together with the density of states (c) shows the global band gap region close to the Fermi energy that extends up to 1.5eV above E_F (a, b from [Kan09], c from [Val10]).

3. Experimental Techniques

3.1 Ultraviolet Photoelectron Spectroscopy (UPS)

The experiments were performed in a μ-metal-shielded UHV chamber equipped with a photoelectron spectrometer (type FOCUS CSA 300) and a helium discharge lamp. This apparatus was constructed and built in the framework of this thesis. The He I line ($h\nu$= 21.23 eV) was used for excitation. The experimental geometry is sketched in Fig. 3.1. The photon beam is directed almost perpendicular (85°) to the entrance lens of the spectrometer and the sample can be rotated in the drawing plane. The data shown are taken under normal emission (i.e., no surface parallel component of the electron momentum), because normal emission spectra yield the correct quantitative values for the sample work function. The electric field vector of the excitation radiation thus has a large component along the surface normal and along the centre of the acceptance cone of the electron spectrometer. The analyzer pass energy was set to 4 eV with 4 mm entrance and exit slits, yielding an energy resolution of < 0.1 eV. For the spectral region close to the Fermi-energy, the angular resolution is about $\pm$4°.

For (co-)deposition of donor and acceptor molecules, in particular for species with low sublimation temperatures, we developed a special load-lock system for crucibles as sketched in Fig. 3.1. The crucibles sit on top of stainless steel tubes sliding in Viton O-ring seals with a differential pumping stage and closing valve in between. Thus, the crucibles can be loaded without breaking UHV in the analysis chamber and can be positioned close to the substrate surface in order to achieve a high deposition yield.

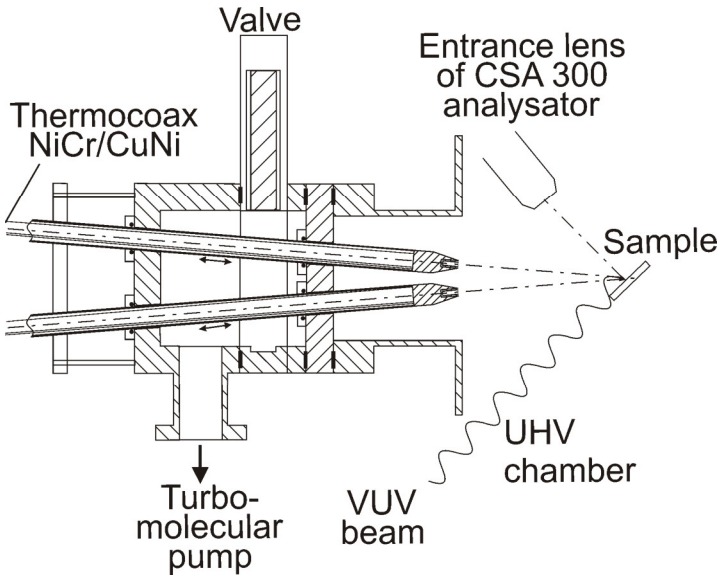

Figure 3.1 Cross section of the crucible load-lock arrangement in the UPS apparatus, developed for the in-situ co-deposition of small amounts of molecular materials. The evaporator is suitable for materials with sublimation temperatures below the bake out temperature of the UHV system.

For UHV deposition of high-purity films we supplied the evaporator with graphite crucible in an oxygen-free high conductivity (OFHC) copper holder with thermocoax heating element and NiCr-CuNi thermoelement for temperature regulation. The maximum crucible temperature is > 770 K. The coaxial current leads ensure magnetic field-free operation. Using a differentially pumped load-lock system, the evaporator could be changed and refilled without breaking UHV. The crucible was placed at a distance of 40 mm from the sample in measuring position in front of the electron spectrometer. In this way, the evolution of the spectra could be observed in small coverage steps during film deposition.

These evaporators are especially useful for materials that cannot withstand the standard heating procedure of a UHV system, because the crucibles can be introduced after the bakeout, when the apparatus is at room temperature again. The base pressure is in the 10^{-10} mbar range. Fig. 3.2 shows a photo of the complete UPS apparatus built.

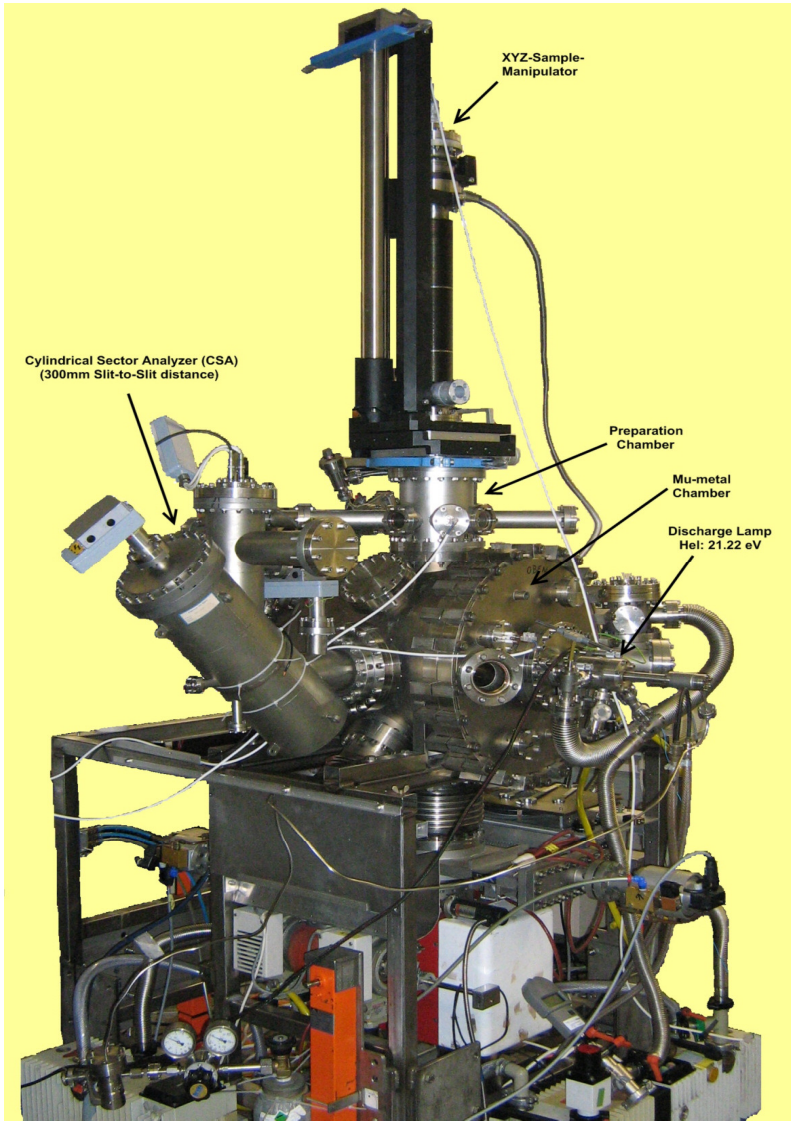

Figure 3.2 Photo of the UPS apparatus, built in the framework of this thesis.

3.2 Infrared Reflection and Absorption Spectroscopy (IRAS)

Infrared spectroscopy (IR spectroscopy) covers a range of techniques, mostly based on absorption or reflection on solid samples. It can be used to identify and study chemical compounds and it delivers information on vibrational excitations. Modern laboratory instruments using this technique are often based on a Fourier transform infrared (FTIR) spectrometer.

The infrared portion of the electromagnetic spectrum is usually divided into three regions; the near-, mid- and far- infrared, named for their relation to the visible spectrum. IR radiation is mostly characterized by wavenumbers (with 8000 $cm^{-1} \cong 1$ eV). The higher energy *near- infrared*, approximately 14000–4000 cm^{-1} (0.8–2.5 µm wavelength) can excite overtone or harmonic vibrations. The *mid-infrared*, approximately 4000–400 cm^{-1} (2.5–25 µm) may be used to study the fundamental vibrations and associated rotational-vibrational structure. The *far-infrared*, approximately 400–10 cm^{-1} (25–1000 µm), lying adjacent to the microwave region, has low energy and may be used for rotational spectroscopy. The names and classifications of these sub-regions are conventions, and are only loosely based on the relative molecular or electromagnetic properties.

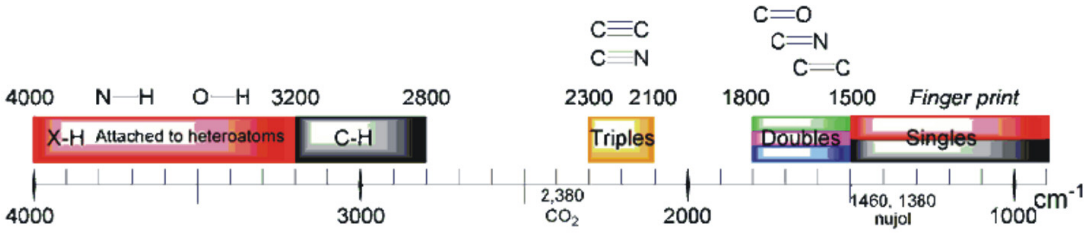

Figure 3.3 Infrared spectroscopy correlation table showing the regions of several typical vibronic bands. From left to right: single-, double- and triple-bonds of carbon and nitrogen and hydrogen attached to carbon, oxygen and nitrogen.

Infrared spectra have been taken using a Fourier spectrometer (type Nicolet 730 FT-IR) in reflection geometry. This spectrometer is equipped with a liquid-nitrogen cooled mercury cadmium telluride (MCT) detector. The present instrument is working in mid-IR range, i.e. wavelength of the incident beam is 2.5-25 µm (corresponding to the range of wave numbers 4000- 400 cm^{-1}), the step resolution is 0.5 cm^{-1}. The IR-instrument is controlled by the OMNIC software package to collect all spectra.

3.3 Near Edge X-ray Absorption Fine Structure (NEXAFS)

For the NEXAFS measurements we exploited Synchrotron radiation in the soft X-ray range from the WERA beamline at the storage ring ANKA, Karlsruhe. WERA is a beamline for soft x-ray spectroscopy, microscopy, and spectromicroscopy: PES, NEXAFS, SXMCD (Soft X-Ray Magnetic Circular Dichroism), PEEM (Photoemission Electron Microscopy). It is owned and operated by the Institute for Solid-State Physics (IFP), Karlsruhe Institute of Technology (KIT). WERA provides important electron spectroscopies in the photon energy range 100 – 1500 eV and combines them in situ with photoemission microscopy. In the total electron yield mode employed, the total drain current from the sample is detected. The electron emission yield originates from a subsequent Auger process that neutralizes the core hole and leads to the emission of Auger electrons and slow secondary electrons. The information depth is about 5 nm in total yield mode. The NEXAFS experimental station is equipped with three experimental chambers (the base vacuum is in the low 10^{-10} mbar range), the sample can be transferred between the preparation chamber and experimental chamber by means of a multi-port sample transfer system. The analysis chamber is equipped with a custom made manipulator with LHe cryostat (the limit for the temperature is 15 K).

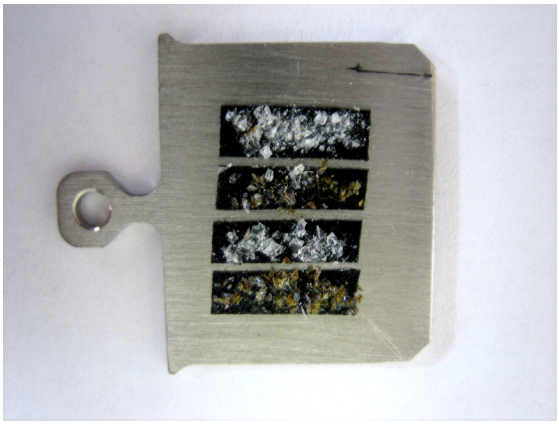

Figure 3.4 Standard Omicron sample holder with six fractions of HMP_x-$TCNQ_y$ microcrystals.

The investigated samples were fixed on the standardized design of the Omicron sample plates with the help of carbon glue or carbon tape, that allow investigations of single crystals and also thin films. Fig. 3.4 shows a sample holder with 4 attached samples (here fractions of HMP-TCNQ fractions. A stepping motor drive allows for precise positioning of the different samples in the Synchrotron beam. The movement between different samples can be programmed so that the whole measuring cycle can be fully automated including sample change. The typical size of the sample for thin films is approximately 4x4 mm, which were studied during beamtimes at ANKA. It makes possible to fix few samples on one plate. Due to this fact three samples were studied during one run. The NEXAFS measurements are controlled by the software package to collect all spectra, for further interpretation. Fig. 3.5 shows a schematic view of the beamline (a) and the three end stations (b).

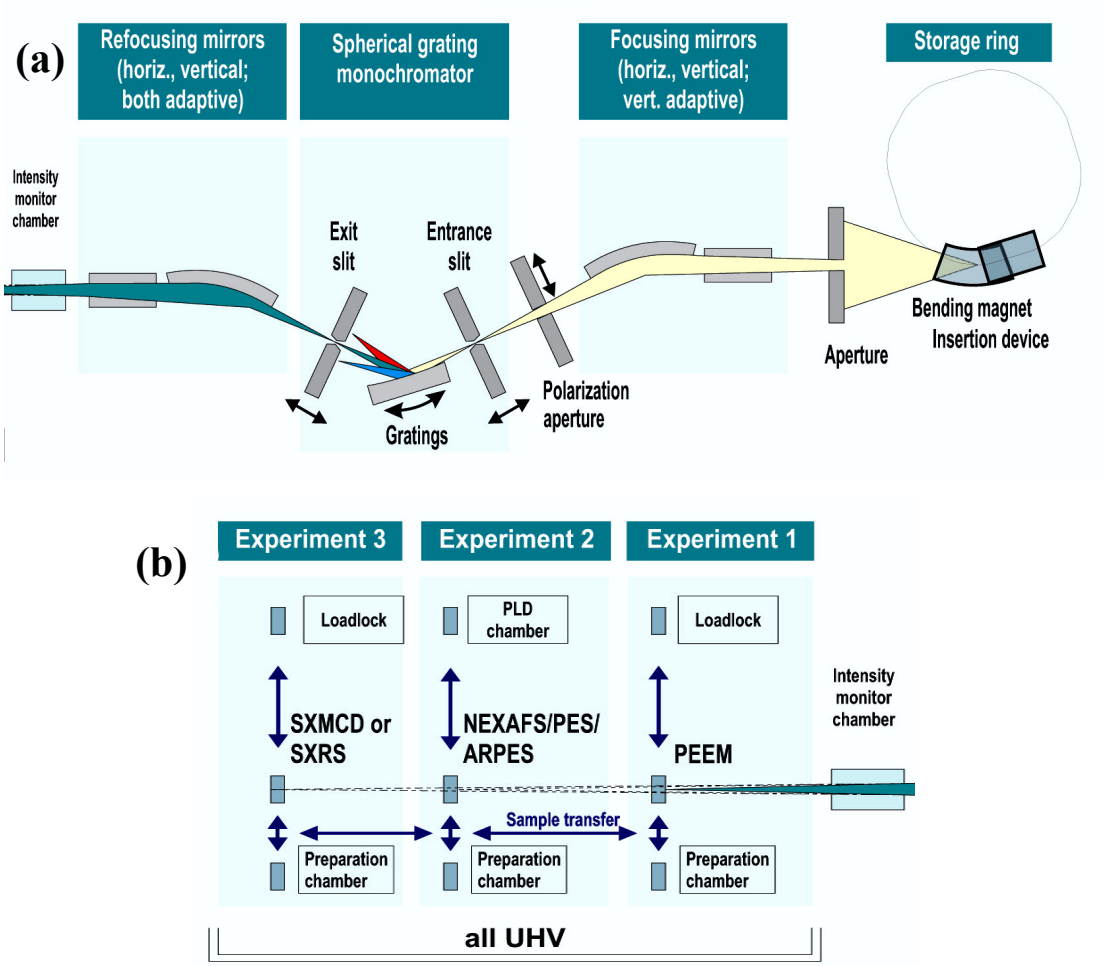

Figure 3.5 Schematic view of the WERA beamline (a) at the storage ring ANKA, Karlsruhe. The beamline supplies three endstations (b), the experiments of the present work were carried out at the "NEXAFS/PES/ARPES" end station (from ANKA web site).

3.4 Hard X-ray Photoelectron Spectroscopy (HAXPES)

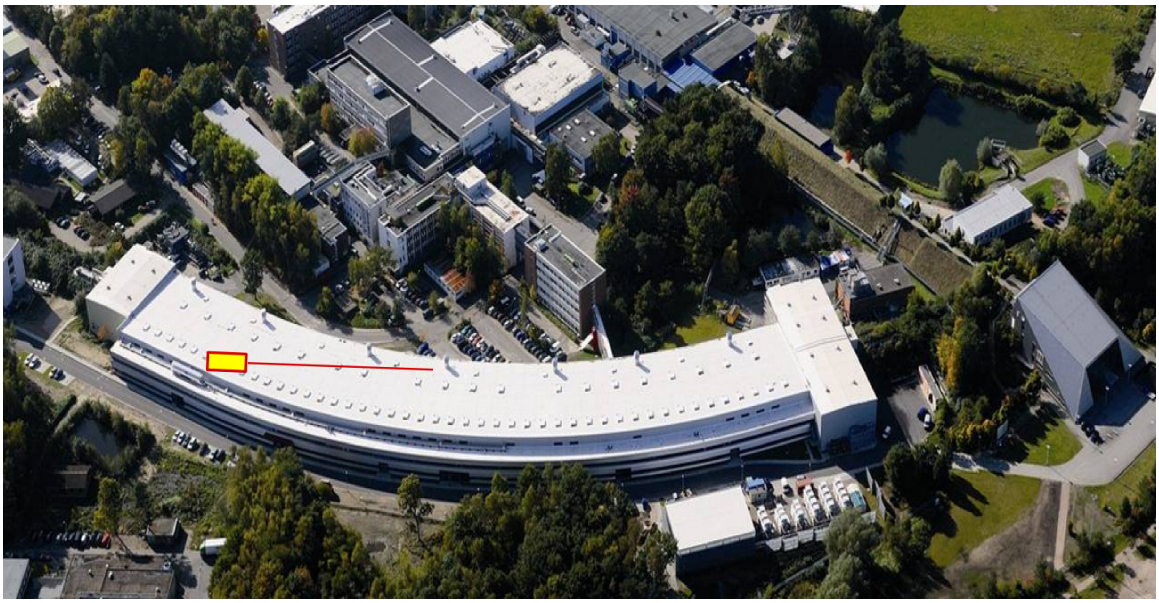

Figure 3.6 View of experimental hall of the storage ring PETRA III at DESY, Hamburg. The experiments of the present work were carried out at the "HAXPES" end station at beamline P09, marked by the yellow rectangle (from PETRA III user handbook).

The HAXPES experiment was performed at PETRA III, the former positron-electron tandem ring accelerator at DESY, Hamburg. This machine is a dedicated storage ring for Synchrotron radiation. Its positron beam energy is 6 GeV with current of 100 milliamperes (mA), making this ring an ideal source for hard X-ray beams with high brilliance. Fig. 3.6 shows an areal view of the experimental hall.

A high resolution HAXPES instrument has been set up at the undulator beamline P09, which went into user operation end of 2010. We succeeded to get one of the first regular beamtimes at this endstation. The beamline (Fig. 3.7) is equipped with a high heat-load double crystal primary monochromator followed by a double channel-cut secondary monochromator; a variety of different Si reflections with different band pass are available. An optional diamond phase retarder serves as efficient circular polarizer. The HAXPES end station is located 95 m from the source (indicated in Fig. 3.6). A Kirkpatrick Baez post-focusing mirror system will later be implemented to demagnify the intermediate focus of a primary set of mirrors down to spot sizes of about 2x2 μm^2 on the sample.

Photoelectrons with kinetic energies up to 15 keV can be measured in different experimental geometries by means of a high-energy electron analyzer (type SPECS Phoibos 225 HV) with a combined Delayline detector (type Surface Concept) and a micro-Mott spin detector. A photo of the set-up is shown in Fig. 3.8. Present energy resolution is about 250 meV at the given conditions. The final resolution is expected to be of the order 50 meV at 10 keV.

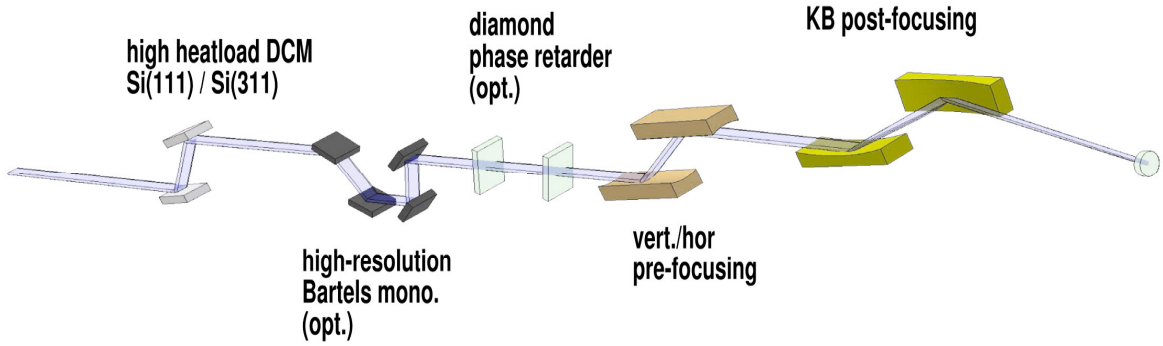

Figure 3.7 Schematic sketch of beamline P09 of PETRA III, where the HAXPES endstation is located.

The analysis chamber is equipped with a custom made 5-axis manipulator with LHe cooling (type OMICRON). The set-up is mounted on a high-precision X-Z-platform. The platform consists of a monolithic granite plate which is placed on three motorized height-adjustable (z-axis) and laterally movable feet. The set-up is fixed to the granite plate. The vertical range of adjustment comprises 50 mm with a resolution of 1 μm and a reproducibility of 5 μm when all three feet are moving. The whole setup rests on a steel supporting plate with 4 air-pads on which the feet are placed. The air-pads assure the lateral movement of the whole set-up for large distances. This makes feasible a quick change of the experimental geometry [Glo11].

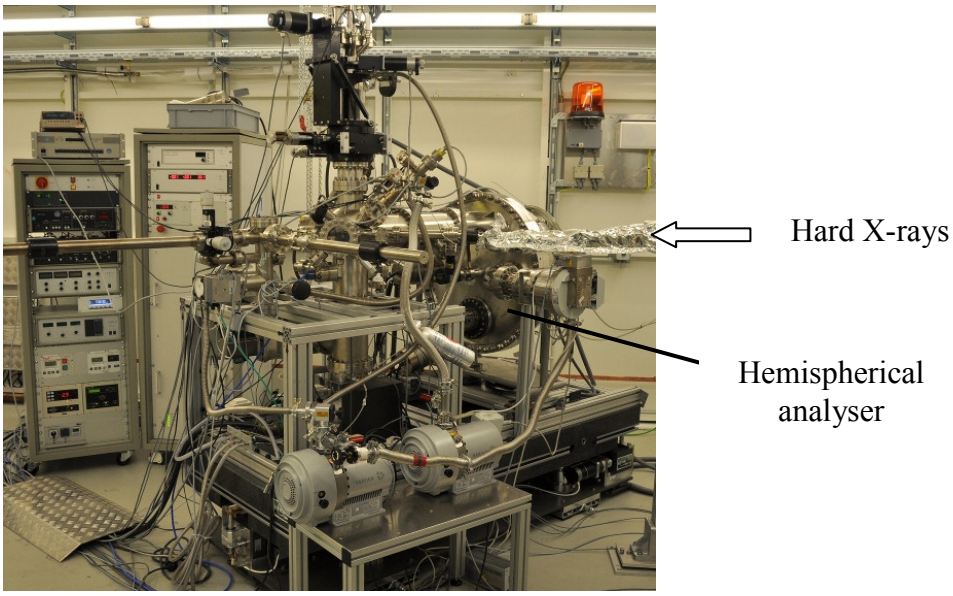

Figure 3.8 Photo of the HAXPES endstation at beamline P09 of PETRA III (photo courtesy Andreii Gloskovski).

4. Preparation of the Charge-Transfer (CT) Compounds

4.1 UHV Co-Deposition of Thin Films

For the present study we used graphite crucibles that had been extensively degassed ex-situ at > 1000 K using an e-beam evaporator in good vacuum. After insertion into the device the loaded crucibles were degassed at typically 50 K below the final sublimation temperature for several hours. Then a gold film was deposited onto a silicon wafer with native SiO_x surface layer using an e-beam evaporator (type FOCUS EFM3) in a separate preparation chamber with transfer to the main chamber using a 3-axes manipulator (type VG Omniax). All freshly deposited gold films exhibited a work function of $\Phi = 5.30$ eV, indicative of a surface with predominant (111)-facets. Φ was determined as difference between the He I photon energy (21.23 eV) and the measured full width of the photoelectron spectrum (with a negative sample bias of -3 V ensuring a correct low-energy cutoff). Given our analyzer resolution, the error in Φ is about 0.1 eV, relative changes could be detected down to $\Delta\Phi <$ 0.02 eV from the steep slope of the low-energy cutoff spectra.

Coronene-hexaone (COHON) and *hexamethoxycoronene* (HMC) were synthesized as described in the literature [Rie08]. Molecular films were sublimed at crucible temperatures of 658 K (COHON) and 483 K (HMC). Due to the small amounts of material (typically 5 mg for one crucible load) a suitable balance had to be found between crucible degassing time and the usable amount of material.

Tetramethoxypyrene (TMP), *Hexamethoxypyrene* (HMP) and *tetracyanoquino-dimethane* (TCNQ) as well as their *mixed phases* were evaporated at the same conditions as the previous molecules, the corresponding crucible temperatures were 420 K, 435 K and 400 K for the complexes, pure TMP and HMP, and TCNQ, respectively.

The evaporated films can be controlled in-situ by UPS and ex-situ by optical microscopy, AFM and STS (in cooperation with the group of Prof. Elmers). Fig. 4.1 shows a typical AFM image and line scan, here for the complex TMP-TCNQ. Further images are shown in appendix A.

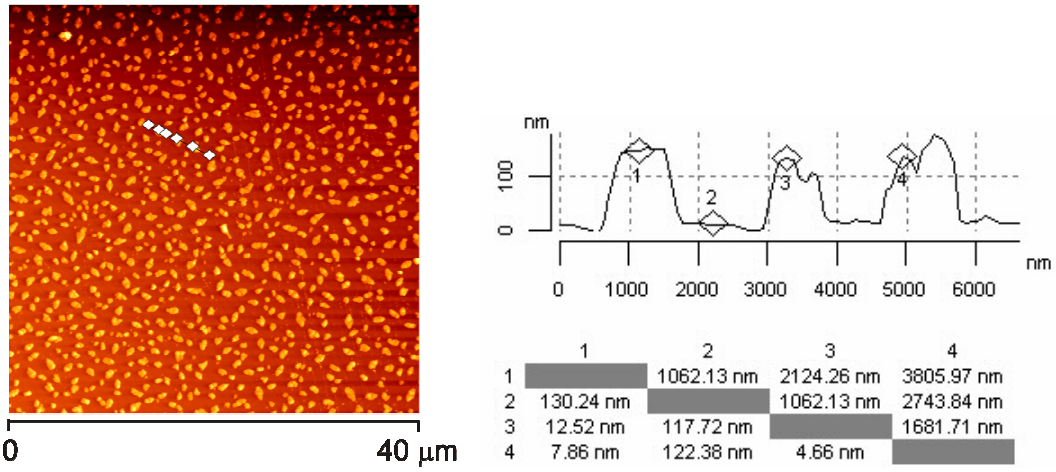

	1	2	3	4
1		1062.13 nm	2124.26 nm	3805.97 nm
2	130.24 nm		1062.13 nm	2743.84 nm
3	12.52 nm	117.72 nm		1681.71 nm
4	7.86 nm	122.38 nm	4.66 nm	

Figure 4.1 Thin film of the TMP-TCNQ mixed phase and its surface profile.

4.2 Solution-Growth of 3D Microcrystals

Melby et al. [Mel62] have grown pyrene-TCNQ in solution and found a weak CT complex; later Amano et al. [Ama71] have grown diaminopyrene-TCNQ in acetonitrile CH_3CN and found an ionic CT salt. The 2D crystals investigated by HAXPES and NEXAFS were grown in the Max-Planck-Institute for Polymer Research by Dennis Chercka (see also [Che09]). In first experiments we just looked at the colour change of concentrated solution of our donor-acceptor moieties providing a broad CT absorption band in the visible range with maximum at about 600 nm.

Crystals were grown by vapour diffusion of hexane into a dichloromethane solution (5 ml, $6{,}2 \cdot 10^{-3}$ mol/l) of the components. Solutions with donor-acceptor mixtures of 1:2, 1:1 and 2:1 stoichiometry were prepared. The components were combined in a glas vial (V = 7 cc; 1,5 cm diameter) and dissolved under sonication. Vapour diffusion assisted crystallizations were performed in a gas-tight chamber (V = 120 cc), filled with 15 ml hexane. The vial containing the solution was placed inside the chamber which was sealed for 4 days.

The crystallites have sizes in the range from several 10µm to several 100µm. X-ray diffraction analysis of TMP-TCNQ microcrystal fractions revealed a mixed-stack geometry as shown in Fig. 4.2 b [Che10]. The complex appears black, whereas crystallites of the pure donors HMP or TMP are colourless transparent and TCNQ is transparent with light green colour. Optical microscopy revealed that there is a mixture of dark and transparent crystals in the vial, examples, see Fig. 4.2c and d. The admixture of bright crystals is maximum in the HMP_2-$TCNQ_1$-stoichiometry. For the 1:1 stoichiometry the admixture is smaller and for the 1:2 stoichiometry there are no transparent crystals. The different phases could easily be distinguished by their colour and the crystal fractions could thus be separated using a micromanipulator under the optical microscope. The NEXAFS spectra revealed that the transparent crystals show no nitrogen K-edge signal. This proves that they contain no TCNQ and consist of pure donor material. Obviously, HMP or TMP microcrystals form during the vapour diffusion process in coexistence with the complex.

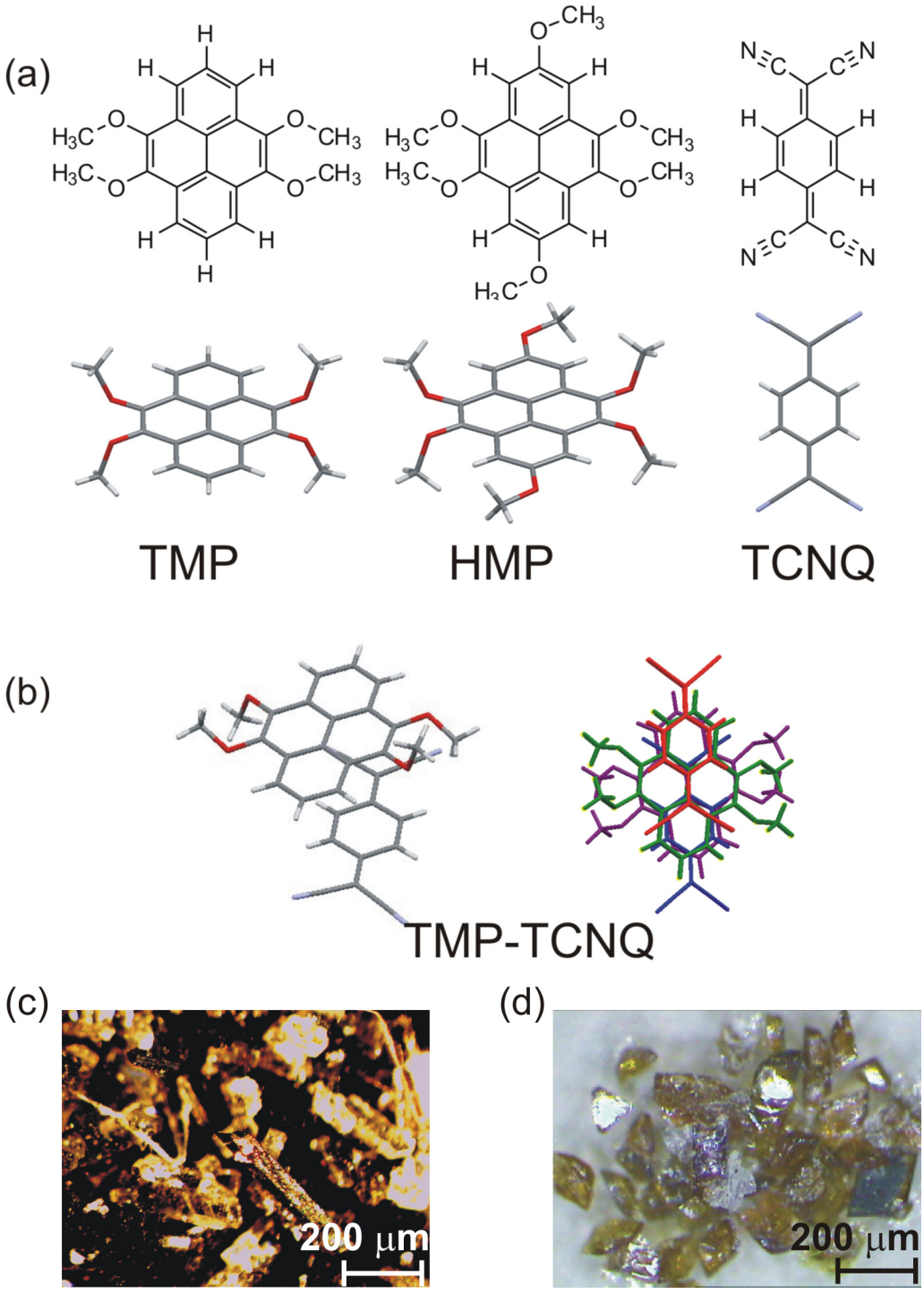

Figure 4.2 Molecular structures (a) and structure of the TMP_1-$TCNQ_1$ complex as obtained from X-ray diffraction (b); the second plot shows a colour-coded top view of the molecular arrangement in four adjacent layers. Optical microscopy of HMP_2-$TCNQ_1$ (c) and TMP_1-$TCNQ_1$ (d) shows coexistence of dark and bright microcrystals (field of view 1mm horiz.).

5. CT-Complex of Donor and Acceptor Derivatives of Coronene

5.1 Short Introduction Into Coronene Chemistry

Polycyclic aromatic hydrocarbons (PAHs) have recently been made larger and larger and the molecules are then called *nanographenes* [Mue08, Wat01, Kan03, Wup07]. Large planar PAHs with 90 carbon atoms and more can be synthesized in a bottom-up approach with the desired size, structure, and symmetry [Wup07]. Moreover, synthesis routes have been developed for functionalization, i.e., the defined attachment of ligand atoms or groups at the periphery. This has, for instance, been shown [Rie08] for the medium-size molecule *coronene* ($C_{24}H_{12}$). The synthetic approach facilitated the realization of a new set of donor and acceptor molecules with a systematic variation of the electronic properties *via* the type and number of substituents at the periphery. Retaining the coronene ring system, the electron affinity and ionization energy can be controlled in a wide range from typical donor behavior for different degrees of methoxy substitution to strong acceptor behavior for coronene-ketones.

In cyclovoltammetry *coronene-hexaone* (COHON, $C_{24}H_6O_6$) is reduced at -0.38 V against ferrocene (standard) [Rie08]. The corresponding electron affinity level is estimated at 4.4 eV below the vacuum level (set to zero), close to the value for TCNQ, which is 4.7 eV [Ack62]. This suggests that COHON is a strong electron acceptor. *Hexamethoxycoronene* (HMC, $C_{30}H_{24}O_6$), on the other hand, is oxidized at 0.74 eV against ferrocene, which corresponds to an ionization energy of 5.5 eV with respect to vacuum. This indicates that HMC is a moderate electron donor. In the present work the electronic structure of mixed films of COHON and HMC was investigated by UPS and NEXAFS, and we compare these results to those obtained from the respective pristine molecular films. Since crystallization from solution cannot be applied to COHON due to its low solubility, the organic films were grown on Au surfaces by (co-)sublimation in ultrahigh vacuum (UHV) as discussed in section 4.1.

For the understanding of such organic films on metallic substrates, the *metal-organic interface* often plays a crucial role and the electronic structure can be rather complex, in particular for systems where charge-transfer occurs, as discussed in recent reviews [Kah03, Cah03, Koc08]. An acceptor molecule in direct contact with a metal surface may form a negatively charged species as was found for TCNQ on Ni (111) [Gie91]. TCNQ on Au, on the other hand, was found to be almost neutral [Fer08]. Its acceptor character does not suffice to form a strong charge-transfer complex with Au, the metal with the highest Pauling electronegativity. The fluorinated TCNQ analog F_4TCNQ ($C_8N_4F_4$) on Au, however, exhibits pronounced electron-transfer from the metal to the molecule in the monolayer [Koc05b]. The energy levels of subsequently deposited organic molecules are then re-aligned relative to the new chemical potential established by the charge-transfer complex at the interface. Consequently, the hole injection barrier (energy difference between the highest occupied molecular level onset and the Fermi-level of the metal) can be reduced substantially (up to 1.2 eV) compared to that found on pristine Au [Koc05b]. In such metal-organic systems interface states (i.e., charge-transfer induced states that do not exist for pristine molecules) [Ran09] play a crucial role. This induces deviations from the linear scaling of level positions with work function [Bra07]. The interface energetic structure

becomes even more complicated when a second organic material is involved that can form an organic-organic charge-transfer complex with the acceptor. Such a complex has frontier energy levels that are hybrids of the respective frontier levels of the individual donor and acceptor molecule, [Azi07] as directly observed for the acceptor-donor pair F_4TCNQ - α-sexithiophene on a Au(111) surface [Jae08]. Organic-metal interface states can also show considerable energy dispersion relations because they result from a hybridization of metal and molecular states leading to anisotropic hybrid bands [Gon08].

Optical microscopy (see Appendix) of films of the pure species reveals bright and homogeneous multilayers of HMC or COHON (in faint red color). For thick films of the mixed phase, however, micrometer-sized dendritic crystallites with dark blue color appear. The strong absorption in the visible spectral range indicates already a HOMO-LUMO gap much smaller than for the pure species. This is the first hint on the formation of a CT-complex.

5.2 Ultraviolet Photoelectron Spectroscopy

The coronene-derivatives COHON (acceptor) and HMC (donor) and their mixed phase deposited on Au surfaces were the first system studied in this thesis. At first, the aim was to screen the UPS-spectra for signatures of an interface charge-transfer (between metal and organic layer) and an inter-molecular charge-transfer in mixed films. *In-situ* molecular beam deposition (and co-deposition for mixed films) during acquisition of UPS spectra allowed observing the evolution of interface energy levels and sample work function Φ in small coverage-dependent steps during layer growth. For the acceptor COHON evidence of electron transfer from the metal to the organic overlayer was found. A characteristic interface state occurred in the energy gap of the pristine molecule, accompanied by a substantial increase of Φ. Parallel to the measurements, density functional theory (DFT) calculations have been performed by S. Naghavi [Nag10a, Nag10b, Nag10c], yielding the scheme of valence orbitals of the substituted species in comparison with the parent molecule coronene as described in section 2.2. Binding energies were calculated using the *Delta-Self-Consistent-Field* approach. As we will see, the trends and size of binding energy shifts induced by the different ligand groups at the periphery of the molecule are correctly predicted. In co-deposited multilayers of COHON and HMC the highest occupied molecular orbital (HOMO) of HMC is shifted towards higher binding energy and the HOMO of COHON is shifted towards lower binding energy, in agreement with the trend anticipated for a weak charge-transfer system.

During an UPS-run, typically 50 spectra were taken in a sequence. The deposition rate was adjusted in the range of 0.3-2 monolayers per minute, corresponding to a partial vapour pressure of $\sim 10^{-8}$ mbar on the sample surface (assuming a sticking coefficient of 1). Spectra series were confirmed in several independent runs, using always fresh Au films as substrates. This procedure gives access to the detailed evolution of peak intensities, peak positions and the corresponding work function changes as function of coverage (which is impossible using an ex-situ film deposition procedure). For comparison, we have also taken spectra for the parent molecule coronene. The results for coronene agreed very well with the spectra reported in literature [Sch02, Yam09].

Acceptor Coronene-hexaone (COHON)

Fig. 5.1a shows a series of UPS spectra for COHON on Au from sub-monolayer to multilayer range, numbered consecutively. Starting from the clean gold spectrum (1) we first observe a reduction of the Au d-band intensity and broad features at binding energies above 4 eV upon COHON deposition. This low-coverage regime is associated with a drop of the work function from the initial value of 5.3 eV for clean Au, see Fig. 5.1b (with corresponding spectra numbers from (a)). In the region of the work function minimum of 4.8 eV, a new photoemission feature appears in the valence region (denoted IS) at a binding energy of 1.75 eV. It reaches an intensity maximum (spectrum 6) and fades out towards higher coverage (spectrum 9). The appearance of this feature is associated with an increase of Φ. Along with the intensity drop of IS, new signals (A and B) appear, centered at binding energies of 3.25 eV and 4.7 eV (spectra 10-12). The work function-*vs*-coverage curve shows two steps in the region of the second and third layer. After a total increase of 0.8 eV it reaches a saturation value of Φ_{COHON}= 5.6 eV for the multilayer film.

The calculated binding energy of the electrons in the HOMO of COHON (Fig. 2.6) translates into a binding energy of 3.18 eV with respect to the Fermi-energy (E_F) taking into account the work function of the thick film. This value lies close to the centre of signal A (3.25 eV) in the high-coverage spectra 10-12 (Fig. 5.1a). The theoretical spectrum (top) was obtained using the binding energy positions from the ΔSCF calculation taking into account a broadening of the photoemission signals by 0.6 eV of full width at half maximum (FWHM). The calculated binding energies are marked as bars below the theoretical spectrum; for symmetry labels, see Fig. 2.6. The oxygen $2p_{x,y}$-derived orbitals with σ-symmetry deserve special consideration. At the given photon energy the partial cross section of oxygen 2p is lower than that of carbon π [Ang88, Tof04]. The σ-orbitals have nodal planes perpendicular to the molecular plane. Hence the corresponding photoemission signals in normal emission vanish for molecules oriented parallel to the surface. In order to account for the lower cross section, the oxygen 2p-derived signal intensities were weighted by a factor of 0.2 in comparison with the π-orbitals. The cross sections of the π-orbitals were assumed to be identical, but the double degeneracy of the E-orbitals has been taken into account. The calculation cannot account for charge-transfer from the metal substrate into the organic overlayer. Thus, the signal IS at low coverage is not reproduced by theory.

The work function-*vs*-coverage curve and the development of the photoemission feature intensities suggest three growth regimes for COHON on Au. The initial rapid drop (ΔΦ = -0.5 eV) is accompanied by a decrease of the Au-derived spectral intensity and the appearance of broad features of additional intensity in the binding energy region between 4 eV and 11 eV. We conclude that in the ***low coverage regime of COHON*** the push-back effect is the dominant mechanism for the change of Φ. It results from the Pauli repulsion of the spill-out charge of the pristine Au surface by the electrons of the adsorbed molecules. The push-back effect reduces the surface dipole of Au, resulting in a decrease of Φ, as observed for many organic species [Ish99]. However, it is possible that the COHON monolayer on Au actually weakly chemisorbs with a net electron transfer from Au into the molecule. Consequently, the push-back effect is to some extent counteracted by a charge-transfer dipole that increases Φ. The fact that no clear indications for charge-transfer induced gap states are observed in the valence region in this initial stage of COHON deposition is consistent with a weak charge-transfer, and has been suggested for similar molecular systems [Duh06]. It is likely that in this initial phase the molecules lie face-on on the surface.

In addition, the carbonyl groups might be bent such that the O-atoms approach the surface closer than the C-atoms, where the π-system stabilizes the larger distance of the ring structure. The tilted dipoles of the carbonyl-bonds (see chapter 3) would lead to a dipole component perpendicular to the surface along with an orientation that also reduces Φ. For instance, for TCNQ and F_4TCNQ, such a bent conformation in the first layer has been discussed in [Ran09]. Thus the initial moderate Φ decrease may result from an interplay of electron push-back, weak charge-transfer, and molecular distortion.

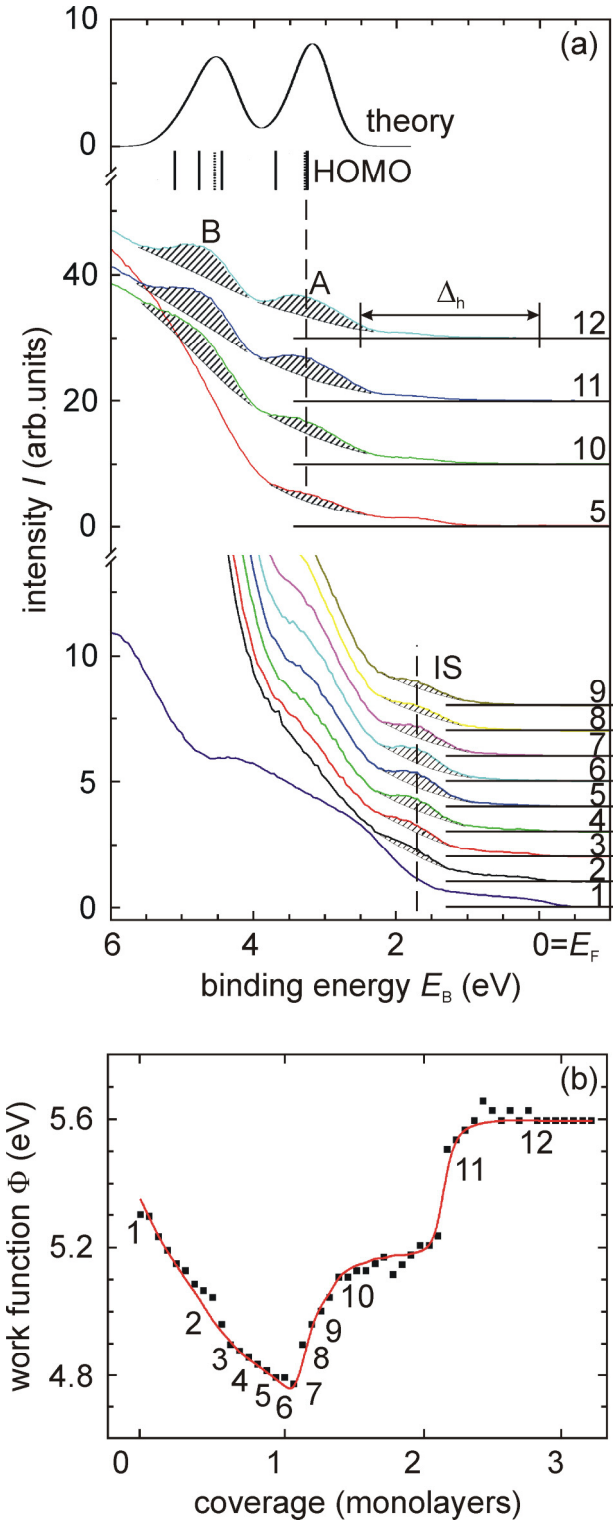

Figure 5.1 Series of He I UPS spectra (a) and corresponding coverage dependence of the work function (b) for coronene-hexaone on Au. Topmost four spectra: intensity ×4.3, features denoted as IS, A and B mark an interface state and two groups of orbitals. The hole injection barrier is Δ_h= 2.4 eV. For comparison, a calculated spectrum on the basis of ΔSCF binding energies (top) is included. Full and dotted bars denote the binding energy positions of π- and σ-orbitals, respectively.

Recent calculations based on the density of interface states approximation [Vaz07] have shown that the proximity of a metal surface can give rise not only to a broadening of the molecular levels but also to a new type of density of states that can be described as a weak continuum superimposed to the discrete molecular spectrum. In fact, the UPS spectra of COHON at sub-monolayer coverage were characterized by broad, unstructured features. As a consequence of this induced density of states there can be a spectral contribution even within the HOMO-LUMO gap region of the molecule. Moreover, the "charge neutrality level" [Vaz04] is no longer in the centre of the gap (as for an undisturbed gas-phase molecule) but is shifted according to the integrated total charge of the isolated molecule in front of the metal surface. The position of this level with respect to the Fermi energy (taking into account the metal work function) determines to what extent charge is transferred from the metal to the molecule or vice versa. The charge neutrality level model turned out to be very powerful when the charge transfer and the intra-molecular and metal-organic bonding dipoles are included. It would be highly desirable to compare the prediction of this model with the present results. Of course, the charge density plots in Fig. 2.5 cannot account for the energetic "pinning" of the molecules to the metal.

Upon further dosage of COHON, the work function increases substantially (by 0.8 eV, appearing almost as two steps of 0.4 eV each in Fig. 5.1b). In the region of the work function minimum, the feature IS appears at E_B= 1.75 eV, i.e. between the HOMO level and the Fermi-edge of the metal. After reaching its intensity maximum (spectrum 6), signal IS is diminished and signals A and B start to grow. Signal IS thus indicates a second layer COHON adsorption species generating a pronounced dipole moment on the surface (as Φ changes dramatically). Energetic position and coverage behavior of signal IS combined with the marked increase of Φ give strong support for an interface state resulting from an electron transfer into the second molecular acceptor layer (on top of the monolayer). Such interface states are also referred to as gap states because they arise in the HOMO-LUMO gap of the pristine molecule [Kah03, Cah03, Koc08]. Similar states have been observed for F_4TCNQ in direct contact with Au [Koc05b]. Signal IS is indicative of a negatively charged second layer of COHON. The IS signal intensity drops with increasing film thickness, i.e. analogously to a metal surface state, the interface state is localized essentially in a single layer. The second COHON layer experiences the surface potential established by the first COHON layer, which is 0.5 eV lower than that of pristine Au (see above). Because of the pronounced electron acceptor nature of COHON, the low effective surface potential of monolayer-COHON/Au substrate may thus suffice for an electron transfer into the LUMO of the second adsorbed COHON layer.

The minimum and the "double step" in the rising part of the work function curve were well reproducible in several preparations. The steep rise of the work function indicates a significant interface dipole possibly accompanied by a change in molecular orientation (from parallel to perpendicular or sandwich-herringbone like arrangement). An orientational transition from parallel to perpendicular geometry has also been observed in other aromatic systems, e.g. benzene on graphite [Sch90]. The dipolar character of the interface with the negative side of the dipole pointing towards vacuum is fully developed after the third layer has started to grow.

In the high-coverage regime, signals A and B reflect the growth of multilayer ***neutral COHON*** on top of the charged interface layer(s). The onset of this growth regime is indicated by saturation of the work function at 5.6 eV. The hole injection barrier (distance between the leading edge of the HOMO and the Fermi-level) is Δ_h= 2.4 eV. The ionization

energy (sum of Δ_h and Φ) is thus 8.0 eV for COHON molecules in the thick film, close to the value for a film of the prototypical acceptor TCNQ [Kah03].

Donor Hexamethoxycoronene (HMC)

HMC on Au was studied in the same way as COHON. Fig. 5.2 shows a series of UPS spectra taken between the sub-monolayer and the multilayer coverage regime (Fig. 5.2a) and the corresponding workfunction-*vs*-coverage curve (Fig. 5.2b). With increasing coverage the features derived from molecular levels develop into three distinct peaks A, B, and C. The theoretical spectrum has been calculated in the same manner as described for COHON (see above). In this case signal A corresponds to the HOMO without overlap with other orbitals. Signals B and C derive from the superposition of several orbitals; for symmetries, see Fig. 2.5.

There is no additional interface state as in the case of COHON. For high coverage (spectrum 7) the maximum of peak A corresponds to a HOMO binding energy of 1.75 eV below E_F. The theoretical spectrum from the ΔSCF calculation (top spectrum) was shifted by 0.23 eV to higher binding energies, in order to obtain best agreement with experiment. The hole injection barrier of the multilayer film is Δ_h= 1.3 eV. Due to the missing mirror plane, there is no strict π- and σ-symmetry. However, we can identify "π- and σ-like orbitals" in analogy to COHON (see e.g. the orbital plots in Fig. 2.5). The σ-like orbitals close to 3.9 eV binding energy (dotted bars in Fig. 5.2a) derive from oxygen $2p_{x,y}$-states and are localized essentially in the methoxy groups. The same weighting factor as for COHON (i.e. 0.2) was applied to these orbitals when calculating the spectrum. The lower-lying σ-like orbitals close to 4.9 eV involve O 2p to a smaller extent and have been weighted by a factor of 0.5.

In the low-coverage range the molecular feature positions are rigidly shifted to lower binding energies, by up to 0.4 eV for spectrum 2 in comparison with spectrum 7 (see bars denoting the peak maxima of A and B in Fig. 5.2a). This is a consequence of photo-hole screening by the image charge in the metal for molecules in the first and second layer, possibly accompanied by subtle molecular conformation changes as HMC is not planar [Koc05a]. The shift is about the same as was measured for Xe on noble metal surfaces [Sch85]. For thick HMC films (above approx. 4 nm) charging sets in, leading to a sudden shift of all photoemission signals to lower kinetic energies. The photo-holes in the organic film are neutralized too slowly, so that charge builds up at the film surface. For COHON no charging was observed even for much thicker layers, pointing on a higher intrinsic (photo-) conductivity.

The corresponding work function-*vs*-coverage curve for HMC on Au, Fig. 5.2b, shows a rapid drop during growth of the first layer and almost saturates at $\Delta\Phi$= -0.5 eV. This behavior reflects the push-back effect, i.e. Pauli repulsion of the spill-out charge of the Au surface as discussed for the low-coverage phase of COHON. The fact that Φ saturation is not fully reached may be due to the intramolecular dipolar bonds, which - depending on details of the molecular orientation - can contribute to Φ. Since HMC is an electron donor, electron transfer from the metal to the molecule can be ruled out on general grounds. The ionization energy for HMC molecules in the multilayer is $\Delta_h + \Phi$ = 6.1 eV, being 0.6 eV higher than the value derived from cyclovoltammetry (5.5 eV) [Rie08].

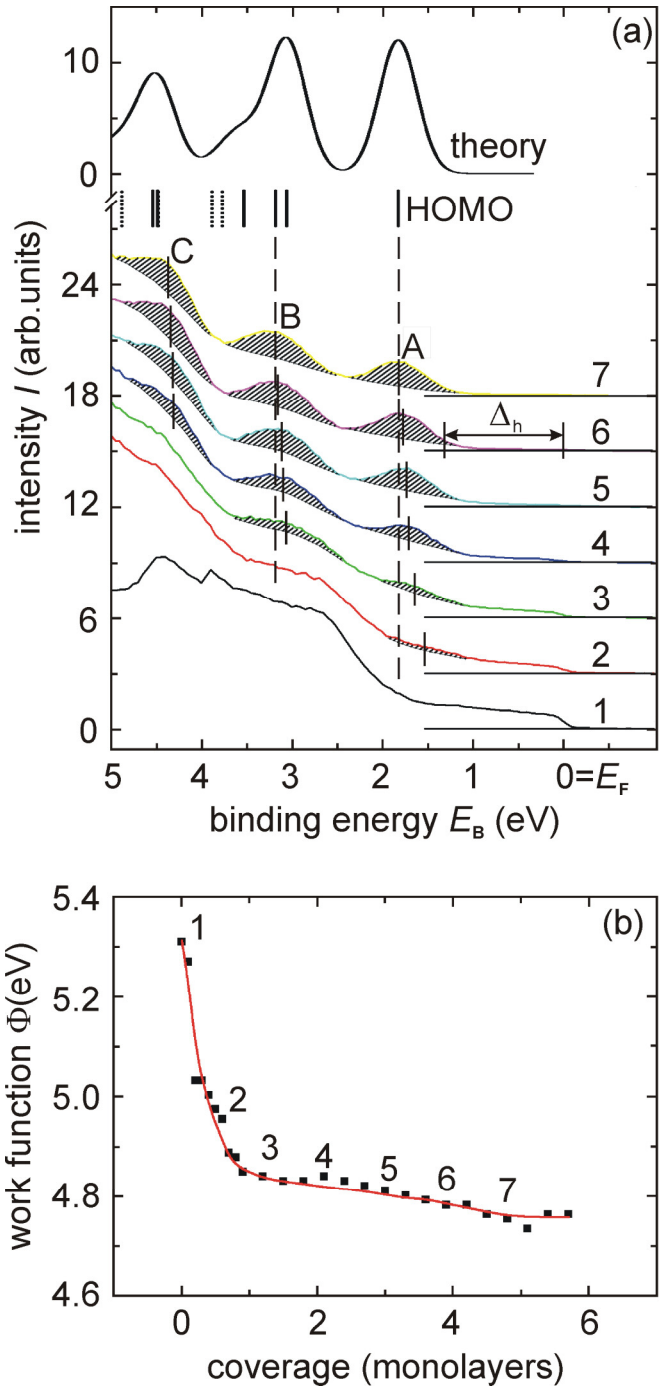

Figure 5.2 (a) Series of He I UPS spectra for hexamethoxycoronene on Au. (b) Corresponding coverage dependence of the work function. Signals A-C correspond to the HOMO and two groups of partly overlapping orbitals. The hole injection barrier is Δ_h= 1.3 eV. For comparison, a calculated spectrum on the basis of ΔSCF binding energies (top) is included. Full and dotted bars denote the binding energy positions of π- and σ-like orbitals, respectively.

Mixed Phase of COHON and HMC

The mixed donor/acceptor phase was obtained by alternating evaporation of several COHON and HMC layers with thicknesses of about 1.5 nm per layer. Fig. 5.3 shows UPS spectra for the mixed phase in comparison with a calculated spectrum and spectra for pure HMC and COHON multilayer films. Upon formation of the mixed phase it appears that the signals derived from the HOMOs of HMC and COHON show significant shifts in opposite directions. The HOMO peak maxima shift from the multilayer spectra by about 0.19 eV to higher binding energy for HMC and by 0.25 eV to lower binding for COHON, as indicated by the arrows. These opposite shifts may indicate that negative charge is transferred from the donor to the acceptor. The charge depletion in the donor (HMC) leads to a reduced intramolecular screening and thus to an increase of binding energies for orbitals located at HMC, whereas the charge excess in the acceptor reduces the binding energies of orbitals located at COHON.

The mixed phase corresponding to the spectrum in Fig. 5.3 was grown on an initial layer of COHON on Au. Spectra series have also been taken with HMC as starting layer on Au. For thick films, where the mixed phase has formed, the spectra were identical. This indicates intermixing down to the interface region.

For the calculation an alternate stacking motif (π-stacking) of donor and acceptor molecules was assumed. Geometry optimization started with symmetrically placed molecules. Optimization in π-stacked aromatic compounds is a demanding task since there is Van der Waals interaction between the layers and correlation is crucial for the dispersion effect [Gri07]. On the other hand, for our large disc-type molecules it is supposed that steric effects between the phenyl rings are dominant and neglection of dispersion is not expected to be a major problem [Pis07]. In this case the structure was optimized with HF/6-31g* to examine the distance between the two layers. No constraint was introduced during the optimization in order to find the stationary point of the potential energy surface. A frequency calculation was done for the optimized structure, demonstraiting lack of imaginary frequencies. The electronic structure calculation was done using B3LYP/6-31G* which includes correlation by including DFT. In addition, to check the calculated distance by Hartree Fock HF-optimization was performed for some smaller and similar structure and found that there is just a small overestimation of the distance. This is expected if correlations are neglected. Fortunately, the effect of layer distance on changing the HOMO energy is in the range of meV with very smooth slope. Therefore, small deviations in the layer distance are probably negligible in this case [Nel00]. The optimized distance between adjacent layers is 0.42 nm which looks at first glance a little high, considering the mean plane separation of 0.33 nm for the coronene-TCNQ complex [Chi04]. However, the steric effect of the OMe group of HMC and O of COHON will play a role. In the calculated complex, H of OMe has a distance of 0.289 nm from O of COHON. Compression of the layer leads to an unstable structure because of the steric effect. According to the optimization, HMC is rotated by 21° against the COHON ring to reduce the steric effect of functional groups. For further details on the calculation, see [Nag10b, Nag10c].

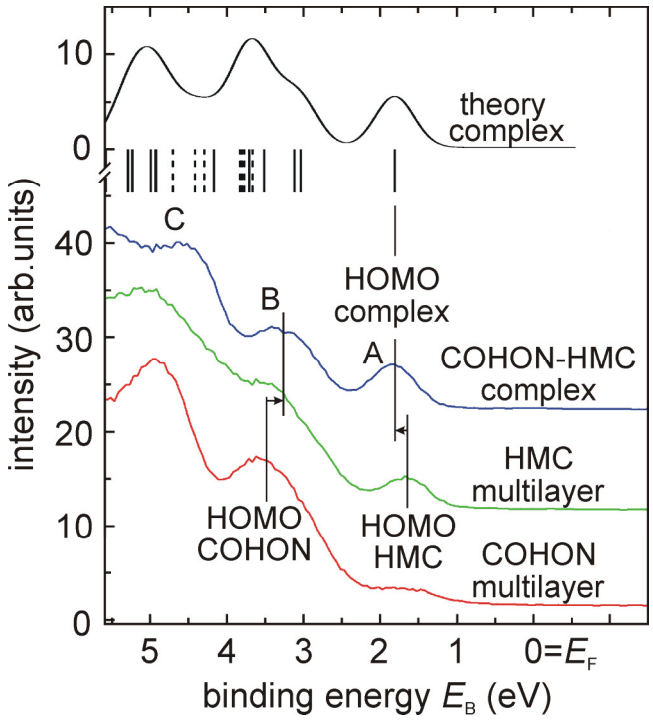

Figure 5.3 He I UPS spectrum for the mixed phase of COHON and HMC (second spectrum) in comparison with a calculated spectrum (theory) and the spectra of the pure moieties (HMC and COHON) in thick films. In the mixed phase the HOMO signals of HMC and COHON are shifted in opposite directions as indicated by the arrows. The theoretical spectrum has been shifted by 0.66 eV to higher binding energy, so that its HOMO peak coincides with the measurement. Full and dotted bars denote π- and σ-like orbitals.

The theoretical spectrum in Fig.5.3 has been calculated assuming a Gaussian broadening of 0.6 eV FWHM, equal intensities of π-like orbitals (accounting for degeneracies) and an intensity factor of 0.5 for the σ-like orbitals involving oxygen 2p. As discussed for HMC, the classification σ- and π-like is based on equivalent orbitals of COHON or coronene. Comparison of theoretical and experimental spectra for the complex shows that the differences are larger than those for the pure compounds. In Fig. 5.3 the theoretical spectrum has been rigidly shifted by 0.66 eV to higher binding energies, in order to align theoretical and experimental HOMO binding energies (taking the measured work function of 5.2 eV for the complex). For the pure species, the rigid shift of the theoretical spectrum led to a good agreement with the measurements, cf. Figs. 5.1 and 5.2. For the complex, the measured spectral features B and C are not well reproduced by the shifted theoretical spectrum. In the calculated spectrum the maxima appear at about 0.5 eV higher binding energies. Obviously the distances between the HOMO and the binding energy positions of the lower-lying orbitals are overestimated by theory.

We may guess that one important reason tor the larger deviation of the DFT calculation from the measured spectra for the complex is the geometrical structure. An X-ray analysis is indispensible for a more reliable basis for theoretical modelling.

In addition to the charge-redistribution argument, new electronic states in a molecular donor/acceptor charge-transfer complex form *via* hybridization of acceptor LUMO and

donor HOMO [Azi07]. In such a picture, the binding energy of the donor HOMO is also stabilized with respect to the neutral molecule, as well is the HOMO of the acceptor destabilized, which is in accordance with our experimental observation. However, the structural complexity of our system precludes unambiguous identification of the underlying details of donor/acceptor charge-transfer and its magnitude. Future experiments must be designed to allow for an absolute control of sample structure (e.g., including *in situ* X-ray diffraction along with UPS measurements), which is presently not readily accomplishable.

5.3 Near-Edge X-ray Absorption Fine Structure

In this section we discuss the results of X-ray absorption spectroscopy for HMC, COHON, and the mixed phase. Measurements in the soft X-ray range gave access to the near-edge X-ray absorption fine structure (NEXAFS) of the oxygen and carbon K-edges. Actually these were the last measurements performed in November 2010, after the paper [Med10a] had been published and the interesting NEXAFS results for the pyrene-derivatives in the complex with TCNQ (see section 6.5) were measured and analyzed.

Fig. 5.4 shows the ***oxygen K-edge NEXAFS spectra*** of the acceptor COHON (a), the donor HMC (d), and two different samples of the mixed phase with excess COHON (b) and excess HMC (c). Thus, (a) represents the fingerprint of the C=O group in the hexaketo-species, (d) represents the signature of oxygen in the hexamethoxy species, and (b and c) show the spectra after CT-complex formation. Obviously, the signature of the electron-donating methoxy-group (–O–C–H_3) is substantially different from the signature of the electron-accepting keto-group (C=O).

The prominent pre-edge peak (N) in the HMC oxygen K-edge spectrum (spectrum d) is separated by about 2.5 eV from the next peak. This resonance is located at 530.5 eV, in good agreement with the position of the lowest-lying peak measured for the methoxy species on Cu (531.7 eV [Ame99]). This low-lying signal derives from the *highest occupied molecular orbital (HOMO) 2e of the methoxy*, having π-symmetry being twofold degenerate and largely oxygen 2p-like (lone pair) with some hybridization with the antibonding π*-orbital of the C-O group. The intensity of transition N (essentially O1s→2p) is very high because it is dipole-allowed and characterized by a large overlap of initial- and final-state wavefunctions in the matrix element. The second signal (O) at about 532.9 eV is associated with the transition into an orbital that derives from the $6a_1$-orbital of the methoxy group, which has σ*-like symmetry. The fact that the 2e derived-orbital can act as final state reveals that the methoxy group is *not fully anionic* in HMC.

We denote the first two resonant transitions in the spectrum of the donor HMC as

Transition N: ***O1s→2e [π methoxy)]*** (5.1)

Transition O: ***O1s→6a$_1$ [σ*.methoxy],***

where we use the orbital designation of an isolated methoxy group. The corresponding orbital symmetry in HMC is E, A1 and A2. For the acceptor COHON (spectrum a) the pre-edge region is smeared out over a large energy range with a broad band of spectral intensity (signal M) setting in already at 524 eV, i.e. far below the K-edge. This is partly a result of the large workfunction of COHON (more precisely, the large ionization potential of COHON molecules in the film) but additional effects obviously play a role as well. We note that smearing out of the optical spectra has also been observed by Rieger et al. for coronene with increasing number of keto-groups [Rie09].

For the mixed phases (spectra b and c) the spectra change and there is some indication that these spectra are not simply the sum of HMC and COHON spectra. In particular, the low-energy spectral intensity has vanished in both mixed-phase spectra. However, peaks are partially overlapping, so that the observed signals cannot be deconvoluted into the contributions from the donor and the acceptor. This is different from the case of complexes

of hexa- and tetramethoxypyrene with tetracyanoquinodimethane, discussed in section 6.5. In that case, oxygen is only contained in the donor and nitrogen in the acceptor, so that NEXAFS constitutes a local probe at the donor or at the acceptor site when selecting the oxygen or nitrogen K-edge, respectively. For this reason, we will discuss the NEXAFS results in much more detail for the model cases of HMP– or TMP – TCNQ in section 6.5.

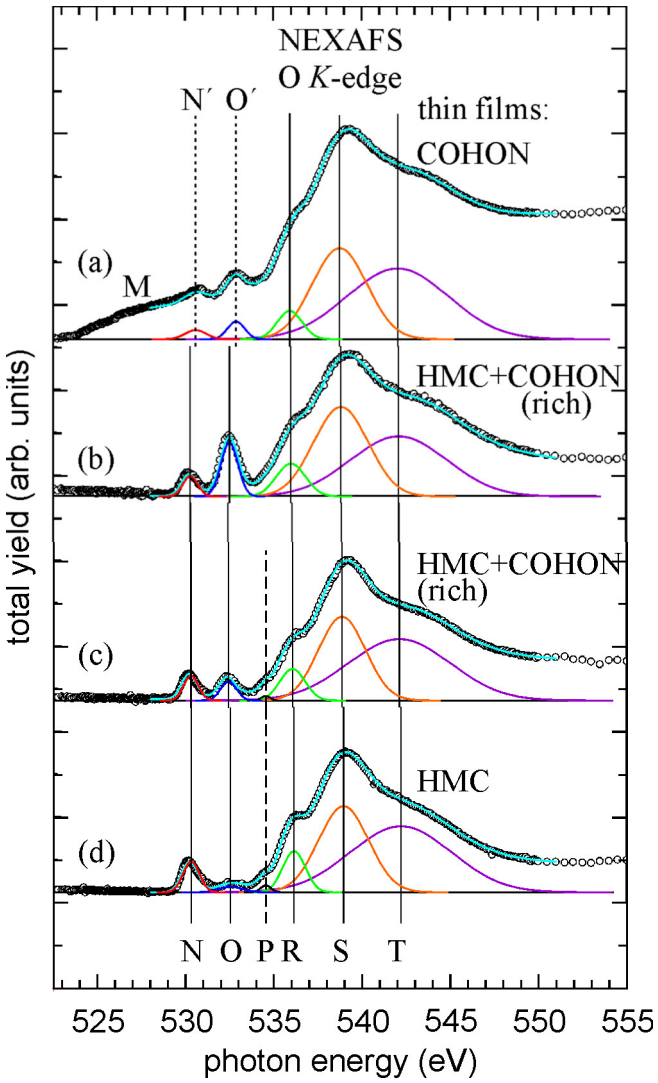

Figure 5.4 Oxygen K-edge NEXAFS spectra of UHV-deposited films of the acceptor coronene-hexaone COHON (a), the donor hexamethoxycoronene HMC (d) and two mixed phases with higher COHON content (b) and higher HMC content (c).

The ***carbon K-edge NEXAFS spectra*** taken for the same samples are shown in Fig. 5.5. Although most carbon atoms are located in the aromatic ring system that is identical for the donor and acceptor moieties, their spectra look remarkably different. The most striking differences concern the fact that the spectra of the mixed phases (b and c) can definitely not be composed as a sum of acceptor (a) and donor (d) spectra. The intense features around 288 – 289 eV in the COHON-rich mixed phase (b) are not present in spectra (a) and (d). The

HMC-rich spectrum (c) resembles that of pure HMC (d) but also shows clear differences, e.g. a strongly enhanced signal E.

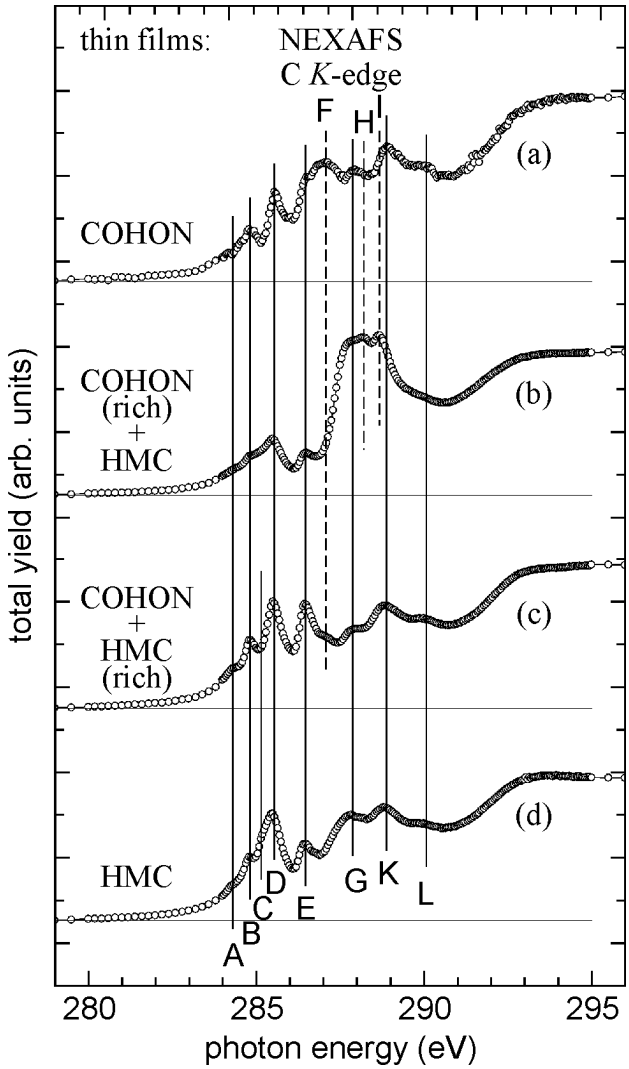

Figure 5.5 Carbon K-edge NEXAFS spectra of UHV-deposited films of the acceptor coronene-hexaone COHON (a), the donor hexamethoxycoronene HMC (d) and two mixed phases with higher COHON content (b) and higher HMC content (c).

Without an advanced NEXAFS calculation, however, it is not possible to analyze these spectra in detail. So we just note the remarkable differences without going into the details of their origin. As mentioned before, the system discussed in section 6.5 constitutes an “ideal” model system because donor and acceptor spectra are completely separated from each other.

5.4 Summary of Results for Coronene Derivatives

Chapter 5 presented a photoemission and NEXAFS study of two substituted disc-type PAHs with donor and acceptor character based on coronene, i.e., the donor hexamethoxycoronene HMC and the acceptor coronene-hexaone COHON. High-purity films of both molecules and their mixed phase were deposited on freshly evaporated Au using a special double evaporator. The adsorption behavior of ***HMC on Au*** follows the "standard" model established for conjugated organic molecules on an inert metal surface: In the monolayer regime a reduction of molecular level binding energies by about 0.4 eV compared to multilayers occurs, due to enhanced image-charge screening of the photo-hole on the metal surface. Upon deposition of the monolayer, the sample work function decreases by 0.5 eV, caused by the push-back effect (i.e. Pauli repulsion of the spill-out electrons of the Au surface).

For ***COHON on Au***, the evolution of spectral features and sample work function is more complex: Up to full monolayer coverage a work function decrease by 0.5 eV is observed. However, due to the electron acceptor nature of COHON we suggest this to be the result of the interplay of Pauli repulsion, weak metal-to-organic charge-transfer, and molecular conformation changes. Beyond monolayer coverage, the work function rises strongly during growth of the second layer, by 0.8 eV. At the same time, an interface state IS shows up in the valence region at 1.75 eV below E_F. This points towards a substantial electron transfer into the second COHON layer, possibly connected with a change of molecular orientation. With further increasing coverage, the intensity of signal IS drops (proving the localization of IS at the interface) and the spectrum of neutral COHON arises with its HOMO at a binding energy of 3.1 eV below E_F.

The ***mixed phase*** was prepared by alternating deposition of 1.5 nm thick multilayers of COHON and HMC. In the corresponding UPS spectra the HOMO of the donor (HMC) is shifted by 0.19 eV to higher binding energy and the HOMO of the acceptor (COHON) by 0.25 eV to lower binding energy. Qualitatively, this type of behavior is anticipated when a charge-transfer from donor to acceptor occurs, involving a hybridization of molecular orbitals. The DFT calculation for the pure species shows good agreement with experiment. For the complex larger deviations are evident. A better theoretical modeling would require a structural analysis of the complex.

NEXAFS measurements at the oxygen and carbon K-edges revealed that the methoxy- and keto-groups have different spectroscopic fingerprints. In particular the oxygen pre-edge features show clear differences. The appearance of the NEXAFS transition into an orbital derived from the HOMO (2e) of the isolated methoxy group reveals that the methoxy group in pure HMC is not fully anionic. Even the carbon spectra show marked differences despite the fact that most carbon atoms are contained in the aromatic ring system that is the same for both moieties. Without going into more details here, we can conclude that the system of unoccupied or partially occupied states appears substantially different for pure donor, pure acceptor and the mixed phase, even if probed at the carbon K-edge.

6. CT-Complexes of Pyrene Derivatives with Tetracyanoquinodimethane

In this chapter, we pursue a second approach, next to the study of complexes with new donors and new acceptors (like the HMC-COHON case of the previous chapter). The combination of new donors with known acceptors and vice versa is very interesting, too, in order to be able to compare with literature data. Here we have chosen a smaller parent molecule, pyrene. Choosing further the classical acceptor TNCQ, we consider similar sized molecules for the CT complex formation. By variation of the number of methoxy groups attached to the pyrene molecule, we can taylor the acceptor strength. Too strong donor-acceptor pairs might lead to complete charge transfer. This could be argued from the HOMO LUMO evaluation of the components, although it should be kept in mind that the orbital energies change upon π-interaction [Nag10b].

The purpose of the study of pyrene derivatives was to investigate the electronic structure of the mixed phase of TCNQ and hexamethoxypyrene (HMP) or tetramethoxypyrene (TMP) and in particular, to compare with the coronene data of chapter 5. The results are compared to those obtained from the respective pristine molecular films. The organic films were grown on Au surfaces by (co-)sublimation in UHV. The spectra give information on the interface of the organic films and the metallic substrate. Clear signatures of an interface CT (between metal and organic layer) and an inter-molecular CT in the compound mixture have been found. The formation of a novel CT phase is corroborated by the appearance of new reflexes in XRD and red-shift in of the CN stretching vibration of TCNQ, observed in infrared (IR) spectroscopy. Density functional theory (DFT) calculations have been performed yielding the energy scheme and symmetries of valence orbitals of the pure moieties and of the compound. We find reasonable agreement between calculated and measured spectra.

6.1 Pyrene and its Methoxy-Derivatives

The HMP and TMP-TCNQ mixed phases can be deposited in very good quality by loading the crucible with a mixture of both molecules. The base pressure before evaporation was about $3 \cdot 10^{-10}$ mbar. Clean Au films were used as substrates with high electronegativity, providing a good reference for the Fermi energy. About 20 nm of Au were evaporated onto Si(100)-wafers immediately before deposition of the organic films. The workfunction of the fresh Au films was consistently 5.3 eV. This indicates that the textured Au surface exhibits Au(111) facets. The substrate was kept at room temperature, the crucible temperatures were 120° C, 135° C and 100° C for the compound, pure HMP, TMP, and TCNQ, respectively.

Figure 6.1a shows the structure of the molecules. Note that the methyl groups (Me = CH_3) are not planar, i.e. TMP does not posses a mirror plane. Figure 6.1b shows AFM-images (atomic force microscopy) for two samples with different coverages. At lower coverage (sample (i)) 3D-crystallites with lateral sizes and height in the 100 nm range appear on a smooth background. The crystallites tend to form rows with lengths of up to several micrometers. At higher coverage (sample (ii)) the crystallites cover the whole surface. The films look dark orange giving evidence for an optical gap in the visible spectral range (films of pure TMP and TCNQ look yellow). In the photoelectron spectra corresponding to sample (i) the Fermi edge of the gold substrate was not visible. This means that the flat parts between the crystallites are not bare Au but are completely covered by the organic film. This suggests that the complex grows in a *Stranski-Krastanov* type mode [Str39] where an initial smooth multilayer covers the whole surface (smooth areas in image (ii)) before 3D crystallites are formed. Similar microcrystals with sizes in the sub-micrometer range have been observed for the TCNQ/BEDT-TTF mixed phase [Sol09].

As a consequence of slightly different evaporation rates, the partial vapour pressures of the two moieties in the molecular beam change with time. Despite of this time-dependent deviation from the 1:1 mixture in the molecular beam, the stable compound favours a 1:1 composition of the mixed phase. We believe that this is due to small sticking coefficients of the molecules for a substrate held at room temperature. As a consequence, surplus donor or acceptor molecules, which are not subject to the CT phase formation, readily desorb from the surface. However, for sufficiently high vapour pressure pure TMP and/or pure TCNQ crystallites start to grow in coexistence with the mixed phase.

X-ray diffractometry was performed employing a Bruker D8 diffractometer with a Cu anode in parallel mode using a Goebel mirror (courtesy Vita Solovyeva, Univ. Frankfurt). In Fig. 6.1c two diffraction patterns (θ - 2θ scans) of TMP-TCNQ thin films grown on Au/Si(100) and on Si(100) substrates are compared with the reference data for pure TMP ([Bau10]) and TCNQ ([Yin88]), simulated using the Mercury 2.2 program code [Mac08]. θ is the angle between the incident ray and the scattering plane. A new crystallographic phase is evident, because new reflections corresponding to lattice plane spacings of d_1= 0.894 nm and d_2= 0.677 nm occur, as marked by the arrows.

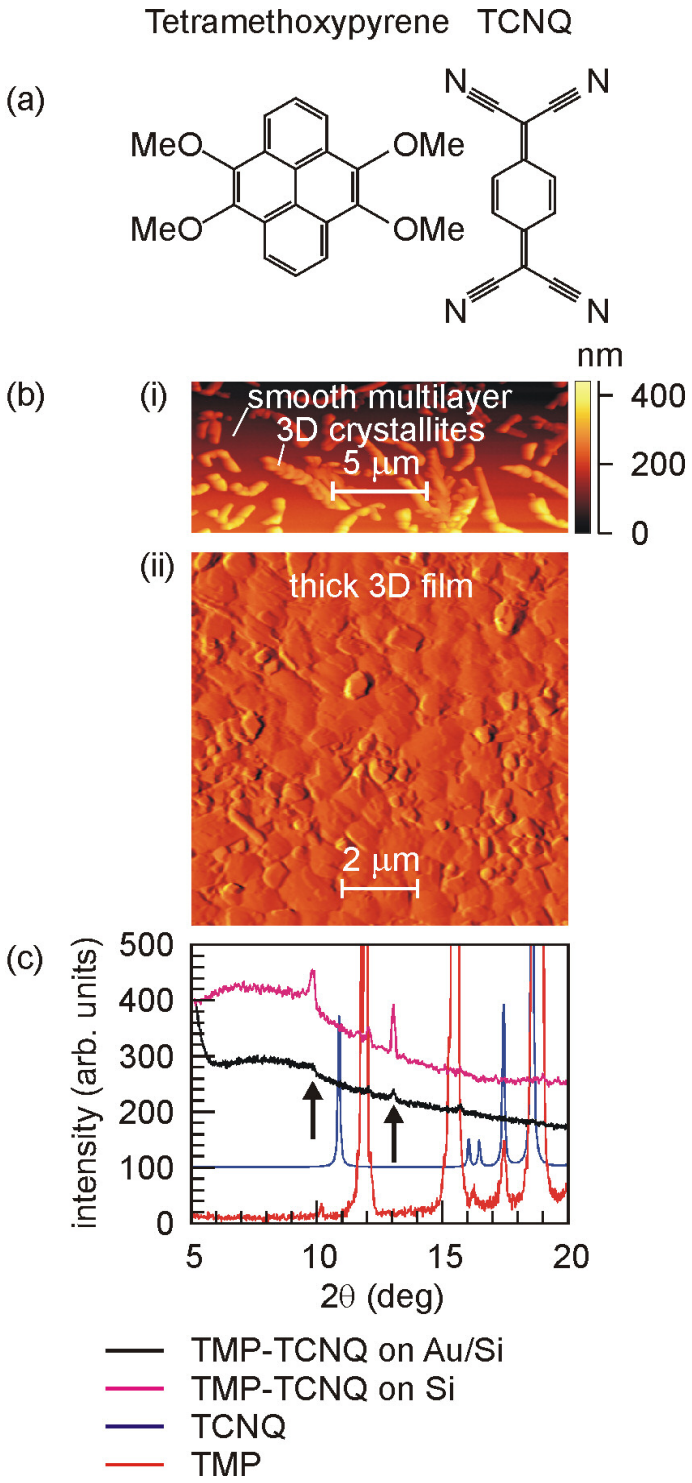

Figure 6.1. Plot of the molecular structures (a), AFM images (b) and X-ray diffractograms (c) of thin films of the mixed phase TMP_1-$TCNQ_1$. Image (i) in (b) shows the coexistence of a smooth multilayer covered with 3D crystallites. Image (ii), taken at higher coverage, shows a thick 3D film with crystallite sizes in the micrometer range. The X-ray diffraction patterns (c) for TMP-TCNQ films grown on Si and Au/Si substrates reveal new diffraction peaks (marked by arrows) in comparison with the reference diffraction patterns for pure TMP and TCNQ.

The diffractograms of the TMP-TCNQ thin films grown on Au/Si (topmost curve Fig 6.1c, thin film) and on Si (second curve, thicker film) reveal no pure TCNQ and only a very small amount of pure TMP coexisting with the new crystallographic phase. A detailed thin film growth analysis and structure resolution is presently in progress.

The structure resolution of the new CT compound is impeded by the presence of pure donor and acceptor phase in the grown TMP-TCNQ thin films. Therefore to get the crystal structure of the TMP-TCNQ complex growth optimization is needed. Presently, we can speculate on the likely stacking geometry of the newly found CT complex. In analogy to another CT compound containing the pyrene molecule: (hexamethoxypyrene - TCNQ) ([Bau10]) a mixed stack geometry in TMP-TCNQ was found, but X-ray structure analysis needs further refinement.

6.2 Infrared Spectroscopy

Since a CT in the complex acts on the strength of chemical bonds, IR spectroscopy is a common tool to study this phenomenon in terms of the characteristic vibrational frequencies. For TCNQ, the CN stretching vibration has proven to be a useful indicator of a CT, see e.g [Chi04].

Infrared spectra have been taken using a Fourier spectrometer (type Nicolet 730 FT-IR) in reflection geometry. Figure 6.2 shows the infrared spectra in the region of the CN stretching frequency for two different thin-film samples of the TMP- TCNQ mixed phase in comparison with pure TCNQ on Au. The spectrum of the low-coverage sample of the mixed phase (i) reveals a CN stretching frequency of 2219 cm^{-1}, being red shifted by 7 cm^{-1} in comparison to pure TCNQ on Au (2226 cm^{-1}). This shift is characteristic for a CT to the acceptor TCNQ on the order of $0.3\,e$, as discussed in [Chi04]. The spectrum of the high-coverage sample (ii) shows a coexistence of red-shifted peak at 2219 cm^{-1} with the unshifted CN vibration (shoulder at 2226 cm^{-1}). The intensity ratio indicates that this sample is predominantly the TMP- TCNQ mixed phase, but contains an admixture of pure TCNQ. The spectrum of the low-coverage sample (i) reveals that this sample contains no admixtures. Such samples are produced at sufficiently low growth rates.

The periodic oscillations superimposed to the spectrum of sample (i) originate from the underlying Au film. Given the photon impact angle normal to the surface and the periodicity of the interference fringes (2.5 cm^{-1}) we estimate a thickness of the underlying Au film of 15 nm. The low-coverage sample (i) contains crystallites of the mixed phase on top of a smooth multilayer (Fig. 6.1b, image (i)), whereas in sample (ii) the surface is completely covered by crystallites (Fig. 6.1b, image (ii)).

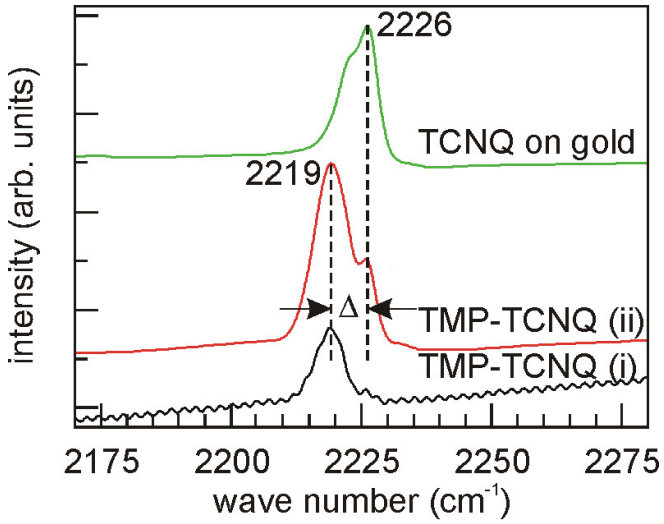

Figure 6.2 IR spectra of the CN stretching vibration in a TCNQ film on Au and films of the mixed phase TMP_1-$TCNQ_1$ on Au at low coverage (i) and high coverage (ii). In the mixed phase the vibration frequency is red-shifted by $\Delta = 7$ cm^{-1}, being indicative of a CT of the order of $0.3\,e$.

6.3 Ultraviolet Photoelectron Spectroscopy

UPS spectra have been taken during film growth as described in section 3.1. Figure 6.3 shows series of spectra taken during deposition of TMP (a) and TCNQ (b) on clean Au surfaces in comparison with theoretical spectra (top). The insets show the corresponding coverage-dependences of the work function Φ, the numbers correspond to the spectra numbers.

For ***TMP on Au*** (Fig. 6.3a) the work function drops rapidly from 5.3 to 4.7 eV during deposition of the first monolayer. This constitutes the "standard" behaviour for polycyclic aromatic hydrocarbon molecules on noble metal surfaces. The drop in Φ reflects the push-back effect, i.e. Pauli repulsion of the spill-out charge of the metal surface by the valence electrons in molecules of the first monolayer. This reduces the surface dipole of the metal. The sequence of UPS spectra shows the growth of signals A, B and C at binding energies of 2.0, 3.0 and 4.6 eV below E_F that do not change their positions as function of coverage.

The system ***TCNQ on Au*** (Fig. 6.3b) shows a more complex behaviour: During the initial phase of adsorption the work function Φ drops slightly by 0.1 eV and then shows a steep rise by almost 0.7 eV. The initial weak variation reflects the interplay between the push-back effect (lowering Φ), a possible CT from Au into the first molecular layer (rising Φ) and, in addition, a possible deformation of the molecule. Bent TCNQ on noble-metal surfaces has been described in [Ran09]. Upon completion of the first monolayer the push-back effect has reached saturation because it is only caused by molecules in direct contact with the metal. However, the CT keeps on so that the work function exhibits a steep rise until the second layer is completed. Above two layers the further increase is rather small and the work function saturates at about 6.0 eV. This high value proves that there is a considerable CT from the metal into the organic film, leading to a strong dipole layer at the organic-metal interface. With increasing coverage the signals A and B grow at binding energies of 3.3 and 4.8 eV below E_F. Their positions do not change as function of coverage.

An important quantity for the electronic properties of such organic films is the *hole injection barrier* Δ_h, defined as the distance between the leading edge of the HOMO and the Fermi-energy of the metal. From Fig. 6.3 we obtain Δ_h = 1.6 eV and 2.7 eV for TMP and TCNQ, respectively. Together with the measured work functions (see insets) we derive ionization energies of $E_i = \Delta_h + \Phi =$ 6.3 and 8.7 eV for TMP and TCNQ molecules in multilayer films, respectively.

Theoretical binding energies E_B of electrons in the molecular orbitals were calculated in delta self-consistent field (ΔSCF) approximation with explicit computation of energies of both the neutral compound and resulting cation after the vertical photo-transition, using the B3LYP/6-31G(d) correlation functional (details are given in [Nag10a]). The electrons in the HOMO have theoretical binding energies of E_B = 6.18 eV and 8.87 eV for TMP and TCNQ, respectively. Taking into account the work functions of the multilayer films (Φ_{TMP} = 4.7 eV and Φ_{TCNQ} = 6.0 eV) these values translate into binding energies of 1.48 and 2.87 eV with respect to the Fermi-energy.

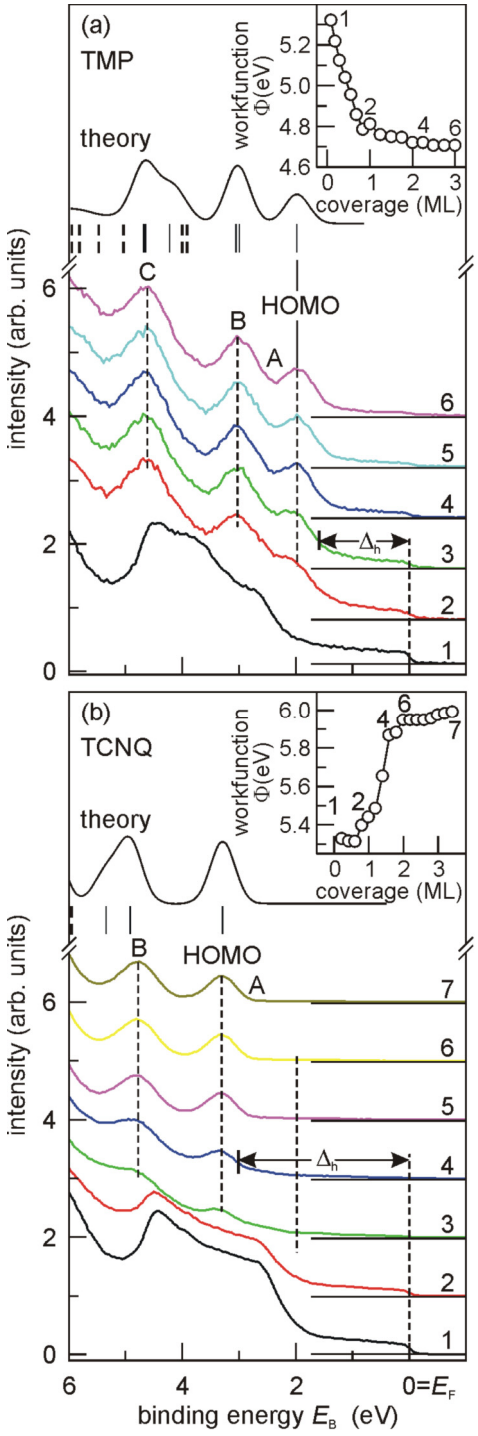

Figure 6.3. Coverage series of He I UPS spectra of TMP (a) and TCNQ on Au (b). For comparison, spectra calculated on the basis of ΔSCF binding energies are included (top) that agree well with the measured spectra. In order to align the HOMO, the theoretical spectra have been rigidly shifted by 0.52 and 0.48 eV to lower binding energy for TMP and TCNQ, respectively. Full and dotted bars denote the binding energy positions of π- and σ-like orbitals, respectively. The insets show the corresponding workfunction-vs-coverage curves (coverage in monolayers ML), numbers correspond to the spectra numbers. Δ_h denotes the hole injection barriers.

The calculated binding energies are 0.52 eV (for TMP) and 0.48 eV (for TCNQ) lower than the maxima positions of the measured HOMO signals (peaks A). The theoretical spectra have thus been aligned at the experimental HOMO positions, i.e. they are rigidly shifted by about half an eV to higher binding energies. The calculated spectra assume a Gaussian broadening of 0.5 eV FWHM. The partial cross sections of the orbitals with π-like symmetry (full bars) were taken to be identical; in particular no degeneracy exists for these molecules. Actually there is no strict π- and σ-symmetries in TMP because of the methoxy groups. However, we can identify "π- and σ-like" symmetries by analogy with the parent molecule pyrene. The oxygen 2*p*-derived orbitals with σ-like symmetry (dashed bars in Fig. 6.3a) deserve special consideration. At the given photon energy the partial cross section of oxygen 2*p* is lower than that of carbon π [Cra02]. Moreover, the σ-orbitals have nodal planes perpendicular to the molecular plane. Hence the corresponding photoemission signals in normal emission vanish for molecules oriented parallel to the surface. In order to account for the lower O 2*p* cross section and the orientational effect, the corresponding signal intensities were weighted by a factor of 0.2 in comparison with the π-orbitals. The orbital at 5.3 eV in TCNQ has a high contribution from nitrogen 2*p*. Likewise, this cross section is lower and the spectral intensity of the 5.3 eV line has thus been weighted by a factor of 0.5.

Except for the shifts aligning the HOMO levels with the experimental signals A, both calculated spectra agree well with the measured spectra. Signal B results from the closely spaced HOMO-1/HOMO-2 orbitals and signal C represents the group of HOMO-3 to HOMO-7. For TCNQ signal B corresponds to HOMO-1 and the nitrogen 2*p*-derived contribution of HOMO-2 in the shoulder.

This shows that the ΔSCF calculation is well suited to analyze the frontier orbital structure of these molecules. The essential reason for the difference between absolute level positions in theory and experiment is the fact that the calculation assumes a single free molecule, whereas the measurements are made for a condensed film on a metal surface. It is interesting to note that the same theory shows a significantly better quantitative agreement for the larger PAHs hexamethoxycoronene and hexaketocoronene in condensed films [Med10a, Ran09].

Figure 6.4 shows a sequence of photoelectron spectra for the ***mixed phase of TMP-TCNQ*** in the range from sub-monolayer to multilayer coverage. The inset shows the corresponding work function-vs-coverage curve, with numbers corresponding to the numbers at the spectra. Adsorption in the low-coverage regime is characterized by the growth of signals A´ and B´ at 1.5 and 2.5 eV below E_F and by an increase in the workfunction by 0.4 eV. Obviously, the organic-metal interface of the mixed phase is polar due to a CT from Au to the overlayer. The Fermi edge vanishes rapidly with increasing coverage, pointing towards *complete wetting*. In spectrum 5 this low-coverage phase is completed, i.e. signals A´ and B´ have reached their intensity maxima and the rise of Φ abruptly ends. The hole injection barrier in this growth regime is $\Delta_h = 1.0$ eV.

The higher coverage regime is characterized by a weak increase in Φ and by the growth of signals A and B, being markedly shifted with respect to the low-coverage signals A´ and B´. Φ reaches a saturation value of 5.75 eV and signals A and B are fully developed at 1.8 and 2.9 eV below E_F (spectrum 8). We attribute the energy level shift between the low-coverage and higher- coverage regimes to a change in the film morphology. In addition, the increased image charge screening of the photo-hole in the first layer (typical for adsorbates on metal surfaces) [Sch85] might contribute to the shift. Spectrum 6 shows the coexistence

of peaks A/B and A′/B′. This spectrum corresponds to a structure similar to sample (i) in Fig. 6.1b that exhibits both smooth areas and 3D crystallites. We thus conclude that signals A′ and B′ result from the initial smooth multilayer, whereas A and B in spectra 7-9 originate from a surface completely covered by three-dimensional TMP-TCNQ crystallites (cf. sample (ii) in Fig.6.1b). The development of UPS spectra in Fig. 6.4 and the AFM images in Fig. 6.1b suggest a Stranski-Krastanov type growth mode for the mixed phase of TMP-TCNQ. A similar growth mode has been observed for hexabenzocoronene on Au (111), where in the first four layers the molecules lie flat on the surface, whereas above four layers 3D bulk crystallites develop [Pro01]. Previous scanning tunnelling microscope STM investigations showed that the mixed phases of F_4TCNQ and α-sexithiophene [Jae08] as well as TCNQ and TTF [Gon08] adsorb in smooth monolayers, where the donor and acceptor molecules form regular patterns.

Spectrum 9 in Fig 6.4 shows a drop in intensity of signals A and B and a broadening of signal B towards higher binding energies (wing to the left). One reason could be the formation of coexisting crystallites of TCNQ, in accordance with the IR measurement, see spectrum (ii) in Fig. 6.2. The calculation reveals that A constitutes the HOMO, whereas B is composed of HOMO-1 and HOMO-2, being closely spaced in energy. The theoretical spectrum in Fig. 6.4 has been rigidly shifted by 0.97 eV to lower binding energies, in order to align the HOMO position with peak A. Like for the pure species, no perfect agreement can be expected because the calculation assumes an isolated TMP-TCNQ complex molecule instead of a 3D crystal. Energy minimization yields a parallel orientation with the centres of donor and acceptor lying above each other with 0.363 nm spacing and 0.6 nm lateral displacement.

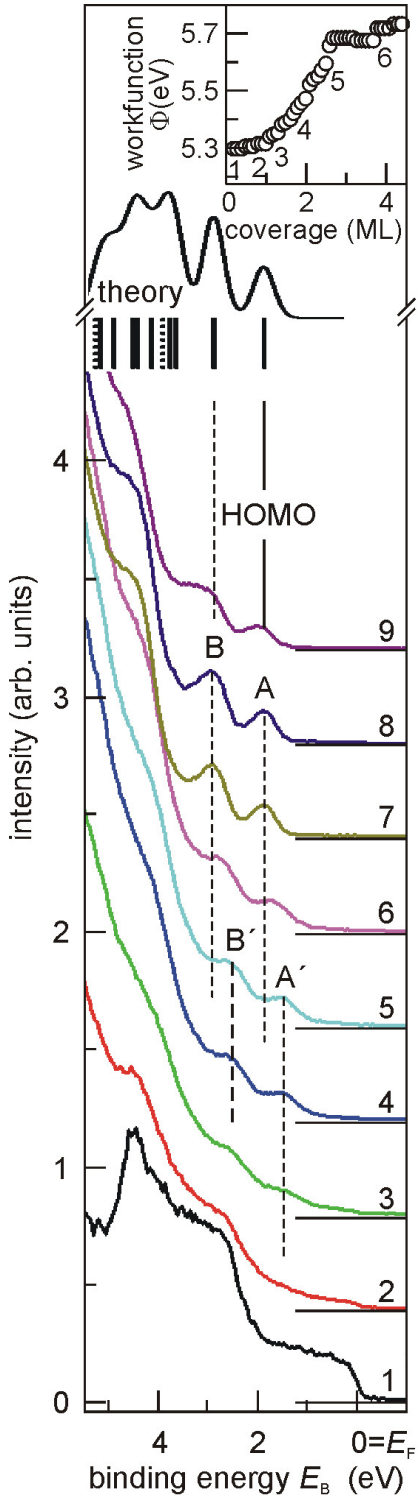

Figure 6.4 Coverage series of UPS spectra taken during the growth of the TMP- TCNQ mixed phase on Au. The inset shows the corresponding workfunction curve, numbers correspond to the spectra numbers. For comparison, a theoretical spectrum is shown (top), calculated on the basis of ΔSCF binding energies. In order to align the HOMO with the experimental signal A the theoretical spectrum has been rigidly shifted by 0.97 eV to higher binding energy.

6.4 Scanning Tunnelling Spectroscopy

The STS measurement has been carried out in cooperation with the group of Prof. Elmers, details will be presented in a forthcoming Diploma Thesis [Per11]. TMP-TCNQ was deposited in UHV under the same conditions as for the prevously described experiments. In this case coverages of TMP-TCNQ corresponding to the coverage regime (i) in Fig. 6.1b were deposited on a clean W(110) surface for which a similar substrate - adsorbate interaction is assumed as in the case of the Au(111) surface used before. In particular, the work functions are almost identical (5.3 eV and 5.2 eV for the Au films and W(110), respectively). STS was performed to obtain differential conductance dI/dU maps and spectra, using a lock-in technique with a 8 kHz bias voltage modulation of 30-50 mV. All bias voltages given are sample voltages with respect to the tip. A $Pt_{80}Ir_{20}$ tip was used that was cut under tensile stress from a thin wire. Spectroscopic data shown here were measured at room temperature directly after the sample preparation with residual gas exposures less than 0.5 L (1 L= 10^{-6} Torr s). Spectroscopic dI/dU curves were recorded on top of homogeneous topographically elevated structures which were identified as areas covered by TMP-TCNQ. The stabilization parameters (U = 0.7 V, and I = 0.35 nA) and modulation amplitude (50 mV) for the results shown here were kept constant. The presented data result from an average of individual spectra measured on homogeneous topographically elevated areas of the sample. Figure 6.5 shows the results for the TMP-TCNQ sample. While the spectra were reproducible for sample voltages -1 V < U < 3 V, the spectroscopic features observed for U < -1 V appeared to be strongly influenced by tip induced states.

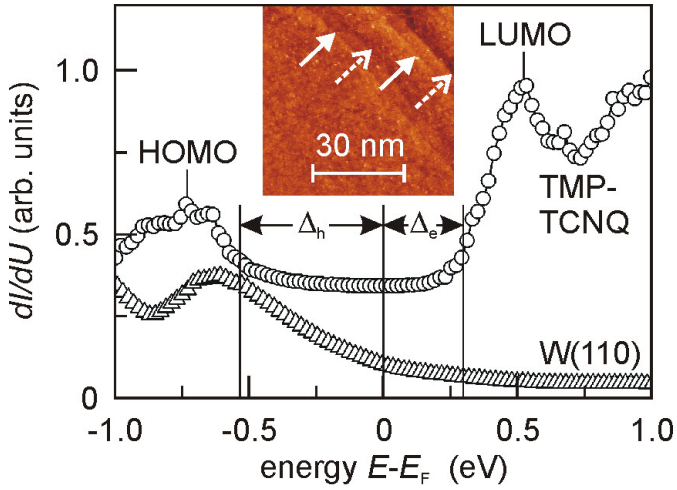

Figure 6.5 Differential conductivity dI/dU spectrum measured at room temperature on an island of TMP-TCNQ, compared with a spectrum from the clean W(110) substrate. For clarity, the TMP-TNCQ spectrum was shifted upwards by 0.2 arb. units. The sample voltage modulation was 50 mV and the tip was stabilized at U = 0.7 V and I = 0.35 nA. The inset shows a processed topographical STM image of the corresponding region where the spectra were measured. Full (dashed) arrows indicate monoatomic substrate (molecular complex) steps indicating an initial step flow growth mode. Δ_h and Δ_e denote the hole- and electron-injection barriers, respectively (from [Med10b], data from [Per11]).

In a simple model, the tunnelling conductance is roughly proportional to the local density of states (DOS) of the sample at the tip position multiplied by the tunnelling probability. For positive (negative) sample bias one measures unoccupied (occupied) sample states assuming a flat DOS for the tip. Pronounced peaks are often observed for surface states or resonant states leaking out into vacuum.

We observe a low and flat differential conductivity between -0.4 and +0.2 eV indicating a low DOS. This region is confined by a pronounced peak at +0.50 eV and a broader peak with a maximum at approximately -0.75 eV. Both features are absent on the clean W(110) surface. Therefore, we identify these peaks as the LUMO and HOMO state of the organic overlayer. Due to the interaction of the molecular states with the metallic substrate one expects a shift in all molecule states relative to the situation for free molecules or to thicker coverages. However, to first approximation one expects the same shift for all states keeping the differences between the energies constant. The difference of the energies of the two peak maxima (1.25 eV) defines the energy gap between HOMO and LUMO for the CT compound. The hole-injection barrier determined by STS (Δ_h = 0.5 eV in Fig. 6.5) is significantly smaller than the value resulting from UPS (Δ_h = 1 eV in Fig. 6.4). The electron injection barrier, i.e. the distance between the metal Fermi edge and the onset of the LUMO is only Δ_e = 0.3 eV.

Quantitative comparison of energy level positions determined by STS and by UPS

Figure 6.6 summarizes the measured and calculated level positions for the acceptor molecule TCNQ (left column), the donor molecule TMP (right column) and their CT complex (center column). In order to be able to compare experiment and theory the energy scale is referenced to the vacuum level. In Figs. 6.3- 6.5 the UPS and STS data are referenced to the Fermi level of the gold substrate. A change in the surface dipole induced by the organic film leads to an according shift in the energy levels that are pinned to the new electrostatic potential in the organic film, as discussed in [Koc08]. The energy levels of the molecules are “biased” by the surface dipole. For TCNQ the CT from the metal into the first layers of the film leads to an interface dipole and the work function increases. For TMP the push-back effect (Pauli repulsion) acting on the spill-out electrons in front of the surface by the molecular electrons leads to a reduction of the metal surface dipole so that the work function decreases. The change in the interface dipole cannot be modelled by theory. Therefore, these work function changes are not taken into account in Fig. 6.6 for sake of a quantitative comparison with theory and the experimental peak energies are given with respect to E_F(Au)= 5.3 eV.

For the ***acceptor TCNQ*** the LUMO determined by the STS-measurement [Tor08] (full line) and the cyclovoltammetry (CV) result [Kin85] (dotted line) agree very well and lie close to the prediction of the molecular orbital calculation (chain line). The HOMO position observed in UPS (thick line) agrees quite well with the calculated ΔSCF binding energy (dashed). The measured optical gap [Tor75] (Δ_{opt} = 3.2 eV) is significantly larger than the difference of the HOMO-LUMO eigenvalues (chain lines, distance 2.4 eV). Due to its large distance from the Fermi level, the HOMO of TCNQ could not be observed in STS. The HOMO position denoted by the thin line at 7.5 eV was derived from the LUMO position measured by STS, adding the value of the optical gap Δ_{opt}.

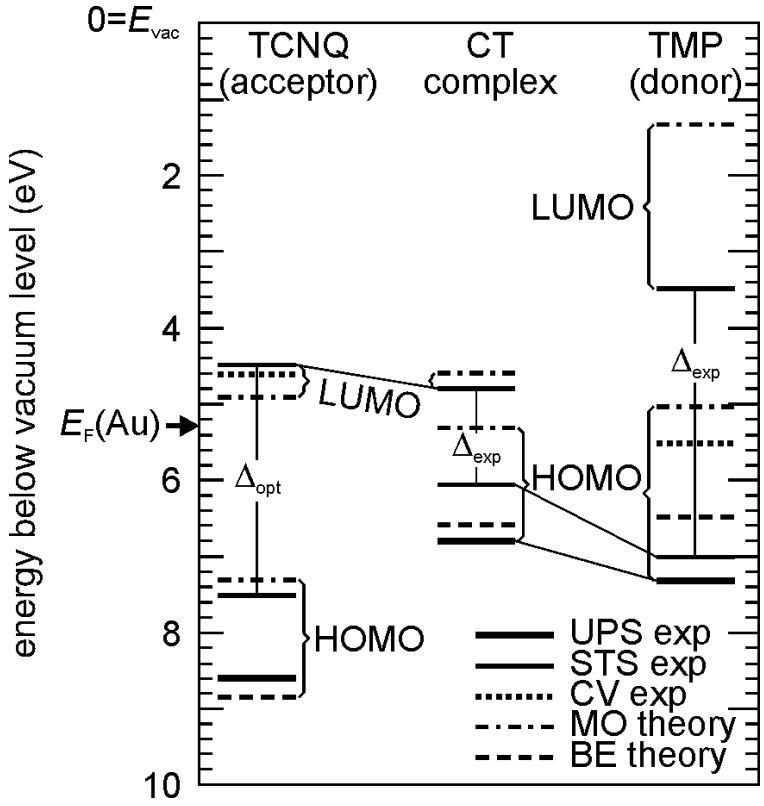

Figure 6.6 Energy scheme of the TMP-TCNQ complex (centre) in comparison with the pure phases of TCNQ (left) and TMP (right). In order to compare with theory, the binding energy scale is referenced to the vacuum level. Thick, thin and dotted lines denote the experimental UPS, STS and CV results, chain and dashed lines represent theoretical molecular orbital eigenvalues and ΔSCF binding energies, respectively. Δ_{opt} is the experimental value [Bau10] for the optical gap of TCNQ, adapted at the STS LUMO level [Kin85]. Δ_{exp} denote the gaps determined by STS for TMP and the complex.

For the ***donor TMP*** the calculated level positions deviate considerably from the measured results. The LUMO (HOMO) eigenvalues lie 2.5 eV (2 eV) higher than the measured STS values. The measured UPS HOMO position lies rather close to the STS value (0.3 eV difference).

The calculated ΔSCF binding energy is about 0.6 eV smaller than the STS/UPS signals. The CV result for the HOMO lies 1.8 eV above the STS/UPS signals, but quite close to the calculated HOMO eigenvalue. Obviously there is a substantial difference between the measurements for the condensed phase (STS, and UPS) of TMP on the one hand and the calculation for free molecules and the CV measurement in liquid environment on the other hand. The size of the gap as determined by STS (Δ_{exp} = 3.5 eV) compares well with the measured optical gap [Bau10] of 3.16 eV and agrees well with the difference of the HOMO-LUMO eigenvalues (3.6 eV).

For the ***CT complex*** STS reveals a strong reduction in the gap to Δ_{exp} = 1.25 eV due to an upward shift of the energy in the HOMO (compared with TMP) by 1.0 eV and a smaller downward shift in the LUMO (compared with TCNQ) by 0.3 eV. The calculation shows

that the HOMO (LUMO) of the complex is derived from the respective orbitals of TMP (TCNQ). The upward shift in the HOMO is also visible in UPS (thick lines). Since STS values have been taken at low coverage, Fig. 6.6 shows the low-coverage UPS signal A´ from Fig. 6.4.

For the complex the difference between the STS and UPS HOMO positions (distance 0.6 eV) is somewhat larger than for TMP. The ΔSCF binding energy prediction (dashed) lies close to the UPS signal. The calculated LUMO eigenvalue (upper chain line) shows good agreement with the STS LUMO position, similar as in the case of TCNQ. The HOMO eigenvalue is substantially too high, i.e. the calculated gap of 0.6 eV is about a factor of 2 smaller than the experimental gap (Δ_{exp} = 1.25 eV). The HOMO of TCNQ becomes HOMO-3 in the complex; it is not shown in Fig. 6.6.

6.5 NEXAFS Detecting Orbital-Resolved Partial Charge Transfer

Despite of the spectroscopic results on the UHV-deposited thin films summarized in Fig. 6.6 and the first results on the crystallographic structure of the solution-grown crystallites [Che10], several important questions still remained unsolved. In particular, there is lack of information on the electronic structure of the solution-grown crystals, because the unavoidable surface contaminations and the small size of the crystallites were prohibitive for UPS and STS analyzes. The probing depth is only 2-3 molecular layers in UPS and only one molecular layer in STS. Therefore, we have performed a first NEXAFS pilot experiment at ANKA Karlsruhe in April 2010. NEXAFS provides a larger probing depth in the order of 5 nm. Thus, surface contaminations were expected to be much less severe than in UPS or STS. Since that pilot experiment was very successful, a series of beamtimes followed and also the coronene-derived systems were studied as discussed in section 5.3.

In NEXAFS measurements an electron is excited from a core level to an empty or partially unoccupied valence electronic state. As this technique gives direct access to the unoccupied density of states, it should be sensitive to the formation of new hole states due to charge transfer in a donor-acceptor complex [Tse10]. By selection of a specific atom via its X-ray absorption edge, the electronic structure in the vicinity of this atom (e.g. in a functional group attached to a large molecule) is probed. For the present experiment the nitrogen 1s and oxygen 1s core levels should be ideal, because these atomic species are located exclusively on the acceptor site (N in the cyano-groups of TCNQ) or the donor site (O in the methoxy-groups of TMP and HMP). This highly specific excitation should provide information on the local electronic structure and thus on local chemical functionalities. We cannot expect carbon K-edge NEXAFS to be particularly useful due to the many non-equivalent C-atoms in both the donor and acceptor ring systems.

The NEXAFS method is described in sections 2.5, 2.6 and 3.3. Fraxedas et al. [Fra03] performed a NEXAFS study of the classical charge transfer salt *tetrathiafulvalene* (TTF, $C_6S_4H_4$) – TCNQ. This compound forms parallel segregated stacks of donors (TTF) and acceptors (TCNQ). Results have been compared with a first-principle calculation of the unoccupied and partially occupied electronic states of the pure materials and the charge transfer compound. Later, Sing et al. [Sin07] studied the same system with particular focus on the renormalized band widths observed in UPS [Cla02, Sig03] for the same compound. By variation of the angle of photon incidence, the symmetry of the observed orbitals for TCNQ was probed and information on molecular orientation was gained [Sin07]. None of these papers addressed the issue of a possible change of the unoccupied density of states upon formation of the CT complex.

In the following we present NEXAFS results for solution-grown 3D crystallites of the complexes HMP-TCNQ and TMP-TCNQ in different stoichiometric mixtures. The preparation procedure is described in section 4.2. The dark fractions of the solution-grown microcrystals were deposited on carbon tape, being a suitable holder for such samples. For comparison, spectra of the pure donors and acceptors have been taken under the same conditions. The study revealed two different signatures of a charge transfer in these new compounds. Strong changes in the intensity of the oxygen pre-edge features for different stoichiometries are a fingerprint of the occurrence of additional hole states at the donor sites. This pre-edge feature is absent in the spectrum of pure donor material, giving evidence of full anionicity of the methoxy group in HMP and TMP. Complementary, two prominent resonances of TCNQ are quenched, indicating partial filling of these states. In addition,

characteristic energy shifts of the donor and acceptor NEXAFS resonances in opposite directions are a further consequence of the charge transfer.

Nitrogen K-edge NEXAFS

Nitrogen is present only in the cyano-groups of TCNQ, its edge fine structure (Fig. 6.7) is a fingerprint of the acceptor. Likewise, oxygen is only contained in the methoxy-groups and thus its spectrum reflects a local spectroscopic probe in the functional group of the donor. The abscissa is identical for all spectra shown. Clearly, the absolute total yield of the nitrogen K-edge spectra grows with increasing TCNQ content of the compounds, cf. sequence of spectra a, b, c and d in Fig. 6.7, the latter taken for pure TCNQ. Vice versa, the intensity of the oxygen features (Fig. 6.8) decreases in the sequence of spectra g, h and i. This proves that the relative donor-acceptor concentrations in the solution from which they are grown show up in the stoichiometry of the 3D crystallites as well.

The spectra for the nitrogen K-edge were deconvoluted into signals A-E by *the fit routine (program Origin)*. In all spectra the fit curve perfectly reproduces the data points, giving evidence of a high reliability of the partial spectra. In the following we relate our spectra to the peak assignment for NEXAFS spectra of pure TCNQ [Fra03]. The first signal A is a π*–type resonance (width 638 meV for the 2:1 compound) and originates from the lower a_u and b_{1u} orbitals. For isolated TCNQ these lie at 2.55 eV and 2.65 eV above the LUMO minimum. At photon energies in resonance with such an allowed dipole transition, a large increase in excitation cross section is observed. These orbitals a_u and b_{1u} originate from the degenerate pair of lowest empty π*-orbitals of the benzene core, which only slightly delocalize towards the cyano-group in TCNQ. We denote the transitions of signal A as

A: $\boldsymbol{N1s \rightarrow a_u, b_{1u}\,[\pi^*\ ring]}$. (6.1)

Signals B and C originate from p-type unoccupied orbitals located in the cyano-group. They are therefore higher in intensity due to the larger overlap with the N1s wavefunction in the dipole matrix element. B is a narrow resonance (width 216 meV FWHM) of σ*-type originating from the b_{1g} and b_{2u} orbitals that belong to the four symmetry adapted combinations of in-plane orbitals of the CN groups, denoted

B: $\boldsymbol{N1s \rightarrow b_{1g}, b_{2u}\,[\sigma^*\ cyano]}$. (6.2)

Signal C is of π*-type and is much broader (632 meV). It derives from the b_{3g} and a_u orbitals and is denoted as

C: $\boldsymbol{N1s \rightarrow b_{3g}, a_u\,[\pi^*\ cyano]}$. (6.3)

Signal D corresponds to the highest π*-type orbital of benzene (b_{2g}) that is delocalized over the whole TCNQ molecule,

D: $\boldsymbol{N1s \rightarrow b_{2g}\,[\pi^*\ ring]}$. (6.4)

The weak feature E originates from delocalized σ*-type orbitals containing σ*(C-C), σ*(C-H) and σ*(C ≡ N) contributions. In summary, the unoccupied states involved in the weaker transitions A and D are essentially delocalized on the benzene ring, whereas states involved in transitions B and C derive from the σ*- and π*-orbitals of the cyano-group. We have checked the σ* and π* character of signals B and C by angle-resolved measurements on thin films.

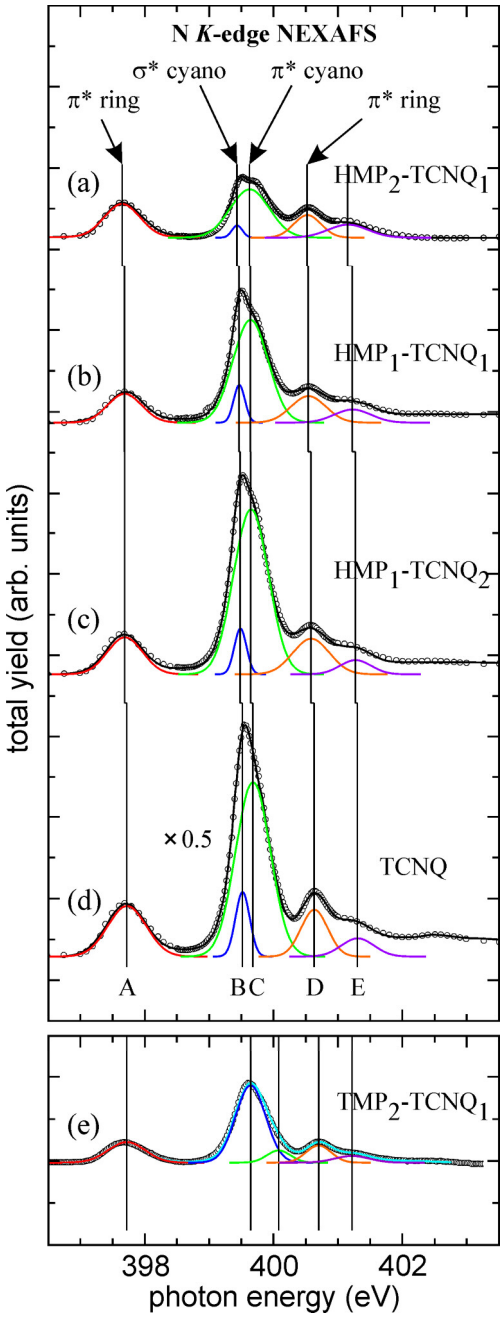

Figure 6.7 Nitrogen K-edge NEXAFS spectra of HMP_x-$TCNQ_y$ complexes with different stoichiometries (a-c), for pure TCNQ (d) and for TMP_2-$TCNQ_1$ (e). The yield scale is the same for spectra (a-d), spectrum (d) was scaled by a factor of 0.5. Circles denote experimental data; thin curves below the spectra mark partial spectra of the transitions as obtained from a multi-peak fit routine; curves through the dots represent the sum of the partial spectra.

With increasing HMP content (sequence d, c, b, a) the signal intensities B and C (separated by about 174 meV) drop substantially. For HMP_2-$TCNQ_1$ (spectrum a) signals B and C appear as a double peak with a separation of about 190 meV. This intensity drop is an indication of charge being transferred into these unoccupied orbitals of the acceptor

molecule. This partial occupation of the frontier orbitals of the cyano group obviously increases with increasing donor content in the compound, as anticipated. We will return to this point when discussing a complementary behaviour found for the oxygen pre-edge signal of the donor molecules. For the TTF-TCNQ complex, only small variations in nitrogen K-edge NEXAFS spectra in comparison with pure, neutral TCNQ have been observed [Fra03].

Oxygen K-edge NEXAFS

Oxygen is only contained in the methoxy-groups of TMP and HMP. So its edge fine structure is a fingerprint of the donor moieties. Fig. 6.8 shows a series of spectra with g, h and i corresponding to the same samples as the series a, b and c in Fig. 6.7. Spectra f and k have been taken for pure HMP and the TMP_2-$TCNQ_1$ complex, respectively. Signals F-K were determined by the fit routine. As for nitrogen, strong intensity changes for different stoichiometries are evident.

The prominent pre-edge peak (F) at about 532 eV in spectra g, h and k (width 993 meV FWHM for the 2:1 compound) is separated by 3 eV from the next signal. The energy position is in good agreement with the position of the lowest-lying resonance measured for the methoxy species on Cu (531.7 eV) [Ame99], where it derives from the highest occupied molecular orbital (HOMO) of the methoxy group, which is only partially occupied. For an isolated methoxy group this orbital has 2e-symmetry (twofold degenerate) and is largely oxygen 2p-like (lone pair). According to a DFT-calculation for HMP [Med10a], the signature of 2e (see bottom left panel in Fig. 6.11) shows up in a group of orbitals (HOMO-3 to HOMO-5), with the symmetry being reduced to a and b_3 and a and b for TMP and HMP, respectively. Since signal F occurs at this energy and is well separated from the next resonances, we assign it to the transitions

F: ***O1s→a,b₃*** for TMP and ***O1s→a,b*** for HMP ***(both π methoxy).*** (6.5)

For pure HMP (spectrum f) this signal is very weak, i.e. the 2e-derived orbitals are almost completely filled (a similar behaviour was found for multilayer methanol [Ame99]). However, in the mixed compounds signal F becomes significant, i.e. the transition channel opens. The signal is maximum for the compounds with 2:1 stoichiometry (spectra g and k) and weaker for the other two complexes (h and i). Since the 2e-derived wavefunctions have their maximum amplitude at the oxygen atom, there is a large overlap of initial- and final-state wavefunctions in the matrix element (essentially O1s → 2p). Thus, the oscillator strength of transition F is very high. For the surface methoxy species on Ni(111) and Cu(111) this transition is also significant, indicating a reduced occupation of the 2e orbital. For Cu, an effective occupation value of 3.6 instead of 4 electrons was found [Ame99].

The second signal G at about 535 eV (width 956 meV for the 2:1 compound) is also maximum for the 2:1 stoichiometry, weaker for the two other compounds and very weak for pure HMP. By analogy with the surface methoxy species [Ame99] we conclude that this signal derives from the $6a_1$ orbital of the methoxy group with essentially σ* (C-O) character. We denote the transitions as

G: ***O1s→a,b (σ* methoxy)*** (6.6)

nothing that in this case a and b derive from methoxy $6a_1$ (being also observed for the methoxy species on Cu and Ni and for multilayer films of methanol [Ame99]). Its intensity behaviour is similar to signal F (see below). The remaining signals H, I and K occur with

similar intensities for pure HMP (spectrum f) and correspond to transitions into orbitals of the aromatic ring system. The enhanced width of the signals reflects the higher delocalization with increasing final state energy.

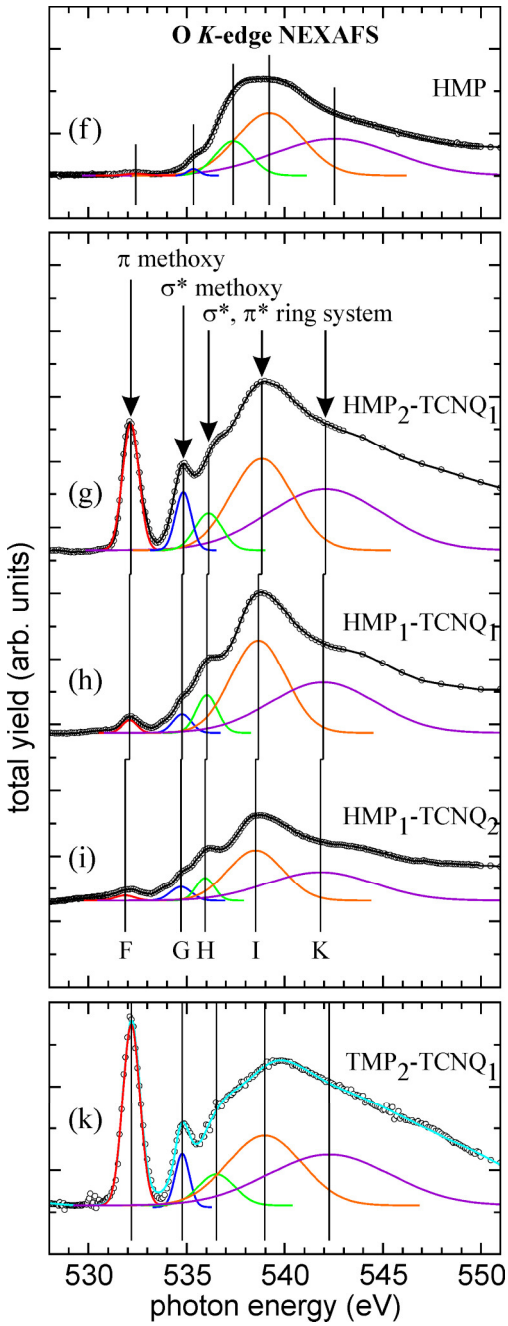

Figure 6.8 Same as Fig. 6.7 but for the K-edge NEXAFS spectra of oxygen. Spectrum (f) was taken for pure HMP, (g – i) correspond to the same samples as (a – c) in Fig. 6.7 and (k) was taken for TMP_2-$TCNQ_1$. Yield scales of (g – i) are identical.

We now quantify the eye-catching intensity variations in the nitrogen and oxygen spectra. Fig. 6.9 shows the intensity variations of the oxygen (a) and nitrogen resonances (b) as function of the HMP/TCNQ ratio. The intensities have been determined as areas under the

corresponding fit curves in the spectra normalized to the area of peak A for nitrogen (Fig. 6.7) and peak I for oxygen (Fig. 6.8). The intensities of signals A and I vary just proportional to the N or O content.

Transitions F and G show the strongest variations with stoichiometry. Their intensities are perfect indicators of changes in the occupation of the frontier orbitals of the methoxy group in the donor molecule. These signals are strongly enhanced for the 2:1 compound, i.e. for maximum HMP content. Likewise, for TMP_2-$TCNQ_1$ (spectrum k in Fig. 6.8) its intensity is also very high. On the other hand, for pure HMP (spectrum f) the signal is almost absent.

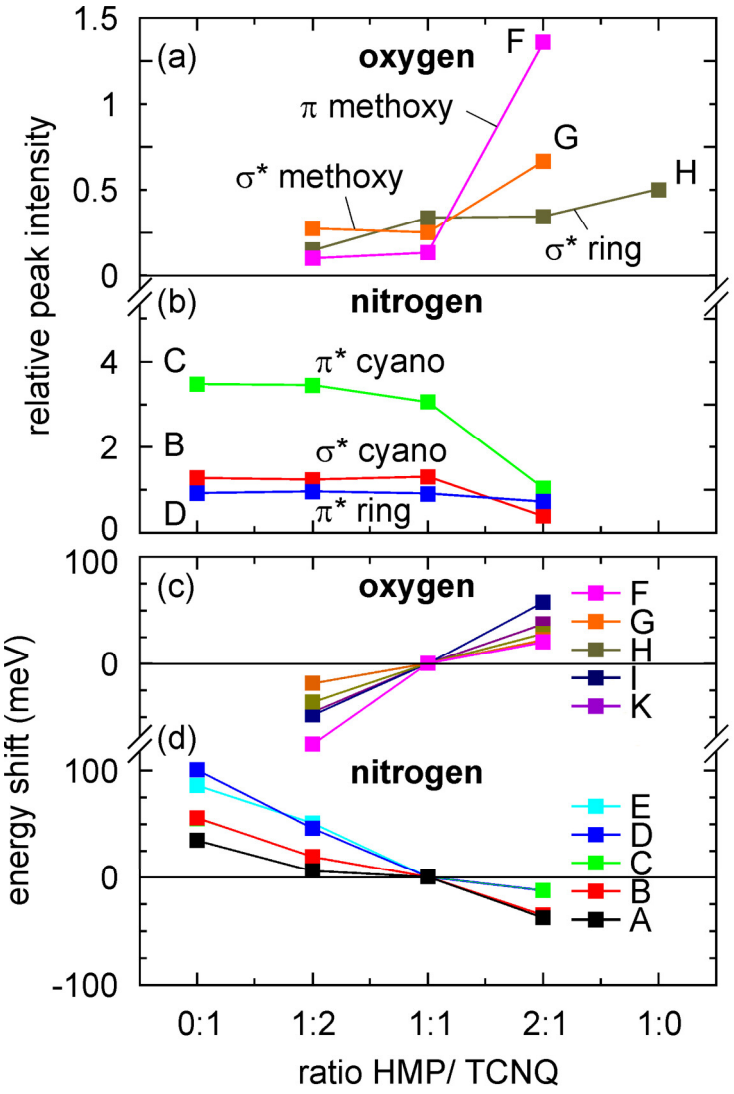

Figure 6.9 NEXAFS resonance intensities (peak areas as derived from the fits in Figs. 6.7 and 6.8) in the oxygen (a) and nitrogen spectra (b) and corresponding energy shifts (c and d). The areas in (a) and (b) are normalized to signals A and I for nitrogen and oxygen, respectively.

The increase of the intensities of resonances F and G in the oxygen spectra (Fig. 6.9a) for the 2:1 compound counteracts the intensity decrease of resonances B and C in the nitrogen spectra (Fig. 6.9b). These intensity variations with opposite behaviour for donor and

acceptor give direct evidence of the participation of these orbitals in the charge-transfer. The intensity increase in the *O1s→(methoxy π and σ*)* -derived transitions directly mirror the charge depopulation in the frontier orbitals of the functional group of the donor. The intensity drop in the *N1s→(cyano b_{1g},b_{2u} and b_{3g},a_u)* transitions indicate partial population of these orbitals of the functional group of the acceptor. The intensity of signal H (associated with σ*-orbitals of the pyrene ring system) also varies with stoichiometry, but not as strong as signals F and G. Signal D (associated with π* of the TCNQ ring) varies only very weakly.

Besides the strong intensity effect the fit revealed systematic energetic shifts as function of stoichiometry that are displayed in Fig. 6.9 (c) and (d) for the resonances involving donor and acceptor orbitals, respectively. As reference (shift zero) we used the resonance positions for the compound with 1:1 stoichiometry. The shifts vary continuously with the HMP/TCNQ ratio and show an opposite sign for the donor and acceptor moiety. With increasing donor content the resonance positions associated with O 1s (donor) and N 1s (acceptor) shift to higher and lower photon energies, respectively. The size of the energy shifts differs significantly for different resonances.

Let us recall the different mechanisms contributing to shifts in the NEXAFS features (see, e.g. [Sto92, Bun10]). The so-called valence shift reflects the redox state of the emitter atom: A change of the redox state changes the screening effect of the valence electrons on the nucleus. In turn, the binding energy of the electrons in the core level changes and the edge position appears shifted. In addition, a chemical shift is induced by different ligands, analogous to the chemical shift observed in XPS. Ligands with higher electronegativity reduce the effective charge density in the region of the excited atom and thus cause a shift of the NEXAFS resonances towards higher energies. Quantitatively, chemical shifts are usually smaller in NEXAFS than in XPS, because the XPS probes the N→N-1 transition of the system, whereas in NEXAFS a transition to a neutral excited complex N→N* is observed, where both the core level and the unoccupied final state undergo a shift. The shifts of initial and final states may partly cancel in the excitation energy. This is illustrated for the present donor-acceptor complex in Fig 6.10. For the case of the donors TMP or HMP the loss of charge in the final-state orbital |f> derived from the 2e -orbital of the methoxy group (going from (a) to (b)) leads to a reduced screening of the nucleus, there by lowering the energy of the initial state |i>. However, at the same time the final state |f> is also lowered in energy due to the attraction of the core hole. As both levels are pulled down the shifts partly cancel. For the acceptor the increase of charge in the final-state orbital, here in the b_{1g}-orbital of the cyano group (going from (c) to (d)) leads to an increased screening of the initial-state |i> and to a smaller lowering of the final-state energy. Consequently both levels rise in energy and the shifts partly cancel.

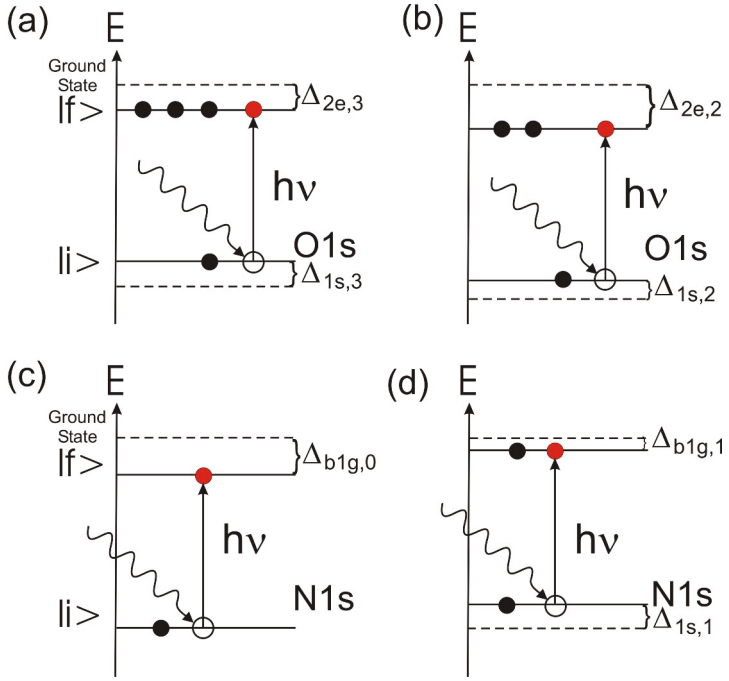

Figure 6.10 Level scheme for the O1s→methoxy 2e (a, b) and N1s→ cyano b_{1g} (c, d) NEXAFS resonances for different occupation of the final state.

The shift of all oxygen-related resonances towards higher photon energies (Fig. 6.9c) indicates an increasing deficiency of valence charge leading to reduced screening of the ion core. Vice versa, the shift of all nitrogen resonances to lower photon energies (Fig. 6.9d) is indicative of an increasing charge density in the valence region. It is interesting to note that the variations in spectral weight of the resonances (Fig. 6.9a, b) and in the resonance positions (Fig. 6.9c, d) do not show the same quantitative behaviour: The spectral weight shows a sudden change between the 1:1 and 2:1 stoichiometry, whereas the shifts vary smoothly. This may reflect the fact that the intensities of the NEXAFS transitions reflect occupation numbers of the final states that are affected by the partial charge transfer into specific orbitals, whereas the energetic positions vary because of the change in net charge of the whole molecule.

It is a surprising fact that the charge deficiency in the donor (HMP) is highest for the compound with maximum HMP content (2:1). The same is found for the TMP_x-$TCNQ_y$ compound with stoichiometry 2:1 (see spectrum k in Fig. 6.8). This is counterintuitive from the chemical point of view. In a simple model the opposite effect might be expected. As the different stoichiometry leads to a different coordination and consequently to a different structure, we conclude that the relative arrangement of HMP and TCNQ must play an important role for the amount of charge transfer.

Fig. 6.11 summarizes the results in terms of a transition scheme including the orbitals involved in the charge transfer. The methoxy group promotes the donor character of HMP and TMP. In CT-complexes a fractional amount of charge is transferred from donor to acceptor. In terms of quantum mechanics this means that the probabilities to find an electron in the orbitals being involved in the charge transfer deviate from integer values. The present measurements show that the orbitals located at the functional groups are strongly involved in that process. Orbitals derived from the frontier orbitals of the methoxy group (2e and $6a_1$) donate charge and orbitals located at the cyano group (b_{3g} and a_u and, to a weaker extent, b_{1g}

and b_{2u}) accept charge. Although the π-orbitals of the ring systems mediate the charge transfer, their occupation numbers is less affected.

Excitations into formally occupied orbitals was also observed by Grioni et al. [Gri89] for various Cu I compounds. Strong transition intensities observed at the Cu L_3 edges give evidence of transitions into hybridised states with partial d-character at the Cu atom in many compounds that formally should have d^{10} atomic configuration. This is interpreted in terms of Cu 3d-4s hybridised states, sharing electrons in covalent bonds with ligands and thus allowing for transitions into formally fully occupied 3d states. We can assign a similar interpretation to our case: The methoxy 2e-derived orbital should be completely occupied. Due to hybridisation with the π-system, however, this orbital becomes allowed as final state for the NEXAFS transition.

As the orbital energies of the methoxy-derived states lie well below the HOMO and those of the cyano-derived states lie above the HOMO, the strong intensity changes observed in the NEXAFS spectra should not be considered as a static charge transfer, but it might be a dynamic effect. In the donor it might result from virtual excitations from the frontier orbitals of the methoxy group to the π-orbitals of the aromatic ring system. In the acceptor from virtual excitations from the π-orbitals of the ring to unoccupied orbitals of the cyano group. The excitonic nature of the methoxy 2e-derived resonance (signal F) is in accordance with the fact that it appears at a transition energy 3 eV below the next transition.

Hard X-ray photoemission results of HMPx-TCNQy microcrystals and thin films of the equivalent compounds will be discussed in Chapter 7.1 together with an energy diagram comparing HAXPES and NEXAFS transitions.

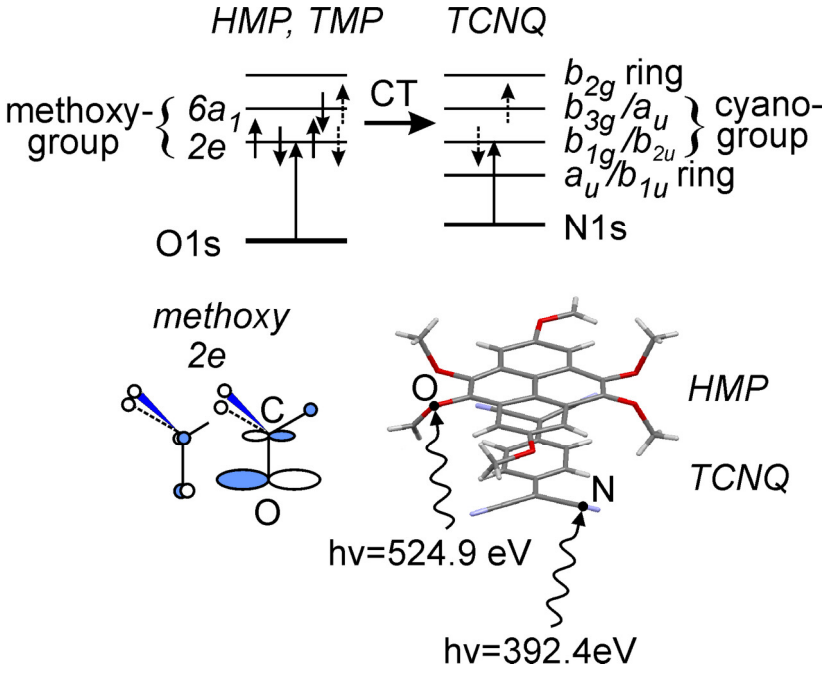

Figure 6.11 Transition scheme describing the details of charge transfer between donor and acceptor. The NEXAFS spectra reveal the frontier orbitals of the methoxy-groups in HMP or TMP (symmetry 2e and $6a_1$ for an isolated methoxy group) as electron-donating orbitals and b_{1g}/b_{2u} and b_{3g}/a_u of the cyano-group of TCNQ as accepting orbitals. Bottom left, structure of the 2e orbital of an isolated methoxy group (after [Ame99]).

6.6 Summary of Results for Pyrene-Derivatives

The functionalized pyrene-derivatives *4,5,9,10-tetramethoxypyrene* (TMP, $C_{20}H_{18}O_4$) and *2,4,5,7,9,10-hexamethoxypyrene* (HMP, $C_{22}H_{22}O_6$) were employed as donors in complexes with the classical strong acceptor *7,7,8,8-tetracyano-p-quinodimethane*, (TCNQ, $C_{12}N_4H_4$). TMP_x-$TCNQ_y$ and HMP_x-$TCNQ_y$ crystals in stoichiometries x:y = 1:2, 1:1 and 2:1 were grown by vapour diffusion of hexane into a dichloromethane solution of the components. In addition, UHV co-deposited thin films of the complex and its constituents have been studied as well.

TMP - TCNQ in 1:1 stoichiometry on Au and Si was studied most extensively using X-ray diffraction and the spectroscopic techniques. New reflexes corresponding to periodicities of d_1= 0.894 nm and d_2= 0.677 nm in X-ray diffraction (θ- 2θ scans) revealed a new crystallographic phase. Infrared spectroscopy shows a softening of the CN stretching vibration of TCNQ by 7 cm^{-1} in the complex as compared with pure TCNQ on Au. This shift is indicative of a CT on the order of 0.3*e*. The occupied and unoccupied frontier orbitals of the CT complex and the pure moieties have been probed by UPS and scanning tunnelling spectroscopy STS, revealing characteristic level shifts and a strong reduction in the HOMO-LUMO gap upon formation of the complex.

In order to interpret the spectra, DFT calculations have been performed using the Gaussian03 code with the B3LYP hybrid functional. The comparison of measured and calculated energy levels of the CT complex and the pure donor and acceptor shows the following: The complex is characterised by a relatively small HOMO-LUMO gap of 1.25eV (referred to the positions of the peak maxima). The calculated LUMO eigenvalue lies close to the LUMO peak measured by STM, the HOMO eigenvalue lies 0.7 eV above the STM HOMO peak; the calculated HOMO-LUMO gap is about a factor of 2 too small. The calculated ΔSCF binding energy of the electrons in the HOMO agrees fairly well with the UPS peak position. Taking the hole-injection and electron-injection barriers Δ_h and Δ_e from the STS spectrum in Fig. 6.5, we estimate an onset of the transport gap of about $\Delta_{transp} \cong \Delta_h + \Delta_e =$ 0.8 eV, making TCNQ-TMP a small-band-gap semiconductor. Measurements and theory clearly show that the small gap arises from the fact that the TMP-derived HOMO shifts towards lower binding energy and the TCNQ-derived LUMO shifts to higher binding energy as compared with the pure moieties. The given values correspond to the low-coverage regime. At higher coverage the HOMO shifts by about 0.4 eV to higher binding energy (A, B in Fig. 6.4), so that the gap will be somewhat larger for thick films or for bulk material of the CT compound. Pure TCNQ and TMP exhibit much larger gaps of more than 3 eV.

For TCNQ, we find good agreement between calculated and measured level positions: The STS LUMO lies close to the calculated LUMO eigenvalue and almost coincides with the CV result. Like for the complex, the UPS HOMO peak lies quite close to the predicted ΔSCF binding energy. The calculated HOMO-LUMO gap is only 20% smaller than the experimental value for the optical gap for TCNQ [Tor75].

For TMP the deviations between experiment and theory are larger. The HOMO and LUMO eigenvalues lie more than 2 eV above the STS values and the ΔSCF binding energy of the HOMO lies 0.8 eV above the UPS signal. However, the CV value for the HOMO is fairly close to the HOMO eigenvalue. We may speculate that the pinning-effect of the energy levels in the thin film to the new electrostatic potential in the organic film due to the

organic-metal interface (as discussed in Ref. [Koc08]), might be responsible for this discrepancy. This pinning is not accounted for by theory and CV measurements are free of such interface effects. This is probably the main reason why the experimental data for the condensed film lie significantly below the calculated values and the CV result.

Besides these near-at-hand differences between condensed and free molecules, there are also *systematic differences between the STS and UPS positions of the HOMOs*. The HOMO levels measured by STS for TMP and for the complex as well as the HOMO position for TCNQ estimated using Δ_{opt} (thin line) lie consistently above the UPS results, the distance being 0.7, 0.6 and 0.3 eV for TCNQ, the CT-complex and TMP, respectively. The differences point on the fact that these two spectroscopies are fundamentally different: STS probes the *ground-state HOMO position via resonant tunnelling from the HOMO into the tip.* The tunnelling matrix element is governed by the overlap integral of (ground-state) wavefunctions in the tip and the molecular film. UPS yields the energies of the *final* (*ionic*) *states being screened by neighbouring molecules.* The electronic transitions in UPS are driven by the photon operator, in the low energy regime of UPS the dipole operator ***er*** is a very good approximation. Energetically, UPS measures the energy difference between the initial neutral *N* electron state and the final *N*-1 electron state. Although both spectroscopies probe "the HOMO", the energy positions are expected to be quantitatively different. E.g. the polarization energy [Sat81], being a significant contribution in UPS from condensed layers (in comparison with free molecules) is absent for STS. The long-range Coulomb attraction acting on the outgoing photoelectrons reduces their kinetic energy. This translates into higher UPS binding energies in Fig. 6.6, in accordance with the observed systematic differences between UPS (thick lines) and STS (thin lines).

The fact that the deviation between UPS and STS HOMO positions is maximal for TCNQ might be connected with the strong interface dipole increasing the work function by 0.7 eV. In this case, the negative side of the dipole is oriented towards the organic film. It is likely that STS experiences only part of this "level biasing" because the tip itself introduces an energy reference level towards the vacuum side, whereas this reference level is missing in UPS.

For the CT-compound we observed the growth of a flat multilayer at low coverage and the appearance of 3D crystallites above about four monolayers. It is likely that the molecules in the first layers lie in a face-on orientation on the surface, whereas the multilayer film attains the bulk structure of the compound. This structural transition from the smooth multilayer to 3D crystallite growth shows up in UPS as a shift in the photoemission peaks towards higher binding energy. In this context it is worthwhile being mentioned that the positions of peak maxima and line shapes in angular resolved UPS of thin films depend on the molecular orientation in the film [Toa09, Che08b, Che08a]. This effect can also be interpreted in terms of orientation-dependent ionization energies [Duh08]. A full structural analysis of the studied thin films is thus highly desirable, such a study is presently being performed.

Near-edge X-ray absorption fine structure (NEXAFS) spectroscopy was established as a tool to study the orbital specific charge transfer in TMP_x-$TCNQ_y$ and HMP_x-$TCNQ_y$ crystals in stoichiometries x:y = 1:2, 1:1 and 2:1. Oxygen and nitrogen K-edge NEXAFS spectra were exploited as local probes of the donor and acceptor molecules, respectively. Oxygen is only contained in the methoxy-moiety of the donor and nitrogen in the cyano-moiety of the acceptor. The orbital selectivity of the NEXAFS resonances allows to precisely elucidate the participation of specific orbitals in the charge-transfer process.

The spectra revealed partial charge transfer from orbitals derived from the frontier orbitals 2e (π) and $6a_1$ (σ^*) of the methoxy-group of the donor to the cyano-orbitals b_{3g} and a_u (π^*) and - to a weaker extent - to b_{1g} and b_{2u} (σ^*) of the acceptor. In particular, the occupation of 2e (being the HOMO of the isolated methoxy-species without charge transfer) reflects a loss of charge in the methoxy-groups. Surprisingly, the charge transfer is maximal for the compounds with highest HMP or TMP contents. As additional signature of a charge transfer, all spectral features of the donor and acceptor are shifted to higher and lower photon energies with increasing HMP content, respectively.

Providing quantitative access to the relative degree of occupation of specific orbitals, the approach constitutes the most direct probing method for the charge-transfer mechanism in organic salts found so far. Although demonstrated for the specific example of pyrene-derived donors with the classical acceptor TCNQ, the method is very versatile and can serve as routine probe for novel CT-complexes on the basis of functionalized polycyclic aromatic hydrocarbons.

The surprising results summarized in Figs. 6.9 and 6.11 are important for future studies. The novel donors hexa- and tetramethoxypyrene in complexes with the classical acceptor TCNQ show an anomalous behaviour for the 2:1 stoichiometry. The hughe signal F is derived from the 2e-orbital being the HOMO of a fully anionic methoxy group. This high signal definitely indicates a large charge transfer from HMP (or TMP) to TCNQ. This charge transfer is much larger than that found for the 1:1 stoichiometry. This behaviour might indicate a pathway to the synthesis of a new class of materials showing a valence instability, i.e. a neutral-ionic phase transition as discussed in [Iwa89] for $TTeC_1TTF$-TCNQ (see also Fig. 2.16b).

7. Hard X-ray Photoelectron Spectroscopy (HAXPES) of CT-Salts

The results of this chapter have been obtained in a beam time in October 2010 at *PETRA III*, Hamburg, the former positron-electron tandem ring accelerator. Owing to the large mean free path of the electrons in the HAXPES range (see Fig. 2.10) the probing depth is of the order of 10-15 nm (at kinetic energies of 6-8keV) and thus surface contaminations play only a minor role. In this energy range, the photoemission cross sections for states with $l \neq 0$ drop rapidly, so that only the ns orbitals have cross sections accessible with sufficient intensity (at least at the present conditions of the beamline). We studied several samples of the *HMP* (or *TMP*) – *TCNQ* family and two samples of the *κ-(ET)$_2$-Br* family.

Spectra have been taken for the oxygen, nitrogen and carbon 1s orbitals for the methoxy-derivatives of pyrene in complex with TCNQ and the sulphur 2s orbital for *κ-Br*. Beam damage due to the hard X-rays was evident. Within 30 minutes of permanent irradiation significant changes became visible. The sample was always moved to a new position before taking the next spectrum. The experimental set-up has been described in section 3.4.

7.1 Tetra- and Hexamethoxypyrene - Tetracyanoquinodimethane

The information depth of HAXPES (10-15 nm) is even higher that that of NEXAFS (5 nm) and both are much larger than the information depth in UPS (< 1 nm). Hence, surface contaminations from the solvent, from impurities in the solution or from ambient air do not show up significantly in HAXPES and NEXAFS. The latter two methods are suitable for the study of solution-grown crystals and films that were transported through ambient air. HAXPES combines the chemical specificity of XPS/ESCA with true bulk sensitivity.

We briefly recall the few existing studies of CT salts using XPS from the literature. A study of *TTF - TCNQ* and related compounds revealed a splitting of about 1.5 eV in the sulphur 2p peak positions between neutral TTF^0 and ionic TTF^+ [Ike77]. This splitting could be used to estimate the amount of charge transfer. The evaluation of the N 1s spectra for the determination of the charge transfer state of *TCNQ* turned out not so simple because of a strong satellite due to shake-up of π-electrons. Evaluation of the molecular mixed valency of *TCNQ* was possible for the complex *(BEDT-TTF)-TCNQ*, where a binding-energy difference of 1.6 eV between neutral $TCNQ^0$ and ionic $TCNQ^-$ occurs [Yuz97, Isa82]. This change is accompanied by a red shift of about 30 cm^{-1} in the *CN* stretching mode (a_g mode) when going from the neutral *TCNQ* to the anion.

The central question in the first pilot experiment was, whether chemical shifts or shake-up satellites between the core-level signals in the complexes compared to the pure donors and acceptors can be detected. We recall that both the UPS spectra and the NEXAFS resonances show small energetic shifts (several 100 meV range) in opposite directions for the donor and acceptor molecules. We will see in the following that much larger shifts are observed in HAXPES spectra.

Series of typical spectra are shown in Fig. 7.1 (a) and (b) for O 1s and N 1s, respectively, taken for fractions of the solution-grown 3D crystallites. Panel (c) shows the line positions and intensities derived from the O 1s spectrum. Panels (d), (e) and (f) show spectra for O 1s,

N 1s and C 1s, respectively, taken for UHV-deposited films. The spectra of the compounds are compared with spectra of the pure donors and acceptors taken under exactly the same conditions.

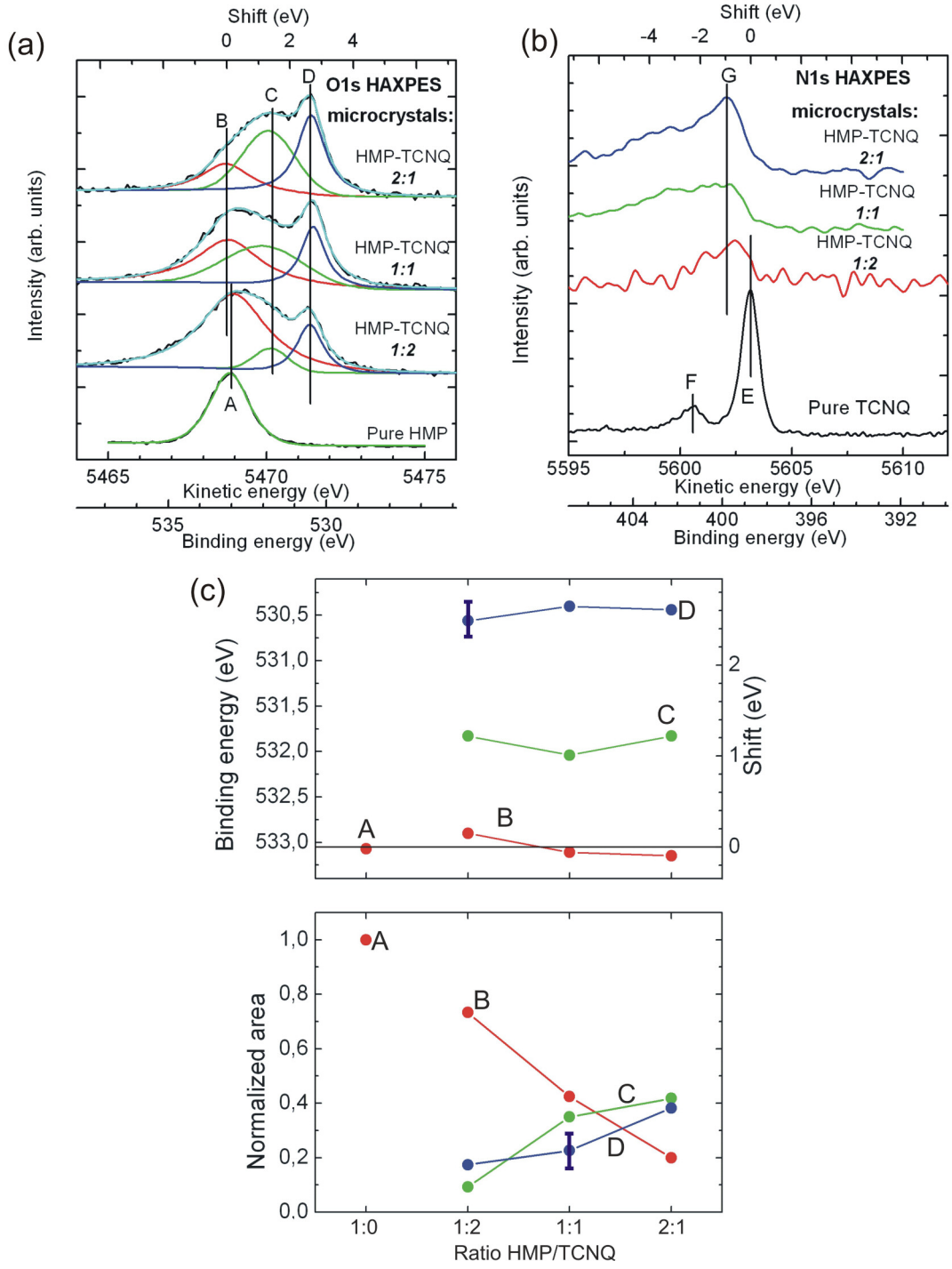

Figure 7.1 Oxygen 1s (a) and nitrogen 1s (b) HAXPES spectra for solution-grown microcrystals of the CT complexes HMP_x-$TCNQ_y$ with x:y = 2:1, 1:1 and 1:2. (c) Binding energies and intensities of O 1s signals from (a). The intensities are normalised to the total area, i.e. the sum of all peaks.

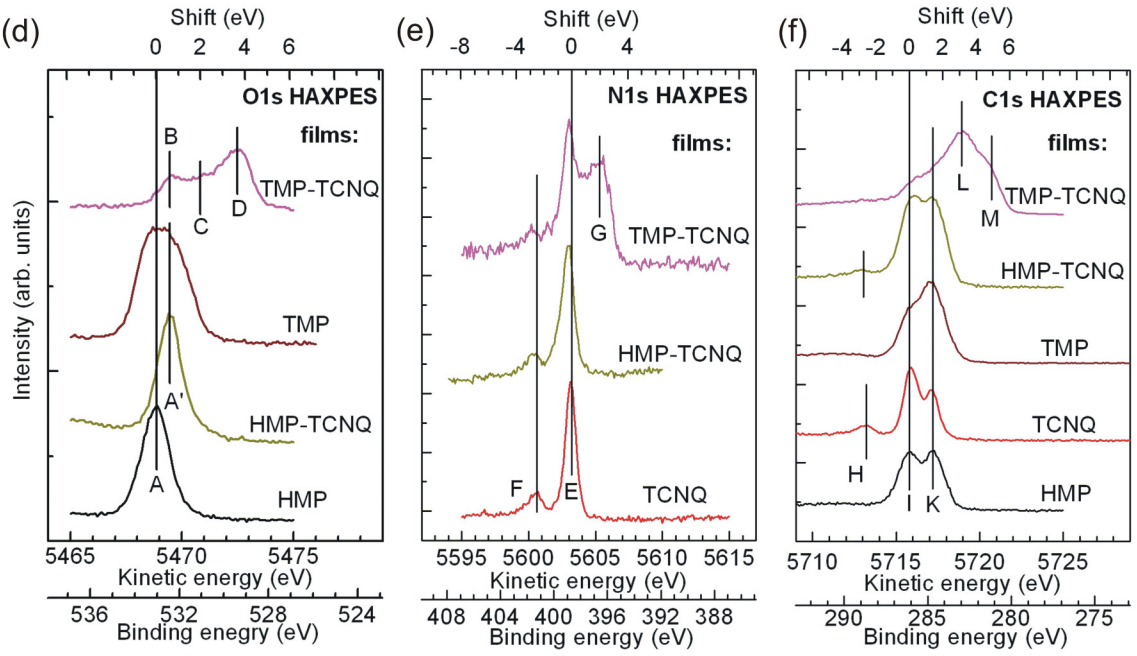

Figure 7.1 (continued) Oxygen 1s (d), nitrogen 1s (e) and carbon 1s (f) HAXPES spectra in UHV-deposited thin films of the co-deposited TMP-TCNQ and HMP-TCNQ. All spectra were taken at hν = 6001.9 eV at PETRA III, Hamburg (energy resolution 440 meV).

For the series of O 1s spectra in (a) a multipeak least-squares fit was performed, deconvoluting the spectra into three clearly distinguishable peaks B, C and D fir the compounds, in comparison with the single line A for pure HMP.

The energy shifts of the signals (scales on top) are referenced to the main line of the pure donor and acceptor. Sizeable shifts up to 4 eV and peak splittings occur giving evidence of the changed chemical environment of the emitter atoms and the amount of charge transfer in the different compounds. Comparison of the oxygen and nitrogen 1s spectra from the UHV-deposited thin films in (d, e) with those from the solution-grown microcrystals in (a, b) reveals that the HMP-TCNQ film shows only slightly shifted the single-line spectra of the pure donor and acceptor. However, the TMP-TCNQ film shows strongly shifted and split signals, characteristic of a CT compound. We may conclude that this HMP-TCNQ film did not lead to formation of a CT-complex but possibly to donor-acceptor phase separation. More systematic measurements would be needed to clarify this question. However, the limited time during the first HAXPES beamtime did not allow for further investigations of the HMP-TCNQ thin film system. In the following, we therefore concentrate on the interpretation of the solution-grown microcrystals that were already investigated using NEXAFS, see chapter 6.5.

We now summarise the results of Fig. 7.1 (a-c), and then discuss the data in the framework of a qualitative model that considers the action of charge transfer on the core-level positions. Finally, we will address the possibility of shake-up processes being involved.

Oxygen is only contained in the methoxy groups of HMP and TMP. The oxygen spectra in (a) thus constitute a local spectroscopic probe in the donor moieties of the compounds. It is eye-catching that the spectrum changes substantially from a single-line spectrum for pure

HMP to a spectrum with three distinct peaks for the three compounds with the spectral weight being strongly shifted towards higher kinetic energy, i.e. lower binding energy (which rules out charging as origin of the shifts). Moreover, the relative intensities change systematically with stoichiometry, see panel (c). The shift scale on top refers to the O 1s signal of pure HMP that appears as a pronounced line at the highest binding energy (signal A). Peak A is thus indicative of neutral HMP with filled orbitals. The spectra of the three compounds consist of a broadened signal at the same energy as observed for pure HMP (signal B) and two signals C and D being shifted by 1.4 and 2.6 eV, respectively. Signal B drops with increasing HMP content by a factor of 4, whereas C and D rise by roughly the same factor. The widths of B and C are substantially larger, whereas D is even narrower than the single line from pure HMP.

The spectrum of the TMP-TCNQ film in Fig. 7.1 (d) shows a three-peak structure similar to the HMP-TCNQ series in Fig. 7.1 (a). However, the shifts are larger: 0.7 eV, 2.0 eV and 3.7 eV for signals B, C and D, respectively. This points on a similar chemical compound. For the HMP – TCNQ film, we observe a single-line O 1s spectrum. The peak A' is shifted by 0.8 eV to lower binding energy, but is clearly just a single line. We conclude that presumably no complex is formed in this film.

Nitrogen is only contained in the cyano-group of TCNQ. The nitrogen spectra shown in panels (b) and (e) thus provide a local probe in the acceptor moiety. For pure TCNQ the spectrum is well-known [Lin88] and shows a strong main peak E and a weaker signal F being shifted by about 2.6 eV to higher binding energy. This weak signal is assigned as a HOMO-LUMO shake-up satellite. In the spectra of the microcrystals (panel (b)), the maximum of the main line G appears shifted by 1eV to higher binding energy, i.e. in opposite direction as observed for O 1s. This is in qualitative agreement with literature data for other TCNQ-containing compounds [Bor77]. The N 1s spectra of the compounds show spectral weight up to several eV towards higher binding energies. Unfortunately, the N 1s spectra of the microcrystals were relatively noisy due to a smaller intensity than found for the other core level signals. The reason for this is not clear and could not be investigated in the first beamtime. The spectra are too unstructured and noisy to allow for a multipeak fit with sufficient significance.

The spectrum of the TMP-TCNQ film in Fig. 7.1 (e) shows a broadened peak G, too, similar to the HMP-TCNQ series in Fig. 7.1 (b). However, peak G is shifted by 2.0 eV to lower binding energies, whereas for the microcrystals, signal G is shifted to higher binding energies. Together with the larger shifts observed in the O 1s spectrum of TMP-TCNQ (panel (d)), we can conclude that in the TMP-TCNQ film sample both core-level spectra appear shifted to lower binding energies. Peak G is at a similar position as the leading signal in the spectrum of a Cu-TCNQ complex [Lin89]. For Cu-$TCNQ_2$ these authors also find a superposition of neutral and shifted TCNQ partial spectra. For the HMP – TCNQ film, we observe a very weakly shifted TCNQ spectrum, again suggesting that no complex is formed in this thin film.

Carbon is contained in both moieties, its 1s spectra are shown in Fig. 7.1 (f). The spectra for pure HMP and TMP clearly show the two carbon species (I and K: methoxy carbon and aromatic ring system). For TCNQ we recognise the ring and periphery carbon species as two peaks and a shake-up satellite at 2.6 eV shift, the small signal H. This is again associated with the HOMO-LUMO shake up as visible in the N 1s spectrum. The spectrum of the HMP – TCNQ complex is a superposition of the HMP and TCNQ partial spectra.

However, in the TMP – TCNQ complex new signals L and M occur that are strongly shifted to lower binding energies. Since carbon is contained in donor and acceptor molecules, the interpretation of these spectra is less straightforward. Counteracting shifts are to be expected.

We now discuss these results in terms of a transition model shown in Fig. 7.2. The left column refers to HAXPES. It is possible to estimate the action of charge transfer on the core-level positions in a simple model that just takes into account the screening of the Coulomb attraction of the nucleus by the different number of electrons in the valence shell. This screening increases with increasing number of valence electrons. For O 1s photoemission, we schematically sketch the situation of three and two electrons being present in the 2e orbital of the methoxy group, (a) and (c), respectively. For N 1s, we show the case of empty and singly occupied b_{1g} orbital, cf. orbital scheme in Fig.6.11. From this simple consideration we expect a shift of the donor core levels to *higher* binding energies when donor orbitals loose electron charge and, vice versa, a shift of the acceptor core levels to *lower* binding energies when the acceptor orbitals become (partially) populated. This simplified model is obviously in contradiction with the results of Fig. 7.1 (a, b), where the shifts are just opposite. The simple model that just takes into account a charge loss or excess in the valence orbitals is not sufficient for an explanation of the results. Instead, we must consider the formation of the complex where shifts can arise due to changes e.g. in the electrostatic environment of the emitter atom. The methoxy group could undergo a conformational transition or a change in its nearest chemical surrounding so that the oxygen atoms experience different local potential which, in turn, could cause a level shift towards lower binding energy despite of the loss in charge due to the charge transfer. We have to keep in mind that the average charge transfer per methoxy group is rather small, since there are six (for HMP) or four (for TMP) such groups in the molecule.

Finally we note that the behaviour for NEXAFS resonance positions is fundamentally different as sketched in Fig. 7.2, right column. In addition to the initial state effect caused by the screening of the nucleus, the final state is pulled down by the presence of the core hole. The amount of final state shift is the larger, the smaller the total occupation of the final-state orbital. If we assume the same occupation as in the HAXPES cases, we have to take into account that the excited electrons (red dots) also reside in the respective orbitals, i.e. the threefold occupied configuration (a) becomes fourfold occupied (b) and analogous for both columns. The essential point is that this lowering of the final-state energy levels counteracts the lifting of the initial levels so that both contributions may cancel each other to a large extent. As a consequence, the shifts observed in NEXAFS are considerably smaller than those observed in HAXPES.

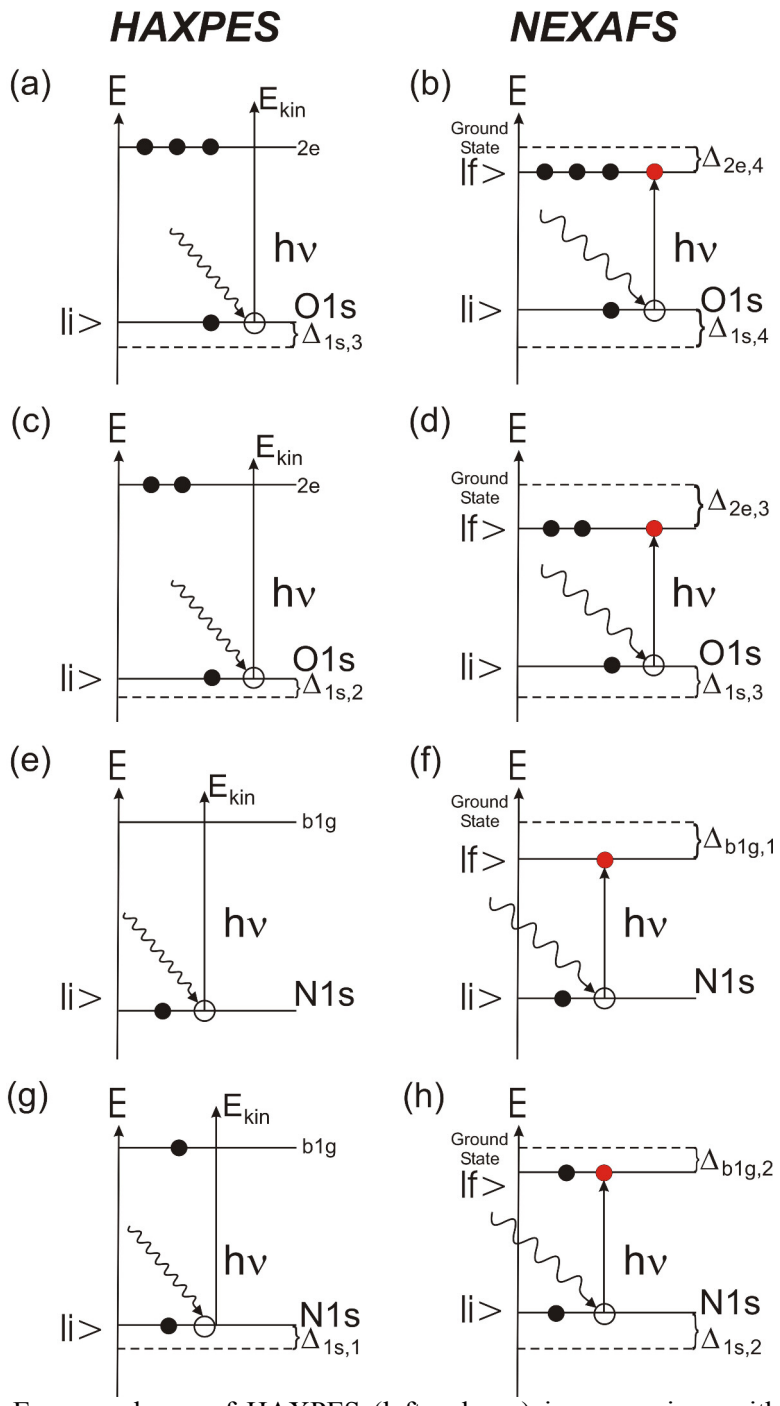

Figure 7.2 Energy scheme of HAXPES (left column) in comparison with NEXAFS (right column). |i > and |f > denote the initial states (both columns) and the final states of the NEXAFS resonant transition (right column).

7.2 Cationic Radical Salt κ-(BEDT-TTF)$_2$Cu[N(CN)$_2$]Br

Introduction

The *cation radical salts* of the *κ-(BEDT-TTF)$_2$X* family (X stands for various kinds of monovalent anions) exhibit different types of order associated with spin-, charge- and/or orbital degrees of freedom. A particularly interesting phenomenon is the interaction-driven transition from the metallic state to the Mott insulator. The microscopic origin of these exciting phenomena and the conditions giving rise to one or the other type of correlation-driven ordering phenomena poses major challenges to both experiment and theory. This fascinating class of materials constitutes an unprecedented model system for exploring the physics of low-dimensional electron systems with both strong electron-electron and electron-phonon interactions. Various members of this class of charge transfer systems are investigated in experimental and theoretical projects of the SFB/TR 49 (Frankfurt, Mainz, Kaiserslautern).

In the κ-phase strong dimerisation of the *BEDT-TTF* (briefly ET) molecules leads to a half-filled conduction band, emphasising a 2D-metal in the ET-layers (an excellent overview is given in [Toy07]). Each dimer donates one electron to the polymeric acceptor layer (which is an insulator). By applying pressure (physical or chemical), the system can be driven across the boundary of the Mott metal-insulator transition, depending on the ratio of bandwidth (or kinetic energy) W and on-site Coulomb correlation energy U [Kan97]. The *κ-(ET)$_2$X* family exhibits a rich phase diagram (being universal for the whole family) with six different phases in the region below 100 K. There are many open questions concerning the interplay of lattice and electronic degrees of freedom. In particular for the superconducting members like *κ-(BEDT-TTF)$_2$Cu[N(CN)$_2$]Br* (studied in this thesis) a number of properties have been observed “whose explanation remains obscure” [Lan11].

It is near at hand that photoemission should give access to these electronically-driven phenomena. Core-level spectroscopy, in particular, allows to address a selected atomic species. Hence a *local spectroscopic probe* can be placed in the “active” 2D metallic layer (in the present case sulphur is only contained in the donor layer). Due to the half-filling of the conduction band, the two ET molecules of a dimer share one unpaired electron. In core-level spectroscopy, the *intra-dimer degrees of freedom* come into play, i.e. the two molecules reveal their individual nature.

However, the surfaces of these materials are highly reactive and their delicate organic nature rules out standard surface preparation techniques like ion bombardment and heating. Classical photoemission experiments were strongly hampered by this surface problem. An early XPS-experiment on *κ-(BEDT-TTF)$_2$Cu(NCS)$_2$* showed that bonding in the BEDT-TTF layer has covalent contributions, whereas the polymeric anion layer exhibits ionic bonding with monovalent copper and trivalent nitrogen [Itt91].

HAXPES, with its information depth of about 15 nm at the present conditions, overcomes the obstacles concerning the surface quality in a perfect way. The surface itself plays only a minor role because about 10 layers are probed (layer spacing 1.6 nm). The results presented in this section were obtained in the first HAXPES beamtime of our group in October 2010. Two single-crystalline samples of *κ-(BEDT-TTF)$_2$Cu[N(CN)$_2$]Br* type *(protonated* and *deuterated* modifications *H8* and *D8,* respectively*)* with sizes of about 1.5 mm were investigated. Both samples were fixed on the same copper sample holder with special carbon-based glue that reduces strain upon cooling. This assured that both samples have the

same temperature, which is important for a quantitative comparison of the spectra. The samples were grown by M. de Souza and coworkers in the group of Prof. Lang at Goethe-University Frankfurt / Main.

A pronounced structure of shifted peaks in sulphur 2s HAXPES core level spectra along with a corresponding breakdown of the main-line intensity was observed in a certain temperature interval and studied systematically in a warming-up series for the protonated sample. In a measurement at 80 K, additional features with even larger shift were observed for the deuterated sample as well, proving that the observed strong effects are not an artefact of sample destruction by the X-rays. A comparative measurement was also performed for the carbon 1s line at 80 K, revealing additional signals as well.

These first measurements provide a *proof-of-principle* of the feasibility of HAXPES studies for this fascinating class of materials. Moreover, the results constitute a general model case showing how core-level spectroscopy with bulk sensitivity provides direct access to subtle electronic details in the vicinity of the Mott transition. For the specific case of *κ-(BEDT-TTF)$_2$Cu[N(CN)$_2$]Br* they shine light on the interplay of the geometrical and electronic structure, degree of localisation and the influence of local disorder in such a highly correlated system with large electron-phonon coupling. On the basis of the HAXPES core-level spectra and in the context of previous experimental results for other measurable quantities we propose a scenario that is in accordance with all existing data: At the *T*-anomaly* the occurrence of two new signals at apparently higher binding energy is a fingerprint of the crossover from the 2D metallic band state at low temperatures to a state with partial localisation of the valence electrons. This state might be spatially inhomogeneous. Close to the *thermal glass-like transition* T_g a third strongly shifted signal occurs which is interpreted as a consequence of sudden total localisation. The breakdown of the metallic state is induced by the structural fluctuations connected with the melting of the frozen disorder of the ethylene endgroups of the ET molecules. At higher temperatures a single-line core-level spectrum with a weak satellite is observed. This first experiment could not clarify all points; in particular the origin of the occurrence of the additional signals must be further elucidated by systematic measurements on similar systems. However, it became clear already from the first results that HAXPES is capable to shine new light into the nature of the Mott transition and related phenomena like the changes in electronic structure at the T*-crossover line.

Discussion of possible extrinsic influences on the core-level spectra

In the beginning, we discuss possible “extrinsic” influences on the observed core-level spectra:

(i) Charging

In XPS on insulating materials the build-up of positive charge on the surface can lead to artefacts in the spectra. If macroscopic charging occurs, the whole spectrum shifts to lower kinetic energies (i.e. apparently higher binding energies) and the features get more and more blurred due to inhomogeneous charge distribution in the light spot. The spectra in Figs. 7.4 and 7.7, however, show clear coexistence of different peaks that exhibit pronounced temperature dependences. Moreover, the main line stays fixed in energy. This, and the fact that all additional signals disappeared at 95 K rules out macroscopic charging as origin of the shifted peaks. However, the results would be compatible with a phase coexistence of

conducting regions with insulating regions that become partially charged. Also, a different behaviour of the near-surface region and the bulk of the material cannot be ruled out from the present measurements

(ii) Radiation damage

Next, we consider whether radiation damage could cause the observed spectral changes. The spectral series in Figs. 7.4 and 7.7 have been taken in the following sequence: The 100 K spectrum and an identical spectrum at 300 K were taken before driving the temperature down to 14 K. Then the sequence with increasing temperature was taken. The spectra at 90 K and 95 K were taken immediately after the 85 K and 87.5 K spectra. This means that the single-peak spectra showing the main line with original intensity were observed at high and low temperatures and before and after taking the full temperature sequence. A further strong indication is a spectrum taken for *D8-Br* at 80 K (Fig. 7.8a). This spectrum was measured for the virgin sample, right upon starting with irradiation. Also, the sequence of the two carbon 1s spectra in Fig. 7.8b was acquired for the deuterated sample without previous irradiation. We thus can rule out sample damage as origin for the observed multiplet features. From other measurements it became clear that sample damage can occur for similar organic species on a timescale of 20 minutes at the given photon flux.

(iii) Possible special behaviour of an individual sample

Pronounced additional signals in the S 2s core-level spectra also occur for the deuterated sample, cf. Fig. 7.8a. The spectral features look different which is to be expected because the two species are located at different regions in the phase diagram. So, the control measurement on *D8-Br* confirmed that the shifted peaks are not a property of an individual sample.

(iv) Phase coexistence of a metallic and an insulating phase

The fact that all spectra show the coexistence of the main line (with reduced intensity) and the additional lines would be compatible with a coexistence of metallic and possible insulating domains on the sample, as was found for the deuterated material in the immediate vicinity of the Mott transition [Sas04b]. For protonated *κ-Br* that is distinctly away from the Mott transition (see phase diagram in Fig. 7.3), the appearance of such a phase coexistence has never been observed and is highly unlikely. It should be stressed, however, that the measurements are compatible with a phase coexistence, either in an ordered way (see below) or in terms of irregular "current paths" that may even fluctuate with time.

The phase diagram

We discuss the results in terms of the amended universal phase diagram of this family of materials shown in Fig. 7.3. In fact, it is the phase diagram of the ET layers under different physical or chemical pressure. The low temperature part of it was already mentioned in section 2.7, but now we have added the temperature region of T*, T_{ins} and T_g, up to temperatures of 90 K. We briefly recall the essential facts: The most prominent feature is the s-shaped first order phase transition line that separates the metallic / superconducting phase from the Mott insulator phase. Characteristic for the low-temperature regime is the proximity of a superconducting and an antiferromagnetic insulating phase. The first-order transition line terminates in a critical end point (black dot). At higher temperatures two crossover lines (denoted by T* and T_{ins}) are evident from experimental results (see below).

Three prominent examples of this class of materials are indicated by vertical thin lines. We studied *κ-(BEDT-TTF)$_2$Cu[N(CN)$_2$]Br* in its *fully protonated* and *deuterated* modifications, abbreviated as *H8-Br* and *D8-Br*. The "chemical pressure" induced by the Br substitution is equivalent to a physical pressure of about 350 bar. Thus, *H8-Br* lies in the region of the *superconductor – metal - anomalous metal* transitions. It shows superconductivity below T_C = 11.6 K and good metallic behaviour above, followed by an anomalous metallic state above the T^*-crossover (dash-dotted line). Full substitution of hydrogen by deuterium reduces the chemical pressure to about 230 bar and brings the material *D8-Br* at ambient pressure into the very interesting region of the s-shaped first order transition between *insulating* and *metallic / superconducting states*. The material with *X = Cu[N(CN)$_2$]Cl* (briefly called *κ-Cl)* lies in the region of the *antiferromagnetic Mott insulator – paramagnetic Mott insulator* transitions. Under pressure, in close proximity of the superconducting state, a quantum spin-liquid phase was found [Shi03].

The quantity W/U is the ratio of bandwidth W to effective on-site Coulomb repulsion U between two electrons on a dimer. The latter is a property of the dimer and is almost independent of the anion or the pressure. The bandwidth (being equivalent to the transfer integral t) is controlled by the dimer separation and can be manipulated by applying pressure (physical or chemical). The ratio W/U is equivalent to pressure; see abscissa of the phase diagram Fig. 7.3. When Coulomb correlations dominate, i.e. at small W/U we find Mott insulator behaviour, like in *κ-Cl*. With increasing W/U there is an insulator-to-superconductor transition or, at temperatures $T > T_c$, an insulator-to-metal transition. Hence the *κ-(ET)$_2$X* family is considered as *bandwidth-controlled Mott-Hubbard system*, in contrast to the *filling-controlled Mott systems* like the high-T_c copper oxide superconductors.

In the *critical end point* the correlation length diverges and fluctuations occur on all length scales, as is well-known for the prominent example of the liquid-gas transition of water. The physics underlying this interesting region in the phase diagram has been discussed in a number of papers [Lef00, Lim03, Fou03, Kag04, Ito96, Kan97, Kin95, Ima98]. In a recent paper of Bartosch et al. [Bar10] the breakdown of the so-called Grüneisen scaling near the critical end point was discussed. In the vicinity of the critical end point, volume changes in response to small changes of temperature or pressure are a "natural consequence of thermodynamics". The paper by Bartosch et al. relies on a purely thermodynamic model. The scaling function does not depend on microscopic details of the underlying system, being described by scale invariance and universality. According to this scaling theory, the anomaly observed in the coefficient of thermal expansion [Sou07] is consistent with the 2D Ising universality class.

The authors introduce "temperature-like" and "pressure-like" scaling variables t and h, respectively (that contain small linear mixing terms). They derive a relation showing that the strongest lattice response *reminiscent of the critical end point* is expected for $\boldsymbol{t \cong 1.74\,|h|^{8/15}}$. The line defined by this condition reaches out to both sides of the critical end point. The observations of a large anomaly in the thermal expansion of *H8-Br* [Lan03], a pronounced dip in the elastic constant of pressurised *κ-Cl* on both sides of the critical end point [Fou03], characteristic changes in the infrared optical reflectance [Sas04a] and a pronounced increase of the low-frequency noise as well as the occurrence of a 3ω-signal in non-linear conductivity measurements [Mue10] are consistent with this prediction.

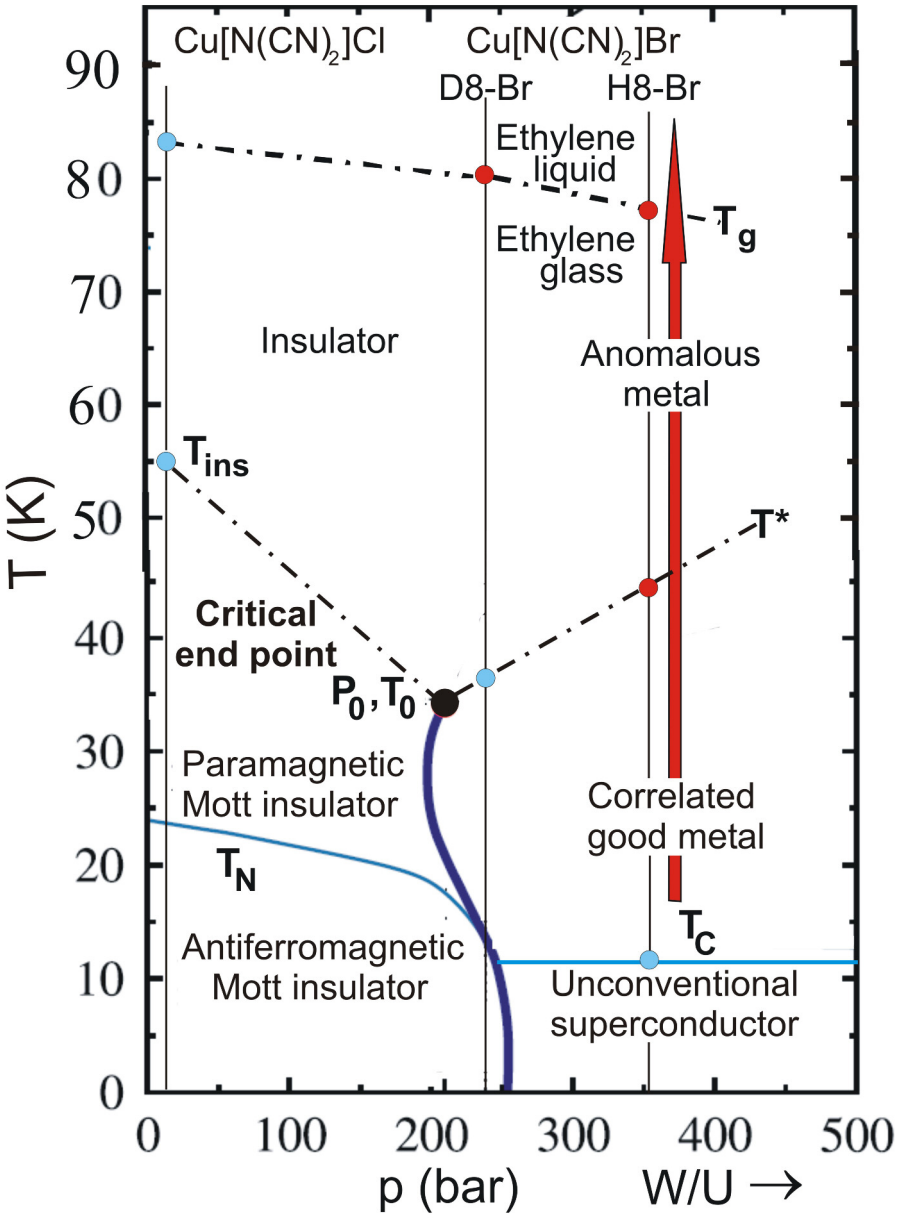

Figure 7.3 T-p phase diagram of the *κ-(ET)$_2$X* family. Three prominent members are denoted on top of the figure and their positions on the p-axis are marked by vertical thin lines. The chemical pressure induced by the ligands places the protonated material *H8-Br* at 350 bar and the fully deuterated *D8-Br* at 230 bar. The red dots denote the present experimental data and the arrow denotes the path of the temperature scan. Pressure is equivalent to the ratio of bandwidth of conduction band W and effective Coulomb repulsion U. Blue dots and lines represent literature results.

Upon approaching the critical end point, the thermal expansivity is more singular than the specific heat, which means that the Grüneisen ratio diverges. The important fact for the present measurements is that *large lattice effects can be expected to reach out way from the critical end point along the lines defined by the mentioned condition.*

The above-mentioned theoretical *t-h condition* yields 40 K for *κ-Br* and thus lies close to the T* crossover observed experimentally and close to the onset temperature of the core-level satellites. The precision of our temperature measurement is estimated to ±3 K. Although Bartosch et al. [Bar10] do not explicitly state this, it is near at hand that the phenomenologically known T* crossover line is identical to the theoretically predicted line given by the above *t-h condition* and also to the onset temperature of our shifted sulphur 2s core-level signals.

Core-level spectra for hydrogenated κ-Br

In the following we present and discuss the HAXPES spectra taken for *hydrogenated κ-Br* in the region between 14 K and room temperature. The red arrow in Fig. 7.3 denotes the path of the temperature scan followed by our experiment. The superconducting regime could not be reached by the existing sample cryostat at the HAXPES beamline at PETRA III.

The changes in the core-level spectra reveal several regimes:

(i) *Regime of coherent transport below the T* anomaly.*

Fig. 7.4 shows a series of sulphur 2s spectra in the region around the T* transition. Between 14 and 40 K all spectra are identical (see two lowest spectra) and exhibit an intense single line. In the following we will call it the ***main line***.

In this region of the phase diagram, we find coherent transport, i.e. *itinerant electron behaviour*. The valence electrons are delocalised as Bloch-waves in the 2D conduction band. This reflects itself in good metallic-like conductivity (a compilation of various experimental results is shown in Fig. 7.12; (d) shows the resistivity). Further, a weak electron-molecular vibration coupling on the $\nu_3(a_g)$ vibration mode of the ET-molecules is observed in infrared optical reflectance spectroscopy [Sas04a]. This region below the T* anomaly is therefore referred to as *correlated good metal*. From the two highest occupied valence orbitals (HOMO and HOMO-1) of the dimers three electrons are delocalised in the conduction band and the fourth resides in the counterion layer. Due to the electron-electron interaction this regime is also referred to as *Fermi liquid phase* or *correlated good metal*.

For a good metal with electrons delocalised in Bloch states, a single core-level line is expected, as known for classical metals. The core hole is screened by the itinerant conduction electrons as depicted in Fig. 7.5. This, in turn, leads to a reduction of Coulomb attraction and thus to an energy gain of the photoelectrons. In the present material the screening will affect the electron energy rather weakly, because of the small charge density. For a typical *κ-(ET)$_2$X* salt the charge density is only $n \approx 10^{21}$ cm^{-3}, being almost 2 orders of magnitude smaller than in copper ($8 \cdot 10^{22}$ cm^{-3}).

The fact that the single-line spectrum persists for temperatures between 14 and 40 K is very important because it implies that at low temperature the Bloch-wave like band state is neither very sensitive on a possible static molecular disorder being induced by the frozen ethylene endgroups (see below) nor on the dynamic thermal disorder.

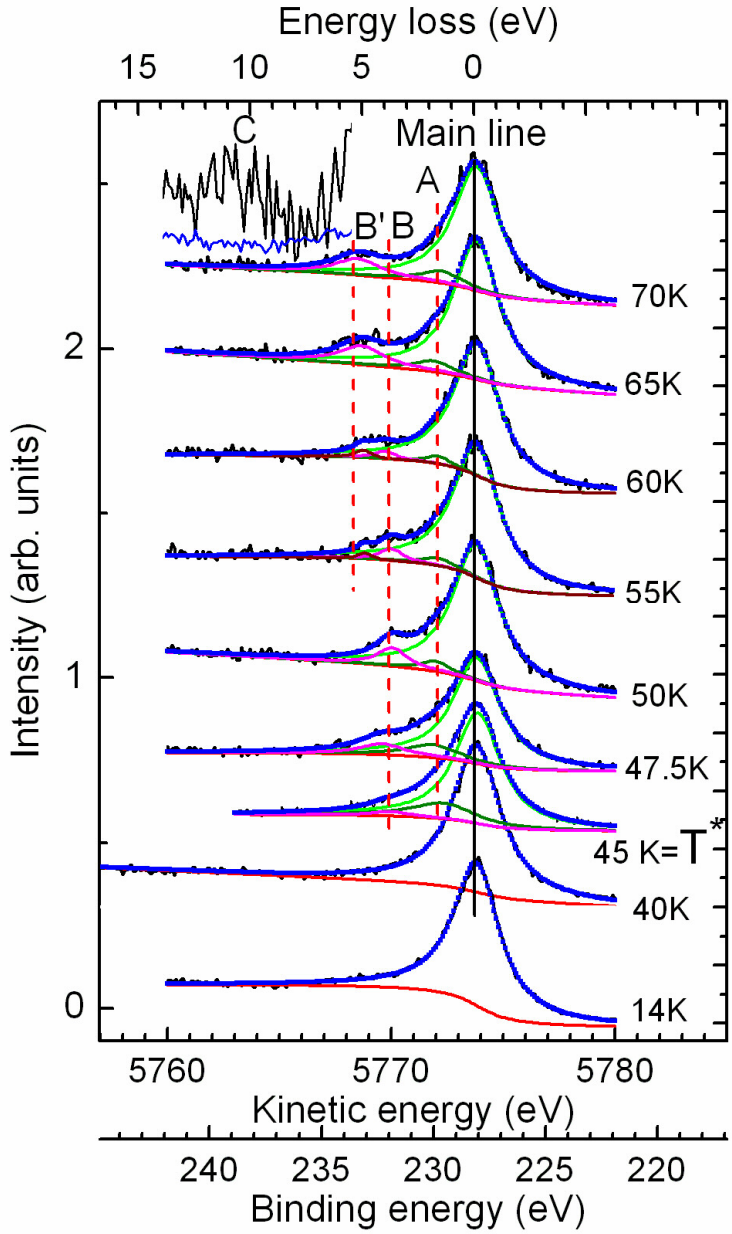

Figure 7.4 Temperature series of sulphur 2s HAXPES core level spectra for the CT complex *κ-(BEDT-TTF)$_2$Cu[N(CN)$_2$]Br* (fully protonated *H8-Br*). The series was taken in the region near to the T*-anomaly during slow warming-up after rapid cooling-down to 14 K. The thin lines below each spectrum show the results of the multi-peak fit routine, the blue line shows their sum. The fits for 14 and 40 K yield a single line (blue line) that coincides exactly with the spectrum (black line). A, B and B' mark the shifted signals, the enhanced part of the 70 K spectrum denotes the weak signal C. The blue line below C shows the corresponding region of the 14K spectrum, for comparison. Spectra were taken at *hν* = 6001.9 eV at PETRA III, Hamburg (energy resolution 440 meV).

With increasing temperature the phonon system is more and more activated. There are 708 phonon branches, 576 internal modes of the ET molecules and 132 low frequency

translational and librational intermolecular modes. With increasing temperature this multitude of possible vibronic excitations is gradually activated, causing strongly increasing scattering probabilities. The conductivity of κ-Br drops strongly from 10^3 $(\Omega\ cm)^{-1}$ in the good metal regime right above T_c (at 12 K) to 10^2 $(\Omega\ cm)^{-1}$ at 30 K and further to 7 $(\Omega\ cm)^{-1}$ in the bad metal regime at 60 K [Yuw91]. In comparison, the value for Cu metal is $6 \cdot 10^5$ $(\Omega\ cm)^{-1}$. The reason is that due to electron-phonon interaction the Drude relaxation time τ drops strongly within this temperature interval. These numbers give a feeling that the low-temperature state of coherent transport is very fragile. We may speculate that coherent transport may break down at elevated temperatures.

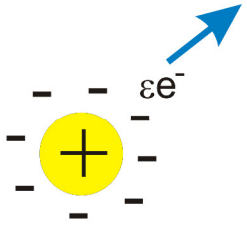

Figure 7.5 Schematic illustration of the screening of the core hole by the itinerant electrons in the *good-metal* regime.

(ii) ***Anomalous metal regime above T****

At 45 K (i.e. at or close to the T*-crossover line), the sulphur 2s line suddenly drops in intensity and a shoulder occurs on the high-binding-energy side of the main line, cf. Fig. 7.4. A least-squares multipeak fit routine reveals two new signals A and B, being separated by about 2 eV and 4 eV from the main line. A third line B' at about 6eV occurs at temperatures above 55K. In the following we will call these additional signals ***satellite lines***. It should be mentioned right at the beginning that it is not clear from the present results whether these lines originate from electronic shake-up processes or if they represent a shifted main line originating from certain regions on the sample. Their precise locations and intensities are determined by the fit routine. The partial spectra are shown as thin lines. The resulting positions (centres of the best-fit Gaussian peaks) and intensities (their areas) are plotted in Fig. 7.6 as function of temperature. The onset temperature of the satellites is identical with the temperature, where also the metallic-like behaviour of the conductivity curve changes [Toy07], visible in the abrupt change of slope, see dR/dT curve in Fig. 7.12d. With increasing temperature the spectral weight of the satellites changes significantly, their maxima are marked by vertical bars: A shows its maximum right at the onset temperature (45K) B shows its maximum at 50K and B' appears at 55 K and shows its maximum at 75K. Above 50K a weak fourth satellite C occurs at a large shift of about 10eV, see enlarged detail in the 70K spectrum. This satellite gains strongly in intensity at 80K as discussed in the next section. All satellites are completely absent in the good metal range at 40K and below. The blue curve below satellite C displays the corresponding enlarged detail of the 14K spectrum, proving the absence of C. All satellites exhibit pronounced intensity variations, but the total spectral weight is constant because it reflects the total number of S 2s electrons. The drop in the main-line intensity thus mirrors the sum of the intensities of the satellites. We note that between 45 and 70 K the drop of the main-line intensity is constant within the error of the fit procedure (see representative error bar at 40K).

In the following we will propose a model explanation where the satellite lines in the core-level spectra above T^* are discussed as a direct spectroscopic *fingerprint of localised electrons at the dimer sites.* The appearance of satellites is well known in core-level spectroscopy and we briefly recall the essential facts. For a closed-shell system or a system

with itinerant electrons photoemission from an s-like core level can lead only to a single final state configuration in the photoemission transition, because the valence shell stays unaffected. In a metal, the itinerant electrons (delocalised in Bloch waves) do not couple to the core hole. No shake-up into a band state occurs. The single-line spectrum at T $\leq$ 40 K is thus the signature of the metallic-band regime.

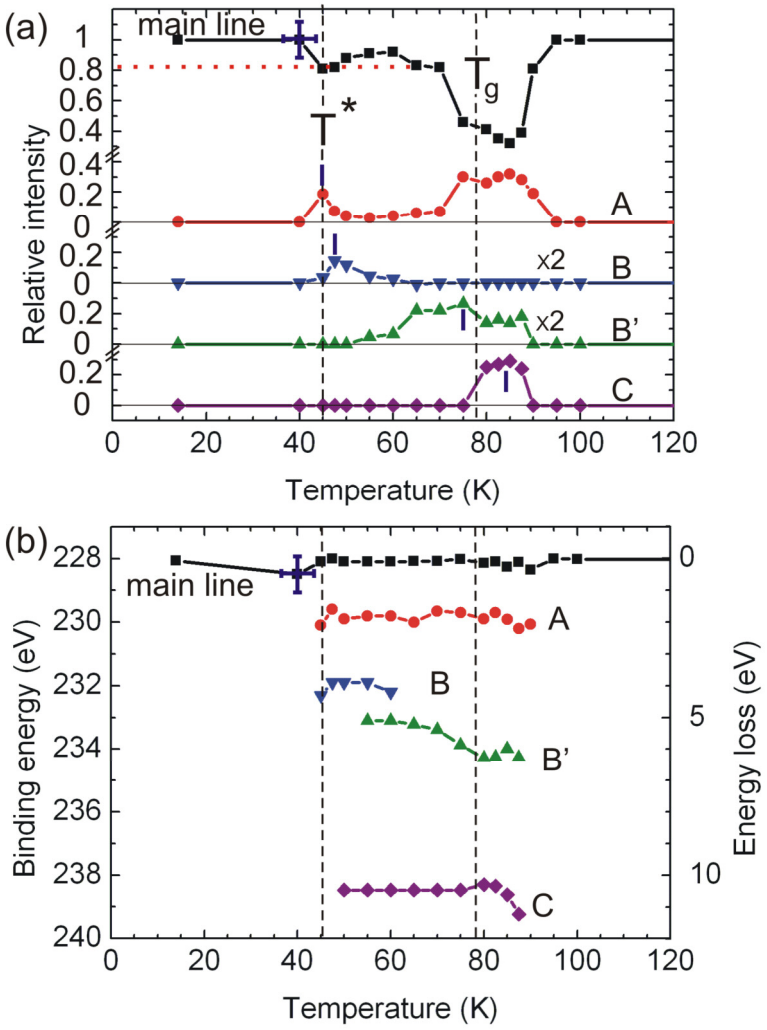

Figure 7.6 Temperature dependence of sulphur 2s HAXPES peak intensities (a) and peak positions (b) for *κ-(BEDT-TTF)$_2$Cu[N(CN)$_2$]Br* measured in a warming-up series starting at 14 K. Values are extracted by a multi-peak fit routine from the series of spectra shown in Figs. 7.4 and 7.7, intensities (integrals under the fit curves) are measured relative to the intensity of the main line at 100 K. Typical error bars are shown at the 40 K points. T* and T_g denote the onset temperature of the anomalous metallic state and the thermal glass-like transition temperature, respectively. Note that shifted lines A and B instantaneously occur at T*, B' rises gradually between 55 and 65 K and C is very weak below 70K and instantaneously becomes intense at T_g. Between 50 and 75K signal C has an intensity of only 0.02, which is not visible on this intensity scale. The maxima of the peaks are marked by vertical bars. The dotted horizontal line in (a) marks an intensity value of 0.83, corresponding to localisation in 1/3 of the dimer sites.

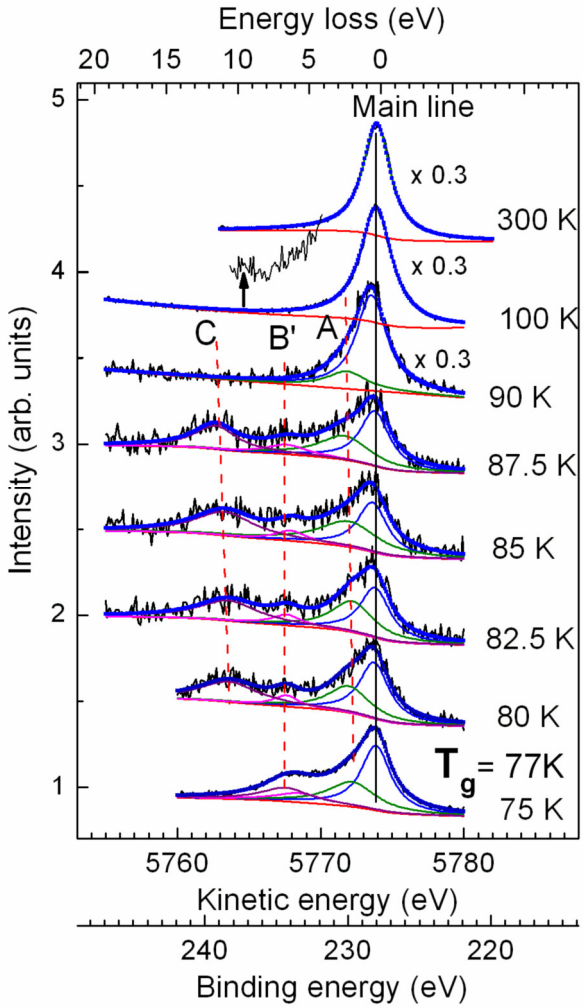

Figure 7.7 Temperature series of sulphur 2s HAXPES core level spectra for the CT complex *κ-(BEDT-TTF)$_2$Cu[N(CN)$_2$]Br (*fully protonated *H8-Br)*. The series was taken in the region near to the thermal glass-like transition temperature T_g during slow warming-up after rapid cooling-down to 14 K. The thin lines below each spectrum show the results of the multi-peak fit routine. The arrow on the magnified part of the 100K spectrum denotes the small remaining feature at higher temperatures. Spectra were taken at *hν* = 6001.9 eV at PETRA III, Hamburg (energy resolution 440 meV).

However for open-shell systems with localised electrons we find additional final state terms, where the configuration of the valence shell has changed by exciting one additional electron into an open shell. This process was extensively discussed and studied for systems with open d-shells [Sta10, Gro01]. The filling of the hole in the valence shell is not a secondary process (like an Auger transition) but it happens instantaneously within the time of the phototransition. Precondition is that the "ligand orbital" being involved (i.e. the orbital from which the shake-up electron originates) has a non-vanishing amplitude in the region where the core-level wavefunction is localised. Then configuration interaction leads to additional final states with an added electron in the valence orbital and a hole in the ligand orbital (also termed *shake-up process*). This filling of the hole in the valence shell costs energy, because

an electron needs to be lifted into the formerly unoccupied state. Thus part of the primary photon energy is needed for this shake-up process, leading to a lower kinetic energy (i.e. higher apparent binding energy), like observed in our experiment. We note that the energy shift of the satellites does not reflect a higher binding energy in the initial state (like a chemical shift) but a *final state effect* including rearrangement of electrons in the valence region. In this respect, core level spectroscopy gives information on the valence region as well.

(iii) *Regime of the thermal glass-like transition around T_g*

When the thermal glass-like transition temperature T_g is approached, the situation changes dramatically, see series of spectra in Fig. 7.7. The main-line intensity drops to roughly half of its initial intensity, the intensity of satellite A increases by a factor of three and the third, strongly shifted signal C at about 10 eV suddenly gains strongly in intensity. C has about the same intensity as A in this region, B' is somewhat weaker. Finally, between 90 and 95 K all satellites disappear and the main line intensity is restored to its initial value.

We briefly recall the nature of the thermal glass-like transition [Mue02]. The ethylene endgroups as most deformable part of the ET molecules can show two different conformations, i.e. eclipsed (with the outer C-C bonds being parallel) or staggered (with the C-C bonds being canted). At high temperatures the end groups are completely disordered due to the strong thermal vibrations. Upon cooling, however, they adopt one of the two possible conformations and the system undergoes a glass transition into a metastable state, away from the thermodynamic equilibrium. In particular for rapid cooling thermodynamic equilibrium cannot establish in this conformational degree of freedom and a *short-range structural disorder* becomes frozen in at the glass temperature T_g. This has a marked effect on the thermal expansion coefficient and lattice constants, see Fig. 7.12b and c, respectively. We will see later, however, that the melting of the ethylene group disorder might *trigger an electronic effect* that may have a large contribution to the behaviour of the lattice. The degree of frozen-in disorder depends on the cooling rate. We assume that due to our fast cooling of 300 K per hour we might have induced a higher degree of disorder than the value found in a high-resolution diffraction experiment by Wolter et al. [Wol07]. For 100 K these authors reported about 90 % of the eclipsed form.

(iv) *The high-temperature regime*

It is characteristic for a glass-like transition that it spans a certain temperature interval. If we take the width of the hysteresis observed between cooling curve and heating curve in Fig. 7.12b as measure, we find that the freezing-in or melting happens in an interval of about 15 K, being centred around T_g. During this interval the system establishes thermodynamic equilibrium. The conformational transitions of the ethylene endgroups become gradually activated leading at the end to the ethylene liquid state in the phase diagram, Fig. 7.3. The hysteretic jump in the thermal expansion coefficient comes along with a cusp-like maximum in the lattice constant perpendicular to the ET layer as well as an abrupt change of slope in the lattice constant along one in-plane axis (see Fig. 7.12b and c). The width of the melting-freezing hysteresis is in fairly good agreement with the temperature interval where satellite A is strongly enhanced and satellite C occurs, compare Figs. 7.12a and b. As mentioned before, the exact width and location of this region depends on the thermal history [Mue02].

Owing to the thermally activated conformational transitions an average geometry will establish within the whole ET layer. This thermally-averaged uniform state comes along

with a *single-line core-level spectrum* which persists up to room temperature. Below we will propose a tentative explanation for this behaviour.

Core-level spectra for fully deuterated D8-Br

For comparison and to verify the phenomenon for a second sample, a few spectra have been taken from the deuterated *D8-Br* sample, mounted on the same holder as *H8-Br*. A spectrum of *D8-Br* was taken at 80 K in exactly the same setting as the 80 K spectrum of *H8-Br*. The result of the comparison is shown in Fig. 7.8a.

A satellite structure occurs as well. It is quantitatively different, because *D8-Br* is located in a different region of the phase diagram, Fig. 7.3. Unfortunately, the limited time in this first beamtime did not allow systematic measurements on *D8-Br*. The high intensity at the left-hand cutoff points on a multiplet spectrum over a wide energy range. On the pressure scale of the phase diagram, *D8-Br* is located at the critical endpoint. The fluctuations can thus be expected to be higher than in *H8-Br*.

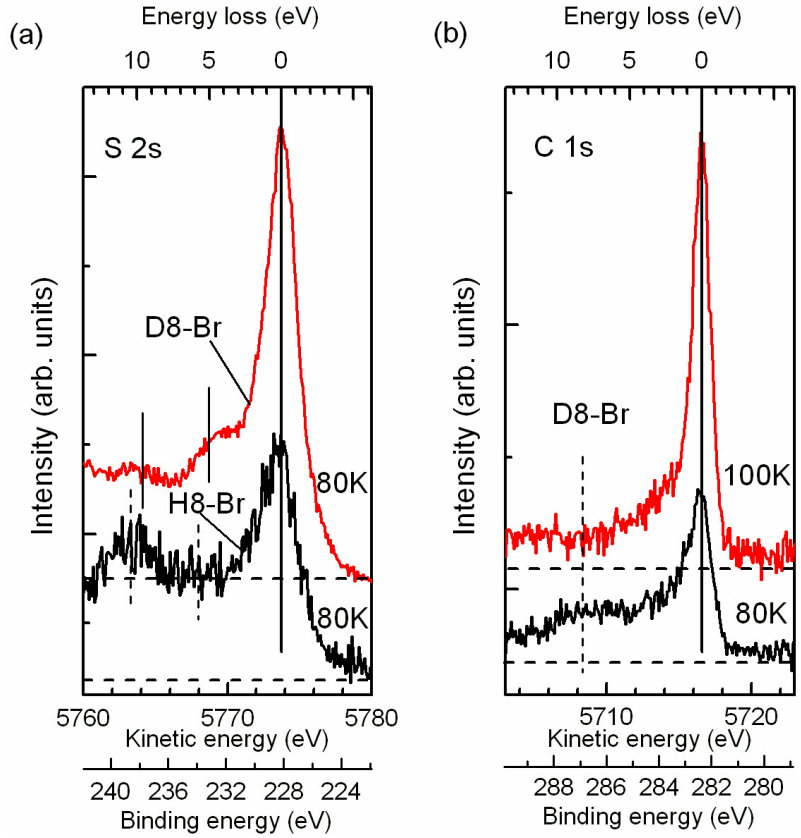

Figure 7.8 (a) Comparison of sulphur 2s HAXPES spectra for the *fully deuterated* material *D8-Br* and the *protonated* material *H8-Br*, both taken at the same temperature of 80 K under identical conditions. (b) Carbon 1s HAXPES spectra of *D8-Br* taken in the temperature region of the anomalies (80 K spectrum) and above that region (100 K spectrum) under identical conditions.

Finally, for the *D8-Br* sample a measurement at the carbon 1s core level has been performed, shown in Fig. 7.8b. At 100 K the carbon 1s spectrum shows a single line, whereas at 80 K a drop of the main-line intensity occurs and an additional shifted core-level

signal appears, too. This gives evidence that satellite signals are not a specific phenomenon of sulphur, but carbon is affected in a similar way. This is to be expected, because the wavefunction of the π-electrons in the valence shell has a non-vanishing amplitude at the carbon 1s core-hole as well. Quantitatively, however, the situation is more complicated than for sulphur, because carbon is also contained in the polymeric anion layer.

Electronic structure of ET monomer, ET dimer and κ-phase

In the next two sections we discuss the core-level spectra in the context of existing literature results for various other quantities and propose a model that explains all observations. First we will have a closer look at the electronic structure of the *ET monomer* and *dimer* and the *κ-(ET)$_2$X* organic solid.

Given our local spectroscopic probe at the sulphur 2s core level, the electronic structure of a *single sulphur atom in the ring system of the ET-molecule* must bear the key for understanding the peculiar behavior of the core-level spectra. In the ET molecules the sulphur atoms have the same structure as in thiophene: a total of 6 valence electrons (S [$3s^2p^4$]), 4 of which are in an sp^2-hybrid wavefunction. The adjacent carbon atoms have 2 electrons less (C [$3s^2p^2$]). For both atoms 2 electrons are in the sp^2-lobes forming the covalent bond to the neighboring ring atoms. The outward-pointing sp^2-lobe of sulphur contains a lone-pair, whereas for carbon the C-H bond contains 2 electrons (like in benzene). So far the situation is quite similar for sulphur and carbon: the sp^2-wavefunction is fully occupied with 6 paired electrons (for carbon it needs the H-atom to donate an electron, for sulphur not). However, for the remaining p_z-orbital forming the aromatic π-system we find a striking difference: For sulphur 2 electrons are in the p_z-orbital, for carbon only one! In other words, the *S-atoms in the ring system constitute a closed shell system* with paired electrons in all orbitals (S [$(sp^2)^2\ p_z^2$]), whereas carbon has an unpaired electron in p_z (C [$(sp^2)^2\ p_z$]). In both cases we have added the electrons from the nearest neighbors in the sp^2 orbitals. In benzene the unpaired electrons lead to the fact that the π-electrons are delocalized over the ring. Each sulphur atom, however, has a lone pair in its π-orbital perpendicular to the ring plane (denoted [p_z^2]).

This difference in occupation number is an important ingredient for understanding the core-level spectra. The structure of the highest occupied molecular orbital of the ET monomer *HOMO$_M$* (the index serves for distinction from the dimer orbitals defined below) is shown in Fig. 7.9a. This is the orbital that is responsible for the outstanding electronic properties of the *κ-(ET)$_2$X* family. The *HOMO$_M$* has π-symmetry, but unlike benzene there are nodal planes between all sulphur atoms and their neighbours. The wavefunction at the carbon sites shows the pairing of the two p_z electrons in a lobe delocalised over the two neighboring carbon atoms. The *HOMO$_M$* wavefunction amplitude is maximal at the inner four sulphur atoms S_i and much smaller at the four outer ones S_o.

When two ET monomers approach each other with parallel molecular planes, the two *HOMO$_M$* orbitals overlap and form two dimer orbitals. These are split by almost half an eV. In molecular terminology we call the *higher-lying, antibonding orbital HOMO* and the *lower-lying bonding orbital HOMO-1*. Each of these can accommodate two electrons.

In the organic solid several new phenomena come into play. In the stacking motif of *κ-(ET)$_2$X* the ET dimers are the basic building blocks occupying an anisotropic triangular lattice, see Fig. 7.9b and c. The bonding situation is quantified in terms of the transfer

integrals (transfer energies) that are a direct measure of the overlap of the molecular orbitals between neighbouring molecules. According to quantum chemical calculations (see [Toy07] and references therein) the intradimer-transfer integrals are more than twice as large as the interdimer-transfer integrals (overlap of molecular orbitals of the adjacent dimers). More recent work yielded even a factor of three, i.e. values of 150 meV and 50 meV for the intra- and interdimer transfer energies, respectively [Jes11]. Consequently, the bonding and antibonding frontier orbitals of the dimer are the entities relevant for the electronic transport properties. The separation of these two orbitals is approximately twice the intradimer-transfer energy, for *κ-Br* separation values of 0.47 eV [Kom96, For97] have been reported. Due to this large separation, a mixing of the two orbitals can be neglected.

The *κ*-phase is a layered structure where the *HOMO* and *HOMO-1* of neighbouring dimers overlap and, due to the periodicity of the lattice, the electronic states develop into two bands. In an extended Hückel-type tight binding calculation (neglecting electron correlations), a 2D bandstructure is derived with the lower bonding and upper anti-bonding band showing opposite dispersion as schematically sketched in Fig. 7.10a.

The donor-acceptor ratio is 2:1, i.e. each dimer transfers one electron to the acceptor layer X. This leads to the scenario that the *HOMO-1* derived band is filled and the *HOMO* derived band is half filled. In terms of the simple, single-electron picture which neglects electron-electron interactions, the partly filled conduction band should be associated with *metallic behaviour*. This is, however, in contrast to the observations, yielding a *variety of different ground states* as discussed in terms of the phase diagram, Fig. 7.3. In order to understand the diversity of phases in this class of materials, the joint and partly competing effects of strong electron-electron Coulomb repulsion, low dimensionality and the strong electron-phonon coupling have to be taken into account. We will return to that point below.

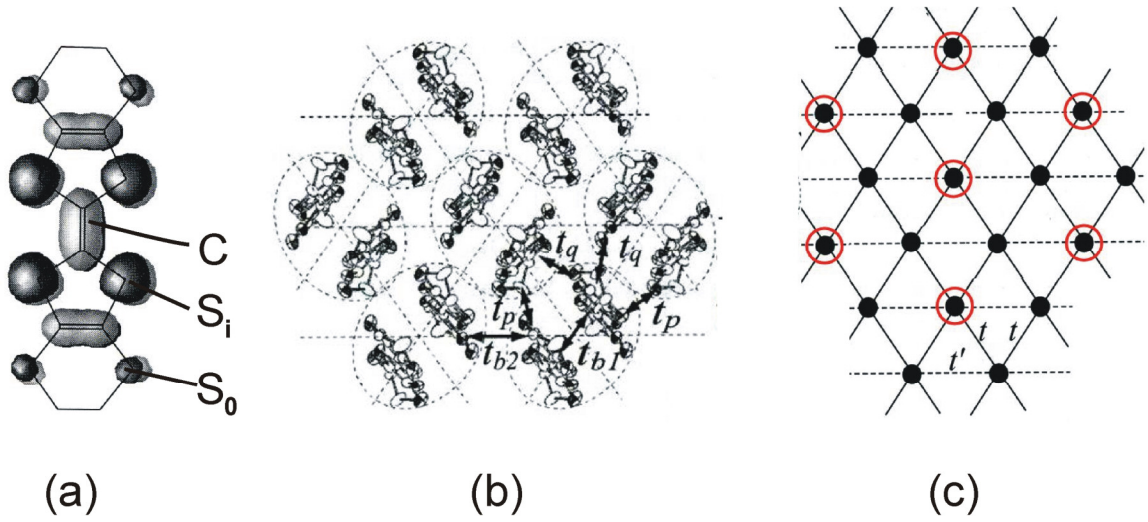

Figure 7.9 (a) HOMO$_M$ of an isolated ET molecule; C, S$_i$ and S$_o$ denote carbon, inner and outer sulphur atoms, respectively. (b) Arrangement of ET molecules in the *κ*-phase stacking motif. (c) Schematic sketch of the triangular lattice with the possible (√3x√3)-R30° commensurate superstructure denoted by circles (after [Toy07]).

Discussion and proposal of a model

In the following we will propose a model that describes all experimental results consistently and is also in accordance with all literature data. As mentioned in the introduction to this chapter, the origin of the satellite peaks cannot be deduced unambiguously from these few measurements of our first HAXPES beamtime. Alternative explanations like a spatially inhomogeneous system with maybe partially charging nanodomains must be investigated by future systematic measurements.

Sulphur 2s and carbon 1s HAXPES provides a local spectroscopic probe right at the building block which is responsible for the exceptional electronic properties of this material. The *characteristic time scale* for the photoemission process can be estimated from the natural line width of a core level, for the given case ca. $\Delta E \approx 2$ eV. The uncertainty relation then yields $\Delta\tau \approx 5 \cdot 10^{-16}$ s. For X-ray absorption it is often argued that the excitation takes place in the period which the photon needs to cross the diameter of the inner shell, yielding an even shorter characteristic time in the order of 10^{-17} s [Sto92]. Both values are very short in comparison with characteristic times of vibrations or fluctuations of the lattice and also short in comparison with the intra-dimer and inter-dimer hopping rates.

Core-level spectroscopy provides a "snapshot" of the electronic configuration in the instant of the photoemission process. We thus expect to observe different fingerprints of the electronic structure if we could measure isolated ET monomers, isolated dimers or the 2D crystalline κ-phase. The surprising fact is that *in κ-Br all three signatures occur as functions of temperature*, as we will explain and discuss in the following.

The central idea of our proposed model is that for open shell systems core-level spectroscopy yields information on the electronic configuration in the valence region. The occurrence of higher-binding-energy satellites is direct evidence of *configuration interaction of the core-hole with valence electrons,* leading to a rearrangement of electrons in the valence shell. For open d-shell systems core-level satellites have been subject to extensive investigations. Multiplet structures can be calculated by program codes, see e.g. [Sta10]. Unfortunately, existing codes up to now do not include partially occupied π-orbitals. Despite of the missing quantitative treatment for π-systems, we can base our interpretation on the analogy with the well-understood situation in open d-shells.

There are several different ways how the localisation can start and progress. One main question is whether a dimer where electrons are localised is fully occupied by three electrons or only by one electron. Fig. 7.10 shows six electronic situations of the dimers, differing in the occupation number of electrons localised in the frontier orbitals. We start with the situation in the *good metal regime (i),* then consider the *effects of partial localisation*, step by step with increasing occupation numbers *(ii–v),* then discuss evidence for a *complete collapse of coherent transport* and finally a possible *quenching of the dimer orbitals*, leading to localisation in the lone-pair p_z-orbitals of the sulphur atoms of *individual monomers (vi)*. The latter proposal is speculative and has to be confirmed by further experiments in the future.

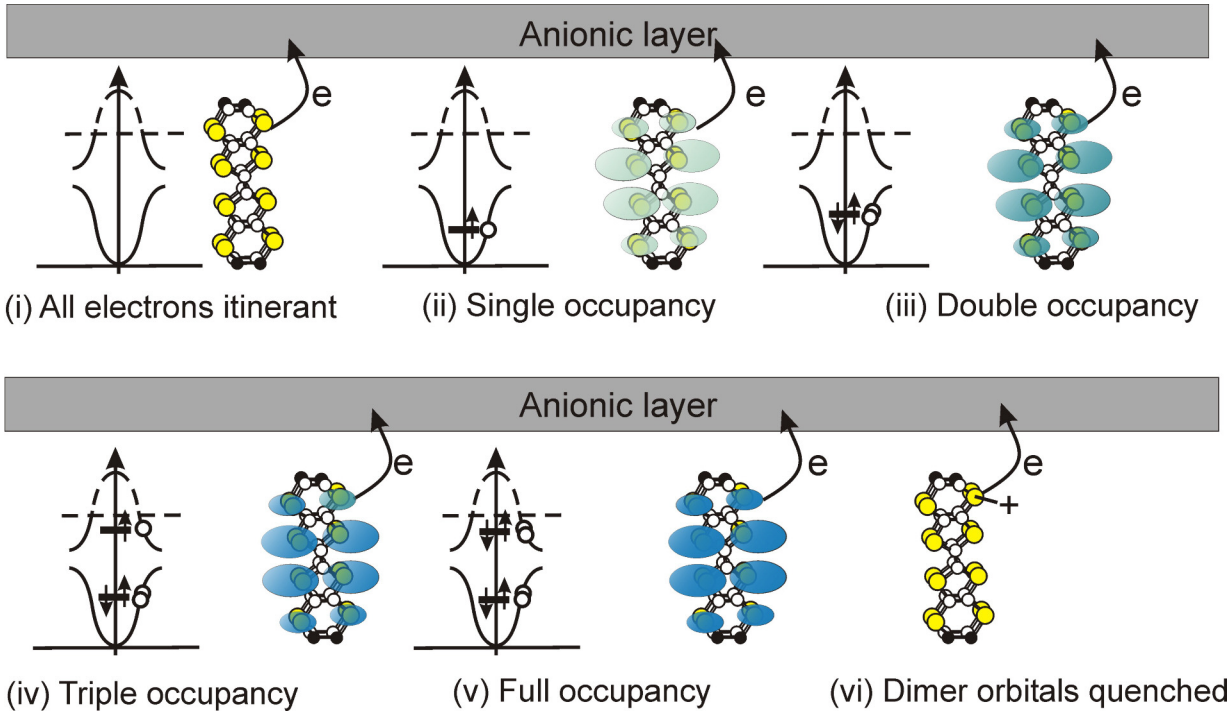

Figure 7.10 Different electronic configurations of the ET-dimers in *κ-Br*. One electron is always donated to the anionic layer, but different numbers of electrons are localised on the dimers. (*i*) *Good metal regime* with all electrons delocalised in Bloch-waves. (*ii, iii*) Scenarios in the range of the *T* anomaly* with single and double occupancy of *HOMO-1*. (*iv, v*) Additional single and double occupancy of *HOMO*, occurring after complete localisation close to the *glass-like transition temperature* T_g. (*vi*) Localisation of the hole on one individual S-atom after possible breakdown of the dimer orbitals. Note that we use the notation *HOMO* and *HOMO-1* from the neutral ET molecule also when these orbitals are unoccupied .

(i) Regime of coherent transport

All three valence electrons of each dimer are in the itinerant band state (Bloch state), as depicted in Fig. 7.10*i*. For simplicity we have drawn Hückel-type tight binding bands (being aware that these cannot describe the correlated system properly). Itinerant electrons in band states cannot couple to the core hole, created in the photoemission process. The core hole does not attract electrons in the wave-state of an itinerant band. All dimer sites contribute to the band and none hosts localised electrons. The spectroscopic signature of this uniform state is the *unshifted main line*. Due to our limited energy resolution we cannot resolve a possible quasiparticle peak in the gap between the upper and lower band. Such a behaviour would be expected for the proposed *pseudogap phase* at low temperatures above T_c [Ich06, Ich08].

In the region of coherent transport the thermal expansion coefficient [Sou07] increases strongly with temperature, see Fig. 7.12b. The lattice expands as a consequence of the increasing thermal excitation of phonon modes. In turn, the transfer integrals (that are also a measure of the kinetic energy) are gradually reduced, whereas the Coulomb energy U stays constant. It means, when we approach the T* crossover line from temperatures below, we encounter the same scenario as if we would approach the first-order Mott transition line (s-

shaped line in Fig. 7.3) from the high-pressure side. The remarkable fact is that we can cross this line by simply rising the temperature. The configuration with minimal energy more and more becomes in favour of localised electrons in the dimer orbitals instead of a electrons delocalised in Bloch-waves. The question is at this point: How does the electronic system respond on this rising tendency for localisation (increasing "localisation pressure")?

***(ii)* T* crossover**

When crossing the T*-line partial localisation sets in. The core-level spectra give evidence of two important facts: The localisation happens instantaneously for many dimer sites, because the drop in main-line intensity and appearance of satellites A and B is not gradual but step-like, cf. Fig. 7.6. Second, they give evidence that at first the lowest valence orbital *HOMO-1 of a certain number of dimer sites is occupied by an unpaired electron* (denoted by the bar in Fig. 7.10*ii*). The dimers where this has happened no longer participate in the band state. Due to the single occupancy vacancies in their valence orbitals exist that allow for the excitation of *shake-up satellites* through configuration interaction with the S 2s core hole. These shake-up transitions are schematically sketched in Fig. 7.11*ii*. The electron in the *bonding HOMO-1* leads to a *contraction* of the dimer.

The unpaired electrons give rise to *strong spin fluctuations*, visible in the strongly rising muon spin relaxation rate [Lan11] at T*, and to a strong increase of 1/f noise in fluctuation spectroscopy, cf. Fig. 7.12f and g. The fact that the drop in main-line intensity stays fixed at 84% (dotted line in Fig. 7.6a) in a large temperature interval up to 70K could be a hint on an *ordered superstructure* (see below).

***(iii)* Anomalous metal regime**

With increasing temperature the core-level spectra give evidence of increasing *double occupancy of the HOMO-1*. Given the sensitivity of our experiment, we see the corresponding signature clearly above 55K. Double occupancy is being paid for by Coulomb energy, so the system first prefers only one unpaired electron in *HOMO-1*. In Fig. 7.6 satellite B (shake-up into the *HOMO-1;* downward triangles in upper panel) has its maximum right at the onset of localisation at 45K and fades out when *HOMO-1* becomes more and more double-occupied. In turn, satellite B is replaced by satellite B', i.e. shake-up into the *HOMO* (upward triangles in Fig. 7.6), transition see Fig. 7.11*iii*. At about 55 K the intensities of B and B' are identical and at 65 K the single-occupancy signature peak (B) has disappeared.

The sum of intensities of B and B' remains constant, giving evidence that the number of dimer sites that has left the coherent transport state does not increase, again pointing on a non-statistical pattern. The coherent band state persists during this range, because its signature, the main line, remais strong in intensity. Two electrons in the *HOMO-1* lead to a *further contraction* of the dimer. The increasing occupation of the bonding *HOMO-1* counteracts the increase of thermal expansion caused by phonon excitation. Nevertheless the "localisation pressure" increases in this regime because the lattice gradually expands.

***(iv)* Collapse of the band state of coherent transport**

At about 8K below T_g we observe a dramatic drop of the main line intensity and a strong increase of the satellite lines A and C. We interpret this sudden change in terms of an *instantaneous collapse of the coherent band state with the electronic system being driven into complete localisation*.. The conduction electrons loose their wave nature and all electrons become localised at the dimer sites. The reason is most likely the onset of the

conformational transitions of the ethylene endgroups. However, it could as well be that the "localisation pressure" finally reaches a level where the energy gain by total localisation is the driving mechanism. The relatively weak interdimer transfer integral (50 meV) is not stable against these thermally induced fluctuations. Now the electrons from the collapsing bands have to occupy the energetically unfavourable upper orbital *HOMO* (upper bar in Fig. 7.10*iv*). as well, because not enough lower-lying states are available. Like in (*ii*) the unpaired electrons in *HOMO* give rise to strong spin fluctuations visible in a further increase in the 1/f noise and the muon spin relaxation rate [Lan11], Fig. 7.12f and g.

An eye-catching spectroscopic fingerprint of this complete localisation on the frontier orbitals of the dimers is the strong intensity gain of satellite C, being shifted by as much as 10eV, see Figs. 7.7 and 7.6. We tentatively attribute it to the shake-up into the lowest unoccupied molecular orbital *LUMO*, see Fig. 7.11*iv,* being the next available free orbital after the *HOMO* is occupied. We assume that at lower temperatures the *LUMO* forms an empty band state as well, so that it does not serve as final state for a shake-up. It seems to be the rule that the shake-up always occupies the nearest available vacant states, most likely due to energetic reasons. E.g., the B'-channel opens when the *HOMO-1* is occupied. The increase of the intensity of satellite A suggests that another transition might be involved as well. However, without numerical calculation we cannot clarify which further shake-up channel is involved.

Now electrons occupy the anti-bonding *HOMO*, leading to an *expansion* of the dimer. We may speculate that this gives a contribution - besides the melting of the endgroups - to the strong rise of the thermal expansion coefficient at this temperature [Sou07], Fig. 7.12b. This energetically unfavourable configuration can be avoided by the system in the range of the T* anomaly, i.e. here the electrons occupy only the lower-lying binding orbital. But 1/3 of the electrons have to occupy the upper orbital, when the metallic band state breaks down.

***(v)* Regime of hopping-transport between the HOMO of the dimers**

After breakdown of the band state, hopping transport leads to *some dimers with full occupancy* as sketched in Fig. 7.10*v*. The number of sites with full occupation will be relatively small, because the Coulomb energy has to be paid for double occupancy of the upper orbital in the Hubbard description; for *κ-Br* we have U ≈ 300 meV [Jes11]. Due to their low concentration, we will not see the spectroscopic fingerprint of double occupation in the spectra.

It is remarkable that the conductivity does not react stronger on the dramatic change of electronic structure. It means that hopping conductivity above the band collapse is quantitatively similar to the thermally distorted band conductivity below. This may be explained assuming that the mean free path of the band electrons finally reaches the interdimer distance. At this point the strongly distorted band conductivity with high Drude relaxation rate is equivalent to interdimer hopping. Spectroscopically, however, there is a dramatic difference between band electrons (even with small mean free paths) and localised electrons (that dwell on the dimer sites).

***(vi)* Ethylene-liquid regime above T_g**

Here we face the surprising fact that all satellites disappear instantaneously between 90 and 95K and also the spin fluctuations suddenly drop strongly, see Fig. 7.12g. A possible explanation for the disappearance of core-level satellites and spin fluctuations might be that *the dimer orbitals are quenched and the electrons find themselves in the $HOMO_M$ of*

individual monomers. This happens at higher temperature than the collapse of the metallic band, because the intradimer transfer energy is 150 meV, i.e. three times larger than the interdimer transfer energy. In the $HOMO_M$ the electrons are localised in a lone-pair orbital at the sulphur sites, see Fig. 7.9a. The only exception is one sulphur atom out of 16 that contains the localised hole because of the charge donated to the X-layer, see + in Fig. 7.10*vi*. Indeed, we recognise a small satellite in the high-temperature spectra, see arrow in the 100K-spectrum in Fig. 7.7.

The reason for the breakdown of the dimer orbitals is most likely the combined action of the activated conformational transitions of the ethylene endgroups, the increasing thermal expansion due to phonon excitation and, maybe as third ingredient, the expansion of the dimers due to occupation of the anti-bonding *HOMO* in steps *iv* and *v* .

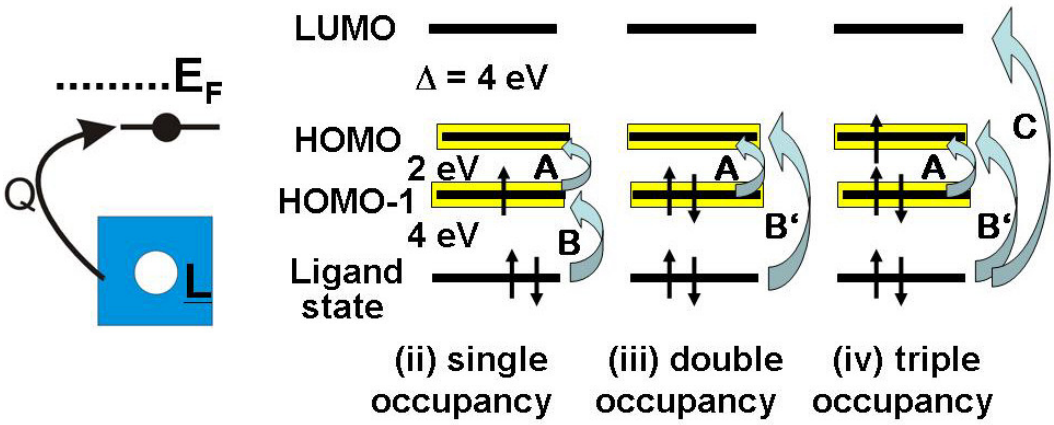

Figure 7.11 Schematic transition scheme proposing a possible origin of the shifted core-level signals in terms of *shake-up transitions* between the frontier orbitals of the dimer. Δ denotes the energy differences between the levels (for the N-1 system, i.e. for presence of the core hole). Q is the energy required to excite an electron from the ligand state to the unoccupied state below the Fermi energy, leaving a hole in the ligand state (denoted as L). The ligand state is an occupied state with a large overlap of its wavefunction with the core hole.

We now address the question whether the localised dimers are distributed statistically homogeneous or in an ordered fashion. We cannot distinguish between these two possibilities by the shifts of the core-level satellites but instead have to consider the intensity behaviour. The reduction of main-line intensity and occurrence of higher-binding-energy satellites at the *T* crossover line* gives evidence of a sudden localisation of electrons in the frontier orbitals of the dimer. Occupation of the lower-lying *HOMO-1* is energetically favourable, therefore localisation starts by filling of this orbital. A number of dimer sites leave the metal state of coherent transport and enters instead a state of an isolated dimer with partially occupied frontier orbitals. As soon as one electron resides on a dimer, this site can no longer participate in the metallic state. One might expect that this is a continuous process with the number of localised dimers gradually increasing with temperature. However, Fig. 7.6 shows that this is not a gradual change, but an instantaneous jump. Moreover, the drop of main-line intensity does not increase with temperature. Within the error of the fit routine it stays fixed at 84% of its initial value for a large temperature interval from 45 to 70 K.

The fact that the main-line intensity stays fixed in a large temperature interval might be a hint on an ordered structure. For disordered current paths, as discussed in the literature, there is no reason why the number of localised dimers should not gradually increase with increasing temperature. The localised charge density distracts charge in the neighbouring dimers and thus might hinder a localisation of the nearest neighbours. The simplest ordered structure in the 2D triangular lattice consist of a *(√3x√3)-R30°* structure with 1/3 of the dimers containing localised electrons. This commensurate superstructure is sketched in Fig. 7.9c (circles). It represents a special case of charge ordering. There will be many anti-phase boundaries and the structure may fluctuate on a small length scale so that it is not clear whether diffraction methods are able to detect the local superstructure.

The quantitative interpretation of the drop of the main-line intensity gives a further hint on 1/3 localisation. We have to account for the fact that only the inner four sulphur atoms S_i contribute significantly to the *HOMO* state, see Fig. 7.9a. It means that 50 % of the initial main-line intensity corresponds to the "passive" four outer sulphur atoms S_o. Loosing 1/3 of all dimers in the metallic state would thus correspond to 1/3 of 50 % of the main-line intensity, i.e. 16.7 %. This agrees well with the measured drop of 16 % within experimental precision (see dotted horizontal line in Fig. 7.6). *This is no proof of the (√3x√3)-R30° structure, but a strong hint on this possibility.*

Close to the temperature of the thermal glass-like transition T_g the ordered superstructure, if it exists, disappears because all dimers become localised. The dramatic intensity breakdown of the sulphur 2s main line and the strong intensity increase of satellites A and C gives evidence that *close to T_g the frontier orbitals of all dimers become occupied* by electrons from the former itinerant band state. The thermal activation of conformation transitions of the ethylene endgroups gives rise to strong structural fluctuations on different length scales. Coherent transport in such a distorted and fluctuating lattice system is no longer possible. The intensity breakdown of the main line directly reflects the *breakdown of the metallic band state*. This situation of total localisation in *HOMO* and *HOMO-1* of the dimers persists in a temperature interval of about 15 K.

The transition from the proposed 1/3 localisation of all dimer sites at T* to complete localization at T_g should be accompanied by an intensity increase of the satellite peaks by a factor of 3. This is approximately the case for the sum of all satellites. Satellite A increases by roughly a factor of three. Satellite B' even slightly drops, because the *HOMOs* of all dimers become (partially) occupied. But the new satellite C rises strongly, taking over the rest of the satellite intensity. Due to the total localisation, the spin fluctuations detected by muon spin relaxation [Lan11] should increase considerably, which is consistent with the observation, see Fig. 7.12g. After breakdown of the dimer orbitals, 15 out of 16 sulphur atoms are in a fully-occupied state, so that for these atoms no possibility for a shake-up process exists. Only 1/16 of the S atoms have a hole in the outermost orbital, which gives rise to the weak satellite peak observed of Fig. 7.7 (see arrow in the 100 K spectrum).

Transition channels in spectroscopic notation

Now we will consider the spectroscopic labelling of the satellite lines in more detail. We recall the characteristics of the satellite signals: At T*, signals A and B appear at shifts of 2 and 4 eV. We associate T* with a sudden localisation of electrons in (approximately) 1/3 of the dimer sites, possibly forming a commensurate superstructure. At 55K the satellite B' appears and gradually takes over the intensity from B. At about 80 K the fourth satellite C

strongly gains in intensity; it is shifted by 10 eV with respect to the main line. At the same temperature, the intensity of A increases by a factor of three, whereas B' drops weakly. We associate this sudden change with the collapse of the metallic band state due to the onset of melting of the ethylene endgroups. The interdimer transfer integral is 50 meV only, i.e. this weak coupling can be distorted relatively easily. Between 90 and 95 K all satellites disappear. We associate this with a possible breakdown of the dimer orbitals (transfer integral 150 meV) driving the electrons into localisation in the monomers, where 15 out of 16 sulphur atoms are in closed-shell configurations.

Sulphur 2s photoemission from dimers with partially occupied frontier orbitals opens several new excitation channels that are connected with shake-up into empty states. In addition to the final state with only the core hole and unchanged valence configuration (denoted *direct channel* and represented by the *main line*), final states with an additional electron in the *HOMO-1, HOMO* or *LUMO* can occur. This happens because the positive charge of the core hole lowers the energy positions of the empty states. If they are lowered below the Fermi energy, they can be occupied during the photoemission process by an electron stemming either from the occupied *HOMO-1* (denoted *HOMO shake-up*) or from a ligand state $\underline{L}$ (denoted *ligand shake-up*), the latter involving another electron from a deeper-lying state, see left panel in Fig. 7.11.

Lifting an electron into the formerly unoccupied state costs additional energy. This energy can only be taken from the photoelectron, therefore these processes appear as satellites at higher binding energies. The binding-energy shifts are not an initial state effect like a chemical shift but result from a rearrangement of electrons in the valence region. A semi-classical picture is that the core-level photoelectrons undergo inelastic excitation processes by interaction with the valence electrons when leaving the molecule. In quantum-mechanical description, however, it happens in the photoemission transition itself due to configuration interaction.

We adapt the notation introduced earlier in this section, however, it must be amended by the π–electrons in the *HOMO* and *HOMO-1* (denoted as $\pi_{\boldsymbol{H}}$ and $\pi_{\boldsymbol{H\text{-}1}}$, respectively). Note that $\pi_{\boldsymbol{H}}$ and $\pi_{\boldsymbol{H\text{-}1}}$ are *shared* by all S-atoms in the dimer. We abbreviate the spectroscopic notation by omitting all electrons that are passive in the transition (i.e. the filled $(sp^2)^2$-configuration and the paired π–electrons in *HOMO-2* and deeper-lying π–orbitals). The following example refers to the case of triple occupancy:

$$S\,[1s^2\,2s^2p^6\,3(sp^2)^2\,\pi^3] \quad \textit{abbreviated as} \quad S\,[2s^2\,3\pi_{\boldsymbol{H\text{-}1}}{}^2\,\pi_{\boldsymbol{H}}] \qquad (7.6)$$

Further, we denote the conduction band in the metallic state as CB and the atomic-like orbital at an individual sulphur atom after breakdown of the dimer orbitals as p_z. $\underline{L}$ denotes the hole state in the ligand orbital. An electron excited into the lowest unoccupied molecular orbital LUMO is denoted as $\pi_{\boldsymbol{L}}$.

Fig. 7.11 gives a schematic sketch of the transition scenario. When we take into account the *LUMO*, we have three frontier orbitals that could be occupied during the photoemission process either by an electron from the *HOMO-1* or from a deeper-lying ligand state. Before the localisation the frontier orbitals *HOMO-1, HOMO* and *LUMO* are empty (strictly, the lowest empty orbital should be termed *LUMO*; however, to avoid confusion, we do not change terminology). Photoemission leads to an N-1 state. The core-hole pulls down the empty states and when they come to lie below the Fermi energy they can be occupied during the photoemission process. The excitation of an electron into the valence-shell vacancy

costs energy Q, see insert on the left-hand side of Fig. 7.11. We write the possible channels of the S 2s core-level photoemission process for the six different occupancy cases of Fig. 7.10 as follows:

(i) Good-metal regime (below T*)

$$S\,[2s^2\,CB] + h\nu \rightarrow S\,[2s\,CB] + \varepsilon p \quad \textit{direct channel only} \quad (7.7)$$

(ii) Single occupancy (onset at T*)

$$S\,[2s^2\,3\pi_{H\text{-}1}] + h\nu \rightarrow S\,[2s\,3\pi_{H\text{-}1}] + \varepsilon p \quad \textit{direct channel} \quad (7.8)$$

$$S\,[2s^2\,3\pi_{H\text{-}1}] + h\nu \rightarrow S\,[2s\,3\pi_{H\text{-}1}^2\,\underline{L}] + \varepsilon p \quad \textit{ligand} \rightarrow \textit{HOMO-1 shake-up } \boldsymbol{B} \quad (7.9)$$

$$S\,[2s^2\,3\pi_{H\text{-}1}] + h\nu \rightarrow S\,[2s\,3\pi_{H}] + \varepsilon p \quad \textit{HOMO-1} \rightarrow \textit{HOMO shake-up } \boldsymbol{A} \quad (7.10)$$

(iii) Double occupancy (increases between T* and T_g)

$$S\,[2s^2\,3\pi_{H\text{-}1}^2] + h\nu \rightarrow S\,[2s\,3\pi_{H\text{-}1}^2] + \varepsilon p \quad \textit{direct channel} \quad (7.11)$$

$$S\,[2s^2\,3\pi_{H\text{-}1}^2] + h\nu \rightarrow S\,[2s\,3\pi_{H\text{-}1}^2\,\pi_H\,\underline{L}] + \varepsilon p \quad \textit{ligand} \rightarrow \textit{HOMO shake-up } \boldsymbol{B'} \quad (7.12)$$

$$S\,[2s^2\,3\pi_{H\text{-}1}^2] + h\nu \rightarrow S\,[2s\,3\pi_{H\text{-}1}\,\pi_H] + \varepsilon p \quad \textit{HOMO-1} \rightarrow \textit{HOMO shake-up } \boldsymbol{A} \quad (7.13)$$

(iv) Threefold occupancy (at T_g)

$$S\,[2s^2\,3\pi_{H\text{-}1}^2\,\pi_H] + h\nu \rightarrow S\,[2s\,3\pi_{H\text{-}1}^2\,\pi_H] + \varepsilon p \quad \textit{direct channel} \quad (7.14)$$

$$S\,[2s^2\,3\pi_{H\text{-}1}^2\,\pi_H] + h\nu \rightarrow S\,[2s\,3\pi_{H\text{-}1}^2\,\pi_H^2\,\underline{L}] + \varepsilon p \quad \textit{ligand} \rightarrow \textit{HOMO shake-up } \boldsymbol{B'} \quad (7.15)$$

$$S\,[2s^2\,3\pi_{H\text{-}1}^2\,\pi_H] + h\nu \rightarrow S\,[2s\,3\pi_{H\text{-}1}\,\pi_H^2] + \varepsilon p \quad \textit{HOMO-1} \rightarrow \textit{HOMO shake-up } \boldsymbol{A} \quad (7.16)$$

$$S\,[2s^2\,3\pi_{H\text{-}1}^2\,\pi_H] + h\nu \rightarrow S\,[2s\,3\pi_{H\text{-}1}^2\,\pi_H\pi_L\,\underline{L}] + \varepsilon p \quad \textit{ligand} \rightarrow \textit{LUMO shake-up } \boldsymbol{C} \quad (7.17)$$

(v) Fourfold occupancy (very weak, not observable)

(vi) Complete localisation on atomic sites

(a) for double occupancy (15 S atoms out of 16)

$$S\,[2s^2\,3p_z^2] + h\nu \rightarrow S\,[2s^2\,3p_z^2] + \varepsilon p \quad \textit{direct channel only} \quad (7.18)$$

(b) for single occupancy (1 S atom out of 16)

$$S\,[2s^2\,3p_z] + h\nu \rightarrow S\,[2s^2\,3p_z] + \varepsilon p \quad \textit{direct channel} \quad (7.19)$$

$$S\,[2s^2\,3p_z] + h\nu \rightarrow S\,[2s^2\,3p_z^2\underline{L}] + \varepsilon p \quad \textit{ligand shake-up} \quad (7.20)$$

The smallest energy transfer (2 eV) is associated with ***satellite A*** and corresponds to the transition *HOMO-1*→ *HOMO* that we find in all three relevant occupancy cases (Eqs. 7.10, 7.13 and 7.16). The strong increase of signal A at 80 K indicates that another shake-up channel comes into play, the clarification of which needs a theoretical calculation. The 4 eV transfer is associated with ***satellite B***, transition *ligand*→ *HOMO-1* that exists only for single occupancy (7.9). The transition changes to the next higher orbital when the *HOMO-1* becomes more and more occupied. The ***satellite B'*** is thus associated with the transition *ligand*→ *HOMO* for double and triple occupancy characterised by an increased energy transfer of 6 eV (7.12, 7.15). The change from B to B' is the origin for the apparent shift of satellite B in Fig. 7.4. It means that in the partially localised state the occupation increases from single to double occupancy with temperature. As possible origin of ***satellite C*** arising for triple occupancy we propose that a transition into the LUMO takes place (7.17). This is

associated with the highest energy transfer of 10eV. The sizes of the level splittings in Fig. 7.11 derive from the satellite spectra, they should be confirmed by a calculation.

Conclusion of own results in the context of literature data

Let us finally resume how the proposed model fits to the other experimental quantities, compiled in Fig. 7.12. In the ***good-metal range*** below T* no satellites occur within the detection limit of our experiment. The thermal expansion coefficient (7.12b) increases linearly with temperature and the lattice constant (c) increases weakly. The DC resistivity (d) increases strongly from 4 Ω right above T_c to about 100 Ω at T*, reflecting the increasing electron-phonon scattering rate. Throughout this range of about 30 K width the core-level spectrum stays unchanged. It means that the *coherent band state persists although the scattering rate increases by more than an order of magnitude*. We conclude that it must be energetically unfavourable for a scattered electron to go into a localised state. Up to T* the scattered electrons find themselves in the band state again, like in a classical metal.

At the temperature of the ***T* anomaly*** all experimental quantities show significant changes, some of them quite abrupt. The shifted core-level signals A and B occur instantaneously and the satellite intensity and corresponding drop of main-line intensity remain constant until 70 K. A possible explanation for the range between the T* anomaly and T_g, the lower-lying anti-bonding dimer orbital HOMO-1 is gradually filled. First via a kind of jump at T* into single occupancy (maybe associated with an spatially-ordered state) and then progressing by filling of the second electron. The thermal expansion coefficient shows a sudden change in slope to a horizontal branch, the lattice constant perpendicular to the layers starts to increase, the conductivity curve shows an inflection point, the 3ω-amplitude (e), low frequency noise (f) and muon-spin relaxation rate (g) suddenly start to rise. All these facts point on a sudden onset of localisation.

The variation of the *DC-conductivity curve* is smooth, because it reflects the continuous drop of the Drude relaxation time due to the gradual excitation of more and more phonon branches. The variation of the *lattice constant* is more complicated because it reflects the combined effect of thermal excitation of the rich (and anisotropic) phonon spectrum and a possible contribution of the electrons changing from the *isotropic metallic bonding* in the good metal phase to the *anisotropic bonding contribution of localised electrons* in the lower-lying bonding and higher-lying anti-bonding dimer orbitals. The filling of 1, 2 and 3 electrons into these orbitals can be expected to cause changes in the molecular geometry.

At the ***thermal glass-like transition temperature T_g*** the most marked effect is the hysteretic change in the thermal expansion coefficient and the cusp-like maximum in the lattice constant (7.12b, c). In literature, the melting of the ethylene endgroups is made responsible for these lattice effects. However, some authors note that the (small) effect of the ethylene groups cannot quantitatively account for the observed massive effects. On the basis of the core-level spectra we suppose that the *melting of the ethylene group disorder triggers an electronic effect* that may have a contribution to the behaviour of the lattice. The onset of ethylene conformational transitions destroy the coherent band state at about 8 K below T_g and forces the electrons into full localisation. This requires occupation of the antibonding *HOMO* which, in turn, leads to an expansion of the intraplane distance of the dimers. Finally, the combined action of endgroup fluctuations and change of intraplane distance may lead to a breakdown on the dimer orbitals themselves, driving the electrons into localisation into the lone-pair orbitals of the sulphur atoms of monomers. As the intradimer

and interdimer transfer integrals differ by a factor of three, the collapse of the band state and the breakdown of the dimer orbitals happen at slightly different temperatures. This explains why satellite C and enhancement of satellite B occur only in a small temperature interval of about 15 K.

Concerning the temperature scale, we estimate an error of $\pm$ 3K. However, we cannot exclude a possible mechanical strain on our sample. Having been glued to the copper sample holder at room temperature, cooling down to low temperatures might exert a compressive strain of unknown size. In turn, this would shift the position on the T* crossover line to the right, i.e. to higher T in the phase diagram, Fig. 7.3.

The quenching of the coherent band state (Fermi liquid state) in two steps, driving the electrons into partial localisation at T* and into full localisation close to T_g has possibly consequences concerning the lattice. First, the bonding action of the partially-occupied *HOMO* at T* and the increasing double-occupation of this orbital is in accordance with the sudden drop in the slope of the thermal expansion coefficient from a linearly increasing branch to a horizontal branch between 40 and 70 K (7.12b). The fact that this branch stays horizontal is compatible with a gradual increase of double occupancy of *HOMO-1* with increasing temperature, in accordance with the gradual transition observed between satellites B and B' in Figs. 7.4 and 7.6. The onset of repulsive contributions by occupation of *HOMO* close to T_g leads to the sudden jump in thermal expansion and to the cusp in the lattice constant perpendicular to the planes (Fig. 7.12b and c).

In complete accordance with our model a *strong enhancement of spin fluctuations* (Fig. 7.12g) is observed in exactly the same temperature interval where the strong satellite features occur. The first strong rise lies closely above T* and a further increase is observed close to T_g. Finally, at the *temperature of disappearance of the satellites a rapid drop of the relaxation rates is observed*. The muon spin relaxation is caused by fluctuating local magnetic fields due to unpaired electrons, thus reflecting especially the single occupation of *HOMO and HOMO-1* of the dimer, i.e. an unpaired electron being delocalised over the dimer.

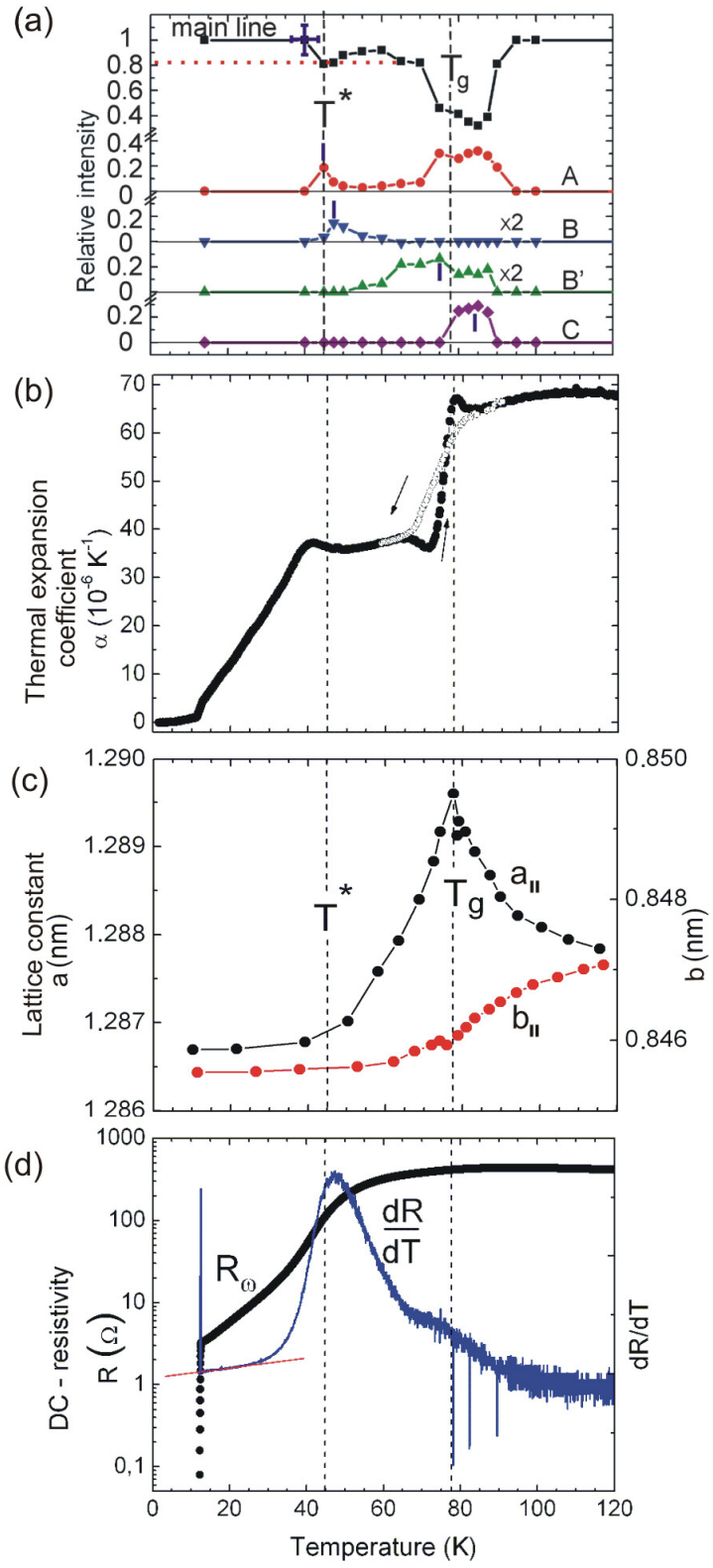

Figure 7.12a-d Compilation of various experimental results for κ-Br, from [Sou07] (b), [Wol07] (c) and [Mue11] (d).

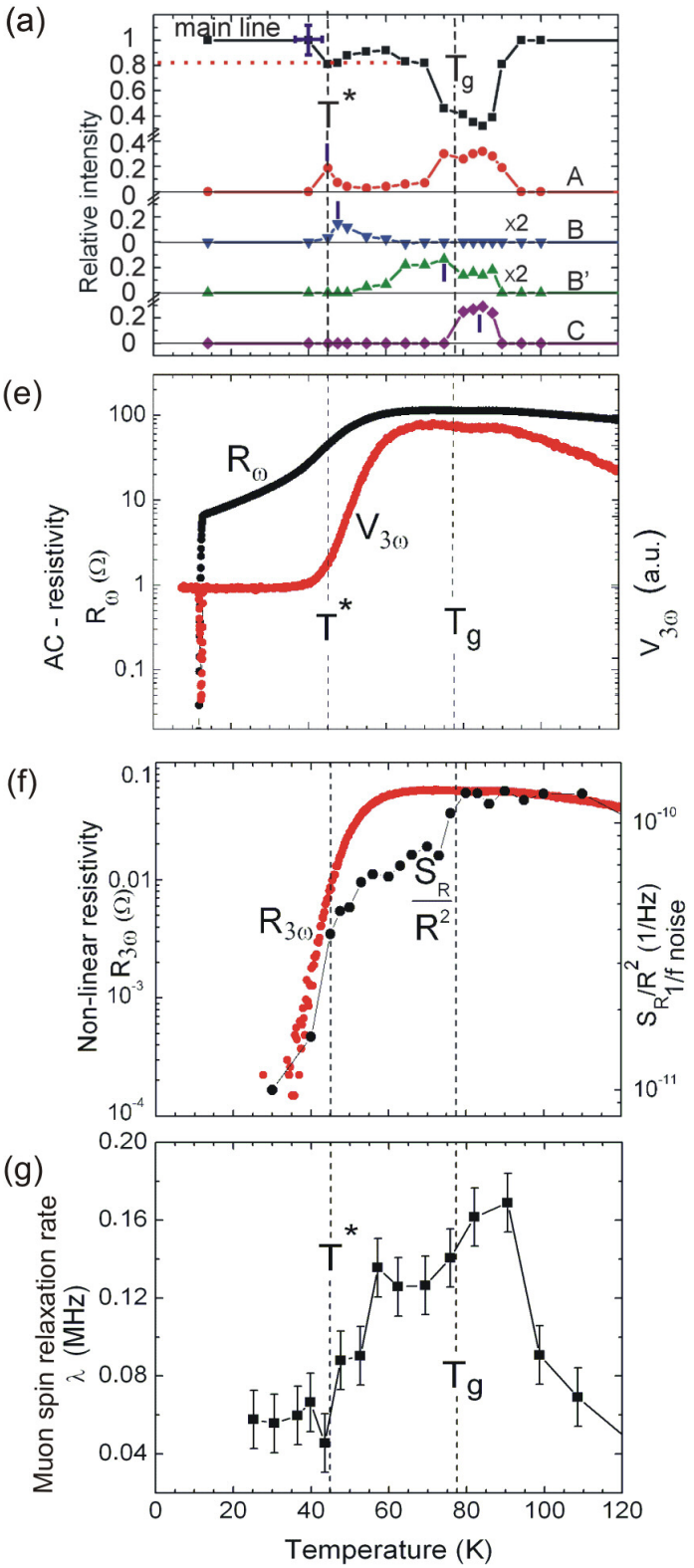

Figure 7.12e-g (continued) Compilation of various experimental results for κ-Br, from [Mue11] (e,f) and [Lan11](g).

8. Summary and Conclusion

The present work aims at a most complete understanding of the electronic structure of various organic charge transfer (CT) salts from three different families of materials by applying various spectroscopic techniques. The electronic structure of the valence region was studied using *ultraviolet photoelectron spectroscopy* (UPS). Due to the high surface sensitivity of UPS the samples were prepared *in-situ* as ultrahigh-vacuum co-deposited thin films, employing a special double evaporator developed for very small amounts of materials in the few-milligram range. This method was particularly powerful to reveal the energetic shifts (in the few 100 meV range) of valence levels, especially the highest occupied molecular orbital (HOMO) in a CT complex in comparison with the pure donor and acceptor moieties. An important aspect of the UPS measurements lies in the direct quantitative comparison with *ab-initio* calculations (from the PhD Thesis of S. Naghavi [Nag10c]), obtained using density functional theory (DFT) with the hybrid functional B3LYP.

Up to very recently it was impossible to perform reliable photoemission experiments for solution-grown crystals due to the unavoidable surface contamination. We have overcome this problem by applying *hard X-ray photoelectron spectroscopy* (HAXPES) at photon energies of 6 keV at the new storage ring PETRA III in Hamburg. At such high energies the mean-free-path of the photoelectrons is much higher than in UPS and classical XPS. This drives the probing depth into the 15 nm range, resulting in true bulk sensitivity. The first HAXPES experiments on CT complexes worldwide reveal that this novel method gives access to large chemical core-level shifts (of the order of several eV) in the CT-complexes. HAXPES results are complementary to UPS data because they provide a local probe of the chemical environment of a selected atom. The valence orbitals studied in UPS are delocalized over the whole molecule or over a donor-acceptor dimer in the complex. Significant beam damage of the delicate samples was obvious in the first experiments. However, it could be overcome by slight movement of the X-ray microfocus on the sample before taking a new spectrum.

As second Synchrotron-radiation based technique, *near-edge X-ray absorption fine structure* (NEXAFS) spectroscopy was systematically applied for several CT-systems. Also for this technique the probing depth was large enough to enable the investigation of solution-grown crystals. In the total-yield mode of NEXAFS the slow secondary electrons are detected, which also have a sufficiently large mean-free-path in the region of 5 nm. The experiments from several beamtimes at the storage ring ANKA, Karlsruhe, revealed that NEXAFS provides a most direct access to details of the CT mechanism. Strong intensity variations of certain pre-edge resonances directly show the change of occupation of the corresponding orbitals. NEXAFS probes the unoccupied densities of states in the immediate vicinity of a given atom, being selected by its fingerprint-like X-ray absorption edge.

These central electron and X-ray spectroscopic studies were amended by *infrared spectroscopy* (IR), probing the vibronic structure of certain functional groups of a molecule in a complex, by results of *X-ray diffraction* (XRD) obtained in cooperation with the group of Prof. Huth, Goethe-University Frankfurt/Main, optical and *atomic force microscopy* (AFM) and by *scanning tunnelling spectroscopy* (STS), performed in cooperation with the group of Prof. Elmers in our institute. The latter method gives access to the HOMO and LUMO levels and is thus complementary to UPS.

All investigations aim on a deeper understanding of details of the CT mechanism from an electronic point of view. In the following we will summarize the results for the three families of CT materials and draw conclusions important for future experiments.

(i) Novel CT-complex based on a donor / acceptor pair derived from coronene

The acceptor *coronene-hexaone* ($C_{24}H_6O_6$, COHON) and the donor *hexamethoxycoronene* ($C_{30}H_{24}O_6$, HMC) were synthesized in the group of Prof. Müllen, MPI for Polymer Research. The complex cannot be grown from solution because no common solvent for both moieties exists. The molecules were UHV co-deposited as pure and mixed phases on gold substrates. At low coverage, COHON adsorption leads to the appearance of a charge-transfer induced interface state 1.75 eV below the Fermi energy, which disappears at multilayer coverage. The formation of a strong interface dipole due to charge-transfer at the metal–organic interface is evident from a rise of the workfunction to 5.6 eV (after an initial decrease at low coverage). HMC on Au shows no interface state and the sample work function decreases monotonically to ca. 4.8 eV due to the "push-back mechanism" (i.e. Pauli repulsion of the spill-out electrons of the Au surface). The hole injection barrier, i.e. the distance of the onset of the HOMO from the Fermi level is Δ_h= 1.3 eV for pure HMC on Au.

When the complex is formed in mixed films, the HOMO peak maxima shift by about 0.19 eV to higher binding energy for HMC and by 0.25 eV to lower binding energy for COHON (Δ_h= 1.49 eV for the complex). These opposite shifts are a direct evidence of a CT: The charge depletion in the donor (HMC) leads to a reduced intramolecular screening and thus to an increase of binding energies for orbitals located at HMC, whereas the charge excess in the acceptor reduces the binding energies of orbitals located at COHON. Further than this charge-redistribution argument, the energy levels in a molecular donor/acceptor CT-complex are expected to form *via* hybridization of acceptor LUMO and donor HOMO. We conclude that mixed films of COHON and HMC constitute a weak charge-transfer system.

The theoretical spectrum calculated for a free HMC-COHON dimer had to be shifted by 0.66 eV to higher binding energy, so that its HOMO peak coincided with the measurement. The corresponding shifts for pure COHON and pure HMC are 0.07 eV and 0.23 eV, respectively. It means that DFT calculations using the B3LYP hybrid functional [Nag10a] show surprisingly good agreement with experiment despite the fact that the calculations did not account for interactions in the molecular films or at the metal-organic interface. Finally, the oxygen and carbon K-edge NEXAFS spectra show significant changes between complex and pure moieties. However, since both atomic species are located both in the donors and acceptors, a quantitative evaluation of the NEXAFS spectra is complicated for this system.

(ii) Family of CT-complexes based on novel donors derived from pyrene and the classical acceptor tetracyanoquinodimethane

This family of CT-complexes uses the novel pyrene-derivatives *4,5,9,10-tetramethoxypyrene* ($C_{20}H_{18}O_4$, TMP) and *2,4,5,7,9,10-hexamethoxypyrene* ($C_{22}H_{22}O_6$, HMP) as donors (synthesized in the MPI for Polymer Research [Kaw11]) in complexes with the classical strong acceptor *7,7,8,8-tetracyano-p-quinodimethane* ($C_{12}N_4H_4$, TCNQ). First, the formation of an intermolecular CT complex became evident for *UHV-deposited thin films of TMP_1-$TCNQ_1$* from the appearance of new reflexes in XRD (d_1=0.894 nm and d_2=0.677 nm). A softening of the CN stretching vibration (red-shift by 7 cm^{-1}) of TCNQ is visible in the IR spectra, being indicative of a CT on the order of 0.3*e* in

the complex. Characteristic shifts in the electronic level positions occur in UPS and STS that are in good agreement with DFT calculations, similar as for the coronene derivatives. Here the theoretical spectra had to be shifted by 0.97 eV for the complex and by 0.52 eV and 0.48 eV for pure TMP and HMP, respectively. STS gives direct access to HOMO and LUMO positions and their pinning to the Fermi energy of a metal substrate. The HOMO-LUMO gap of the CT complex is 1.25 eV, being much smaller than the gaps (> 3.0 eV) of the pure moieties. The electron- and hole-injection barriers are 0.3 eV and 0.5 eV, respectively. More details of the STS method and further results for the HMP-TCNQ complex can be found in the Diploma Thesis of S. Perkert [Per11]. Systematic deviations between the STS and UPS level positions can be understood from the different underlying mechanisms of these 2 spectroscopies.

Microcrystals of TMP_x/HMP_x - $TCNQ_y$ in different stoichiometries x:y = 1:1, 1:2 and 2:1 were grown from solution via vapour diffusion [Kaw11]. Owing to the element specificity of NEXAFS, the oxygen and nitrogen K-edge spectra are direct spectroscopic fingerprints of the donor and acceptor moieties. The orbital selectivity of the NEXAFS resonances allows to precisely elucidate the participation of specific orbitals in the charge-transfer process. Strong changes in certain pre-edge peaks reveals that charge is transferred from orbitals derived from the methoxy-orbitals 2e (π^*) and $6a_1$ (σ^*) to the cyano-orbitals b_{3g} and a_u (π^*) and - a weaker extent - to b_{1g} and b_{2u} (σ^*). In addition, small energetic shifts with different signs for donor and acceptor resonances appear, similar as observed in UPS. The intensity of the resonant transition into the 2e-derived orbitals reflects the hybridisation of these orbitals with the π-system. Surprisingly, the charge transfer out of the orbitals derived from methoxy 2e and $6a_1$ increases with increasing HMP content of the complex. This is in contrast with expectation and gives a strong hint on the importance of the geometric structure for the amount of charge transfer. Presently, a full structural analysis is only available for TMP-TCNQ, which is a mixed-stack system.

HAXPES measurements were performed for thin-film samples and the same fractions of microcrystallites in different stoichiometries. In the compound *HMP_x - $TCNQ_y$* the nitrogen 1s line (being a fingerprint of the cyano-group in TCNQ) shows a splitting and a shift to *higher* binding energies (up to about 6 eV shift) with increasing HMP content. Vice versa, the oxygen 1s line (being a fingerprint of the methoxy-group in HMP) shows a marked splitting and a shift to *lower* binding energies (up to about 2.5 eV shift). The core-level shifts are thus more than one order of magnitude larger than the shifts of the valence levels measured by UPS. Quantitative evaluation of these data is in progress, it requires accompanying *ab-initio* calculations of XPS binding energies.

(iii) CT-complexes from the family of cationic radical salts κ-$(BEDT\text{-}TTF)_2Cu[N(CN)_2]Br$

Two members of the organic (super-)conductors of the κ-$(ET)_2$-X family, synthesized by the group of Prof. Lang from Goethe-University Frankfurt / Main were studied using HAXPES in the low temperature range. This material is characterized by a strongly-correlated π-electron system with close proximity of superconductivity and antiferromagnetic insulating states. A charge transfer from the BEDT-TTF (briefly ET) molecules to the polymeric X-layer leads to a quasi-2D metallic conduction band. We looked at the S 2s line, because sulphur is contained only in the donor molecules. The S 2s spectra are thus a local probe in the 2D metallic ET layer with its half-filled conduction band.

Although it was intended as a pilot experiment, the first HAXPES beamtime yielded already results that shed new light into the highly debated role of the electronic degrees of freedom for the observed anomalies in many physical parameters, e.g. a cusp in the spin-lattice relaxation rate, a pronounced minimum in the velocity of sound, unusual behaviour in the thermal expansion coefficient and changes of spin susceptibility and resistivity. Unexpected large shifts in the S 2s HAXPES spectra of *κ-(BEDT-TTF)$_2$Cu[N(CN)$_2$]Br* with pronounced temperature dependence are a highly promising result for future systematic investigations on this class of CT-salts. In the temperature region between the onset of the anomalous metallic state (T^*~ 50 K) and slightly above the thermal glass-like transition (T_g ~ 77 K) the S 2s core level spectrum changes dramatically, as measured in a warming-up series starting at 14 K. At T^*, the main-line intensity drops to 80 % of its initial value and two new signals, one in the high-binding-energy shoulder and one shifted by 4 eV arise. When approaching T_g, the main line intensity further drops to 40 % and a third signal appears, being strongly shifted by up to more than 10 eV. Above the thermal glass-transition region, all shifted lines disappear and the main line intensity is restored to its initial value. The first measurements on materials from the *κ-(BEDT-TTF)$_2$X* family constitute a *proof-of-principle* of the feasibility of HAXPES studies for this fascinating class of highly-correlated 2D systems. The results show how core-level spectroscopy with bulk sensitivity provides direct access to subtle electronic details in the vicinity of the Mott transition. They shine a light on the importance of the electronic degrees of freedom for the peculiarities of the phase diagram. A model has been proposed that is in accordance with the present results and experimental data from literature.

Outlook

The studies of the present work have shown that a full understanding of details of the CT-mechanism needs a comprehensive investigation using different spectroscopic techniques. After getting started it became clear that UPS yields fingerprints of a CT in terms of small level shifts in the 100 meV range that opened the door for further investigations. The comparison with DFT calculations gave valuable information on the various complexes based on functionalized polycyclic aromatic hydrocarbons. These measurements will be continued and amended by Inverse Photoemission (IPE) measurements.

Providing quantitative access to the relative occupation of specific orbitals, through the selection of a certain core-level, NEXAFS constitutes the most direct probe of the CT-mechanism in organic salts found so far. Although demonstrated for the specific example of pyrene-derived donors with the classical acceptor TCNQ (and an analogous measurement for the coronene derivatives), the method is very versatile and will serve as routine probe for novel CT-complexes in the future.

First HAXPES measurements on several compounds constitute the *proof-of-principle* of the suitability of this new method for the study of solution-grown CT complexes. Previously, the unavoidable surface contamination of such materials has been prohibitive for electron spectroscopic measurements. Although not much systematics could be gained in the first measurements, it is clear that the core-level shifts are more than one order of magnitude larger than the shifts of the valence levels measured by UPS. This is important information for future investigations on such systems, and HAXPES will become an important tool for the study of all kinds of CT-complexes.

From the present work emerge various suggestions for further experiments. In the future full X-ray investigations of the COHON-HMC and HMP-TCNQ complexes are necessary, inverse photoemission spectroscopy (a surface science technique used to study the unoccupied electronic structure of surfaces) [Bud07a, Bud07b, Dos77] will give access to unoccupied bands and NEXAFS will serve as a fast routine technique. Conductivity measurements will be performed in cooperation with groups in Frankfurt. The joint output of these different methods will shed more light on the mechanism of the charge transfer.

Finally, for many systems, in particular the HMC-COHON mixed phase, further experiments should investigate possible influences of growth parameters (temperature, deposition rate) of the mixed films on the electronic structure, along with a structural analysis by X-ray diffraction. Structure analysis is crucial for a complete understanding of the charge transfer mechanism.

For the materials of the *κ-(BEDT-TTF)$_2$X* family, systematic studies in a wider regime of the phase diagram are highly desirable in order to validate the conclusions of this thesis. Highest priority has a full investigation of *D8-Br* and also of the Mott-insulator system *κ-Cl* on the low-pressure side of the first order transition line. In HAXPES, insulators can easily be studied because a conductive metallic coating (like a few nm of Al or Au) is tolerable due to the high probing depth of 15 nm. A further subject of high current interest is the spin diffusion within the layers. Electrons can diffuse several hundreds of nanometers without interlayer hopping [Ant09]. This phenomenon might be accessible by future spin-resolved experiments with high spatial resolution.

List of used abbreviations

2PPE	Two Photon Photoelectron Spectroscopy
AFM	Atomic Force Microscopy
BEDT-TTF	Bisethylenedithiotetrathiafulvalene
COHON	Coronene -hexaone
CT	Charge Transfer
DFT	Density Functional Theory
DOS	Density of States
EDX	Energy-dispersive X-ray Spectroscopy
ESCA	Electron Spectroscopy for Chemical Analysis
EXAFS	Extended X-Ray Absorption Fine Structure
FTIR	Fourier Transform Infrared Spectroscopy
FWHM	Full Width at Half Maximum
HAXPES	Hard X-ray Photoelectron Spectroscopy
HF	Hartree Fock
HMP	Hexamethoxypyrene
HOMO	Highest Occupied Molecular Orbital
IMFP	Inelastic Mean Free Path
IRAS	Infrared Reflection and Absorption Spectroscopy
LUMO	Lowest Unoccupied Molecular Orbital
MO	Molecular Orbital
NEXAFS	Near Edge X-ray Absorption Fine Structure
OFHC	Oxygen-Free High Conductivity
PEEM	Photoemission Electron microscopy
PES	Photoemission spectroscopy
SCF	Self Consistent Field
SEM	Scanning Electron Microscopy
STS	Scanning Tunneling Spectroscopy
SXMCD	Soft X-Ray Magnetic Circular Dichroism
TCNQ	Tetracyanoquinodimethane
TMP	Tetramethoxypyrene
UHV	Ultra High Vacuum

UPS	Ultraviolet Photoelectron Spectroscopy
VUV	Vacuum Ultraviolet
XAS	X-ray Absorption Spectroscopy
XPS	X-ray Photoelectron Spectroscopy

Appendix: Optical and AFM images of UVH-deposited films

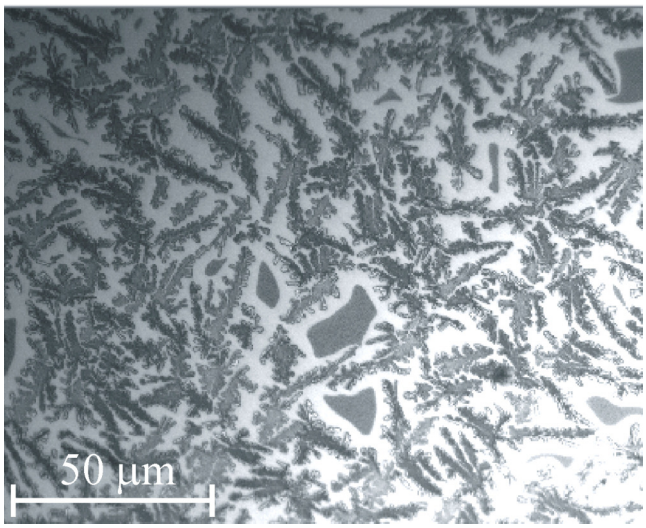

Figure A1 Optical image of bilayer film of hexamethoxycoronene on coronene-hexaone on Au.

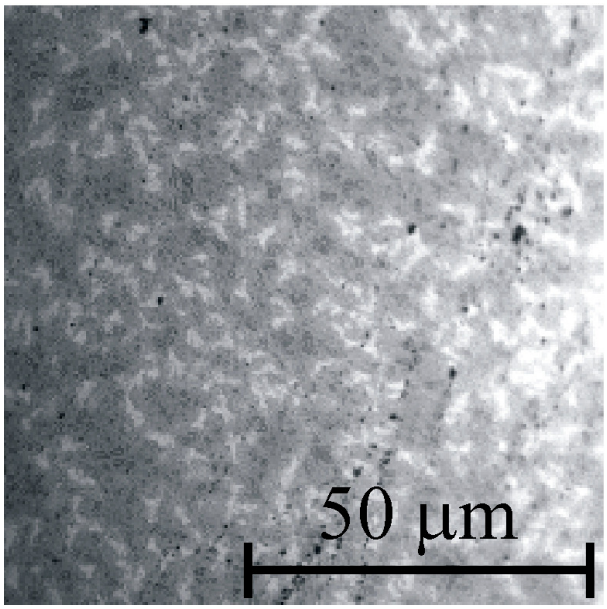

Figure A2 Optical image of multilayer sandwich film of the hexamethoxycoronene - coronene-hexaone mixed phase on Au.

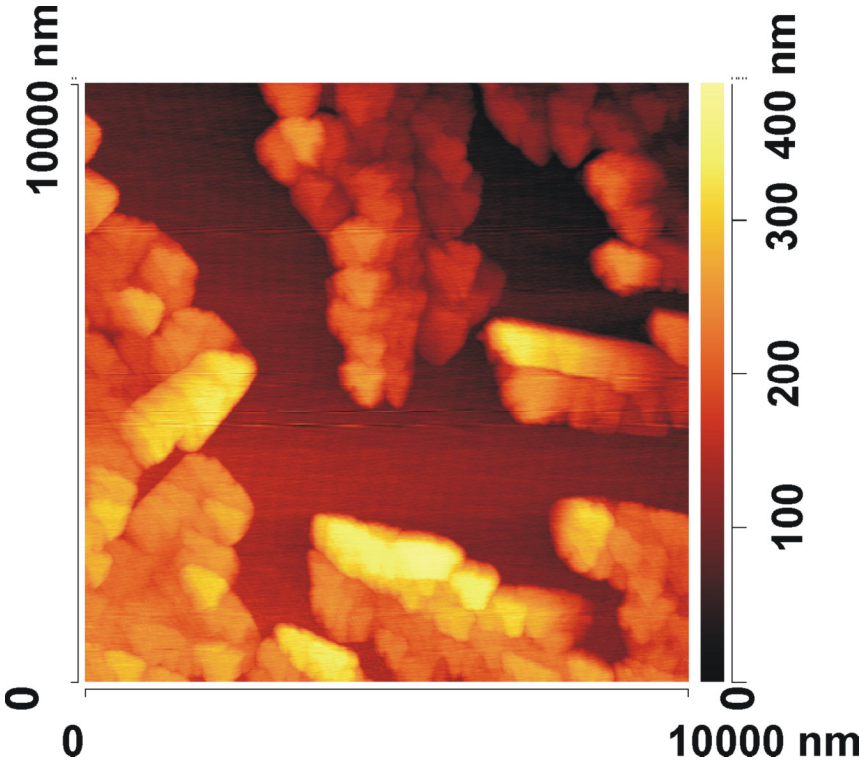

Figure A3 AFM image of a bilayer film of hexamethoxycoronene on coronene-hexaone on Au.

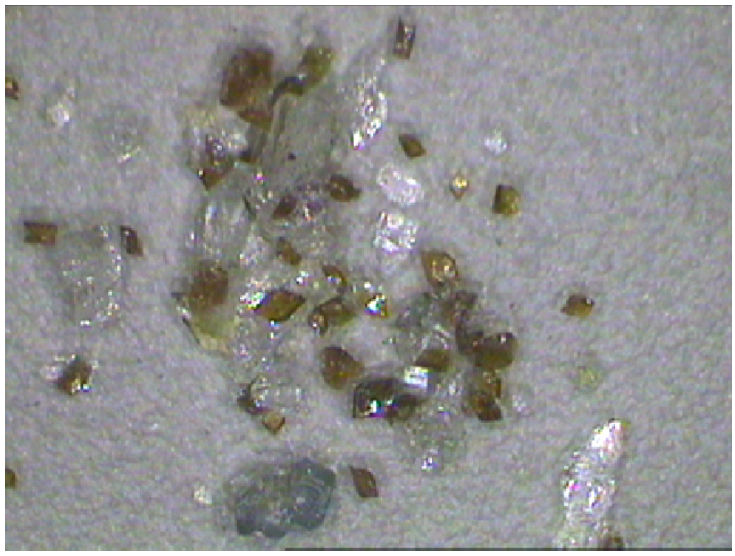

Figure A4 Optical image of solution-grown crystals of tetramethoxypyrene (TMP)-tetracyanoquinodimethane (TCNQ) (field of view 1 mm horizontally). The bright crystals are pure TMP, the dark ones are TMP_1-$TCNQ_2$ crystals.

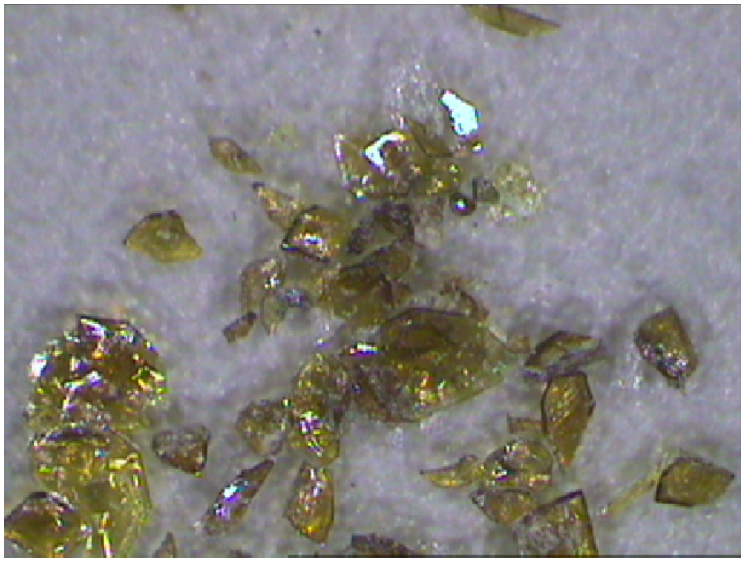

Figure A5 Optical image of solution-grown crystals of tetramethoxypyrene $(TMP)_2$-tetracyanoquinodimethane $(TCNQ)_1$ (field of view 1 mm horizontally).

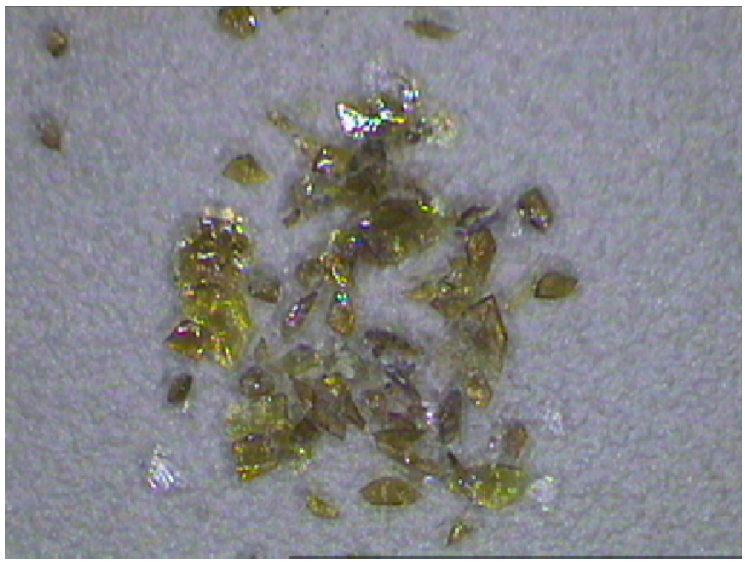

Figure A6 Optical image of solution-grown crystals of tetramethoxypyrene $(TMP)_2$-tetracyanoquinodimethane $(TCNQ)_1$ (field of view 1 mm horizontally). The bright crystals are pure TMP, the dark ones are TMP_2-$TCNQ_1$crystals.

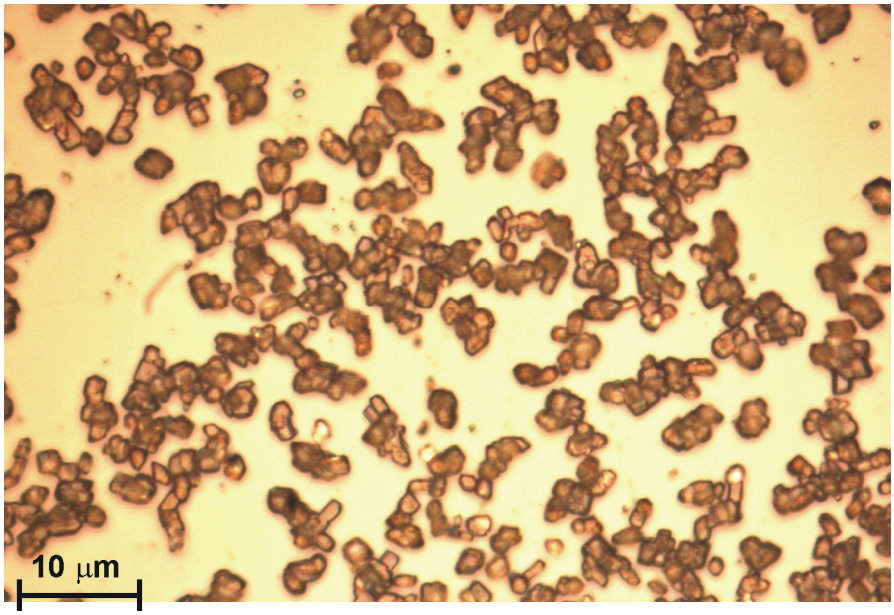

Figure A7 Optical image of the UHV-deposited tetramethoxypyrene-tetracyanoquinodimethane CT complex.

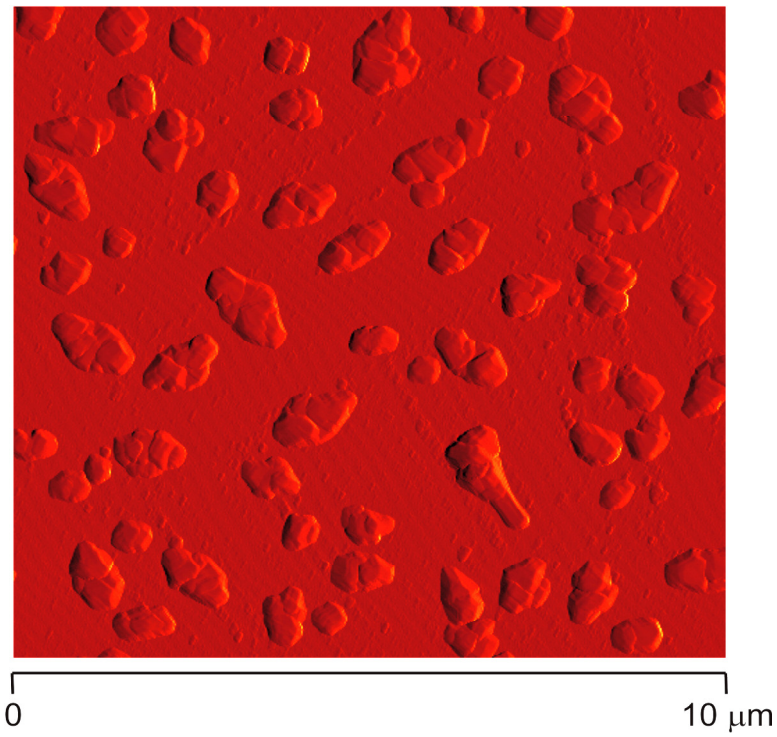

Figure A8 AFM image of a thin film of tetramethoxypyrene- tetracyanoquinodimethane.

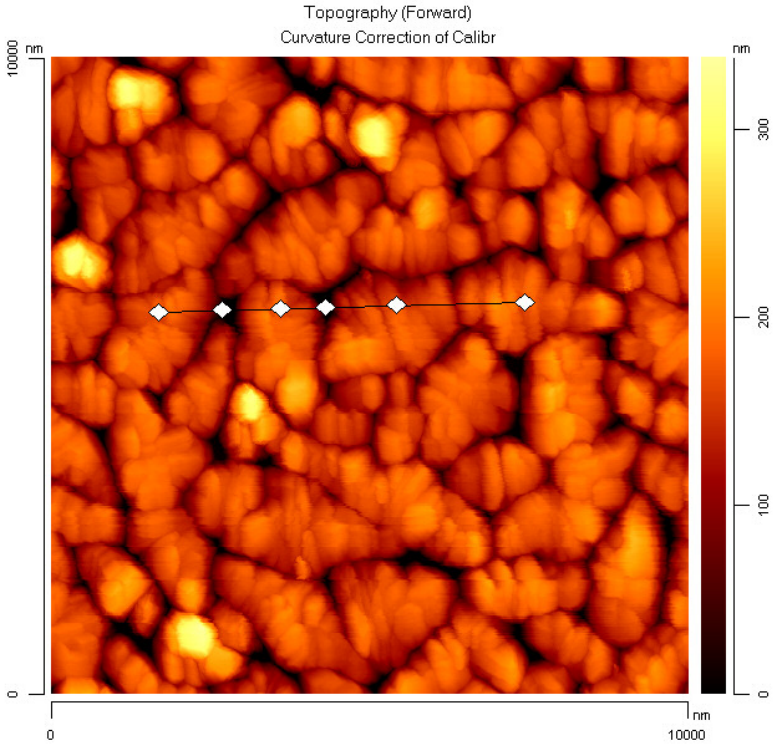

Figure A9 AFM image of a thin film of tetramethoxypyrene- tetracyanoquinodimethane after one hour of annealing at 353 K.

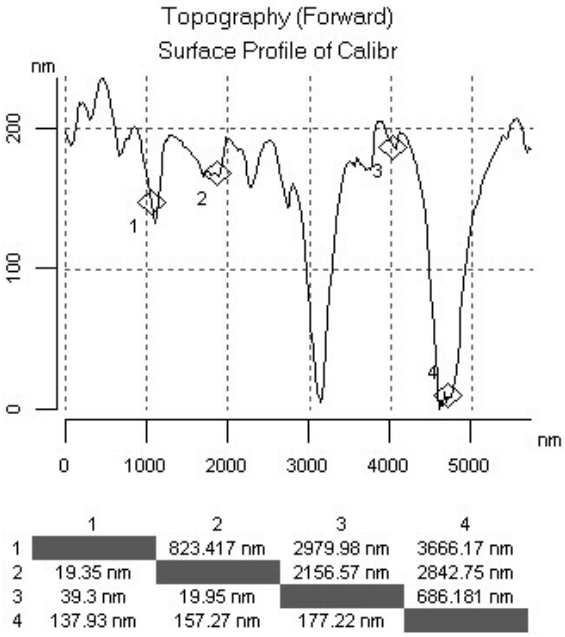

	1	2	3	4
1		823.417 nm	2979.98 nm	3666.17 nm
2	19.35 nm		2156.57 nm	2842.75 nm
3	39.3 nm	19.95 nm		686.181 nm
4	137.93 nm	157.27 nm	177.22 nm	

Figure A10 Topography of a film of tetramethoxypyrene- tetracyanoquinodimethane after one hour of annealing at 353 K. The size of the microcrystals as well as their hight is approximately 100 nm.

Bibliography

[Ack62] D. S. Acker and W. R. Hertler, J. Am. Chem. Soc. **84** (1962) 3370.
[Ali07] S. Alibert-Fouet, I. Seguy, J. F. Bobo, P. Destruel, H. Bock, Chem. Eur. J. **13** (2007) 1746.
[Ama71] T. Amano, H. Kuroda, and H. Akamatu, Bulletin of the Chemical Society of Japan, **44** (1971) 1758.
[Ame99] K. Amemiya, Y. Kitajima, Y. Yonamoto, S. Terada, H. Tsukabayashi, T. Yokoyama, and T. Ohta, Phys. Rev. B **59** (1999) 2307.
[Ang88] G. C. Angel and J. A. R. Samson, Phys. Rev. A **38** (1988) 5578.
[Ant09] Á. Antal, T. Fehér, A. Jánossy, E. Tátrai-Szekeres, and F. Fülöp, Phys. Rev. Lett. **102** (2009) 086404.
[Azi07] E. F. Aziz, A. Vollmer, S. Eisebitt, W. Eberhardt, P. Pingel, D. Neher and N. Koch, Adv. Mater. **19** (2007) 3257.
[Bar10] L. Bartosch, M. de Souza, M. Lang, Phys. Rev. Lett. **104** (2010) 245701.
[Bau10] M. Baumgarten (2010), private communication.
[Blu02] N. Blümer, PhD theses, Universität Augsburg, (2002).
[Bor77] Yu.G. Borodko, M.G. Kaplunov, T.M. Moravskaya, and K.L. Pokhodnya, Phys. Stat. Sol. **83** (1977) 141.
[Bra07] S. Braun and W. Salaneck, Chem. Phys. Lett. **438** (2007) 259.
[Bro74] F.C. Brown: Solid State Phys. **1** (1974) 29.
[Bud07a] M. Budke, V. Renken, H. Liebl, G. Rangelov, and M. Donath, Rev. Sci. Instrum. **78** (2007) 083903.
[Bud07b] M. Budke, T. Allmers, M. Donath, and G. Rangelov, **78** (2007) 144521.
[Bun10] G. Bunker, Introduction to XAFS, Cambridge university press, 2010.
[Bun84] Bunker, G. B. *An x-ray absorption study of transition metal oxides, University of Washington,* Ph.D. Thesis, 1984.
[Cah03] D. Cahen and A. Kahn, Adv. Mater. **15** (2003) 271.
[Car75] T.A. Carlson: *Photoelectron and Auger Spectroscopy,* Plenum, New York, 1975.
[Cas09] V. Casagrande, A. Alvino, A. Bianco, G. Ortaggi, and M. Franceschin, J. Mass. Spectrom. **44** (2009) 530-540.
[Che08a] W. Chen, H. Huang, S. Chen, X. Y. Gao, and A. T. S. Wee, J. Phys. Chem. C **112** (2008) 5036.
[Che08b] W. Chen, H. Huang, S. Chen, Y. L. Huang, X. Y. Gao, and A. T. S. Wee, Chem. Mater. **20** (2008) 7017.
[Che10] D. Chercka, Diploma Thesis, 2010, Univ. Braunschweig
[Chi04] X. Chi, C. Besnard, V. K. Thorsmolle, V. Y. Butko, A. J. Taylor, T. Siegrist and A. P. Ramirez, Chem. Mater. **16** (2004) 5751.
[Cla02] R. Claessen, M. Sing, U. Schwingenschlögl, P. Blaha, M. Dressel and C. S. Jacobsen, Phys. Rev. Lett. **88** (2002) 096402.
[Col70] R. H. Colton and D. E. Henn, J. Chem. Soc. *B* (1970) 1532.
[Cor96] E. Coronado, P. Delhaes, D. Gatteschi, and J. S. Miller. *Molecular magnetism: from molecular assemblies to the devices.* Springer, (1996).
[Cra02] C. J. Cramer, *Essentials of computational chemistry: theories and models*, Wiley, Chichester, 2002.
[Cra03] A.M. van de Craats, N. Stutzmann, O. Bunk, M.M. Nielsen, M. Watson, K. Müllen, H.D. Chanzy, H. Sirringhaus, and R.H. Friend, Adv. Mater. **15** (2003) 495-499.

[Dos77] V. Dose, Appl. Phys. **14** (1977) 117.
[Duh06] S. Duhm, H. Glowatzki, V. Cimpeanu, J. Klankermayer, J. P. Rabe, R. L. Johnson and N. Koch, J. Phys. Chem. B **110** (2006) 21069.
[Duh08] S. Duhm, G. Heimel, I. Salzmann, H. Glowatzki, R. L. Johnson, A. Vollmer, J. P. Rabe, and N. Koch, Nature Mater. **7** (2008) 326.
[Fad74a] C.S. Fadley: Chem. Phys. Lett. **25** (1974) 225.
[Fad74b] C.S. Fadley: J. Electron Spectrosc. **5** (1974) 895.
[Fer08] I. Fernández-Torrente, K. J. Franke and J. I. Pascual, lnt. J. Mass Spectr. **277** (2008) 269.
[Fle10] I. Fleming, *Molecular Orbitals and Organic Chemical Reactions*, Willey, 2010.
[For97] A. Fortunelli, A. Painelli, J. Chem. Phys. **106** (1997) 8051.
[Fou03] D. Fournier, M. Poirier, M. Castonguay, and K. D. Truong, Phys. Rev. Lett. **90** (2003) 127002.
[Fra03] J. Fraxedas, Y. J. Lee, I. Jimenez, R. Gago, R. M. Nieminen, P. Ordejon, and E. Canadell Phys. Rev. B **68** (2003) 195115.
[Fri03] M. J. Frisch and J. A. Pople, *Gaussian 03, revision A.1*, Gaussian Inc., Pittsburgh, 2003.
[Gar74] A.F. G. and A.J. Heeger, Acc. Chem. Res. **7** (1974) 232-240.
[Gav08] J. Gavnholt, T. Olsen, M. Engelund and J. Schioøtz, Phys. Rev. B **78** (2008) 075441.
[Gel74] U. Gelius: Phys. Scr. **9** (1974) 133.
[Gie91] J. Giergiel, S. Wells, T. A. Land, J. C. Hemminger, Surf. Sci. **253** (1991) 31.
[Glo11] A. Gloskovskii, G.H. Fecher, C. Feher, S. Thiess, H. Schulz-Ritter, W. Drube, in preparation 2011.
[Gon08] N. Gonzales-Lakunza, I. Fernández-Torrente, K. J. Franke, N. Lorente, A. Arnau and J. I. Pascual, Phys Rev. Lett. **100** (2008) 156805.
[Gos75] O. Goscinski, B.T. Pickup, G. Purvis: Chem. Phys. Lett. **22** (1973) 167-171.
[Gri07] S. Grimme, J. Antony, T. Schwabe and C. Mück-Lichtenfeld, Org. Biomol. Chem. **5** (2007) 741–758.
[Gri89] M. Grioni, J. B. Goedkoop, R. Schoorl, F. M. F. de Groot, J. C. Fuggle, F. Schafers, E. E. Koch, G. Rossi, J.-M. Esteva, and R. C. Karnatak, Phys.Rev. B **39** 1541 (1989).
[Gro01] F. deGroot, Chem. Rev. **101** (2001) 1779.
[Hal97] H.S Nalwa. *Handbook of Organic Conductive Molecules and Polymers*, volume 1. John Wiley and Sons, (1997).
[Han65] N. B. Hannay, T. H. Geballe, B. T. Matthias, K. Andreas, P. Schmidt and D. Macnair, Phys. Rev. Lett. **14** (1965) 225.
[Har70] W.A. Harrison, *Solid State Theory*, McGraw-Hill, New York, (1970).
[Her50] G. Herzberg: Molecular Spectra and Molecular Structure, I. Spectra of Diatomic Molecules, Van Nostrand, New York, 1950.
[Hoh64] P. Hohenberg and W. Kohn, Phys. Rev. **136** (1964) B864-B871.
[Hue03] S. Hüfner, *Photoelectron Spectroscopy*, Springer Berlin-Heidelberg, 2003.
[Ich06] K. Ichimura and K. Nomura, J. Phys. Soc. Jpn. **75** (2006) 051012.
[Ich08] K. Ichimura, M. Takami, and K. Nomura, J. Phys. Soc. Jpn. **77** (2008) 114707.
[Ike77] I.Ikemoto, T. Sugano and H. Kuroda, Chem. Phys. Lett. **49** (1977) 45-48.
[Ike80] I. Ikemoto, M. Yamada, T. Sugano, and H. Kuroda, Bull. Chem. Soc. Jpn. **53** (1980) 1871-1876.

[Ike82] I. Ikemoto, K. Kikuchi, K. Yakushi, H. Kuroda and K. Kobayashi, Solid State Commun. **42** (1982) 257.
[Ima98] M. Imada, A. Fujimori, Y. Tokura, Rev. Mod. Phys. **70** (1998) 1039–1263.
[Isa82] I. Ikemoto, K. Kikuchi, K. Yakushi, H. Kuroda, K. Kobayashi, Solid State Communications **42** (1982) 257-259.
[Ish98] T. Ishiguro, K. Yamaji, and G. Saito, *Organic superconductors*. Springer, 1998.
[Ish99] H. Ishii, K. Sugiyama, E. Ito and K. Seki, Adv. Mater. **11** (1999) 605.
[Ito96] H. Ito, T. Ishiguro, M. Kubota and G. Saito, J. Phys. Soc. Jpn. **65** (1996) 2987-2993.
[Itt91] R. Itti, H. Mori, K. Ikeda, I. Hirabayashi, N. koshizuka, and S. Tanaka, Physica C **185-189** (1991) 2673-2674.
[Iwa89] Y.Iwasa, T.Koda, Y.Tokura, S.Koshihara, N.Iwasawa, and G.Saito, Appl. Phys. Lett., **55** (1989) 2111-2113.
[Izy08] Yu. A. Izyumov and N. I. Chashchin, Theoretical and Mathematical Physics, **154**(1) (2008) 52–63.
[Jae08] F. Jäckel, U. G. E. Perera, V. Iancu, K.-F. Braun and N. Koch, Phys. Rev. Lett. **100** (2008) 126102.
[Jes11] H. Jeske, private communication 2011.
[Jol78] W.L. Jolly, In *Electron Spectroscopy: Theory, Techniques and Applications* Vol. 1, ed. By C.R. Brundle, A.D. Baker, Academic, New York, 1978.
[Kag04] F. Kagawa, T. Itou, K. Miyagawa, and K. Kanoda, Phys. Rev. B **69** (2004) 064511.
[Kag05] F. Kagawa, K. Miyagawa, and K. Kanoda, Nature (London) **436** (2005) 534.
[Kah03] A. Kahn, N. Koch, and W. Gao, Journal of Polymer Science B **41** (2003) 2529.
[Kan09] H. C. Kandpal, I. Opahle, Y.-Z. Zhang, H. O. Jeschke, and R. Valentí, Phys. Rev. Lett. **103** (2009) 067004.
[Kan97] K. Kanoda, Hyperfine Interact. **104** (1997) 235 and Physica **C 282-287** (1997) 299.
[Kat02] T. Kato and T. Yamabe, J. Chem. Phys. **117** (2002) 2324-2331.
[Kaw11] S.-i. Kawano, M. Baumgarten, D. Chercka, V. Enkelmann, and K. Müllen to be submitted 2011.
[Kin85] A. M. Kini, D. O. Cowan, F. Gerson, and R. Möckel, J. Am. Chem. Soc. **107** (1985) 556.
[Kin90] A.M. Kini, U. Geiser, H.H. Wang, K.D. Carlson, J.M. Williams, W.K. Kwok, K.G. Vandervoort, J.E. Thompson, and D.L.Stupka, Inorg. Chem. **29** (1990) 2555-2557.
[Kin95] H. Kino and H. Fukuyama, J. Phys. Soc. Jpn. **64** (1995) 2726-2729.
[Koc05a] N. Koch, G. Heimel, J. Wu, E. Zojer, R. L. Johnson, J.-L. Brédas, K. Müllen and J. P. Rabe, Chem. Phys. Lett. **413** (2005) 390.
[Koc05b] N. Koch, S. Duhm, J. P. Rabe, A. Vollmer and R. L. Johnson, Phys. Rev. Lett. **95** (2005) 237601.
[Koc08] N. Koch, J. Phys.: Condens. Matter **20** (2008) 184008.
[Koh65] W. Kohn and L.J. Sham, Phys. Rev. **140** (1965) A1133-A1138.
[Kom96] T. Komatsu, N. Matsukawa, T. Inoue, G. Saito, J. Phys. Soc. Jpn. **65** (1996) 1340.
[Kra79a] M.O. Krause: J. Phys. Chem. Ref. Data **8** (1979) 307.
[Kra79b] M.O. Krause, J.H. Oliver: J. Phys. Chem. Ref. Data **8** (1979) 329.
[Lan03] M. Lang, J. Müller, F. Steglich, J. A. Schlueter, A. M. Kini and T. Sasaki, Synth. Met. **107** (2003) 133–134.
[Lan10] M. Lang, private communication, 2010.
[Lan11] T. Lancaster, S. J. Blundell, F. L. Pratt, and J. A. Schlueter, Phys. Rev. B **83** (2011) 024504.

[Lef00] S. Lefebvre, P. Wzietek, S. Brown, C. Bourbonnais, D. Jérome, C. Mézière, M. Fourmigué, and P. Batail, Phys. Rev. Lett. **85** (2000) 5420–5423.
[Lim03] P. Limelette, P. Wzietek, S. Florens, A. Georges, T. A. Costi, C. Pasquier, D. Jérome, C. Mézière, and P. Batail, Phys. Rev. Lett. **91** (2003) 016401.
[Lin88] J. M. Lindquistt and J. C. Hemminger, J. Phys. Chem. **92** (1988) 1395.
[Lin89] J. M. Lindquistt and J. C. Hemminger , Chem. Mat. **1** (1989) 72-78.
[Loi05] A. Loi, I. Manunza, and A. Bonfiglio, Appl. Phys. Lett. **86** (2005) 103512.
[Lon65] R. E. Long, R. A. Sparks and K. N. Trueblood, Acta, Crystallogr. **18** (1965) 932.
[Mac08] C. F. Macrae, I. J. Bruno, J. A. Chisholm, P. R. Edgington, P. McCabe, E. Pidcock, L. Rodriguez-Monge, R. Taylor, J. van de Streek, and P. A. Wood, J. Appl. Cryst. **41** (2008) 466.
[Man10] R. S. Manna, M. de Souza, A. Brühl, J. A. Schlueter, and M. Lang, Phys. Rev. Lett. **104** (2010) 016403.
[Man70] R. Manne, T. Aberg: Chem. Phys. Lett. **7** (1970) 282.
[Mar78] R.L. Martin, D.A. Shirley: *In Electron Spectroscopy: Theory, Techniques and Applications*, Vol. 1, ed. By C.R. Brundle, A.D. Baker, Academic, New York, 1978.
[May05] W. Ma, C. Yang, X. Gong, K. Lee, and A. J. Heeger, Adv. Functional Mat. **15** (2005) 1617.
[Med10a] K. Medjanik, D. Kutnyakhov, S. A. Nepijko, G. Schönhense, S. Naghavi, V. Alijani, C. Felser, N. Koch, R. Rieger, M. Baumgarten, and K. Müllen, Phys. Chem. Chem. Phys. **12**, (2010) 7184-7193.
[Med10b] K. Medjanik, S. Perkert, S. Naghavi, M. Rudloff, V. Solovyeva, D. Chercka, M. Huth, S. A. Nepijko, T. Methfessel, C. Felser, M. Baumgarten, K. Müllen, H.J. Elmers, and G. Schönhense Phys. Rev. B **82** (2010) 245419.
[Med10c] K. Medjanik, S. A. Nepijko, H. J. Elmers and G. Schönhense, P. Nagel, M. Merz, S. Schuppler, D.Chercka, M. Baumgarten and K. Müllen, arXiv 1012.3467 (2010) and to be published.
[Mel62] L. R. Melby R.J. Harder, W.R. Hertler, W. Hahler, R.E. Benson and. W.E. Mochel, J. Am. Chem. Soc. **84** (1962) 3374-87.
[Mue02] J. Müller, M. Lang, F. Steglich, J. A. Schlueter, A. M. Kini, T. Sasaki, Phys. Rev. B **65** (2002) 144521.
[Mue04] J. Müller, M. Lang, F. Steglich, J. A. Schlueter, J. Phys. IV France **114** (2004) 341.
[Mue08] K. Müllen and J. P. Rabe, Acc. Chem. Res. **41** (2008) 511.
[Mue10] J. Müller, J. Brandenburg, J.A. Schlueter, G.L. Gard, J. Phys.:Conf. Ser **200** (2010) 012133.
[Mue11] J. Müller, private comunication, 2011.
[Nag10a] S. Naghavi, T. Gruhn, V. Alijani, G. H. Fecher, C. Felser, K. Medjanik, D. Kutnyakhov, S. A. Nepijko, G. Schönhense, R. Rieger, M. Baumgarten, and K. Müllen, J. Mol. Spec., in print, and arXiv 1012.3028 (2010).
[Nag10b] S. Naghavi, T. Gruhn, C. Felser, K. Medjanik, and G. Schönhense, publication in preparation.
[Nag10c] S. Naghavi, PhD thesis, Johannes Gutenberg Univ. Mainz, 2010.
[Nal97] H. S. Nalwa, *Handbook of organic conductive molecular and polymers*, Wiley, 1997.
[Nel00] S. F. Nelsen, D. A. Trieber, M. A. Nagy, A. Konradsson, D. T. Halfen, K. A. Splan and J. R. Pladziewicz, J. Am. Chem. Soc. **122** (2000) 5940–5946.
[Nem76] V.V. Nemoshkalenko, V. G. Aleshyn, *Electron spectroscopy of the crystals*, Kiev Naukova Dumka, 1976.

[Oba10] M. Obara, A. Sekiyama, S. Imada, J. Yamaguchi, T. Miyamachi, T. Balashov, W. Wulfhekel, M. Yabashi, K. Tamasaku, A. Higashiya, T. Ishikawa, K. Fujiwara, H. Takagi, and S. Suga, Phys. Rev. B **81** (2010) 113107.
[Ope08] C. P. Opeil, B. Mihaila, R. K. Schulze, L. Mañosa, A. Planes, W. L. Hults, R. A. Fisher, P. S. Riseborough, P. B. Littlewood, J. L. Smith, and J. C. Lashley , Phys. Rev. Lett. **100** (2008) 165703.
[Par59] L.G. Parratt, Rev. Mod. Phys. **31** (1959) 616.
[Par89] R. G. Parr and W. Yang, *Density-functional theory of atoms and molecules*, Oxford University Press, Oxford, 1989.
[Pau39] L. Pauling, *The Nature of the Chemical Bond, Cornell University Press, Ithaca*, NY, (1939) 174–178.
[Per11] S. Perkert Diploma thesis, Johannes Gutenberg Univ. Mainz (2011) in preparation
[Pis07] W. Pisula, Ž. Tomović, M. D. Watson, K. Müllen, J. Kussmann, C. Ochsenfeld, T. Metzroth and J. Gauss, J. Phys. Chem. B **111** (2007) 7481-7487.
[Pro01] H. Proehl, M. Toerker, F. Sellam, T. Fritz, and K. Leo, Phys. Rev. B **63** (2001) 205409.
[Ram94] A. P. Ramirez, Supercond. Rev. **1** (1994) 49.
[Ran03] M. Randic, Chem. Rev. **103** (2003) 3449.
[Ran09] G. M. Rangger, O. T. Hofmann, L. Romaner, G. Heimel, B. Bröker, R.-P. Blum, R. L. Johnson, N. Koch and E. Zojer, Phys. Rev. B **79** (2009) 165306.
[Reh78] J.J. Rehr, E.A. Stern, R.L. Martin, E.R. Davidson: Phys. Rev. B **17** (1978) 560.
[Rie08] R. Rieger, M. Kastler, V. Enkelmann and K. Müllen, Chem. Eur. J. **14** (2008) 6322.
[Rie09] R. Rieger, private communication, 2009.
[Rit78] J.J. Ritsko, A.J. Epstein, W.R. Salaneck, and D.J. Sandman, Phys. Rev. B **17** (1978) 1506.
[Roh98] U. Rohr, P. Schlichting, A. Böhm, M. Gross, K. Meerholz, C. Bräuchle, and K. Müllen, Angew. Chem. **37** (1998) 1434-1437.
[Rud11] M. Rudloff, PhD theses, Johann Wolfgang Goethe Univ. Frankfurt (2011) in preparation.
[Sar07] S. Das Sarma, E. H. Hwang, and W.-K. Tse, Phys. Rev. B **75** (2007) 121406.
[Sas04a] T. Sasaki, I. Ito, N. Yoneyama, N. Kobayashi, N. Hanasaki, H. Tajima, T. Ito and Y. Iwasa, Phys. Rev. B **69** (2004) 064508.
[Sas04b] T. Sasaki, N. Yoneyama, N. Kobayashi, Y. Ikemoto and H. Kimura Phys. Rev. Lett **92** (2004) 227001.
[Sat81] N. Sato,K. Seki, and H. Inokuchi J. Chem. Soc., Faraday Trans. 2 77, 1621 (1981).
[Sch02] P. G. Schroeder, C. B. France, B. A. Parkinson and R. Schlaf, J. Appl. Phys. **91** (2002) 9095.
[Sch10] G.Schönhense, M. de Souza, K. Medjanik, A. Gloskowski, H.J. Elmers, J. Müller and M. Lang, in preparation.
[Sch85] G. Schönhense, A. Eyers, U. Friess, F. Schäfers and U. Heinzmann, Phys. Rev. Lett. **54** (1985) 547.
[Sch90] G. Schönhense, Physica Scripta T **31** (1990) 255.
[Sea79] M.P.Seah and W. A. Dench, *Surface and interface analysis* **1** (1979) 1.
[Shi03] Y. Shimizu, K. Miyagawa, K. Kanoda, M. Maesato, G. Saito, Phys. Rev. Lett. **91** (2003) 107001.
[Shi73] D.A. Shirley: Adv. Chem. Phys. **23** (1973) 85.
[Sie03] E. M. Siegbahn, *Faraday Discuss*. **289** (2003) 124.

[Sig03] M. Sing, U. Schwingenschlögl, R. Claessen, P. Blaha, J. M. P. Carmelo, L. M. Martelo, P. D. Sacramento, M. Dressel, and C. S. Jacobsen, Phys. Rev. B **68** (2003) 125111.
[Sin07] M. Sing J. Meyer, M. Hoinkis, S. Glawion, P. Blaha, G. Gavrila, C. S. Jacobsen, and R. Claessen Phys. Rev. B **76** (2007) 245119.
[Soe95] S. Söderholm, P.R. Varekamp, D. Schweitzer, Phys. Rev. B **52** (1995) 9629.
[Sol09] V. Solovyeva, K. Keller, and M. Huth, Thin Solid Films 517 (2009) 6671.
[Sou07] M. de Souza, A. Brühl, Ch. Strack, B. Wolf, D. Schweitzer, and M. Lang, Phys. Rev. Lett. **99** (2007) 037003.
[Sta10] E. Stavitski, F. M. F. de Groot, Micron **41** (2010) 687-694.
[Ste83] E.A. Stern, J.J. Rehr: Phys. Rev. B **27** (1983) 3351.
[Ste94] P.J. Stephens, F.J. Devlin, C.F. Chabalowski, and M.J. Frisch, J. Phys. Chem **98** (1994) 11623-11627.
[Sto92] J. Stöhr, *NEXAFS Spectroscopy*, Springer Series in Surface Science **25** (1992).
[Str39] I.N. Stranski and L. Von Krastanow, *Abhandlungen der Mathematisch-Naturwissenschaftlichen Klasse*, Akademie der Wissenschaften und der Literatur in Mainz, **146**, (1939), 797.
[Suz06] T. Suzuki, J. Levy, and J.T. Yates, Nano Lett. **6** (2006) 138-143.
[Sza82] A. Szabo, N.S. Ostlund: *Modern Quantum Chemistry: Introduction to Advanced Electronic Structure Theory*, Macmillian, New York, 1982.
[Sza99] A. Z. Szarka, L. A. Curtiss, and J.R. Miller, Chemical Physics **246** (1999) 147-155.
[Sze81]S. M. Sze, *Physics of Semiconductor Devices* ,Wiley, New York, (1981).
[Tan91] S. Tanuma, C.J. Powell and D.R. Penn, Surf. Interface Anal. **17** (1991) 911-926.
[Tic73] I. J. Tickle and C. K. Prout, J. Chem. Soc. Perkin Trans. **2** (1973) 727.
[Tin64] M. Tinkham: *Group Theory and Quantum Mechanics*, McGraw-Hill, New York, 1964.
[Toa09] T. Toader, G. Gavrila, W. Braun, J. Ivanco, and D. R. T. Zahn, Phys. Stat. Sol. (b) **246** (2009) 1510.
[Tof04] D. Toffoli and R. R. Lucchese, J. Chem. Phys. **120** (2004) 6010.
[Tor08] I. F. Torrente, K. J. Franke, and J. I. Pascual, Intern. J. Mass Spectrom. **277** (2008) 269.
[Tor75] J. B. Torrance, B. A. Scott, and F.B. Kaufman, Sol. State Commun. **17** (1975) 1369.
[Toy07] N. Toyota, M. Lang, and J. Müller, *Low-Dimensional Molecular Conductors*, Springer Series in Solid-State Sciences Vol. 154 (Springer-Verlag, Berlin, 2007).
[Tru77] K. D. Truong and A. D. Bandrauk, Can. J. Chem. **55** (1997) 3712.
[Tse10] T.-C. Tseng, C. Urban, Y. Wang, R. Otero, S. L. Tait, M. Alcami, D. Ecija, M. Trelka, J. M. Gallego, N. Lin, M. Konuma, U. Starke, A. Nefedov, A. Langner, C. Wöll, M.A. Herranz, F. Martin, N. Martin, K. Kern, and R. Miranda, Nat. Chem. **2** (2010) 374-379.
[Val10] R. Valenti, private communication, 2010.
[Vaz04] H. Vázquez, R. Oszwaldowski, P. Pou, J. Ortega, R. Perez, F. Flores and A. Kahn, Europhys. Lett. **65** (2004) 802.
[Vaz07] H. Vázquez, Y. J. Dappe, J. Ortega and F. Flores, J. Chem. Phys. **126** (2007) 144703.
[Wat01] M. D. Watson, A. Fechtenkötter and K. Müllen, Chem. Rev., **101** (2001) 1267.
[Wei10] F. Weickert, M. Brando, F. Steglich, P. Gegenwart, M. Garst, Phys. Rev. B **81** (2010)134438.
[Wil68] R. M. Williams and S. C. Wallwork, Acta Crystallogr. B **24** (1968) 168.

[Wil92] J. M. Williams, J. R. Ferraro, R. J. Thorn, K. D. Carlson, U. Geiser, H. H. Wang, A. M. Kini and M.-H. Whangbo, *Organic Superconductors*, Prentice Hall, Englewood Cliffs, 1992.
[Wol07] A.U.B. Wolter, R. Feyerherm, E. Dudzik, S. Süllow, C. Strack, M. Lang, and D. Schweitzer , Phys. Rev. B **75** (2007) 104512.
[Wup07a] J. Wu, W. Pisula, and K. Müllen, Chem. Rev. **107** (2007) 718-747.
[Xia06] S. Xiao, J. Tang, T. Beetz, X. Guo, N. Tremblay, T. Siegrist, Y. Zhu, M. Steigerwald, and C. Nuckolls, J. Am. Chem. Soc. **128** (2006) 10700-10701.
[Yam09] Y. Yamakita, M. Yamauchi and K. Ohno, J. Chem. Phys. **130** (2009) 024306.
[Yam98] Y. Yamashita, M. Tomura, J. Mater. Chem. **8** (1998) 1933.
[Yin88] M. Yingde, Z. Jintao, Z. Zhigui, Y. Ke, Z. Hengbin, G. Chunxiao, W. Zongmu, Y. Ling, J. Songchun, F. Yuguo, Jilin Daxue Ziran Kex. Xue. **99-4** (1988).
[Yuw91] R. C. Yu, J.M.Williams, H. H.Wang, J. E. Thompson, A. M. Kini, K. D. Carlson, J. Ren, M.-H. Whangbo, and P. M. Chaikin, Phys.Rev. B **44** 6932 (1991).
[Yuz97] L. Yu and D. Zhu, Physica C **282-287** (1997) 1899-1900.